U.PORTO

FEUP FACULDADE DE ENGENHARIA
UNIVERSIDADE DO PORTO

Master Thesis

Viability of an innovative manufacturing process using forged carbon for manufacturing a high-performance zero-emission vessel hydrofoil wing

João Moreira Ribeiro Alegre

Supervisors:
Prof. Carolina Furtado Pereira da Silva
Prof. Antonio Torres Marques

Master in Mechanical Engineering

Porto, March 2026

Acknowledgements

Firstly and foremost, I would like to thank the entire FEUP Academic Solar Team (FAST). The feeling to see my Team grow the way it did and as FAST as it did is something very hard to put into words. A heartfelt thanks to all team members I had the privilege to work with throughout these two years and who actually made my dream become reality. I wish you all the best in the challenges that lay ahead and I hope you know that I will be watching closely every single step of the way. This thesis is my last technical contribution to this incredible project, and I honestly hope it helps FAST to keep innovating, not being afraid of making things their own way and get bigger, better and faster prototypes on the water!

I express my full gratitude to the supervisors for this project, Prof. Dr. Carolina Furtado and Prof. Dr. Antonio Torres Marques, specially for allowing me to go trough with my own thesis idea. To Prof. Dr. Carolina, I will always be grateful for the opened way that all my ideas have been received at her office (both the great and the not so good ones), and specially for the courage of embarking with us as a Faculty Advisor right from the first days of FAST's existence. I would also like to thank Prof. Dr. Antonio's for all his passionate contributions and help during this work, where I had the opportunity to see in the first person his eloquence when addressing mechanical engineering - true masterclasses on composite materials. Many people don't understand that what is now an established Team at a national and international level would not be more then a few words and ideas if we hadn't had the full support of dynamic, interested and motivated Professors such as Prof. Dr. Carolina and Prof. Dr. Antonio. I was very lucky to be able to work with such inspiring experts and their encouragement, patience, and dedication during this process was essential for me to be able to develop such topics.

I would also like to thank everyone evolved in all the extensive laboratory sessions: Eng. Miguel Figueiredo and Rui Silva responsible for the mechanical testing laboratory at FEUP, Emilia Soares responsible for the micrography laboratory at FEUP, Dr. Pedro Campos for all the help and important insights on experimental testing and Dr. Nathan Klavzer for his help in performing the tomographic scans. Thank you for showing me the great work and practices typical from FEUP's unique excellence.

A very special thanks to everybody that one way or another shared this incredible journey at FEUP with me, from the summer internships to mentorship programs, awards, conferences and even some study sessions, I was fortunate enough to be part of it all and I really feel my journey at UP couldn't have been more complete. I have to thank my cousin Manuel for a lot more things then just the ones related with my academic path, but this is should be a good start. To Diogo for representing in a very good way the level of pride, excellence and self-demand typical from FAST and to actively instill those values on my project. To Goncalo for representing the companionship and supportiveness of the great team he now leads. Last but certainly not least, I would like to thank my very special Ana Maria, the greatest gift from my journey, for helping me all the way, specially the final push during these final weeks.

Finally, to my family, specially my parents, I want to thank you with all my heart, for the support and love during this time.

Thank you all for believing in me.

Abstract

Viability of an innovative manufacturing process using forged carbon for manufacturing a high-performance zero-emission vessel hydrofoil wings

João Moreira Ribeiro Alegre

Many aspects related with Forged Carbon structural components, specially its mechanical behavior, have never been explored or even documented. Some of the most fundamental parameters related with this kind of material are not yet possible to find on the literature, making it very challenging to truly design any high-performance component using this manufacturing technique. In this work, the most critical microstructural, mechanical and environmental parameters are determined experimentally, analyzed and given the results obtained, the viability of this process is also discussed considering most relevant factors that actively play a role on its safe performance, sustainability and efficiency. A T-shaped hydrofoil designed for the ATLANTICO solar vessel (the first competitive prototype by FAST) was used for the analysis on this project.

First, the manufacturing technology was studied and adapted in order to guarantee the highest representativeness between the specimens manufactured for experimental testing and the component that is intended to validate. In this context, after analyzing the microstructure of several specimens via optical micrography and micro-tomography (this way characterizing the microstructure as well as the probable failure modes and void distribution on both 2D and 3D visualization), the mold technology, design and impregnation process have been successively altered and optimized. It was then possible to obtain the mechanical properties avoiding defects related with the manufacturing process and ensuring a stable geometric tolerancing among different specimens as much as possible.

Experimental testing was performed by following the respective ASTM standards regarding density determination and tensile properties, on this last case with the implementation of DIC in order to obtain a correlation of the displacement fields using the GOM software. During the second testing phase, given the possibility of orthotropy behavior detected in the first testing phase, the standard ASTM D3039 was also adapted in order to determine the strain concentration around a circular hole. By interpolating the DIC data obtained from this tests using a *Matlab* script and comparing it with a the numerical solution for the same problem, it was intended to be able to depict the level of orthotropy characteristic of this specific mold design. All the specimens concerning the circular hole train concentration failed outside of the circular hole section, indicating that the high VVF detected on the micro-tomography scans for the geometry of these specimens, is competing with the 5 mm circular hole. This, allied with the typical noise induced by the DIC, severely compromised the outputs of these tests.

The hydrodynamic loads were determined numerically for two distinct load cases (take-off and cruise conditions) using the *XFLR5* software, complemented with a *Matlab* script, used to compute the corresponding load components for specific finite regions along the wingspan. Finally, these load cases were simulated using a simplified half-wing numerical CAE model that approximated the load distribution computed for each spanwise section to a set of Lift, Drag and Pitching Moment solicitations applied on the hydrodynamic center of each section. In the model, this load distributions were successively adapted and the stress analysis of the structure was performed. This model also allowed for the determination of the Margins of Safety relative to each of the load cases, by adding a safety coefficient in order to account for any eventual unsteady flow effects (waves, maneuvering, rapid pitch changes) and therefore, validate the structural integrity of the part.

A Life Cycle Assessment (LCA) was also conducted using the MarineShift360 software, in order to evaluate and compare the environmental impacts associated with this manufacturing technology relative to other approaches commonly used for hydrofoil wings, focusing specifically on a cradle-to-gate analysis. Additional parameters such as stiffness, strength and cost were also characterized for each of the alternative manufacturing processes submitted for comparison on the LCA.

Keywords: Hydrofoil, Composites, Experimental testing, Finite Element Method, LCA.

Contents

Acknowledgements i

Abstract iii

List of Figures vii

List of Tables xi

List of Symbols xiii

1 Introduction 1
- 1.1 Context . . . 1
- 1.2 Methodology . . . 3
- 1.3 Thesis layout . . . 4

2 Background 5
- 2.1 Composite materials . . . 5
  - 2.1.1 Composites in hydrofoil wings manufacturing . . . 6
  - 2.1.2 Forged carbon process . . . 10
  - 2.1.3 Failure modes on Forged Carbon components . . . 15
- 2.2 Microstructural analysis and measurement . . . 18
  - 2.2.1 Optical Micrography . . . 19
  - 2.2.2 X-ray Computed Tomography . . . 22
  - 2.2.3 Digital Image Correlation (DIC) . . . 27
- 2.3 Mechanical testing in composites . . . 30
- 2.4 Hydrofoil design theory . . . 37
  - 2.4.1 Hydrofoil geometry . . . 37
  - 2.4.2 Hydrodynamic Loads . . . 38
  - 2.4.3 ATLANTICO specially designed Hydrofoil Type-B . . . 45

3 Experimental testing 49
- 3.1 Specimen preparation . . . 49
- 3.2 Standards . . . 51
  - 3.2.1 Laboratory methodology . . . 51
- 3.3 Mold design . . . 54
- 3.4 Microstructure analysis . . . 56
  - 3.4.1 Optical Micrography . . . 56
  - 3.4.2 Micro-CT . . . 60
- 3.5 Experimental Results . . . 65
  - 3.5.1 Tensile Test - ASTM D3039 . . . 65
  - 3.5.2 Tensile Test for strain concentration at an open circular hole . . . 71

4 Numerical Simulations **77**
4.1 Stress concentration around a circular hole - ASTM D3039 Specimen 77
4.1.1 The infinite plate load case verification 77
4.1.2 Simulation of the D3039 specimen 79
4.1.3 Strain concentration around on the D3039 specimen circular hole 82
4.2 Hydrodynamic model 87
4.2.1 XFLR5 87
4.2.2 Load distribution 92
4.3 Hydrofoil load cases 93
4.3.1 Numerical model 93
4.3.2 Stress analysis 97
4.3.3 Margin of safety 101

5 Life Cycle Analysis **104**
5.1 Methodology 104
5.1.1 Goal and scope definition 104
5.1.2 Functional unit - Materials and methods 105
5.1.3 System boundaries 107
5.1.4 Impact assessment and indicators 107
5.2 Life Cycle Inventory (LCI) 108
5.2.1 Bill of materials and process 108
5.3 Life Cycle Impact Assessment 111
5.3.1 Results 111
5.3.2 Discussion and limitations 114

6 Conclusions **117**
6.1 Achievements 117
6.2 Future Work 119

A Carbon fiber datasheet **127**

B IN2 Epoxy Infusion Resin datasheet **133**

C Effect of Laminate Layup and Stacking Sequence on Stress Concentration **136**

D Inventory Explanation Report **137**

List of Figures

1.1 ATLANTICO Prototype 1
1.2 Comparison between the drag values of ATLANTICO with and without hydrofoils. (model taken from a specially developed *Matlab* script using ATLANTICO drag curves). 2

2.1 Schematic reinforcement arrangements in composites 6
2.2 Schematics of both Twill (left) and Plain (right) configurations 7
2.3 Hand lay−up method [15] 8
2.4 Vaccuum bag process [15] 8
2.5 Resin Transfer Molding method [15] 9
2.6 Compression Molding method [18] 9
2.7 MDF machined molds for Type-B hydrofoil 11
2.8 Impregnation of the carbon fiber on the bottom mold part 12
2.9 Effect of fiber length on mechanical properties, normalized against continuous fiber properties [22] 13
2.10 Microscopic images of failed SMC samples and failure mode description according to [25] 16
2.11 Magnification (schematic configuration for darkfield microscopy) adapted from [33] . 19
2.12 Airy disks and resolution. (a-c) Airy disk size and related intensity profile (point spread function) as related to objective numerical aperture, which decreases from (a) to (c) as numerical aperture increases. (e) Two Airy disks so close together that their central spots overlap. (d) Airy disks at the limit of resolution. Adapted from [33] 20
2.13 Objective specifications. Adapted from [35] 22
2.14 Schematics of X-ray conversion and magnification (adapted from [37]) 23
2.15 Principles of a tomographic measurement [40] 24
2.16 Beam hardening in simulated scans. (A-D) Simulated scans without and (E-H) with beam hardening, showing that dark streaks occur along the lines of greatest attenuation, and bright streaks occur in other directions. Scatter produces artifacts that look similar to this. [42] 25
2.17 Example of an histogram where the two peaks indicate a clear threshold value (adapted from [44]) 26
2.18 DIC evolution (from left to right): obtain a pattern on the sample for tracking; capture images of the sample during deformation; analyze the images to compute the sample surface displacements. [48] 27
2.19 Detail of the specimen surface prepared with a random speckle pattern. Nomenclature details [47] 29
2.20 Coupon dimensions for random-discontinuous specimens. Adapted from [55] 32
2.21 Progressive micro-cracking leading to ultimate failure in unidirectional composite under transverse tension. Adapted from [24] 32
2.22 Semicircular curved beam specimen for determination of interlaminar tensile strength. Adapted from [24] 34

2.23 Composite laminate with circular hole under uniaxial tensile loading. Adapter from [24] 35
2.24 Values of Es/E for the 24D-T3 aluminum alloy when subjected to different applied stresses. Adapter from [56] . . . 36
2.25 Cambered foil section scheme . . . 37
2.26 Dimentions for the unswept wing [58] . . . 37
2.27 Fliteboard E-Foil strut system (left) and the Luna Rossa AC75 racing yacht wings (right). [59, 60] . . . 38
2.28 Fluid element representation - notation for the stresses . . . 39
2.29 Pressure distribution around a foil section [62] . . . 40
2.30 Resultant aerodynamic force acting at the centre of pressure [58] . . . 41
2.31 Variation of the lift coefficient with the angle of attack [58] . . . 42
2.32 Wing-tip trailing vortices representation . . . 43
2.33 Effect of downwash on the local flow over a local airfoil section of a finite wing [65] . . . 43
2.34 Effect of wing-tip vortices on a cambered foil - 2D vs 3D evolution [63] . . . 44
2.35 Hydrofoil system on the boat . . . 45
2.36 Comparison between edge flap control (left) and varying incidence control (right) [2] 46
2.37 Comparison between the two profiles: AG25 (green) and NACA 63_1412 (red) . . . 46
2.38 OpenFOAM simulation on the hydrofoil wing + strut assembly (for the definition of the critical areas [71] . . . 47
2.39 Final hydrofoil wing configuration . . . 48

3.1 Specimen preparation - labeled specimens after compression for bonding of the tabs 50
3.2 Optimal DIC painting speckle. . . . 51
3.3 Specimen preparation - Excel table regarding the complete process . . . 51
3.4 System alignment - Specimen alignment on the grip using a bench vise and a clipper. 53
3.5 2D Hydrofoil section mold after de-molding . . . 55
3.6 Final PETG mold assembly model . . . 55
3.7 Specimen preparation - Optical microscopy . . . 56
3.8 Specimen preparation - Optical microscopy . . . 57
3.9 Distortion on the fiber alignment . . . 57
3.10 Examples of intra-tow voids . . . 58
3.11 Examples of inter-tow void . . . 58
3.12 Examples of resin-pocket void . . . 59
3.13 Fiber breakage example . . . 59
3.14 Matrix crack example . . . 60
3.15 Interior view of the ZEISS VersaXRM 615 . . . 61
3.16 Dragonfly interface during void segmentation. . . . 62
3.17 Definition of the orthogonal viewing planes used for volumetric analysis. . . . 63
3.19 3D discretization - color code for void volume - during segmentation (using only lower ostu). . . . 63
3.18 Stacked orthogonal views of the reconstructed volume during ROI segmentation. . . . 64
3.20 Void volume histogram. . . . 65
3.21 GOM Correlate output - Displacement field for specimen 7. . . . 66
3.22 Experimental setup. . . . 68
3.23 Stress–strain curve obtained from DIC for Specimen 7. . . . 68
3.24 Stress–strain curves for the specimen batch. . . . 69
3.25 Examples of failure types . . . 69
3.26 Failure codes according to D3039 standard [55]. . . . 70
3.27 Strain field around the circular hole obtained using GOM interface - sections at $\theta = 90°$ and $\theta = 0°$. . . . 72
3.28 Location of the remote stress furface component on GOM. . . . 72

3.29 Adimensional strain for 3 different DIC frames (obtained using GOM Correlate). . . . 73
3.30 Strain field distribution curves - Raw data; MLS Smoothing and Curve fitting equation. 73
3.31 Strain field longitudinal distribution in GOM - Sections + Surface component for remote strain determination. 75
3.32 Strain field longitudinal distribution. 75

4.1 Infinite plate simulation part module and partitions 78
4.2 Meshing around the circular hole 79
4.3 Distributions of stress concentrations for different relations of half-width to hole radius W/r along the distance to the mid-plane through half-thickness $2d/B$. Adapted from [79]. 80
4.4 Final model with the modified BC's. 82
4.5 Obtained values for K_t for the different values of E_2 with polynomial regression curve equation for the ASTM D3039 specimen. 82
4.6 Stress and strain distributions similarity for the quasi-orthotropic model. 83
4.7 Set of nodes from the transversal path created on Abaqus 83
4.8 Set of nodes from the longitudinal path created on Abaqus 84
4.9 Reaction forces [N] for the different material models plot from *Abaqus* 85
4.10 Transversal strain distribution. 85
4.11 Longitudinal strain distribution. 86
4.12 Comparison between the script results on models obtained numerically and experimentally 87
4.13 XFLR5 interface for direct foil design - NACA63-412. 88
4.14 XFLR5 interface for direct foil design - NACA63-412. 88
4.15 XFLR5 interface for direct foil design - Wing geometry edition. 89
4.16 Example of C_p and downwash visualization using XFLR5 - defined for 6° AoA. 89
4.17 Polar plots obtained in XFLR5 for the cruise speed AoA 1°. 90
4.18 Lift Coefficient distributions 91
4.19 Drag Coefficient distributions 91
4.20 Pitching Moment Coefficient distributions 92
4.21 Lift per unit span during Take-off conditions. 93
4.22 Hydrofoil model - Split Solidworks feature. 94
4.23 Hydrofoil model mesh. 95
4.24 Hydrofoil model trailing edge mesh detail - poor geometry. 95
4.25 Hydrofoil model RF kinematic couplings. 96
4.26 Hydrofoil model Loads and BC's. 96
4.27 Von Mises stress distribution - Take-off conditions (isotropic model). 98
4.28 Von Mises stress distribution - Cruise conditions (isotropic model). 98
4.29 Displacement distribution - take-off conditions (isotropic model). 98
4.30 Displacement distribution - cruise conditions (isotropic model). 99
4.31 Nodal discrepancies on the trailing edge elements. 99
4.32 S_33 distribution along a spanwise section. 100
4.33 Mesh convergence study. 101
4.34 Similarity between the Principal and Longitudinal Stresses. 102

5.1 LCA structure and main phases. 105
5.2 System boundaries considered for this study (manufacturing phase only). 109
5.3 Production process of 1kg carbon fiber from PAN fibers (adapted from [85]). 110
5.4 Relative Global warming potential fossil (GWP). Three aluminum wings (in blue); Three CF Prepeg wings (in orange); Three FC wings (in green); Three FC re-use wings (in red). 111

5.5 Relative Cumulative Energy Demand (CED). Three aluminum wings (in blue); Three CF Prepeg wings (in orange); Three FC wings (in green); Three FC re-use wings (in red). 111
5.6 Waste factor discrepancy for FC (in blue) and CF Prepeg (in orange). 112
5.7 Envionmental impact of composites under end-of-life scenarios (adapted from [98]). GMT, (Glass-Mat-Reinforced Thermoplastics); NFRP (Natural Fiber Reinforced Plastics). 116

List of Tables

2.1 Mechanical properties for different manufacturing techniques adapted from [5] (for Aluminum the minimum yield strength is reported, while for the composites the ultimate strength is reported) . . . 10
2.2 Datasheet Properties of the Carbon Fibre Chopped Tow . . . 13
2.3 Datasheet Properties of the IN-2 Epoxy Infusion Resin . . . 14
2.4 Comparison between AG25 and NACA 63412 -SolidWorks section properties for 100mm chord . . . 46
2.5 Wing geometric features . . . 48

3.1 Specimen 32 volumetric measurements . . . 52
3.2 Density for specimen 32 . . . 52
3.3 Ideal material proportions for a 3D printed forged carbon mold . . . 54
3.4 Main technical specifications of the ZEISS VersaXRM 615. . . . 61
3.5 DIC setup and acquisition parameters . . . 66
3.6 Relative dimensional errors and suitability of specimens for testing . . . 67
3.7 Mechanical properties of suitable specimens (Regular FC) . . . 67
3.8 Mechanical properties of the forged carbon material . . . 70
3.9 Geometric tolerancing of specimens used for strain concentration at an open circular hole . . . 71
3.10 Interpolation results exported by the script for the experimental tests. Being S and C the fitting parameters for the equation $\frac{\epsilon}{\epsilon_{rem}}(y) = S\sigma_{xx}(0,y) + C$. . . . 74

4.1 Stress concentration factors K_t for circular hole transverse path tests - relative error between the force/displacement models. . . . 79
4.2 Reference values for $G_{12} = 10000$ MPa . . . 81
4.3 Reference values for $G_{12} = 7000$ MPa . . . 81
4.4 Representative orthotropic material properties for different layups . . . 81
4.5 Ke and Kt values for the different material models . . . 84
4.6 Remote stress and characteristic length for an imposed displacement of 4 mm. . . . 85
4.7 Interpolation results exported by the script for Abaqus simulations. . . . 86
4.8 Material properties used for isotropic and orthotropic models . . . 94
4.9 Sectional hydrodynamic load distribution for take-off conditions - taken from XFLR5. 97
4.10 Vertical and horizontal force components along the span - compensation for 6°. . . . 97
4.11 Sectional hydrodynamic load distribution for cruise conditions - taken from XFLR5. . 97
4.12 Vertical and horizontal force components along the span - compensation for 1°. . . . 97
4.13 Stress and strain values for the take-off conditions (neglecting the stress field discrepancies around the trailing edge). . . . 100
4.14 Stress and strain values for the cruise conditions (neglecting the stress field discrepancies around the trailing edge). . . . 100

4.15 Mesh refinement study showing the influence of mesh density on computational cost and maximum displacement. . . . 100
4.16 Tensile safety margin evaluation for the hydrofoil under cruise and take-off conditions - Isotropic approach. . . . 102
4.17 Tensile safety margin evaluation for the hydrofoil under cruise and take-off conditions - Orthotropic approach. . . . 103

5.1 Material properties and constituent weight percentages used for the hydrofoil manufacturing scenarios. . . . 106
5.2 Orthotropic woven ply equivalent mechanical properties adapted from [90]. . . . 106
5.3 Bill of materials for the hydrofoil alternatives. . . . 108
5.4 Margin of Safety for the different materials. . . . 113
5.5 Maximum displacement and relative difference for each model. . . . 113
5.6 Cost comparison between different manufacturing materials. . . . 114

C.1 Comparison of Measured and Predicted Stress Concentration Factors and Strengths for Various Layups . . . 136

List of Symbols

Acronyms and abbreviations

AoA	Angle of Attack
AR	Aspect Ratio
ASTM	American Society for Testing and Materials
BC	Boundary condition
BMC	Bulk Molding Compound
CFRP	Carbon Fiber Reinforced Polymer
CT	Computed Tomography
DIC	Digital Image Correlation
FAST	FEUP Academic Solar Team
FEM	Finite Element Method
FRP	Fiber Reinforced Polymer
GFRP	Glass Fiber Reinforced Polymer
LCA	Life Cycle Analysis
MAC	Mean Aerodynamic Chord
Micro-CT	Micro Computed Tomography
MLS	Moving Least Squares
RAM	Random Access Memory
ROI	Region of Interest
RTM	Resin Transfer Molding
SMC	Sheet Molding Compound
TMC	Thick Molding Compound
UD	Unidirectional
Vf	Fiber Volume Fraction
XRM	X-ray Microscopy

Variables

$(E_s)_\infty$	Secant modulus at far-field stress
α_i	Induced angle of attack
$\bar{\nu}_{xy}$	Average Poisson's ratio
$\bar{\sigma}_0$	Applied far-field average stress
$\bar{\sigma}_{\max}$	Maximum circumferential stress at the hole boundary
$\bar{c}$	Mean aerodynamic chord (MAC)
$\bar{E}_x, \bar{E}_y$	Average Young's moduli in the x and y directions
$\bar{G}_{xy}$	Average in-plane shear modulus
γ_{ij}	Engineering shear strain
Λ	Wing sweep angle
λ	Taper ratio ($c_{\text{tip}}/c_{\text{root}}$)
λ	Wavelength of light (Chapter 2)
$\mathbf{S}$	Compliance tensor
ν	Poisson's ratio
ν_{ij}	Poisson's ratio relating strain in direction j to stress in direction i
ρ	Mass density
σ_r	Radial stress
σ_y	Yield stress
σ_∞	Applied far-field stress
σ_θ	Circumferential stress
σ_{ij}	Cauchy stress tensor components
σ_{xx}	Normal stress in the x direction
τ	Shear stress
$\tau(x)$	Local wall shear stress
τ_{ij}	Shear stress components
θ	Angular coordinate around the hole
ε_{ij}	Infinitesimal strain tensor
a	Hole radius
a_0	Two-dimensional lift curve slope
a_{3D}	Three-dimensional lift curve slope

AR	Aspect ratio
b	Wingspan
C_D	Drag coefficient
C_f	Skin-friction coefficient
C_L	Lift coefficient
C_M	Pitching moment coefficient
C_p	Pressure coefficient
c_{root}	Root chord length
c_{tip}	Tip chord length
C_{D0}	Zero-lift drag coefficient
C_{D_i}	Induced drag coefficient
C_{ij}	Components of the stiffness tensor
D	Drag force
E	Young's modulus
e	Oswald efficiency factor
E_s	Secant modulus
G	Shear modulus
I	Transmitted X-ray intensity
I_0	Incident X-ray intensity
K_t	Stress concentration factor
K_t^∞	Stress concentration factor for an infinite plate
k_σ	Stress concentration factor
L	Distance between the applied load and the test section
L	Lift force
M	Finite-width correction parameter
M	Pitching moment
n_e	Number of elements
n_n	Number of nodes
n_p	Number of points
P	Applied tensile load
p	Hydrostatic pressure

R	Hole radius
r	Radial distance from the hole center
r	Radius of curvature of the streamline
R_R	Resolution limit according to the Rayleigh criterion
S	Wing planform area
t	Time variable
U	Local flow velocity magnitude
u_i	Displacement component in the i direction
U_∞	Free-stream velocity
W	Specimen width
x_i	Spatial coordinate in the i direction

Operators

$(\bullet)^T$	Transpose of $(\bullet)$
$(\bullet)^{-1}$	Inverse of $(\bullet)$
δ_{ij}	Kronecker delta
$\nabla(\bullet)$	Gradient of $(\bullet)$
$\|\bullet\|$	Norm or jump of $(\bullet)$
$\partial(\bullet)/\partial(*)$	Partial derivative of $(\bullet)$ with respect to $(*)$
$\sum$	Summation operator

Chapter 1

Introduction

1.1 Context

Hydrofoils were inadvertently discovered in 1861, marking the beginning of a revolutionary shift in naval architecture for both military and passenger vessels. The idea of lifting the hull of a vessel above the water using submerged wings was intended to reduce the hydrodynamic drag and significantly increase speed and efficiency. Although its practical application would only gain traction decades later, hydrofoils play an increasingly important role in modern marine transportation, from high-speed ferries and military craft to cutting-edge electric racing boats and recreational vessels [1].

Today, hydrofoils are at the forefront of innovation in sustainable marine design: by lifting the hull out of the water, they reduce the energy consumption compared to conventional hulls, making them ideal for integration with electric and hybrid propulsion systems. This synergy is particularly valuable in cases such as the FAST's zero emission competition prototype - ATLANTICO (Figure 1.1).



Figure 1.1: ATLANTICO Prototype

ATLANTICO has a considerably large structure for a Solar Boat Class vessel - more then 6 meters long and 2.3 meters beam - also, it carries almost 6 m^2 of solar panels, a 1.5 kWh battery and a 15 kW electric motor. The boat has a catamaran configuration with three sets of T shaped hydrofoils and the hulls, being entirely constructed using natural fibers, weight more than 50 kg each, leading to a lightship displacement of around 220 kg. In applications such as the one described for ATLANTICO, the efficiency can be highly improved by the implementation of hydrofoils. In Figure 1.2, it is possible to see the drastic difference in the behavior of the Drag curve when we consider a configuration with hydrofoils compared to the one considering the just the effect of the two hulls, indicating to an increase in efficiency of more the 200% for velocities around the endurance speed.

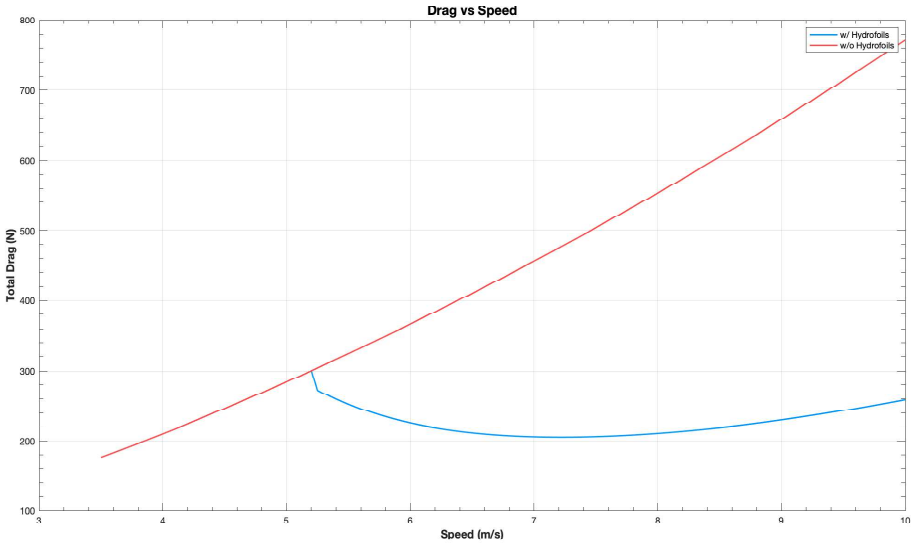


Figure 1.2: Comparison between the drag values of ATLANTICO with and without hydrofoils. (model taken from a specially developed *Matlab* script using ATLANTICO drag curves).

The materials used in hydrofoil construction reflect the need for lightweight, strong, and durable components. High performance composites such as carbon fiber reinforced polymers and marine grade aluminum are commonly employed due to their excellent strength-to-weight ratios and durability. However, their manufacturing processes can be complex and cost-intensive, often involving precision molding and autoclave curing [2]. This leads to variability of the mechanical properties, multiple and complex failure modes and susceptibility to flaws. The lack of in-service design data means that tools and expertise to predict the behavior of these structures draw a lot of interest, not only from the student teams but naturally from the entire industry.

The proposed manufacturing process is an adaptation of the general compression molding technique, which uses short, randomly oriented carbon fibers combined with resin to have the required conformability to the complex geometries, having no specific pressure or temperature requirements.

The objective of this thesis is to evaluate the viability of implementing this alternative manufacturing process, aiming at reduce the environmental impact of hydrofoil production in the life cycle, while simultaneously lowering the cost and complexity of the process, in this case using the real hydrofoil wings of the ATLANTICO prototype as an example.

1.2 Methodology

This thesis addresses an innovative manufacturing process, and a gradual approach was implemented to try to get a concise conclusion about the framework.

At first, two models of carbon fiber parts (previously manufactured by the Team) were analyzed in order to understand the structure of the process, its main problems, and eventual limitations: the first being the real size hydrofoil mold (machined in MDF wood) and the second one, a 3D printed mold representing a section of the hydrofoil wing at the root (with around 125 mm chord length).

Afterwards, an intensive research was performed on a series of studies that already addressed processes similar to the one proposed in this thesis. Significant contributions were made by John et al. [3], performing a preliminary study on the same material used for this work and experimental testing on a practical application. Regarding the manufacturing process specifications, both Mitsubishi [4] and Lamborghini [5] have presented a detailed description of their own alternatives and methodology approaches on this process. Many more general studies such as John et al. [6], Zeyu et al. [7] or Thomason et al.[8] have managed to perform extensive comparisons between compression molding and other CFRP manufacturing techniques, capturing the behavior of most of the possible variables on these processes.

However, as referred in the previous section, the bibliography on the Forged Carbon Composites is very limited and these three last examples do not specifically address this technique but rather similar methodologies. Therefore, an extensive research was performed in order to select the best methods and standards to adapt in order to experimentally determine a precise estimation of the mechanical behavior of this material. Based on the literature, a concise list of possible failure modes was also established in order to understand which kind of analysis would be the most conclusive.

After gathering this information, the next step was the design of 3D printed molds that allowed the experimental testing of this material according to those standard specifications. Optimizations and modifications were iteratively implemented on these molds based on both experience and technical advancements along this work.

An extensive specimen manufacturing phase was conducted, experimenting with different kind of configurations and the microstructure analysis of the specimens was also performed via optical micrography and X-ray tomography in order to depict the overall morphology and behavior of the final material.

Given the results, several numerical models were developed and analyzed, the first one being a 3D panel method based simulation on XFLR5 in order to determine the load distribution along the wing for real practical load cases from the ATLANTICO prototype. Then, a FEM model was implemented in order to check the structural integrity of the part, given the loads taken from this analysis.

Lastly, the models were analyzed and the final optimized process was proposed. The environmental performance of the proposed manufacturing approach was then evaluated through a Life Cycle Assessment (LCA), in which the main stages of the hydrofoil manufacturing process were modeled and their associated environmental impacts quantified. This analysis focused on a cradle-to-gate system boundary and allowed a comparison between the forged carbon solution and alternative hydrofoil manufacturing approaches commonly used in practice.

1.3 Thesis layout

This thesis is divided in different chapters:

- **Chapter 2 - Background**: where relevant background on composite materials, FEM, hydrodynamics and experimental testing is provided.
- **Chapter 3 - Experimental Testing**: where the design, implementation, results from the experimental testing are reported and analysed.
- **Chapter 4 - Numerical Simulations**: where the implementation and verification of the FEM models are discussed.
- **Chapter 5 - Life Cycle Analysis**: where obtained results are combined into a comparative LCA between different processes.
- **Conclusion and future work**: where the achievements and potential future work are discussed.

Chapter 2

Background

In this chapter, background concepts related with the manufacturing and structural problems at hand are covered, leading up to the definition of aspects that will be used for the viability analysis of the proposed method for the hydrofoil wing manufacturing. A review of concepts relative to hydrofoil design, hydrodynamic loads, composite materials and failure modes associated with the forged carbon process will be addressed.

2.1 Composite materials

Many of the materials we find on our daily basis are composites. We can find them in the nature, as it is the case of the wood or even our bone structure, and it is also possible to find them in many industrial applications, such as in the maritime field for the case of Fiber Reinforced Polymers (FRP).

The main attribute of the composite materials is the way that a more rigid and resistant component (in this case, the fiber) is bound with a continuous phase material called the matrix (in this case the resin). Another interesting attribute of these materials is the possibility of adapting its mechanical properties in determined directions, given that the different orientation, properties and geometry of the fibers will lead to a significant anisotropy of the material. This anisotropy can be very useful in cases where it is possible to get a good estimation of the direction of the main mechanical solicitations. This way, the composite material should always be manufactured given the direction where it will be requested the most [9].

Other, less well known advantages include part-count reduction, electromagnetic transparency, resistance to erosion and wear, acoustic and vibration damping, thermal and acoustic insulation, low thermal expansion, tunable thermal conductivity, self-healing behavior, adjustable permeability, improved fire resistance, lightning-strike protection, and magnetoelectric responsiveness [10].

The usage of carbon-fiber-epoxy became more and more popular in marine applications due to the increasing development of hydrofoil craft and other high-performance vessels, supplanting the more traditional glass fiber/polyester resin [11]. This phenomenon is mostly related with dramatic difference in the properties of these two options. Despite the glass fiber being evidently cheaper than carbon fiber, in components where the demand is as high as in an hydrofoil wing, carbon arises as the most suitable solution due to its stiffness, strength and moisture resistance [9].

The main limitations on the usage of fiber composites are, as referred previously, its price and its lower impact strength when compared with glass fiber [12]. However, the impact strength can be improved given the modifications in the manufacturing process as is seen in the next sections - one of the main characteristics of the method proposed in this work.

2.1.1 Composites in hydrofoil wings manufacturing

It is well known that in the early developments of hydrofoil construction the materials used were mainly metals, such as marine grade aluminum or aluminum−copper alloys that were then machined. Even high tensile steel has been documented to be a suitable option for larger, more demanding vessel applications [1]. The growing interest in the application of 3D printing for the production of hydrofoil wings has been noticeable, however, its application has so far been limited to small scale tests and is not yet suitable for scaling up to crewed vessels [13] [14].

The need to achieve high performance and sustainable solutions led the industry to discover alternative materials and manufacturing processes that were able to guarantee the best possible specific mechanical properties (such as fatigue resistance, stiffness and corrosion). Since their emergence in the 1970s, composite materials have been widely adopted across the transportation sector. In the case of marine lifting surfaces, the initial reluctance to employ composite materials has gradually diminished, supported by extensive research and growing performance demands leading to the predominance of *Fiber Reinforced Polymers* in hydrofoil construction nowadays.

As referred in the begging of this section, FRP consists of a fibrous reinforcement embedded within a polymeric matrix where fibers such as carbon, glass or flax are frequently employed due to their strength, stiffness and fatigue resistance while polymer matrices bind these fibers ensuring correct alignment as well as enabling stress transfer and offering protection from mechanical abrasion and environmental factors such as moisture, ultraviolet radiation and chemical attacks, being an excellent option for marine applications [12].

Important parameters on FRP

The behavior of fiber reinforced composites depends on several factors besides the material of its constituents. The fiber arrangement, orientation and concentration are decisive parameters, having a fundamental influence on the resulting mechanical properties of the composite.

In terms of arrangement, it is possible to find continuous and discontinuous fibers, where for the case of continuous fibers, the strength and stiffness are optimized along the direction of the fibers, usually presenting improved overall mechanical properties. On the other hand, for discontinuous fiber composites, the properties strongly depend on the length and amount of fibers. Although short fibers allow for easier manufacturing and adaptability on complex geometries, they usually result in lower strength and stiffness compared to the equivalent case using continuous fibers.

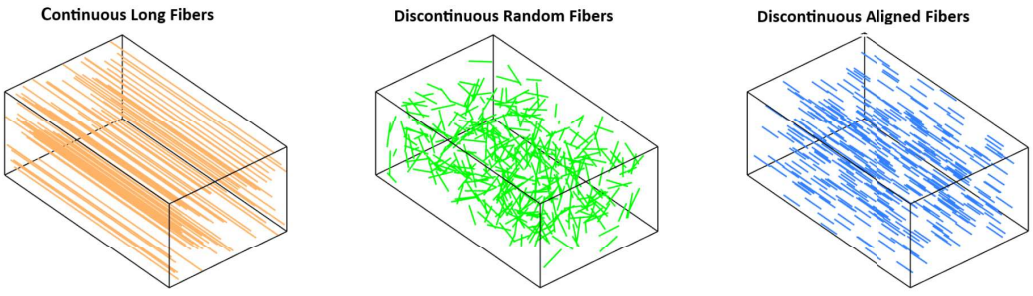


Figure 2.1: Schematic reinforcement arrangements in composites

The manufacturing process (such as the one proposed in this work) plays a critical role in ensuring the mechanical properties of discontinuous fiber composites to be similar to those of continuous fiber composites.

For the case of structural composites such as in the case of laminates, it is possible to play with the orientations of each ply through different planar arrangements called *fabrics*. These fabrics can

present different configurations regarding the orientation of the tows along the fabric direction such as the case of a *twill* (two tows in the fabric direction weave over−and−under two tows in the cross direction) or *plain* (where the tows are alternately passed over−and−under each other, to provide symmetry and good stability) [15].

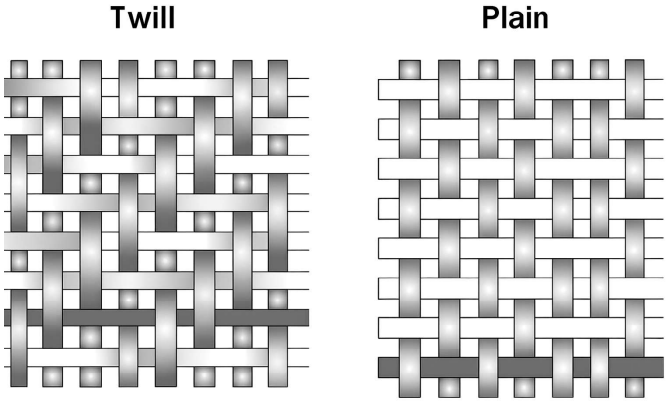


Figure 2.2: Schematics of both Twill (left) and Plain (right) configurations

In terms of concentration, both the fiber and resin content on a composite are usually expressed in terms of the volume fractions,

$$FVF = \frac{V_f}{V_c} \tag{2.1}$$

Where V_f and V_c are the fiber and laminate volumes respectively. It is also possible to transform a volume fraction into a mass fraction,

$$FWF = \frac{\rho_f}{\rho_c} FVF \tag{2.2}$$

The density of the composite can be computed with weight fractions:

$$\frac{1}{\rho_c} = \frac{FWF}{\rho_f} + \frac{(1 - FWF)}{\rho_m} \tag{2.3}$$

Also, depending on the manufacturing process the VVF, void volume fraction, may have slightly higher or lower values. Its evaluation is critical for each particular case. It is possible to compute the VVF using the expression bellow

$$FVF + MVF + VVF = 1 \tag{2.4}$$

Where MVF is the matrix volume fraction.

As a general rule, void volume fractions of composites are the highest in processes where resin is applied to the dry fibers at the time of lamination and are lowest when the resin application and curing is made under pressure.

Convencional processes for hydrofoil wings manufactured using FRP

In composite materials, the manufacturing process plays a critical role in determining the final properties of a component, including its mechanical properties, durability, and surface finish. Although traditional manufacturing techniques are already widely established, it is critical to understand the variables involved in each of them in order to be able to innovate and develop new manufacturing methods to meet the growing demand and complexity of these components.

Among the most traditional methods is the hand lay−up process, where the fibers are impregnated manually with resin on a mold. This technique is extremely simple and therefore one of the least expensive options for manufacturing relatively small components, however, the mechanical quality of the final part depends heavily on the worker's skill and experience [15]. This is the main reason why it is less suitable for high performance components.

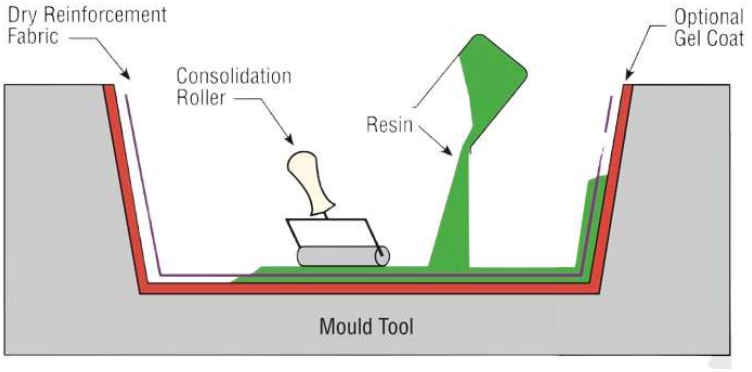


Figure 2.3: Hand lay−up method [15]

For hydrofoil wing manufacturing is more common to perform a hand lay−up process using *prepegs* - that are fabricated overlapping the fiber and resin in silicone sheets (around 0,125 mm thick) being then pressed and partially cured in order guarantee the intended degree of reaction (controlled by the stoichiometric conditions) for each application - allowing for a much more controlled lay−up process.

The usage of prepegs allows for a better control of the fiber to resin ratio (leading to a higher FVF on the final part when compared with hand lay−up), more effective fiber alignment and given these characteristics, inevitably better overall mechanical performance in parameters such as resistance, rigidity and higher fatigue life [16]. Despite these advantages, it often brings out problems in storage, transportation, high cost, and further restricted large-scale applications [7].

In both variations of the hand lay−up process it is possible to improve the consolidation of the fiber impregnation on the final part by covering the lay−up with a vacuum bag where the air is evacuated throughout a one−way valve, removing the exceeding resin and eventual voids of air between layers (guaranteeing higher fiber content and fiber wet−out) [9].

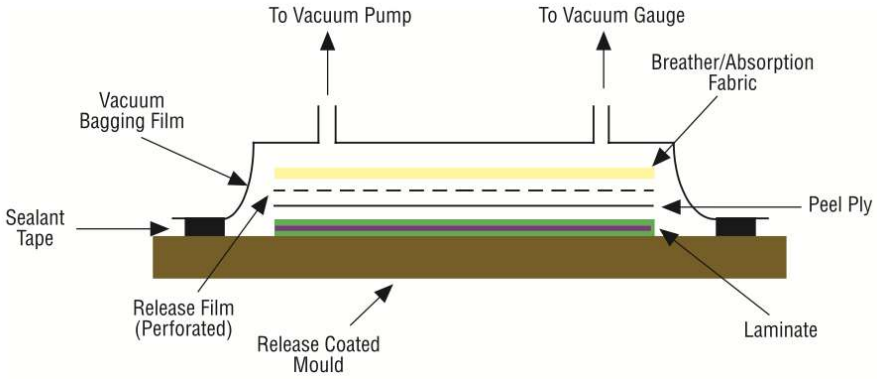


Figure 2.4: Vaccuum bag process [15]

A similar alternative to hand lay−up is the RTM process - *Resin Transfer Molding* - where the fibers are already placed inside the mold and a low viscosity resin is injected through a pressure

gradient, being partiality cured at entrance and fully cured inside the mold itself by the action of temperature. There is also a variation of this process - R−RIM (*Reinforced Reaction Injection Molding)* where the main difference is that in R−RIM the resin and hardener are mixed rapidly at the entrance of the mold [9].

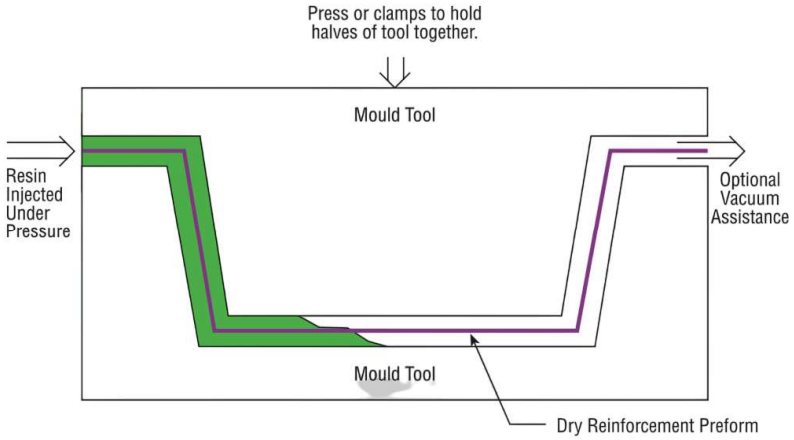


Figure 2.5: Resin Transfer Molding method [15]

It is important to notice that RTM processes are seriously restricted by the resin fluidity: as dry fibers are required to be fully impregnated during the injection process, the resin should have a low viscosity and a wide injection temperature range. This restricts its application range in cases such as in the case of epoxy resins since they show poor fluidity leading to the appearance of cracks and defects when epoxy−based components are subjected to external forces [7].

Finally, the Compression Molding − CM − is the process where the usually preheated molding material is placed into a heated mold cavity and then compressed under pressure until it cures and takes the shape of the mold. Due to the both controlled pressure and temperature, the cure is performed in an even and rapid way, guaranteeing minimal material waste along the process [17].

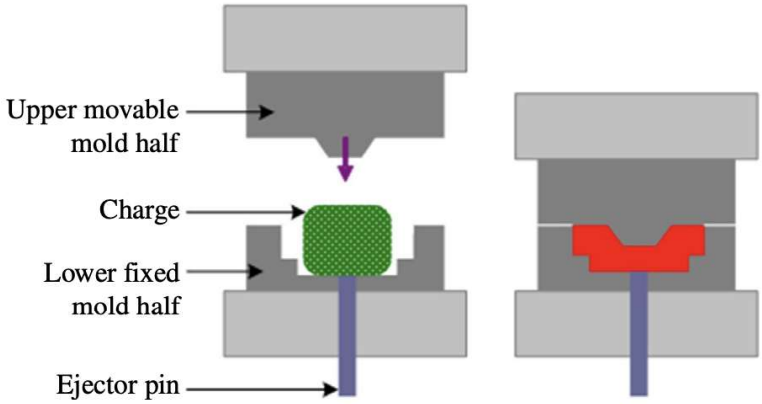


Figure 2.6: Compression Molding method [18]

In the CM process, it is possible to use several different types of intermediate compounds obtained from the mixture of resin and short fibers usually obtained from roving, such as [18]:

- Bulk Molding Compound (BMC) − dough like, highly flowable and adaptable mixture containing short chopped fibers (3−12 mm). It is ideal for small to medium parts with complex

geometries due to its excellent moldability.

- Sheet Molding Compound (SMC) – sheet-like material with medium length chopped fibers (typically 10–50 mm). It has moderate flow behavior inside the mold and is suitable for medium to large structural components requiring good mechanical performance.

- Thick Molding Compound (TMC) – a very thick, paste like compound similar to SMC but with significantly higher viscosity and often longer fibers. It provides high stiffness and strength and is often used for thick, highly loaded structural components.

With either of these options, the CM process allows for a strong final product with good surface finish and minimal waste, having one of the lowest initial setup cost for molding of complex composite parts. It is also important to notice that it is a process that is inevitably more suitable for flat or moderately curved parts with no undercuts and the final product has less then ideal consistency (variation in both mechanical properties fiber distribution) [17].

2.1.2 Forged carbon process

Recent composite technology research and development efforts have focused on new out of autoclave material forms, and automated processes that could lead to an increase in production efficiencies. For a long time that the transportation industry has been aiming at reducing composite part cost and increasing production rate, leading to the appearance of several innovative manufacturing processes and technologies in order to achieve these goals.

This work proposes an alternative manufacturing process that is based on a methodology first proposed in Lamborghini Sesto Elemento [5], being similar to an advanced compression molding technique, utilizing carbon fiber sheet molding compounds. It allows for a cheaper, simpler and faster alternative to the conventional composite manufacturing methods, being suitable for parts that present complex geometries and subjected to combine loadings (typically manufactured in aluminum).

Just by taking into consideration this preliminary work developed in Lamborghini, it was possible to obtain approximately a 32% weight reduction for the front arm and 22% on the redesign of the rear arm [5]. The overall cost also has reportedly came down since the manufacturing time was reduced to an impressive 2–3 minutes positioning and 4 minute cure.

Table 2.1: Mechanical properties for different manufacturing techniques adapted from [5] (for Aluminum the minimum yield strength is reported, while for the composites the ultimate strength is reported)

Material	**Tensile strength (MPa)**	**Tensile modulus (GPa)**
6xxx Aluminum	260	70.0
Prepreg 2x2 twill quasi-isotropic	745	41.4
RTM stitched NCF quasi-isotropic	634	34.5
Forged Composite®	246	33.8

As it is possible to see (Table 2.1), Forged Composite®technology was able to produce attractive results for the high-performance market, however, at the time the Lamborghini research did not consider the use of chopped carbon fiber + epoxy resin and required sophisticated molding techniques to manufacture the components. In fact, there is no consistent scientific research highlighting the properties of the composite parts obtained from this alternative methodology.

Methodology

The concept behind this process is to compress the carbon fiber compound using a mold usually composed by a bottom part (including the cavity of the component intended for manufacturing) and a top piston–like part that is used to compress the mixture. These compression mold tools will comprise of two or more parts which close together leaving the cavity where the component will be formed. In almost all circumstances this mold will be in a block like format to provide strength and make the clamping or compression process more practical. Strategic partitions and chamfers can be added to the mold in order to ease the de-mold process as it is possible to see in Figure 2.7.

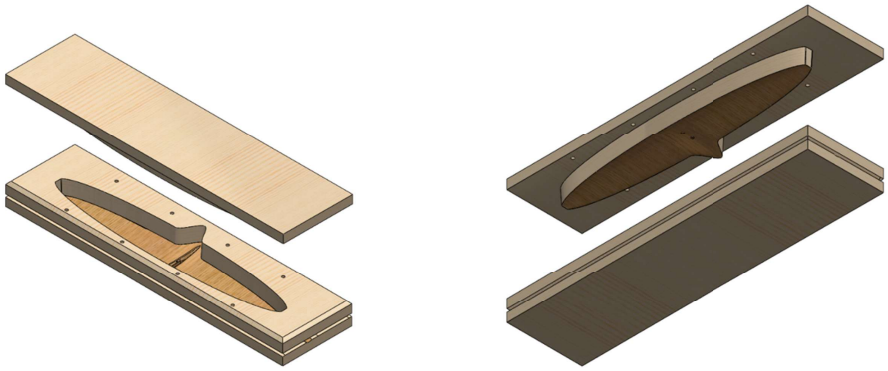


Figure 2.7: MDF machined molds for Type-B hydrofoil

Given the morphology of the process, it was noticed during manufacturing that additional concerns must be considered when designing tooling for forged carbon applications. For example, when dimensioning the piston-like section, it is important to increase the total length of the piston to at least 25% of the depth of the final component as well as include a oversize around that area since it allows the steady flow of the excess resin to be squeezed out through the parting line, guaranteeing the correct fiber to resin ratio. It is also a good practice to include a slight draft angle of 2–3 degrees to allow the mold to easily separate, in multi-part tooling it is often possible to design the mold so that it can separate away from a completely parallel piston feature [19].

The mold preparation procedure will depend on the type of material used for its construction, however it does not diverge largely from the more common processes. For the case of MDF, it is enough to sand the mold (especially on the closure surfaces) and apply 3 to 5 layers of a porosity sealer such as the Mikon®399 MC Sealer. Additionally, before every process it is mandatory to clean the mold in order to remove eventual residuals of cured resin and apply the release agent.

After this process, everything will be ready for the impregnation of the carbon fiber and matrix. Ideally, the amounts of each of the materials should be defined previously by using the following steps:

- Compute the total part volume V_{part}
- Select the ideal fiber volume fraction V_f
- Compute the resin and fiber volumes
- Convert fiber volume to fiber mass (using the density of carbon fiber tow) $m_{\text{fiber}} = V_{\text{fiber}} \cdot \rho_{\text{fiber}}$
- Convert resin volume to resin mass (using the density of the final mixture product) $m_{\text{resin}} = V_{\text{resin}} \cdot \rho_{\text{mixture}}$
- Add at least 10%–20% extra resin for wet-out and waste.

As it is possible to see in Figure 2.8, the impregnation process is mostly manual and can be done using the most common consolidation tools such as spreaders, rollers or even laminating spatulas.



Figure 2.8: Impregnation of the carbon fiber on the bottom mold part

The last phase would be to close the molds using clamps for a general application or an hydraulic press for the case of more complex and wider parts such as the hydrofoil wing - where a total compression force of around 10 kN has the applied uniformly.

Being a widely adaptable process, it is possible to use a very wide range of resin types and even different fibers as it will be seen in the next section. In this case, the materials considered for the hydrofoil wing were the ones used by FAST for the manufacturing of the first three wing batch designed for ATLANTICO (shipped from *Easy Composites* [19]).

Fiber characterization

Several different kinds of fibers are suitable for usage in a process so versatile as the one proposed on this work, not only in terms of various local reinforcements but also by using other materials such as flax, glass or even hemp fibers to manufacture the compound [20].

It is also possible to find examples in the literature highlighting the differences in both mechanical properties and moldability of carbon fiber compounds obtained from different tow sizing: A good example is the one of FMC™methodology where it is able to improve both by strength as well as optimal FVF for each component, just by adjusting the tow size in critical areas from sizes ranging 15k to 3k - leading to very economic solutions that are suitable for a large field of applications, from simply aesthetic parts to some primary structures [4].

The effects of varying fiber length have also been documented to be a critical characteristic on both the tensile modulus, tensile strength, and impact resistance of other FRP materials [21]. As shown in Figure2.9, the normalized properties tend to stabilize at fiber lengths above 10mm and present a highly sensitive behavior around the typical short fiber length range (from around 1 to 10 mm) and for the typical forged carbon components length (from 5mm to 30mm) this effect is less pronounced.

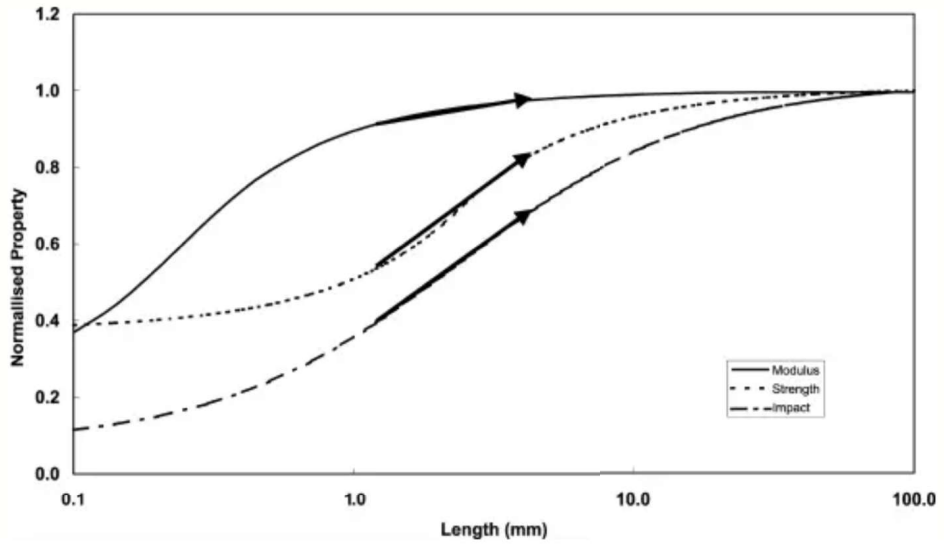


Figure 2.9: Effect of fiber length on mechanical properties, normalized against continuous fiber properties [22]

The findings reported by Thomason also point out the effects of fiber volume fraction in fiber reinforced plastics are particularly noteworthy and may show some divergence relative to the conventional rule of mixtures,

$$E_c = FVF\,E_f + (1 - FVF)E_m, \tag{2.5}$$

where E_c is the composite modulus, FVF is the fiber volume fraction, and E_f and E_m are the fiber and matrix modulus, respectively.

While this assumption may be true for the flexural modulus, a clear plateau in the tensile Young modulus is observed at approximately $FVF = 0.4$ [8]. Furthermore, it has also been demonstrated that both tensile strength and impact strength reach a maximum at fiber weight contents of approximately 40–50%, corresponding to $FVF \approx 0.2$–0.3 for the case of glass fiber reinforced polypropylene.

Given the morphology of the proposed manufacturing process, the first fiber used for testing purposes was the one recommended by the manufacturer [19]: The 7440−44−0 Carbon Fiber Chopped Tow − a mixture made from virgin standard modulus fiber with 94% carbon fiber (in graphite form) and other components such as epoxy or polyester resin traces as it is possible to see in appendix A. The main properties are listed bellow.

Table 2.2: Datasheet Properties of the Carbon Fibre Chopped Tow

Property	**Value**
Carbon fibre type	PAN-based carbon fibre (graphitic)
Carbon content	≥ 94%
Sizing content	≤ 1.8% (epoxy or polyether traces)
CAS number	7440-44-0
EINECS number	231-153-3
Form	Short fibre (chopped tow)
Colour	Black / charcoal grey
Melting point	> 2760 °C
Bulk density (short fibres)	0.1 to 0.5 kg/dm^3

Resin characterization

Now that the fiber used is fully characterized, it is also important to define the resin systems, properties and general behavior.

The polymer matrices can be broadly classified into thermosetting and thermoplastic polymers. Thermosetting polymers, such as epoxy resins, unsaturated polyesters, and vinyl esters, are widely used due to their favorable mechanical properties, chemical resistance, and thermal stability [23].

These polymers require curing, a process that transforms the resin from a liquid into a solid through chemical cross-linking, creating a rigid three-dimensional structure. Epoxy resins specifically exhibit strong adhesion to reinforcing fibers, good mechanical strength, and chemical resistance, retaining a high percentage of their mechanical properties even at elevated temperatures (up to approximately 150 degrees), making them particularly suitable for structural applications. However, thermosets typically show limitations such as brittleness, moisture sensitivity, limited shelf life, and demanding manufacturing requirements, including restrictive curing cycles involving high temperatures and extended processing times.

Recent works from Mitsubishi Chemical [4] show remarkable mechanical properties for carbon fiber molding compounds manufactured with their FMC™methodology. By working with different thermosets such as epoxy and vinyl ester (VE) resins, it was possible to make a comparative study in terms of tensile strength, tensile modulus, flexural strength, flexural modulus, spiral flow and cost of difference for the cases of both resins showing relevant results: for a FVF around 52.5% it is possible to obtain tensile strengths around 320 MPa using vinyl ester resin and only 270 MPa for the epoxy, given practically the same values for de Young Modulus (around 33 GPa and 35 Gpa respectively).

Given the morphology of the proposed manufacturing process, the resin used for testing purposes was the one recommended by the manufacturer [19]: the IN2 Epoxy Resin – a high performance low viscosity epoxy resin, as it is possible to see in appendix B. The main properties are listed bellow:

Table 2.3: Datasheet Properties of the IN-2 Epoxy Infusion Resin

Property	**Value**
Material type	Epoxy resin (formulated amine hardener)
Appearance (mixed)	Clear
Viscosity @ 25°C (mixed)	225 mPa·s
Density @ 25°C (mixed)	1.105 g/cm^3
Pot life @ 25°C (AT30 Slow)	80–100 min
Pot life @ 25°C (AT30 Fast)	9–14 min
Gelation time @ 25°C (Slow)	8–11 h
Gelation time @ 25°C (Fast)	2–4 h
Demould time @ 25°C (Slow)	18–24 h
Demould time @ 25°C (Fast)	6–8 h
Cured density @ 25°C	1.08–1.12 g/mL
Hardness (Shore D/15)	84.5–88.5 (Slow), 86–90 (Fast)
Maximum T_g	92–98°C (Slow), 75–81°C (Fast)
Flexural strength	112–124 MN/m^2 (Slow), 95–109 MN/m^2 (Fast)
Maximum strain (flexural)	5–7% (Slow), 4–6% (Fast)
Strain at break (flexural)	6–8% (Slow), 7–9% (Fast)
Flexural modulus	3.15–3.55 MPa (Slow), 2.5–3.1 MPa (Fast)
Tensile strength	65.5–73.5 MPa (Slow), 67–75 MPa (Fast)
Elongation at break (tensile)	6–8% (Slow), 5–7% (Fast)
Water absorption (24 h, RT)	0.12–0.20% (Slow), 0.22–0.27% (Fast)

Many of these characteristics are also dependent on the type of catalyzer (hardener) used to mix with the resin. The hardeners are usually organic peroxides that, once mixed with the resin are responsible for the initiation of the chemical reaction that leads to the cure of the resin, creating a three dimensional array of covalent bonds. The conditions during this curing process (specially temperature) will also alter the mechanical properties of the matrix [9]. In order to achieve the most optimized process for the given component, these parameters should all be taken into consideration and its effect must be understood.

Mechanical characteristics of Forged Carbon components

It is now necessary to understand the mechanical behavior of the obtained material, considering elastic deformation. For the elastic domain, the constitutive relations between stress and strain are linear and given by Hooke's Law:

$$\sigma_i = C_{ij}\,\varepsilon_j \tag{2.6}$$

Here, C_{ij} are the scalar entries of the stiffness tensor $\boldsymbol{C}$, which characterizes the material's resistance to deformation in various directions.

Assuming the stiffness matrix is invertible, the strain components can be expressed in terms of the stress components using the compliance matrix:

$$\varepsilon_i = S_{ij}\,\sigma_j \tag{2.7}$$

In this case, S_{ij} are the components of the compliance tensor S, defined as the inverse of the stiffness tensor:

$$S = C^{-1} \tag{2.8}$$

Due to the symmetry of the stiffness tensor ($C_{ij} = C_{ji}$), the compliance tensor also satisfies the relation $S_{ij} = S_{ji}$ [24].

Given the morphology described in the previous section for the forged carbon process, it is plausible to expect that the material will present an isotropic behavior since both the resin and fiber impregnation are performed in a completely arbitrary manner. For many reasons, mainly related with the complex material flow pattern inside the mold, this may not be entirely true. The real behavior tends to a middle ground between what would be an ideal isotropic model and an orthotropic one (having three mutually perpendicular planes of symmetry). For this case, it will reduce the compliance matrix to only 9 independent constants, being that it can be written in terms of equivalent engineering constants:

$$[S_{ij}] = \begin{bmatrix} \frac{1}{E_1} & -\frac{\nu_{21}}{E_2} & -\frac{\nu_{31}}{E_3} & 0 & 0 & 0 \\ -\frac{\nu_{12}}{E_1} & \frac{1}{E_2} & -\frac{\nu_{32}}{E_3} & 0 & 0 & 0 \\ -\frac{\nu_{13}}{E_1} & -\frac{\nu_{23}}{E_2} & \frac{1}{E_3} & 0 & 0 & 0 \\ 0 & 0 & 0 & \frac{1}{G_{23}} & 0 & 0 \\ 0 & 0 & 0 & 0 & \frac{1}{G_{13}} & 0 \\ 0 & 0 & 0 & 0 & 0 & \frac{1}{G_{12}} \end{bmatrix} \tag{2.9}$$

This will be also a symmetric matrix, given the material reciprocity.

2.1.3 Failure modes on Forged Carbon components

Now that the manufacturing process was defined as well as its characteristic mechanical properties, it is critical to understand the most common failure modes on this type of composites. These failure modes depict the way that the real model is more likely to fail and therefore will significantly affect the viability of the process for the given application.

Given that the information on Forged Carbon specimens is very limited, the main failure modes taken into consideration will be the ones that have already been documented for the CM variation, the especially the Cold Press Molding technique, since that given the similarity within the two processes, they are expected to present similar failure modes as well.

Matrix cracking

Matrix cracking is a failure mode mainly caused by heterogeneity, strong stiffness mismatch and load transfer limitations between the matrix and the fiber that lead to the creation of localized stresses that exceed the matrix's tensile strength, creating small cracks to initiate and grow along the weaker resin pathways before any fiber damage occurs. It is a typical phenomena on composites presenting a discontinuous and small fiber architecture since they are likely to cause resin rich pockets, gasps and other "weak links" that lead to the localized stresses described previously.

Additionally, for the case of Forged Carbon process, given the significant difference that the fibers show regarding their stiffness when compared to the resin, under tensile loading, this mismatch causes the matrix to carry the same dis-proportionality in terms of strain in regions where fibers are not aligned with the load.

Matrix failure has been documented to occur in chopped carbon fiber SMC composites since the epoxy matrix carries most of the load in regions where fibers are misaligned or absent [25]. As the tensile load increases, the highly heterogeneous/random structure creates localized stress concentrations in the resin causing the matrix failure even before the fibers have been affected. Once initiated, these cracks grow along the resin-rich paths, undermining load transfer and setting the stage for subsequent failure mechanisms.

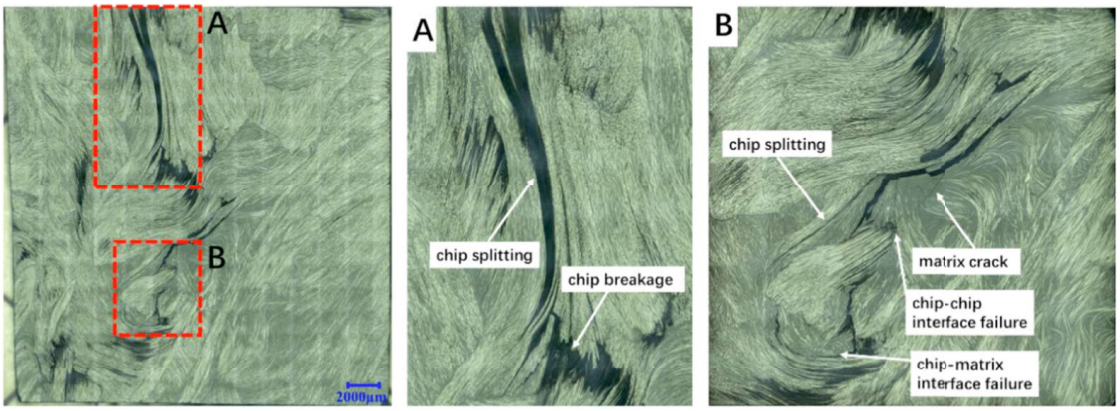


Figure 2.10: Microscopic images of failed SMC samples and failure mode description according to [25]

It is possible to find on the literature many ways to identify these cracks. Micro tomography imaging technique (to be seen in further detail during the next chapters) is one of the most clear ways to do this as well as depict their propagation. They appear as narrow, elongated low-density regions in the segmentation and it is usually possible to see their propagation through resin-rich areas or between adjacent fiber bundles without directly fracturing the fibers [26].

Behind the appearance of matrix cracks are many different types of composite defects either due to the manufacturing process or even the morphological properties of the materials used. Identifying the type, size and depth of defects is of great significance for determination of material failure and life calculation and provides necessary information for formulating appropriate maintenance and repair plans [26].

The main types of defects are described bellow:

- Voids: enclosed regions of missing material within the composite, usually formed due to air entrapment, incomplete resin infiltration, or curing-related effects during manufacturing (being usually associated with resin starved areas). In μCT reconstructions, voids appear as well-defined low-density volumes and are quantified in terms of size, morphology, and volume fraction, as they influence local stress concentrations and overall material quality. A high *VVF* may be caused by insufficient flow of resin during cure resulting in a foaming action, or resin contamination with a material that is gaseous at the cure temperature.

- Fiber waviness: out-of-plane or in-plane undulations of fiber bundles (wrinkles, folds, kinks) can form during layup or due to resin flow and compaction pressures. This refers to geometric deviations of fibers from an intended straight or statistically uniform orientation, introduced during manufacturing [27].

- Dry Spots: insufficient resin infiltration in some regions (especially between fiber bundles) results in areas with lack of resin which are not typical voids but localized resin starvation caused by flow imbalances [28]. Very likely to occur due to non-uniform resin flow or premature resin gelation during impregnation.

- Blister: a blister is a raised area near the surface of a laminate in which there are localized bulges or pockets trapped between fibers and matrix or between layers. These are often considered a variant of voids but act differently in terms of processing origin and localization near surfaces or interfaces [29].

- Resin-Rich Regions: areas with a locally reduced fiber volume fraction, resulting in excess matrix material. Identified in μCT scans by their lower density relative to fiber-dominated zones. Often associated with manufacturing technique [26].

- Pinhole: typically a small (micrometer size) through-thickness void that connects the interior of the composite to the surface. Likely to be originated from trapped air escaping during the curing process - specially in processes that are not vacuum assisted (being very common in CM). Besides having a negative effect in the component's structural integrity, the presence of pinholes also enables moisture to penetrate the composite decreasing its environmental resistance [30].

Debonding

Debonding is a term that refers to the loss of adhesion or separation between the reinforcing fiber surface and the surrounding polymer matrix at their interface. Appears in μCT imaging as planar crack-like features propagating along interlaminar regions. Characteristic of layered composite architectures and associated with interlaminar stresses or impact-related damage.

At the interface, load is primarily transferred through shear stresses between matrix and fiber. When these stresses exceed the interfacial strength, debonding initiates. In chopped fiber composites, the fiber ends are where stress concentrations will be the highest and it is a very common location for the initiation of this phenomena.

From the mechanical behavior point of view, the presence of debonding of the material is critical for aspects such as reduced effective elasticity modulus or stress redistribution leading to local damage evolution [31].

Fiber breakage

Fiber breakage is a primary structural failure mode where individual reinforcing fibers crack or rupture under load. In this case, the carbon fibers will carry most of the load in a composite. Under high tensile stress (especially along the fiber direction), once fibers reach their ultimate strength,

they fail. The progressive breaking of fibers leads to eventual global failure of the composite. This is typically characterized by a catastrophic failure with relatively little plastic deformation [25].

If we consider for instance compression loading, other variations of this phenomena have already been documented such as shear failure or kink band formation. The second being referred to as the most dominant failure mode in chopped fiber reinforced composites by [32] and [6]. These kink bands arise from a combination of fiber microbuckling and matrix shear deformation, forming a localized inclined zone where fibers rotate collectively. This phenomenon is triggered by initial fiber misalignment and progresses as the matrix yields under shear, allowing fibers to tilt and collapse in a coordinated manner. This leads to a catastrophic failure on a broad region of coordinated fiber rotation and matrix damage.

2.2 Microstructural analysis and measurement

Microstructural analysis serves to verify the integrity and quality of a material. For the case of composites with small reinforcements it is specially useful in order to analyze aspects such as homogeneity, *FVF*, void content, the quality of resin impregnation, the presence of resin-rich or fiber-rich areas - this way, making it possible to access the influence of production parameters on the final quality of the different components. Additionally, it is also possible to get a decent insight on the defects before loading the material and their evolution given the different failure modes described in the previous section. In this section, three main techniques will be described given the different phases they were used along the project:

- Optical Microscopy: while several advanced techniques such as scanning electron microscopy (SEM) and transmission electron microscopy (TEM) are available for this type of analysis, optical microscopy (OM) remains a prevalent choice given its ease of use, accessibility and the relative high resolution (around 50 μm) obtained for such a simple method. The OM technique can be used not only for an initial prediction of the internal structure of a typical forged carbon specimen but also to get some of the most "macro" aspects of the microstructure analysis (such as void size and distribution).

- X-ray Computed Tomography: This technique allows to achieve great resolutions while getting a full 3D overview of the material via non-destructive testing. X-ray computed tomography (X-ray CT) is based on the acquisition of multiple radiographic projections while the sample is rotated, followed by a tomographic reconstruction of the internal structure, resulting on resolutions of around 0.5–10 μm, depending on the system configuration, sample size, and scanning parameters. This allows for the characterization of internal features such as pores, cracks, inclusions, and their spatial distribution throughout the volume of the specimen.

- Digital Image Correlation (DIC): this technique is a non-contact optical method used to measure full-field surface displacements and strains during mechanical loading. Digital image correlation (DIC) is based on the comparison of digital images of a specimen surface acquired before and during deformation. A random speckle pattern applied to the specimen surface is tracked using correlation algorithms, allowing the displacement of small subsets of pixels to be calculated.

  The reason behind the implementation of this technique during mechanical testing (over the usage of extensometers for example) is mainly due to the unpredictability and randomness of forged carbon specimens. This way, the full-field capability of DIC for providing a clear discretization on strain localization as well as damage initiation and evolution, is a very valuable insight into the mechanical response of the material that could not be obtained from point-wise measurement techniques.

2.2.1 Optical Micrography

Optical microscopy is the field of science that uses visible light and a lens system to observe objects of interest whose dimensions are too small to be seen otherwise with only bare eyes. Microscopes must fulfill two requirements, the first being that the object of study must be visually enlarged above the resolving capability of the eye, and secondly, the enlarged image must be clear enough so that it can be interpreted and analyzed. These two parameters are defined by magnification and resolution, respectively.

Magnification

The magnification is a ratio that indicates how many times the apparent size of an object is being increased. It is called the apparent size because what is in fact enlarged is not the physical dimensions of the structure itself, but its visual projection. The overall magnification of a microscope is achieved through a sequence of optical elements, each contributing a defined magnification factor. The final image magnification corresponds to the product of the magnifications introduced by the individual components in the optical path.

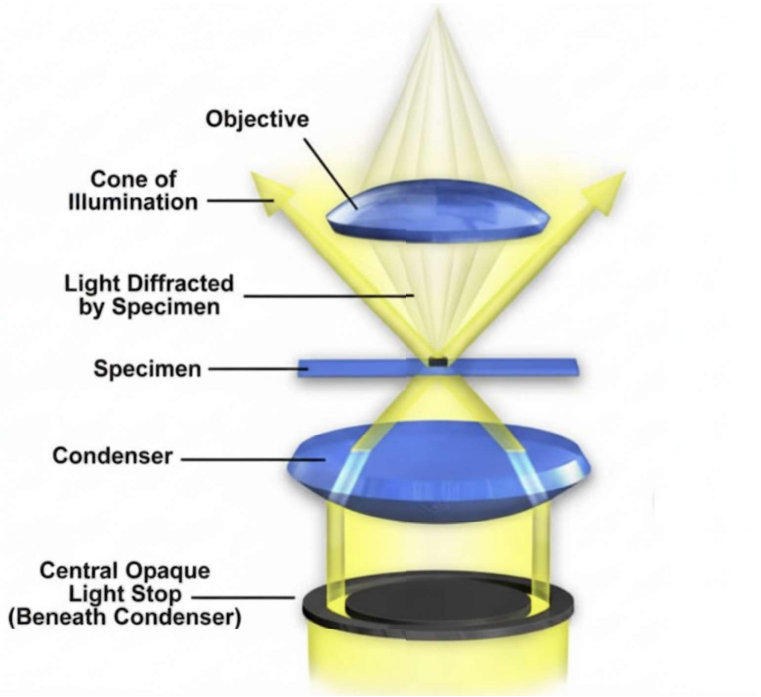


Figure 2.11: Magnification (schematic configuration for darkfield microscopy) adapted from [33]

In a conventional optical microscope, the total magnification M is typically expressed as

$$M = M_o \cdot M_e, \tag{2.10}$$

where M_o denotes the magnification of the objective lens and M_e represents the magnification of the eyepiece. The objective forms a real, intermediate image of the specimen, which is subsequently magnified by the eyepiece to produce the final virtual image observed by the user.

Stereo microscopes (with separate optical paths) have two main types of magnification: fixed and zoom (panoramic). Fixed magnification uses a matched pair of objective lenses with a preset power, while zoom magnification allows continuous adjustment across a range. Auxiliary objectives can further increase zoom magnification by a set factor, and swapping eyepieces in both systems changes the overall magnification.

Resolution

The resolution is a parameter that indicates how much detail can be obtained out of an optical system. In other words, it is the minimum distance between two adjacent points at which they can still be distinguished as individual entities rather than a single-merged point. In all optical systems, including microscopes, the resolution is intrinsically dependent on the way light propagates and interacts with its elements, due to a phenomenon called diffraction of light.

Let's consider an infinitesimal light source propagating in spherical wave fronts containing coherent point sources (wavelets). When the light meets an obstacle such as an aperture, only a few wavelets from the wave front are allowed through. These wavelets behave like individual point sources, emitting light at a synchronous pace. Due to constructive and destructive interference of light, a pattern in form of dark and bright zones emerges after the aperture. In the three-dimensional space, the spot where most of the constructive interference occurs has an elongated shape that differs from the actual shape of the infinitesimally small light source. This diffraction pattern is known as the point spread function (PSF), and its projection in a plane orthogonal to the direction of the light propagation is known as Airy pattern.

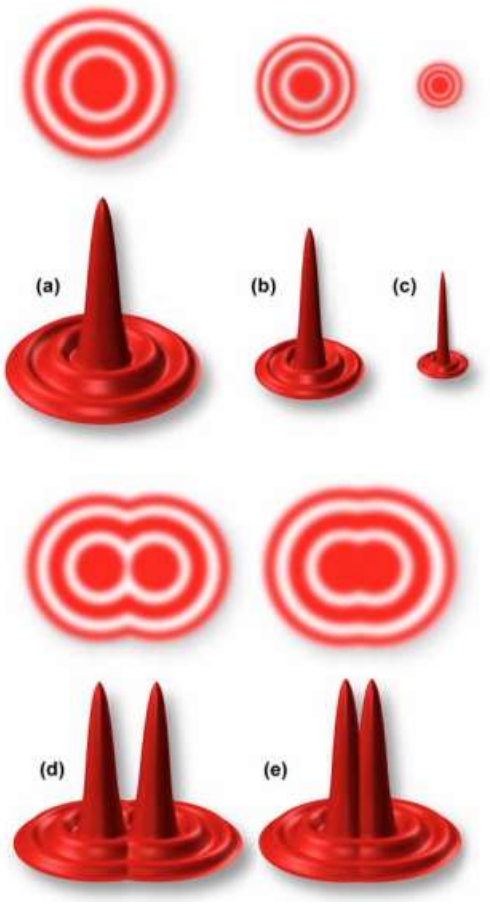


Figure 2.12: Airy disks and resolution. (a-c) Airy disk size and related intensity profile (point spread function) as related to objective numerical aperture, which decreases from (a) to (c) as numerical aperture increases. (e) Two Airy disks so close together that their central spots overlap. (d) Airy disks at the limit of resolution. Adapted from [33]

To understand optical resolution, consider two proximal emitting sources. If the physical distance between them exceeds the system's resolution limit, they remain distinguishable as discrete

entities. However, as that distance decreases, the overlap of their respective Airy disks increases. Eventually, the patterns merge to a degree that the optical system can no longer discern the two sources as individual objects a threshold often defined by the Rayleigh criterion.

In a microscope, the size of the diffraction pattern is related to the wavelength of light (λ) and the numerical aperture (NA) of the objective lens. The most common criteria to define the resolution limit of an optical microscope is in fact the Rayleigh criterion. It establishes the resolution limit (R_R) of an optical microscope as the distance between two emitters when the maximum of one Airy disk overlaps with the first minimum of the second. Mathematically, it is expressed as in equation [34]:

$$R_R = \frac{1.22\lambda}{2NA} \tag{2.11}$$

Therefore, the diffraction is a phenomenon present in all optical systems, which limits and determines their resolution, being, by definition, diffraction-limited optical systems.

Difference from a normal microscope

Unlike the compound light microscope, which primarily utilizes transmitted (diascopy) illumination, on this kind of microscopes there is a strong reliance on reflected light to examine an object's surface. This makes it an essential instrument for studying specimens that are too dense or opaque for traditional compound microscopy. While most stereoscopic systems lack a condenser for focusing transmitted light, certain configurations allow for diascopy by positioning a light source or mirror beneath a transparent stage.

Darkfield microscopy can be done with either transmission or reflected light using stereoscopes which have been properly fitted with illuminators. Therefore, a defining advantage of these microscopes is their significant working distance and depth of field. However, these features are governed by an inverse relationship with optical resolution: as the resolution increases to distinguish between two closely spaced points, the available working distance and depth of field are proportionally reduced. Although its magnification power is considerably lower than that of a compound microscope-typically reaching a maximum of 100× - it remains highly effective for macroscopic analysis. For instance, the generous working distance at low magnification facilitates the detailed inspection and manipulation of large solid objects, such as fracture surfaces, to identify specific points of interest [35].

Additionally, a wide set of techniques can be implemented for enhancing the performance for specialized imaging methods and requirements. The objective lens is the most critical element, as it determines the numerical aperture and the theoretical resolution limit of the system, meaning that the smallest details may lead to significant improvements. This way, it is critical to be able to identify and understand its specifications, such as the ones resented in Figure 2.13.



Figure 2.13: Objective specifications. Adapted from [35]

The performance of an optical microscope is fundamentally dictated by the quality and alignment of its primary components: the objective lens (for determining the theoretical resolution limit of the system), the eyepiece (for facilitating the final magnification), and the condenser (for providing optimal illumination to the specimen).

However, the practical resolution of components such as eyepieces, condensers or objectives is often limited by optical aberrations. Monochromatic aberrations, such as spherical aberration and astigmatism, arise from lens geometry and lead to localized blurring or field distortion. Chromatic aberrations occur due to the dispersion of light, where different wavelengths fail to converge at a single focal point, manifesting as color fringing. As it is also possible to see in Figure 2.13 objective designs, such as apochromats, are specifically engineered to compensate for these defects to provide a diffraction-limited imaging experience [33]. Additionally, plan-correction is frequently applied to these lenses to ensure a flat field of view, eliminating the field curvature that otherwise causes sharpness to degrade toward the periphery of the image.

Finally, the role of illumination in these systems is essential for visualizing fracture surfaces and three-dimensional structures that are otherwise impenetrable to light. This is because the microscope base facilitates both reflected and transmitted light paths, allowing for techniques such as darkfield, resulting in a high-contrast imaging of the specimen against a dark background, which is critical for resolving minute surface characteristics and semi-transparent details that standard brightfield illumination might obscure.

2.2.2 X-ray Computed Tomography

X-ray computed tomography (CT) is an X-ray imaging technique that has progressed significantly since its origins as a medical imaging technique around 1970. The increasing resolution and source flux with the introduction of microfocus CT enabled higher geometric magnification achieving a scale suitable for analysis of composite materials (specially, their internal defects) via non-destructive scanning of the object in 3D.

Damage in laminated composites is inherently three-dimensional, involving complex, interacting effects of the previously described failure modes (such as matrix cracking, fiber breakage, delamination) [36]. For these cases, traditional two-dimensional microscopy techniques, whether optical or electron-based, require destructive sectioning of the specimen, that is likely to limit observations to a single plane and obscure the true geometry/connectivity of cracks and interfaces. As described previously, 2D methods are essential for a preliminary characterization of the material after manufacturing, being insufficient for the complete analysis of a three-dimensional process such as Forged Carbon and its failure mechanisms.

For this purpose, micro-CT appears as an exceptionally powerful tool for improving understanding of these failure processes and calibrating cohesive zone laws in wide range of different types of composite structures. This section aims to describe the main principles behind the CT technology applied to the manufacturing process proposed in this work.

Principles of X-ray Imaging Techniques

A CT image represents a reconstructed volumetric 3D map of a material's X-ray absorption, derived from multiple angular 2D radiographic projections, where attenuation varies with both material density and thickness due to differential absorption of X-ray photons (i.e. different contrast). Usually, for composite scanning purposes, this is obtained by rotating the object around an axis since it enables higher resolution then rotating the source and detector around the object - a more common procedure in medical CT applications. In the composite CT setup, an X-ray source generates a diverging cone of photons that passes through the rotating sample (Figure 2.14). As the samples rotates through a full 360° (or at least 180° plus the cone angle), a detector system typically composed of a scintillator that converts transmitted X-rays into visible light and a coupled photodetector records all the projection images from different viewing angles.

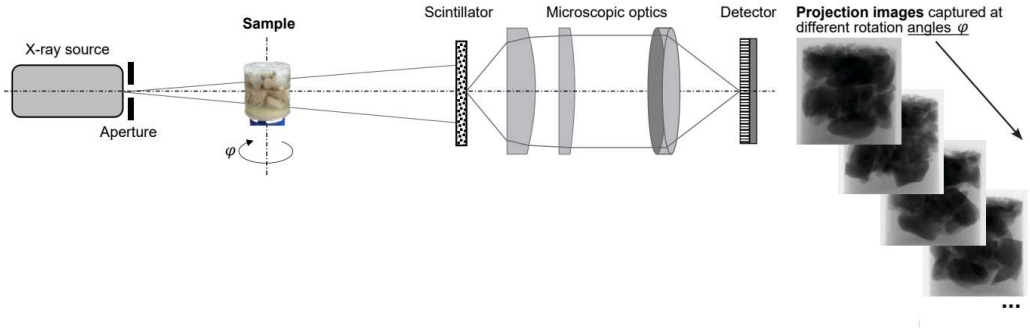


Figure 2.14: Schematics of X-ray conversion and magnification (adapted from [37])

These images then have to be reconstructed in order to achieve the three-dimensional geometry. The most widely used reconstruction algorithm is the *filtered backprojection* algorithm, that can provide accurate results for small to moderate cone angles. The idea behind reconstruction is to compute the absorption coefficient distribution in the sample based on the observed projections. For this, it is important to understand that the relationship between the transmitted and incident X-ray intensities follows the Beer-Lambert law:

$$I = I_0 e^{-\mu s} \tag{2.12}$$

Where:

- I is the transmitted intensity (mass $\cdot$ time^{-3}),
- I_0 is the incident intensity (mass $\cdot$ time^{-3}),
- μ is the linear absorption coefficient (length^{-1}),
- s is the thickness of the object the X-rays pass through (length).

Hence, it is easy to understand that since the absorption coefficient is a function of the location of the measured point on the object, it is possible to use multiple projections to figure out the absorption coefficient distribution in the scanned object. Using this, the algorithm reconstructs the the 3D volume with the projections in a staggered process: first, the projection data is geometrically weighted to compensate for beam divergence and variations in sampling density. Then data is filtered - a process called downweighting [38] - along the detector rows to correct the blurring inherent to backprojection. Finally, the filtered projections are backprojected (as seen in Figure 2.15) into a three-dimensional volume using the beam geometry [39].

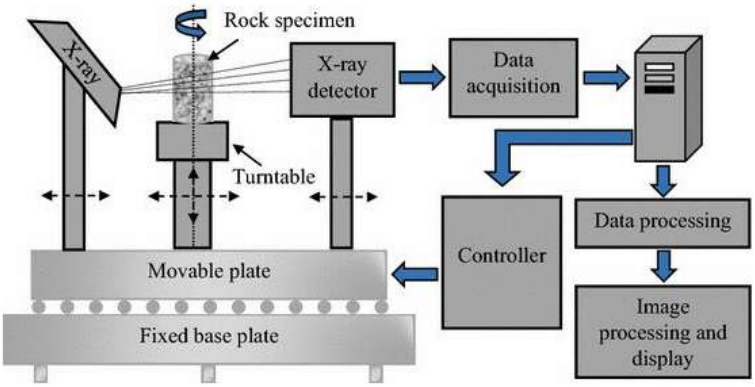


Figure 2.15: Principles of a tomographic measurement [40]

Is is possible to categorize the micro CT scanners in several ways. It is critical to understand each of these before performing a new scan in order to guarantee that the parameters are cohesive and suited for the specific application [38].

- Size - it is possible to categorize Micro-CT scanners as benchtop and full-size models. Benchtop models are less expensive, require less maintenance, and are easier to use. However, the X-ray energy is limited to 130 kV in most cases. The sample size is also limited. Many full-size models are compatible with 160 kV or 225 kV X-ray sources and accommodate larger samples. These tend to be more expensive and require more maintenance and expertise.

- Geometry - in terms of geometry, the main types were already described previously. The most common for medical CT being the gantry geometry. For composite CT scanning, the geometry of almost all scanners has the X-ray source and the detector fixed and rotate the sample, with everything aligned on a horizontal straight line. As stated before, this is done in order to increase the magnification.

- Magnification mechanism - usually, the cone beam geometry is the most used mechanism for image magnification due to its versatility and low implementation cost. It uses mechanical magnification, characteristic of the divergence of the cone beam defined by the distance of the specimen to the source. This phenomena is the main reason for achieving such high resolutions when it is possible to place the specimen close to the source. The parallel beam magnification mechanism on the other hand, is based on optical magnification where there is almost no divergence. The sample is closer to the scintillator, requiring very high powers on the x-ray source and sophisticated optics in order to achieve a parallel beam geometry, therefore increasing the cost of these systems. Despite this fact, this type of mechanism is excellent for high resolution imaging since it eliminates the effect of source drifting (the drift is not magnified and the images are much less blurred).

- X-ray energy - in Micro-CT scanning, higher excitation voltage (better penetrative capability of the X-ray) helps to image larger and denser samples, but it also means higher costs and limitations when imaging small and light samples well. Therefore, the most relevant parameter in order to define the source energy is in fact the density of the specimen since it will determine how much absorption the material has for that given energy. When analyzing composites, it is typical to use between 50 kV and 100 kV even tough larger scanners can go up to 225 kV or even higher. Decreasing the energy may require longer exposure time to obtain god signal-to-noise ratio and have much higher sensitivity to changes in the atomic number on the sample [41]. It is also possible to alter the exposure when the results are not sufficient for highest values of source energy.

- Contrast method - there are two main types of contrast methods: the absorption contrast, being the most common X-ray imaging mechanism, is based on the absorption rate of the material (dependent mostly on the thickness and density). It is also possible to use phase contrast that although being able to enhance the contrast of very lightly-absorbing materials such as animal and plant tissues, is a much more expensive method. The diffraction patterns resulting from the phase shifts can be exploited to improve the contrast between adjacent regions of varying material density (being extremely useful for crack detection) [36].

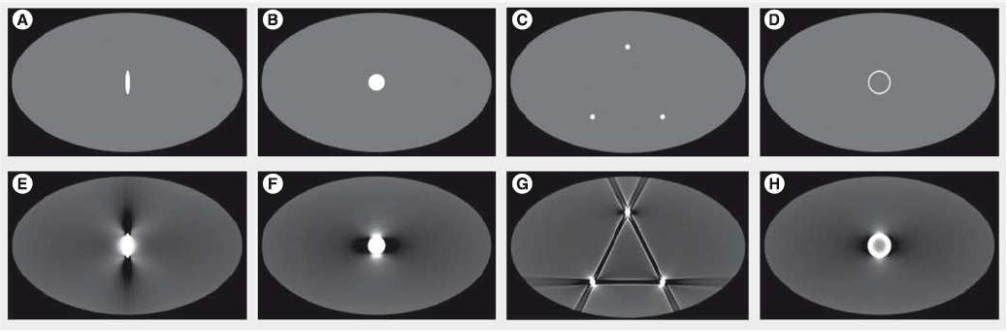


Figure 2.16: Beam hardening in simulated scans. (A-D) Simulated scans without and (E-H) with beam hardening, showing that dark streaks occur along the lines of greatest attenuation, and bright streaks occur in other directions. Scatter produces artifacts that look similar to this. [42]

By considering the combined effect of these parameters during the preparation of the CT scan it is possible to guarantee optimal image quality, reliable results, and efficiency for the intended application. However, it is still important to consider that in the majority of CT scans, it is possible to have degradation of the CT images leading to image artifacts: features, patterns, or any change in gray level observed in X-ray CT images that are arise from the imperfection of the measurement procedure and therefore do not represent the true features of the scanned object. The most common types are presented bellow [36]:

- Beam hardening - polychromatic X-ray beams lose their lower energy photons more rapidly as they pass through matter. This selective absorption increases the mean beam energy and breaks the linearity assumed in CT reconstruction for the ideal, monochromatic scenario. The result is cupping (darker centers in homogeneous objects) and streaks between dense regions as in figure 2.16. Monochromatic synchrotron sources largely avoid this effect.

- Ring artifacts - these appear as concentric rings around the rotation axis and originate from defective or miscalibrated detector pixels. Because the same pixel error persists across all projections, reconstruction backprojects it into a full circular ring. Even tough it can be easily correctable, these rings will obscure fine structural details.

- Centreing errors - when the specimen is not perfectly aligned with the rotation axis, or when it drifts laterally during scanning, projections become inconsistent. This misalignment produces blurring, double edges, or geometric distortions in the reconstructed slice. Stable mounting and precise alignment are essential.
- Streaking artifacts - streaks may arise from beam hardening, but also from extremely dense regions that fully attenuate the beam. Sharp interfaces between materials with large attenuation differences can also cause under-sampling of edge gradients, producing bright or dark streaks radiating from those boundaries.
- Motion artifacts - any movement of the sample during acquisition mechanical vibration, relaxation during in-situ loading, or rotational drift creates inconsistencies between projections. Reconstruction from these inconsistent data leads to blurring, ghosting, or streaking.

Segmentation using DragonFly

The final phase would be the segmentation of the voxels (the 3D unit of graphic information) where the labeling of the specified regions of interest (ROIs) is performed according to the material composition given the different gray levels of the CT data. Machine Learning and deep learning can be implemented for challenging segmentation tasks.

Threshold segmentation is the most basic and conventional technique being an extremely fast alternative and providing a relatively accurate results since the noise level is kept low, high contrast and the presence of artifacts is reduced [43]. It uses this principle described previously where each image is divided in different phases according to the difference in gray level of each voxel, and therefore, the different peaks on the respective histogram, as it can be seen in figure 2.17.

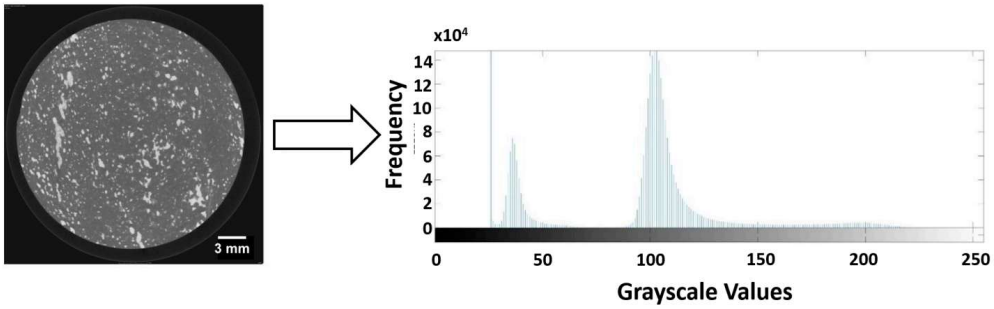


Figure 2.17: Example of an histogram where the two peaks indicate a clear threshold value (adapted from [44])

The Dragonfly software is a well-established reference for advanced segmentation and quantitative analysis. Using this software it is possible to significantly improve segmentation accuracy in complex composite material structures (such as one where the different sized chopped fibers present a random three dimensional distribution) using the deep learning segmentation module. The combination of conventional and deep learning methods enables robust, reproducible segmentation of fibers, matrix, pores, and damage features, supporting detailed quantitative characterization of composite microstructures from volumetric μCT data.

Otsu thresholding, one of the most common, is an algorithm used in 3D image analysis, where the optimal threshold is automatically derived from the image grayscale histogram. While effective for separating pores or air from the mineral matrix, its accuracy may decrease in heterogeneous samples or in the presence of partial volume effects and low-contrast interfaces [44].

The improvements obtained from the implementation of different segmentation techniques has already been documented for critical parameters such as detection rate and precision [45] [46].

2.2.3 Digital Image Correlation (DIC)

Digital image correlation (DIC) is an optical-based technique used to measure the evolving full-field 2D or 3D coordinates on the surface of a test piece throughout a mechanical test. The measured coordinate fields can be used to calculate derived field quantities of interest (QOIs), such as displacements, strains, strain rates, velocities, and curvatures. In contrast with the traditional measurement techniques, DIC is a highly versatile method since that by being a non-contact technique it is suitable for a variety of applications and is fully independent of the type of material being tested and its dimensions.

A fundamental assumption underlying Digital Image Correlation (DIC) is that the surface pattern of the specimen, whether naturally occurring or artificially applied, will follow the deformation of the underlying material. When a single camera system is employed, only two-dimensional (2D) surface coordinates can be measured (configuration commonly referred to as 2D-DIC), and in contrast, three-dimensional (3D) surface measurements require a minimum of two cameras arranged at a stereo angle, enabling 3D photogrammetry in combination with image correlation (approach known as stereo-DIC) [47].

DIC analysis can be performed using several different dedicated softwares, which are generally classified into local and global correlation methods. In local DIC approaches, the displacement solution at a given point depends solely on the image information contained within a small neighborhood surrounding that point and is independent of the solutions at other locations. Conversely, global DIC methods enforce spatial continuity by introducing dependencies between neighboring points, such that the solution at a given location is influenced by the deformation of the surrounding region.

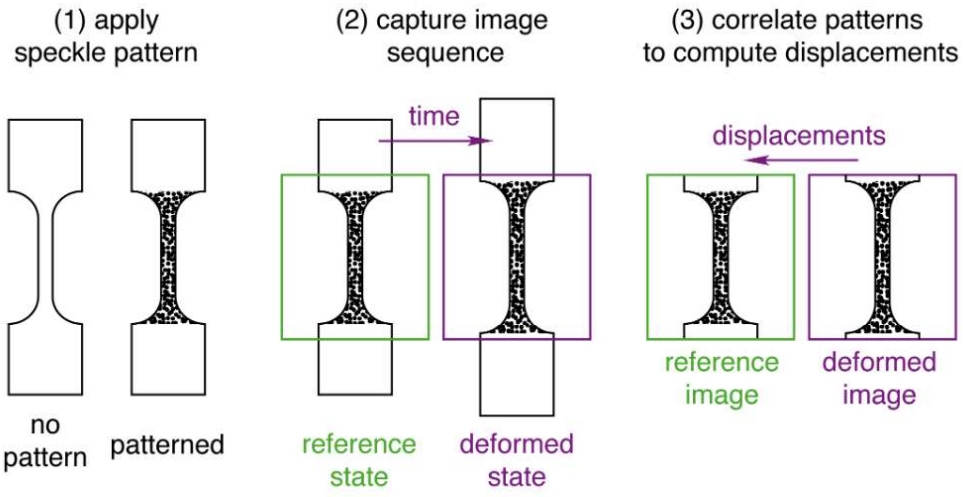


Figure 2.18: DIC evolution (from left to right): obtain a pattern on the sample for tracking; capture images of the sample during deformation; analyze the images to compute the sample surface displacements. [48]

In practice, the DIC algorithm analyzes a user-defined region of interest (ROI) within the acquired images, which is populated by a set of interrogation or measurement points. In local DIC, each interrogation point is associated with a small image subset, typically defined on a regular grid with a specified step size, allowing adjacent subsets to overlap if required. The correlation process consists of tracking these subsets from a reference image, acquired prior to deformation, to subsequent images captured during deformation. This is achieved by approximating the grayscale intensity distribution within each subset using an interpolant function, which is then allowed to

deform according to a predefined subset shape function. A correlation or matching criterion, often combined with weighting functions, is used to identify the displacement that best matches the reference subset to its corresponding deformed configuration.

For the case of composite materials, DIC has been referred to as a promising technique for composite deformation characterization. For FRP tensile loading [49], the Young Modulus has proved to be consistent with the values obtained using a conventional strain gauge. However, due to possible external vibrations, camera movement or light fluctuations is not recommended to use the strain map directly from DIC as it shows too many variations.

Measurement parameters

Before conducting the DIC measurements, it is critical to understand what is intended to obtain from the tests, consider the limitations of the method and important parameters to adjust in order to achieve the most optimized output:

- Reference image - even tough it is possible to use incremental correlation, specially for situations where the DIC pattern suffers significant changes during the test (where the best results are obtained by correlating each image with the previous one), the most common methodology is by selecting a single reference image. It is critical that the reference image is taken before the application of any load so that the specimen is undeformed since all the subsequent images will be correlated tracking over the interrogation points back to this reference.

- Frame rate - the frame rate must primarily satisfy the temporal resolution required to capture the fastest variations of the quantities of interest, which depends on the specific test (as the example of elastic-plastic transition or maximum strain before necking). Also, it is important to limit the displacement between consecutive frames to within roughly one subset size to ensure reliable correlation. This sets a minimum frame rate based on specimen velocity and image scale guaranteeing that the algorithm will be able to locate the subset position in all frames [50].

- Surface pattern - ideally, a smooth, random pattern with the highest contrast possible is the goal. Black/white ratio of 50:50 is reported to work the best since it avoids the formation of regions that cannot be properly recognized. The speckle size has to be adapted given the size of the specimen and camera resolution so that values around 3-5 pixels per speckle are obtained (as reported in [51]).

- Filtering - DIC typically provides a high precise, low noise displacement field, but numerical differentiation amplifies noise, leading to significant random error in strain fields. Filtering can be applied at the image, displacement, or strain level, though it inevitably smooths gradients and reduces local detail. For regions undergoing homogeneous deformation, global approaches such as smoothing splines effectively reduce noise but increase information loss as the averaging area grows. In contrast, specimens with strong strain gradients benefit from local filtering, which preserves spatial detail at the cost of higher residual noise.

- Grid Spacing - grid spacing defines the distance between adjacent facets and therefore the density of measurement points. Smaller spacing increases facet density and computational cost, but its effect on displacement accuracy is generally limited. In contrast, facet overlap improves the precision and accuracy of the derived strain field. The optimal spacing depends on the specimen and expected strain distribution: uniform strain fields can be analyzed with larger spacing, while regions with high strain gradients or complex geometries require smaller spacing to capture local variations.

Correlation

As referred before, performing the correlation by searching for each pixel of the reference image in the deformed one is not efficient from the computational point of view. The strategy is to subdivide the reference image into many small windows called subsets (or facets as in figure 2.19), in which each subset has a unique speckle pattern allowing the software the software to retrieve only the displacement for those specific pixels.

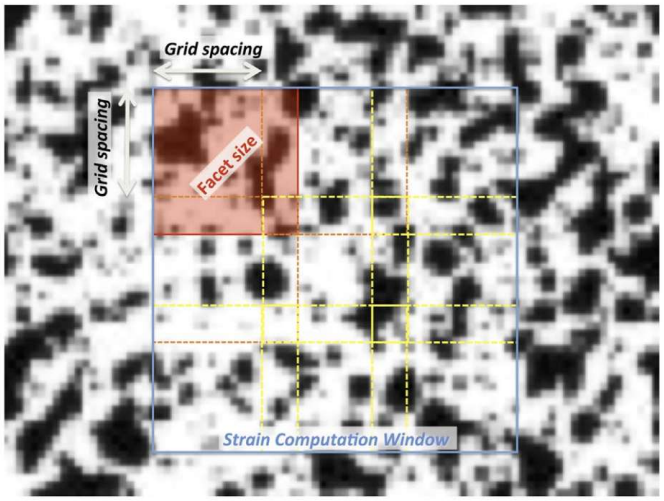


Figure 2.19: Detail of the specimen surface prepared with a random speckle pattern. Nomenclature details [47]

The three main components of the correlation process are the matching criterion, the interpolation function and the shape function.

During correlation, the algorithm locates each reference point in the deformed image by comparing gray-level patterns within a subset. The best match is the position in the deformed image whose gray-level distribution aligns more closely with that of the reference subset, based on a defined matching correlation criterion. Among the most common matching criterion is the sum of squared differences (SSD) criterion. This criterion evaluates the similarity between a subset in the reference image and its corresponding subset in the deformed image by computing the squared grey-level difference for each pixel. It is defined as

$$\chi^2 = \sum_i (G_i - F_i)^2 \tag{2.13}$$

where F_i and G_i denote the grey values of pixel i in the reference and deformed subsets, respectively. The displacement parameters are obtained by minimizing χ^2, meaning that the optimal subset position is the one that yields the smallest grey-level mismatch. SSD is computationally efficient and conceptually straightforward, but it assumes consistent illumination between images. Variations in brightness or contrast increase the residual χ^2 even when the subset is correctly aligned, which can degrade correlation quality. For this reason, illumination insensitive criteria such as NSSD or ZNSSD are often preferred in DIC applications, although the fundamental principle of minimizing a grey-level mismatch remains the same.

The second component required in DIC is interpolation because the correlation algorithm evaluates grey levels at subpixel coordinates. Since a digital image represents a discrete sampling of an underlying continuous intensity field, the grey value at a non-integer position must be estimated from neighboring pixels. An interpolation function reconstructs a locally continuous intensity distribution, allowing the correlation criterion to be evaluated accurately during subset matching.

There are a lot of different interpolation functions, however not all of them are good for every situation. The user can choose which one to use, considering that a good option should match the value at pixel locations, minimize the phase and the amplitude errors and provide filtering to the results.

Finally, the last component of the correlation algorithm is the shape function. The subset does not only translate between the reference and deformed images, it may also rotate, stretch, shear, or undergo more complex distortions depending on the local deformation field [52]. The subset shape function defines how each point within the subset is mapped from its coordinates in the reference image to its corresponding location in the deformed image. A first-order shape function provides the necessary degrees of freedom being sufficient for most DIC applications. Higher-order shape functions introduce additional terms that allow the subset to represent more complex deformation patterns or compensate for oversized subsets, but they also increase the number of unknown parameters and the computational cost of the correlation process.

2.3 Mechanical testing in composites

The analysis and design of composite structures requires the input of reliable experimental testing and subsequent data. This can be done in many different ways: micromechanical, mesomechanical, macromechanical, and structural. Since there is little information about the forged carbon composite, it is intended to perform a complete characterization of the basic properties of the laminate for use as an input in structural design and analysis, investigate analytical predictions of mechanical behavior and study of material and structural behavior for specific geometries and loading conditions. For this purpose, it includes the following types and applications of testing [24]:

- Characterization of constituent materials (i.e., fiber, matrix, and interphase) for use in micromechanics analyses. Knowing these properties, one can predict, in principle, the behavior of the lamina and hence of laminates and structures.
- Characterization of the basic microstructure, which forms the fundamental building block of all laminated structures.
- Determination of interlaminar properties.
- Material behavior under different conditions of loading (such as tensile loading).
- Experimental stress and failure analysis of composite structures, especially those involving geometric discontinuities such as free edges, cutouts or joints.
- Assessment of structural integrity by means of nondestructive testing - Techniques such as Optical Micrography and X-ray Computed Tomography (addressed previously).

Determination of constituent materials

In order to predict the macroscopic behavior of the material, the characterization of the constituent properties via micromechanics is critical. Since the material used for this work is widespread commercially, many of these properties (mainly the ones determined for the fiber or resin independently) are already presented on the technical datasheets (see Appendix A and Appendix B), being sufficient for the intended results. However, much more detailed tests can be performed such as: single filament test method (ASTM D3379-89 and ASTM D4018) for longitudinal properties, shear properties (as proposed in [53]), matrix characterization (according to ASTM D638-02 and D882-02), pushout and pullout tests for interlaminar properties or even thermal characterization methods.

Physical characterization of composite materials

Physical characterization of composites includes the determination of density, fiber volume ratio, void volume ratio, coefficients of thermal expansion, coefficients of moisture expansion, and heat conduction coefficients.

Density is determined following the standard ASTM D792-00:

- Step 1 Weigh the specimen in air to the nearest 0.1 mg.
- Step 2 Attach the specimen to an analytical balance with a thin wire and weigh while the specimen and a portion of the wire are immersed in distilled water.
- Step 3 Weigh the wire alone, partially immersed up to the same point as in the previous step.

The density of the material at 23°C (73.4°F) is determined as follows [54]:

$$\rho = \frac{a}{a + w - b} \times 0.9975 \tag{2.14}$$

where:

- ρ = density (in g/cm^3)
- a = weight of specimen in air
- b = apparent weight of fully immersed specimen and partially immersed wire
- w = apparent weight of partially immersed wire
- 0.9975 = density of distilled water at 23°C (in g/cm^3)

It is important to notice that this procedure is mostly used in plastics and therefore does not take into consideration the void volume fraction effect on the final density of the material.

Regarding the fiber volume ratios, methods such as ignition or burnout method, based on ASTM specification D2584-02 or acid digestion method, described in ASTM specification D3 17 1-99 are proposed, however, for the scope of this work, since advanced imaging techniques such as X-ray Computed Tomography will be used, this specifications will not be addressed.

Finally, for thermal and moisture expansion, can both be fully characterized in terms of two principal coefficients (one for each of the 2 orthogonal plain directions of the laminate). Determination of these coefficients consists of measuring the principal direction strains in the composite as a function of the temperature/moisture concentration.

Material behavior - determination of tensile properties

Uniaxial tensile tests are conducted aiming to determine the following properties:

E_1, E_2 = longitudinal and transverse Young's moduli, respectively

ν_{12}, ν_{21} = major and minor Poisson's ratios, respectively

F_{1t}, F_{2t} = longitudinal and transverse tensile strengths, respectively

ε_{1ut}, ε_{2ut} = longitudinal and transverse ultimate tensile strains, respectively

Tensile specimens are straight sided coupons of constant cross section with adhesively bonded tabs. The specimens are have different recommended dimensions given the application. For the case of random or discontinuous fiber orientation composites, the recommended geometry is the one presented in Figure 2.20.

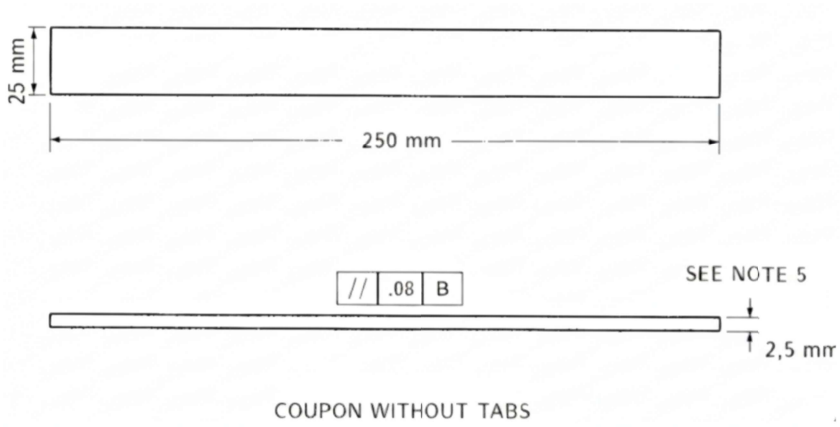


Figure 2.20: Coupon dimensions for random-discontinuous specimens. Adapted from [55]

The specimens are loaded to failure under uniaxial tensile loading. A continuous record of load and deformation is obtained by an appropriate digital data acquisition system. Axial and transverse strains are obtained by means of a pair of two-gage rosettes mounted on both sides of the specimen. For this case, is was preferable to perform DIC on the 2D behavior during the test, considering the highly anisotropic structure of the forged carbon composite. As already seen before, typical fractures of tensile coupons consist on fiber breakage, matrix cracking/splitting and debonding as seen in the example for unidirectional composite (Figure 2.21).

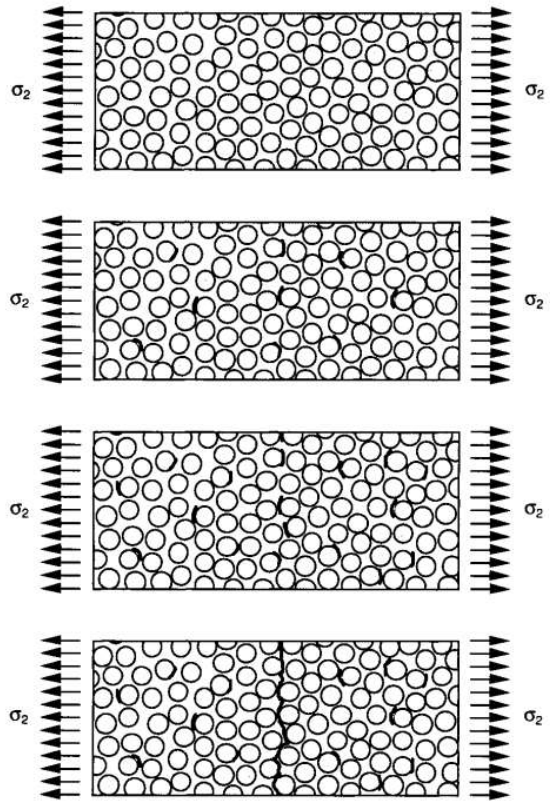


Figure 2.21: Progressive micro-cracking leading to ultimate failure in unidirectional composite under transverse tension. Adapted from [24]

Material behavior - determination of through thickness properties

Specially for thicker ply composites (above 20mm thick) is it required to perform the analysis as a 3D state stress distribution. Through-thickness testing is more problematic than in-plane testing because it is difficult to fabricate material of sufficient thickness and uniform quality. Actually, this is the exact case of forged carbon composites, where in order to manufacture a specimen for through-thickness testing, the proportions between the mold bottom and the piston-like compression mold dimension would be so high that it would be almost impossible to guarantee uniform thickness distribution, acceptable finish or even quality finishing. Given all these limitations, even though different tests have been proposed over the years, the amount of data is limited.

The idea is then to combine different methods in order to achieve different objectives:

- assessment of laminate integrity in the out-of-plane direction for quality control of the lamination process
- generation of design allowables for thick composite laminates subjected to three dimensional states of stress
- evaluation of laminate resistance to delamination caused by interlaminar tensile stresses near free edges under in-plane loading

The most commons methods used for through thickness properties all involve machining the specimen (usually rectangular cross section) in the thickness direction and performing the different tests using only that section of the specimen. An alternative is the split ring test [24]: An indirect test for determination of through-thickness tensile strength. It consists of a curved laminated beam specimen loaded in tension, as shown in Fig . Under this loading, a pure interlaminar radial tensile stress, is induced in the apex of the specimen test section. For semicircular geometry this stress can be closely estimated by the following relation:

$$\sigma_z = \frac{3PL}{2bhR} \tag{2.15}$$

where:

- P = applied tensile load
- L = distance between load and test section
- b = beam width
- h = beam thickness
- R = mean radius of circular section

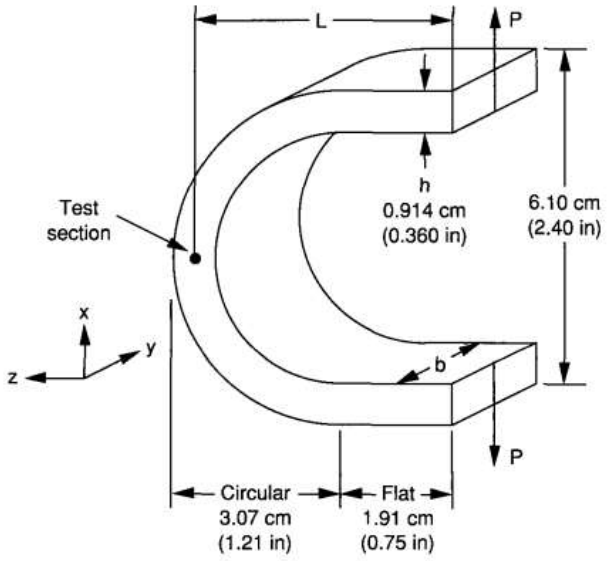


Figure 2.22: Semicircular curved beam specimen for determination of interlaminar tensile strength. Adapted from [24]

Characterization of composites with stress concentrations - Circular hole

The changes in stress distributions around notches can significantly reduce the strength and safe life of a composite due to damage growth around these areas. It is possible to determine these changes in stress distribution and concentration by linear analysis, finite element methods and experimental methods.

The problem of failure of notched composite laminates has been dealt with by several approaches. One approach is based on concepts of linear elastic fracture mechanics carried over from homogeneous isotropic material. However, for the case of composite materials, it is rare the case were the material behaves in an homogeneous, isotropic manner. It is much more common to identify damage, delamination or matrix cracks during loading, making this a very coarse approach.

A second approach is based on actual stress distribution near the notch and applies simplified fracture criteria - failure occurs when the average stress over an assumed characteristic dimension from the boundary of the notch equals the tensile strength of the unnotched material. Experimental methods using strain gauges, imaging techniques and moire fringes have proven very useful in studying the deformation and failure of composite laminates with circular holes or even through-the-thickness cracks of various size. The usual approach in these cases is to load composite specimens under uniaxial and biaxial tension, measure deformations by means of experimental strain analysis techniques, and determine strain distributions, failure modes, and strength reduction ratios.

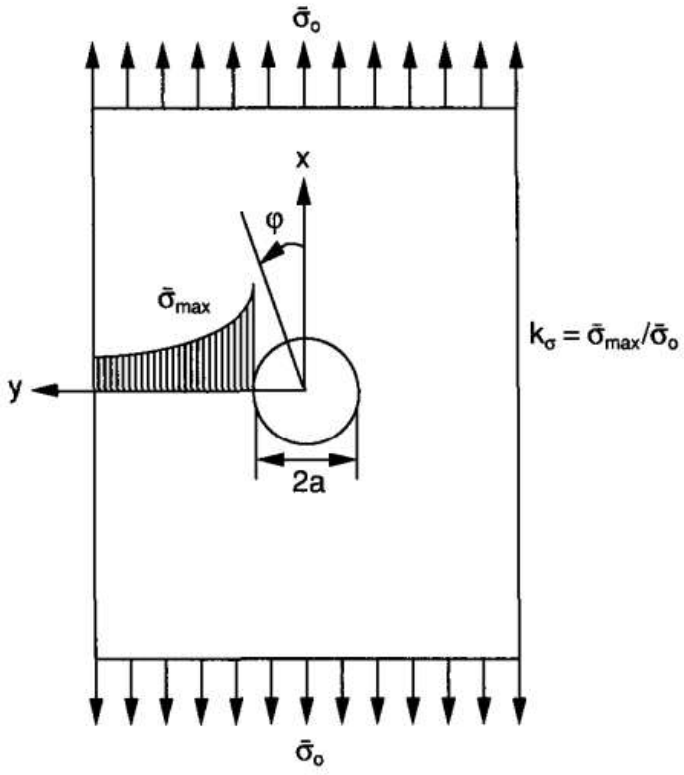


Figure 2.23: Composite laminate with circular hole under uniaxial tensile loading. Adapter from [24]

For the circular hole on an "infinite" plate, considering an orthotropic composite under uniaxial loading along a principal axis x, the maximum stress is the circumferential stress on the hole boundary at $\phi = 90°$. The stress concentration at this location is obtained as [24]:

$$k_\sigma = \frac{\bar{\sigma}_{\max}}{\bar{\sigma}_o} = 1 + \sqrt{2\left(\sqrt{\frac{\bar{E}_x}{\bar{E}_y}} - \bar{\nu}_{xy}\right) + \frac{\bar{E}_x}{\bar{G}_{xy}}} \tag{2.16}$$

where:

- $\bar{\sigma}_o$ = applied far-field average stress
- $\bar{\sigma}_{\max}$ = maximum circumferential stress on the hole boundary at $\varphi = 90°$
- $\bar{E}_x, \bar{E}_y$ = average Young's moduli in the x- and y-directions
- $\bar{G}_{xy}$ = average shear modulus
- $\bar{\nu}_{xy}$ = average Poisson's ratio

By comparing this equation with the ones obtained for the isotropic and incompressible material, it is possible to confirm their identicalness [56]:

$$k_\sigma = 1 + 2\frac{(E_s)_{a,\pi/2}}{(E_s)_\infty} \tag{2.17}$$

Also, for this conditions, the radial, circumferential and shear stresses at a location separated of a distance r=a of the center of the hole were also defined as:

$$\sigma_r = \frac{\sigma_\infty}{2}\left[1 - \frac{a^2}{r^2} + \frac{E_s}{(E_s)_\infty}\left(1 - \frac{4a^2}{r^2} + \frac{3a^4}{r^4}\right)\cos 2\theta\right] \tag{2.18}$$

$$\sigma_\theta = \frac{\sigma_\infty}{2}\left[1 + \frac{a^2}{r^2} - \frac{E_s}{(E_s)_\infty}\left(1 + \frac{3a^4}{r^4}\right)\cos 2\theta\right] \tag{2.19}$$

$$\tau = -\frac{\sigma_\infty}{2} \cdot \frac{E_s}{(E_s)_\infty}\left(1 + \frac{2a^2}{r^2} - \frac{3a^4}{r^4}\right)\sin 2\theta \tag{2.20}$$

As it is possible to see in Figure 2.24, for an isotropic material, the ratio between secant and elastic modulus is 1 except for higher values of applied stress (plastic deformation begins), verifying the predicted behavior for an orthotropic composite.

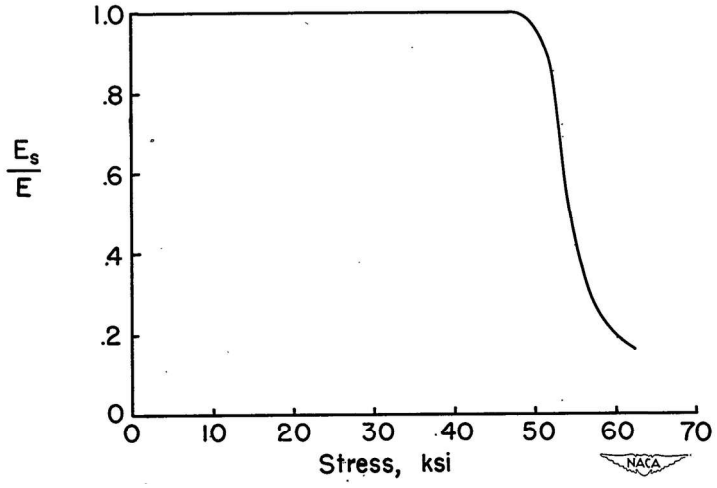


Figure 2.24: Values of Es/E for the 24D-T3 aluminum alloy when subjected to different applied stresses. Adapter from [56]

The stacking sequence is known to have a significant influence on strength and failure patterns: just from analyzing the data on Appendix C, the strength ratio varies from around 0.3 to 0.9 just by changing the laminate layup and stacking sequence for boron/epoxy plates. Stacking sequences resulting in tensile interlaminar normal stresses near the boundary of the hole have also proven to reduce the strength of the laminate.

The influence of hole diameter in uniaxially loaded plates can be described using the average stress criterion. According to this approach, failure occurs when the axial stress, averaged over a characteristic distance a_0 from the hole boundary, reaches the unnotched laminate strength $\bar{F}_0$. The resulting strength reduction ratio, defined as the ratio between notched and unnotched strength, is given by [24]:

$$k_F = \frac{\bar{F}_N}{\bar{F}_0} = \frac{2}{(1+\xi)\left[2 + \xi^2 + (k_\sigma - 3)\xi^5\right]} \tag{2.21}$$

where

$$\xi = \frac{a}{a + a_0} \tag{2.22}$$

2.4 Hydrofoil design theory

2.4.1 Hydrofoil geometry

The hydrofoil wing is the component responsible for almost all of the lift force generated in ATLANTICO prototype, allowing the boat to lift its hull off the water, therefore increasing its efficiency, range, and versatility of applications.

Being very similar to a general wing, an hydrofoil wing is also constituted by foil sections - the basic 2D element of any lifting surface in a fluid - working on the water instead of the air [57].

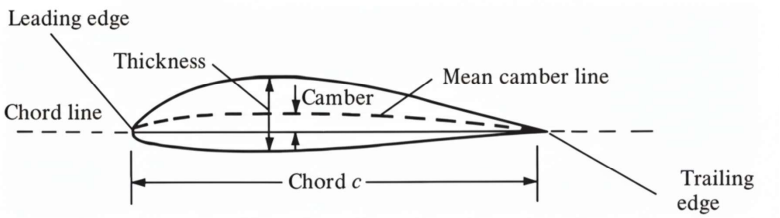


Figure 2.25: Cambered foil section scheme

The complex geometry of an hydrofoil wing can be defined by several different parameters. In this section, the main features relevant to this work will be addressed. Starting with the 2D section composing the hydrofoil wing, it is possible to define its leading edge (LE), trailing edge (TE), chord c and the chord line (that defines the angle of attack AoA, taking into consideration its angle relative to the direction of the oncoming flow).

The wing itself can be seen as a 3D extension of this 2D foil section, having a general geometry similar to the one represented in 2.26. This way, it is also possible to define its semi-span s, the Mean Aerodynamic Chord (MAC) and planform area S.

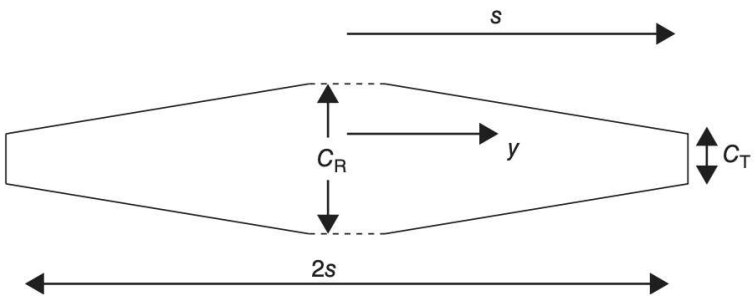


Figure 2.26: Dimentions for the unswept wing [58]

The MAC ($\bar{c}$) is a critical parameter, representing the chord of a rectangular wing that has the same total area and pitching moment as the actual wing. The formula for the Mean Aerodynamic Chord is defined using an integral expression over the semi-span (s) [57]:

$$\bar{c} = \frac{2}{S}\int_0^s c(y)^2\,dy \tag{2.23}$$

Similarly, the total wing planform area, S, can also be defined, being given by the integral of the chord c along the span.

$$S = 2\int_0^s c(y)\,dy \tag{2.24}$$

Having defined the mean geometric chord as $\bar{c}$, then we can rewrite S as $S = b\bar{c} = 2s\bar{c}$.

Finally, it is also important to define the aspect ratio (AR) of the wing. AR is no more than a measure of the slenderness of the wing planform and is given by the ratio of the square of the full span (b) to the wing area (S), which, using the mean chord $\bar{c}$, can also be expressed as [58]:

$$\mathrm{AR} = \frac{b^2}{S} = \frac{(2s)^2}{b\bar{c}} = \frac{b}{\bar{c}} \tag{2.25}$$

In the foiling world, it is possible to see all kinds of combinations of these parameters in the most distinct applications. From the most straight forward examples such as the ones used in small E-Foil boards - where the hydrofoil wings are usually fixed, present a perfectly elliptic shape and are usually in sets of maximum two wings - to the highly complex solutions found in many passengers ferries or racing yachts - where the wings present one (and sometimes more) degrees of freedom, are actively controlled and present a much complex geometry (sometimes even with added flaps and ailerons).



Figure 2.27: Fliteboard E-Foil strut system (left) and the Luna Rossa AC75 racing yacht wings (right). [59, 60]

For the case of ATLANTICO, the solution found was a simple, reliable and robust carbon fiber structure, named by the team as Type-B hydrofoil (described in detail further on this section).

2.4.2 Hydrodynamic Loads

Fundamental principles of the flow

The loads exerted by the fluid on the wing are determined from the pressure and wall-shear stress fields around its surface. To further understand these interactions, let us consider an infinitesimal fluid element such as the one represented on Figure 2.28

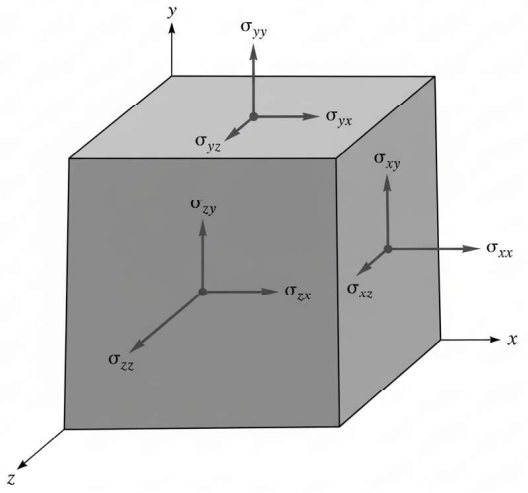


Figure 2.28: Fluid element representation - notation for the stresses

Given that the hydrofoil works in water, the velocity magnitude of the flow is significantly lower than the speed of sound, i.e. $|\mathbf{v}| \ll a$, with $a \approx 1481$ m/s at 20°C . Thus, the density of the fluid is assumed to remain constant at all times, i.e. $\frac{\partial \rho}{\partial t} = 0$, and consequently the velocity field can be shown to be *divergence-free*, i.e. [61].

$$\nabla \cdot \mathbf{v} = 0 \tag{2.26}$$

In the same way, the *differential* form of the mass conservation equation for incompressible fluids can be written as follows

$$\frac{\partial u_i}{\partial x_i} = 0 \tag{2.27}$$

In order to establish the fluid stresses acting on the wing, we can develop the equation differential form of the momentum equation by assuming the conditions for a Newtonian fluid, where the viscous stresses are proportional to the rate of deformation and viscosity coefficient of the fluid (in this case, water) as in 2.28

$$\tau_{ij} = \mu \left(\frac{\partial u_i}{\partial x_j} + \frac{\partial u_j}{\partial x_i} \right) \tag{2.28}$$

Then, for the infinitesimal fluid element we can define the stress tensor, σ_{ij}, that is obtained by the sum of the contribution of the hydrostatic pressure (*isotropic pressure* term) and the viscous stresses (*shear-stress* term) that arise from a movement with velocity gradients.

$$\sigma_{ij} = -p\delta_{ij} + \mu \left(\frac{\partial u_i}{\partial x_j} + \frac{\partial u_j}{\partial x_i} \right) \tag{2.29}$$

This way, from the balance of the gravitational force (per volume unit), force caused by pressure (per volume unit), viscous force (per volume unit) and linear momentum we get to the Navier-Stokes equations, as presented bellow

$$\rho \frac{Du_i}{Dt} = -\frac{\partial \tilde{p}}{\partial x_i} + \mu \frac{\partial^2 u_i}{\partial x_j^2}, \quad (i,j) = (1,2,3) \tag{2.30}$$

Or written in cartesian form

$$\begin{aligned}
\rho\frac{du}{dt} &= \rho g_x - \frac{\partial p}{\partial x} + \mu\left(\frac{\partial^2 u}{\partial x^2} + \frac{\partial^2 u}{\partial y^2} + \frac{\partial^2 u}{\partial z^2}\right) \\
\rho\frac{dv}{dt} &= \rho g_y - \frac{\partial p}{\partial y} + \mu\left(\frac{\partial^2 v}{\partial x^2} + \frac{\partial^2 v}{\partial y^2} + \frac{\partial^2 v}{\partial z^2}\right) \\
\rho\frac{dw}{dt} &= \rho g_z - \frac{\partial p}{\partial z} + \mu\left(\frac{\partial^2 w}{\partial x^2} + \frac{\partial^2 w}{\partial y^2} + \frac{\partial^2 w}{\partial z^2}\right)
\end{aligned} \tag{2.31}$$

These are non linear partial differential equations of second order that can be used to find the solutions for several problems regarding viscous flows. They have four unknowns, p, u, v, and w and for cases where the fluid is incompressible, should be combined with the continuity equation (2.27).

Another essential property for the study of fluid flow is the ability to represent the governing equations in dimensionless form. In this work, the *Reynolds number*, Re, is defined as follows:

$$Re \equiv \frac{\rho u_0 L_0}{\mu} = \frac{u_0 L_0}{\nu} \tag{2.32}$$

Where ν is the *kinematic viscosity* of the fluid, computed as $\nu = \mu/\rho$, and L_0 and u_0 are problem-dependent reference length and velocity values, respectively. The *Reynolds number*, Re, indicates the relative importance of the diffusive (viscous) and convective (inertial) fluxes in the fluid flow, and governs the nature of the flow, particularly its transition to turbulence [61].

Loads on an hydrofoil

In the study of lifting surfaces, the stress fields described in the begging of this chapter are usually represented by mean of integrated force coefficients.

As seen before, it is possible to consider the flow around the hydrofoil wing as incompressible, showing a behavior similar to the one presented in Figure 2.29 where it is possible to see the pressure face, yielding positive pressure oriented toward the hydrofoil, while the suction face shows negative pressure. It is also possible to see the adverse pressure gradient caused by the decrease of the velocity along the profile chordwise direction [61].

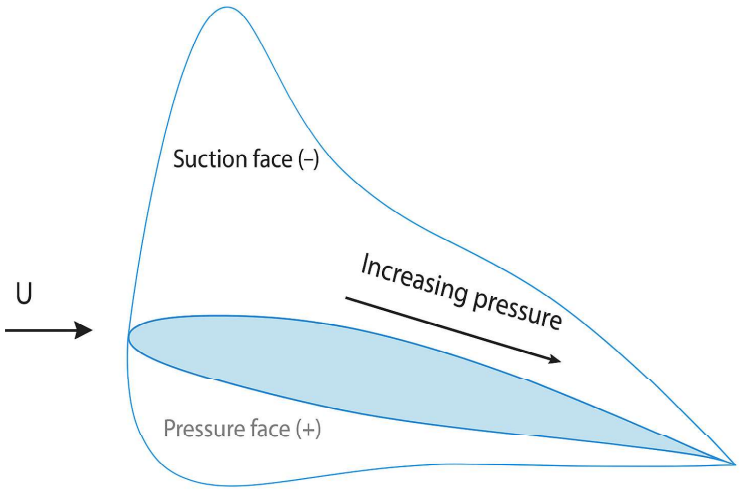


Figure 2.29: Pressure distribution around a foil section [62]

The curvature of streamlines around an airfoil forces fluid particles to follow bent paths and requiring a centripetal acceleration U^2/r toward the local center of curvature. This results radial pressure gradient for an incompressible fluid of density ρ is, from radial force balance [63]

$$\frac{\mathrm{d}p}{\mathrm{d}r} = \rho\frac{U^2}{r}, \tag{2.33}$$

where r denotes the local radius of curvature of the streamline measured from the centre of curvature to the streamline itself. This implies a lower static pressure on portions of the suction surface where the local velocity is larger (smaller r) and a pressure recovery toward the trailing edge where the flow decelerates as described for 2.29.

It is usefull to represent this pressure distribution by means of a dimensionless pressure coefficient, C_p, such that

$$C_p(\mathbf{x}) = \frac{p(\mathbf{x}) - p_\infty}{q_\infty}, \qquad q_\infty = \frac{1}{2}\rho_\infty U_\infty^2 \tag{2.34}$$

where $p(\mathbf{x})$ denotes the *local static pressure*, and p_∞, ρ_∞, and U_∞ represent the *free-stream static pressure*, *density*, and *velocity magnitude*, respectively. The quantity q_∞ is referred to as the *dynamic free-stream pressure* and is widely used in aerodynamic analyses.

Similarly, the local wall shear stress $\tau(\mathbf{x})$ can be expressed in dimensionless form through the *skin-friction coefficient*, C_f, defined as

$$C_f(\mathbf{x}) = \frac{\tau(\mathbf{x})}{q_\infty}. \tag{2.35}$$

Here, $\tau(\mathbf{x})$ represents the *local wall shear stress*. The coefficients C_p and C_f provide a normalized measure of pressure and viscous forces acting on the surface, facilitating comparison between different flow conditions and geometries.

By integrating these coefficients over the wing surface, we can then obtain the force coefficients for the lift and drag components (depending on the considered direction) and obtain the resultant force.

The resultant force (on the hydrofoil cross section) acts through a point on the chord known as the *centre of pressure* (CP). Even though he moment due to hydrodynamic forces in this point is zero, its location on the chord changes depending on the AoA [63].

The total aerodynamic force can be decomposed into two orthogonal components: the lift L, acting normal to the free-stream direction, and the drag D, acting parallel to it. Due to the offset between the CP and a chosen reference point on the chord, a pitching moment M is also generated [58].

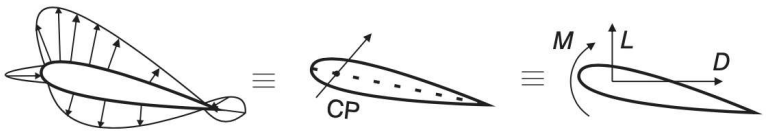


Figure 2.30: Resultant aerodynamic force acting at the centre of pressure [58]

It is convenient to express these quantities in non-dimensional form using the free-stream dynamic pressure and the airfoil chord length c. The corresponding aerodynamic coefficients are defined as

$$C_L = \frac{L}{q_\infty S}, \qquad C_D = \frac{D}{q_\infty S}, \qquad C_M = \frac{M}{q_\infty S c}, \tag{2.36}$$

C_L, C_D, and C_M being the lift, drag, and moment coefficients, respectively.

All of these coefficients are known to have a high dependence on the AoA value. This relationship can be seen clearly on the example of the *lift coefficient* versus AoA for the general symmetric and cambered airfoil examples in Figure 2.31. It is possible to see an approximately linear relation up to a certain angle, called the stall angle, α_{stall} where the *lift coefficient* has its maximum value. The slope of this linear part the curve for low α values is called the *lift curve slope* and has a theoerical value of 2π per radian. Experimental measurements show that in practice, this value is slightly lower, and this value works rather as a majorant of this slope on common profiles [64].

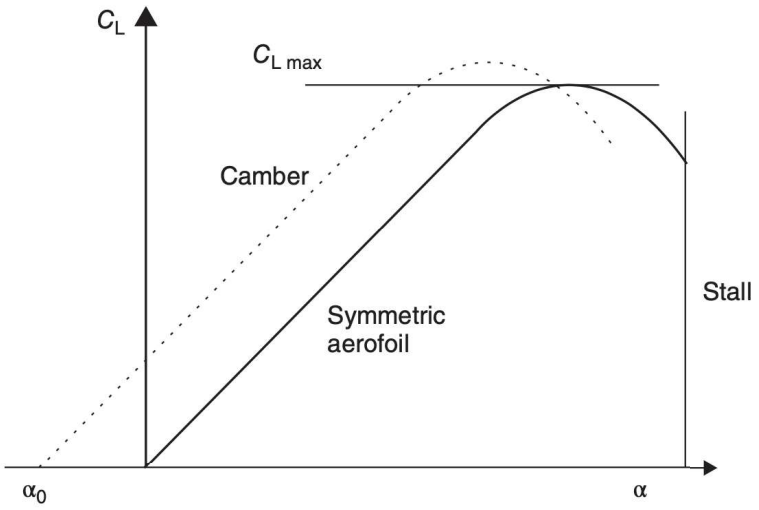


Figure 2.31: Variation of the lift coefficient with the angle of attack [58]

After this linear behavior, seen only for low values of α, further increase of the angle of attack will result in the decrease of the *lift coefficient*.

The phenomenon of stall in lifting surfaces, under the assumption of incompressible flow, is fundamentally governed by viscous effects. The critical mechanism is the boundary-layer separation, which is precipitated by the inability of the fluid layer near the surface to overcome an intense adverse pressure gradient, resulting in a significant increase in associated drag and a loss of lift [63].

Stall behavior is critical in the design of any lifting system, as it determines whether dynamic instability introduced into the system is reversible. In finite lifting surfaces, the planform geometry and the resulting spanwise lift distribution exert significant influence on the stall progression, dictating the sequence in which different sections of the surface exhibit flow separation. The robust prediction and control of stall occurrence are therefore central aspects in the successful design of both aerodynamic and hydrodynamic lifting surfaces.

Loads on finite wings

Even tough the bases of the hydrodynamic behavior of the wing can be understood by taking into consideration the flow around its two-dimensional cross section, in practice, a wing is a three-dimensional body and important nuances that arise.

In a finite wing, it is possible to observe a phenomenon of longitudinal vorticity that occurs along its entire span with higher intensity in the wingtip region. This happens mainly because of the pressure differential between the upper and lower surfaces of the wing, causing a deflection of the flow towards the wing-tips. This results in a spanwise velocity that is responsible for the generation *chordwise vorticity*, which will cause *wing-tip trailing vortices* [63].

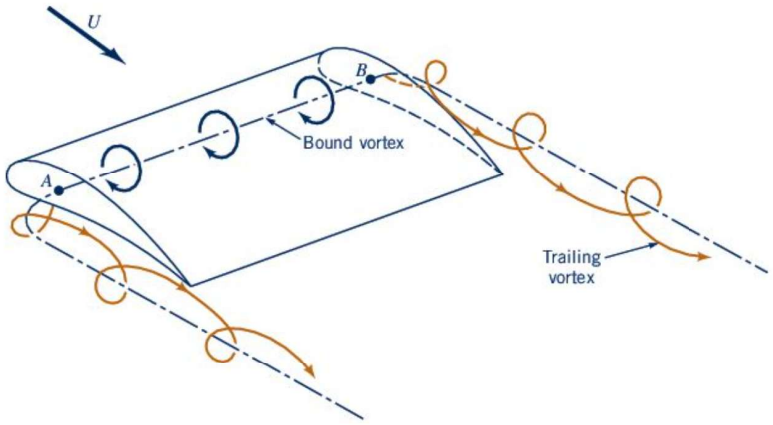


Figure 2.32: Wing-tip trailing vortices representation

The vortices released in the wing-tips are responsible for the appearance of a field of descending induced velocities, v_i, so, each section will now experience a different effective velocity field which will result in the decrease of the angle of attack - an effect called *downwash*. In Figure 2.33 it is possible to see the α_i, *induced angle of attack*, caused by this effect, leading to a decrease in the local α_{eff}, *effective angle of attack*.

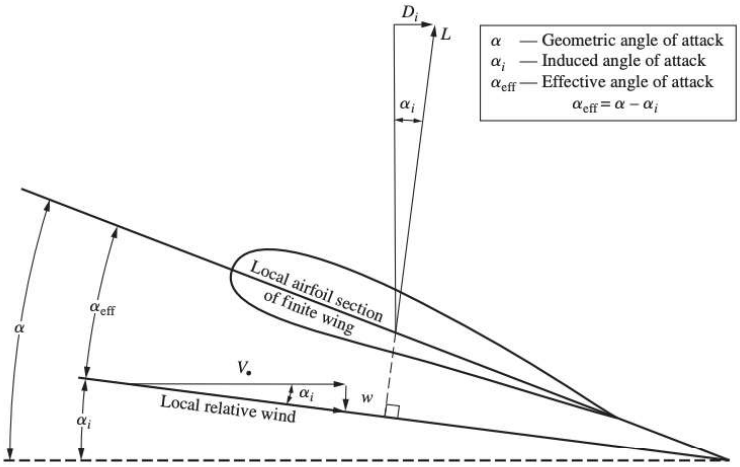


Figure 2.33: Effect of downwash on the local flow over a local airfoil section of a finite wing [65]

The effects of wing-tip vortices will lead to several consequences such as the creation of induced drag, proportional to the lift and α_i, increasing the total drag of the wing

$$C_D(C_L) = C_{D_0} + C_{D_i} = C_{D_0} + \frac{C_L^2}{\pi e AR} \tag{2.37}$$

Where e is called the *Oswald efficiency factor* (for a perfectly elliptical wing $e = 1$). It will also decrease the overall performance of the wing, create disturbances on the wake (affecting the stern hydrofoil) and decrease the value of the *lift curve slope* - according to the Prandtl lifting line theory, for the case of an elliptical wing, this variation is only dependent on the AR value [63]

$$a_{3D} = \frac{a_0}{1 + \frac{a_0}{\pi \cdot AR}} \tag{2.38}$$

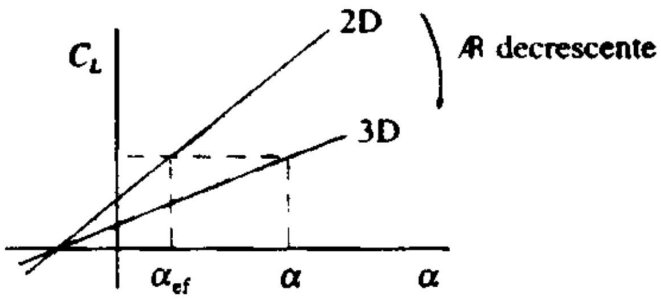


Figure 2.34: Effect of wing-tip vortices on a cambered foil - 2D vs 3D evolution [63]

If all these effects are taken into account, it is possible to establish an acceptable prediction of the spanwise load distribution on the hydrofoil wing. Since hydrofoil usually show a reletively high AR and non-critical conditions, we can consider for example the strip theory, one of the simplest methods available where the wing is assumed to be composed of a number of elemental chordwise *strips* that each has a *lift coefficient* proportional to the local α and that the lift on one strip has no influence upon another [58]. The lift on the wing would then be obtained from 2.39

$$L_{\text{TOTAL}} = \int_0^s dL = \frac{1}{2}\rho V^2 c a_1 \int_0^s \alpha(y)\, dy \tag{2.39}$$

For the case of a tapered wing, the chord variation along the span $c(y)$ must be included in the integral. Similarly, to include the hydrodynamic effects mentioned previously, the value a_1 (lift curve slope of the strip) should be adjusted taking into consideration an appropriate hydrodynamic model or simply by using the experimental expressions presented by [66]

$$a_W(y) = a_1 \left[1 - \left(\frac{y}{s}\right)^2\right] \tag{2.40}$$

$$a_W(y) = a_1 \left[1 - \left(\frac{y}{s}\right)^2\right]^2 \tag{2.41}$$

$$a_W(y) = a_1 \cos\left(\frac{\pi y}{2s}\right) \tag{2.42}$$

Take off and cruise operating conditions

At a speed of approximately 10 knots, ATLANTICO is projected to generate sufficient hydrodynamic lift to elevate its hull an estimated 25 cm above the water surface. This critical operating condition – known as take-off – is one of the most demanding loading scenario the vessel must endure. Take-off conditions are commonly used for wing design since they have the maximum predominance of the lift forces and induced drag [57].

Cruise conditions represent the longest and most common scenario in typical flight operations. Therefore, the lifting surface configuration must be optimized for maximum efficiency, where minimizing drag plays a significant role in maximizing the vessel's range for a given energy supply, or maximizing cruise speed while maintaining power requirements.

Although the importance of achieving the maximum cruise efficiency was the main priority for the team when designing the presented *type-B* wing, in the context of this work, ensuring flow stability and structural integrity hold the most significant role.

The analysis of these two flight stages has been studied extensively in aerospace applications, and hydrofoil design is currently following the same methodological tendencies [58].

The need for performing modal analysis on the hydrofoil is well established in both numerical and experimental studies in the literature [67][68].

For the ATLANTICO type B hydrofoil, it is essential to verify that the natural (resonance) frequencies of the aft hydrofoil lie outside the propulsion and operational excitation band produced by the 15 kW electric motor mounted directly above on the propulsion column. Specifically, both take-off and cruise conditions must be checked to ensure no overlap exists between the motor's excitation spectrum (including harmonics) and the hydrofoil's structural modes, since sustained forcing near a natural frequency can induce large amplitude responses and accelerate fatigue in an already highly solicited structure [58].

2.4.3 ATLANTICO specially designed Hydrofoil Type-B

ATLANTICO is equiped with a set of three T-shaped hydrofoil wings (Figure 2.35): two located along the longitudinal centerline of the vessel and mounted on each hull, and one positioned at the stern, mounted at the center of the aft carbon-fiber beam. These foils are adjustable and automatically controlled, allowing the hulls to lift above the water surface and compensate for sea disturbances, while also enabling control of the vessel's pitch and roll according to operational requirements.

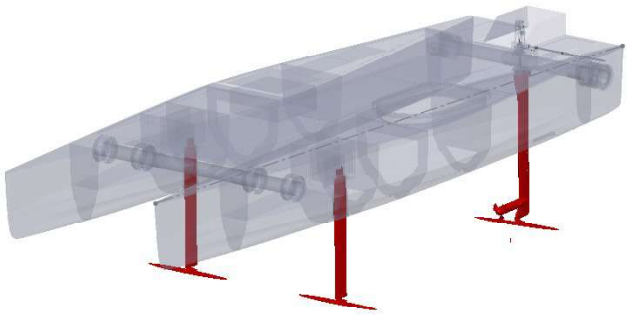


Figure 2.35: Hydrofoil system on the boat

The geometry for the wing came from two main assumptions: one being the weight of the vessel - estimated at the time to be around 300 kg (pilot included) - and the other being the maximum take off speed of 10 knt (nautical miles per hour), taking into consideration the competitive requirements for the several races [69].

Also, since ATLANTICO will be competing in several different regatta venues and conditions, a fully-submerged foil system was chosen giving the vessel its ability to be decoupled from direct sea and wave interactions, reducing external disturbances and enabling better stability when compared with a surface-piercing foil system [2].

In terms of the control system, the solution found aimed at the most simple connection between the hydrofoil wing and strut, leading to the implementation of a varying incidence control on the entire wing. This strategy allows to simplify the actuation and reduce the weight of the system when compared with a varying edge flap control.



Figure 2.36: Comparison between edge flap control (left) and varying incidence control (right) [2]

NACA Profile

As referred in the previous sections, the hydrofoils are the basic elements that constitute the hydrofoil wing: these are detailed streamlined geometries that, when set at a suitable angle of attack, generate more lift then drag for the right conditions.

The methodology to find the optimal foil profile was based on achieving the maximum efficiency in order to increase the autonomy of the vessel. This usually means increasing the AR as much as possible [70]. For our case, the limitations were imposed by the competition itself where, according to the regulations, the maximum beam for the boat is 2.4 meters. Given that the two hulls were already separated by approximately 1.4 meters, the higher span value possible for the wings was 820mm. This value also led to the definition of the chord value at the root of the wing C_R by computing the approximate value of S using the general lift equation given a maximum Lift Coefficient C_L of 1.5 - a majorant of the typical values for hydrofoils - and an elliptically shaped wing, obtaining a C_R value of around 125mm [71].

At this point, it was possible to estimate the range of Reynolds (Re) values for the amplitude of service velocities and predict which 2D profile is the most suitable for the wing.

Given that for the operational conditions, the wing experienced Re values between 1×10^5 and 9×10^5, it is then more straight forward to select a set of airfoil profiles that are suitable for such application. From this process, two main profiles were considered: the AG-25 and the NACA 63_1412.

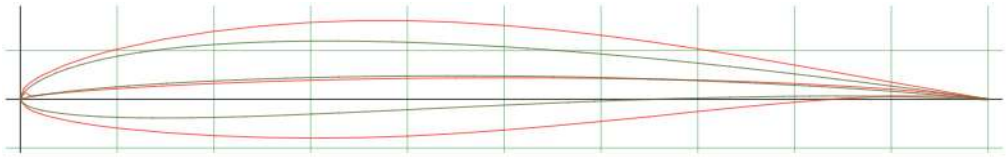


Figure 2.37: Comparison between the two profiles: AG25 (green) and NACA 63_1412 (red)

Despite the slightly higher efficiency of the AG-25 profile in the range of velocities considered for analysis, the NACA 63_1412 was the one to be used on the wing given that it has much higher moments of inertia I_x and I_y (roughly twice that of the AG25 as in table 2.4) and a much higher section area (40% increase) for the same chord value, ensuring a much higher resistance to bending and therefore less deflection for the same hydrodynamic loads.

Table 2.4: Comparison between AG25 and NACA 63412 -SolidWorks section properties for 100mm chord

Property	**AG25**	**NACA 63412**
Section area	$474.08\,mm^2$	$755.52\,mm^2$
Polar Moment of Inertia (J)	$240,699\,mm^4$	$362,762\,mm^4$
Principal I_x (minor axis)	$1,618.8\,mm^4$	$6,018.8\,mm^4$
Principal I_y (major axis)	$239,080\,mm^4$	$356,743\,mm^4$

Fixtures and additions

The wing symmetry, provided by the inverted T configuration on both struts and propulsion column, allowed for the simplification on many of the aspects regarding the hydrofoil morphology and respective mountings. An elliptical planform wing design as chosen, obtained by approximating both leading and trailing edges curves to the ones of an ellipse with a semi-major axis equal to s and the minor axis equal C_R. This ensures the most efficient form, since it will ensure the lowest induced drag, drad induced by the lift and the highest lift coefficients compared to all other planforms shapes [72].

After performing numerical simulations on the assembly hydrofoil wing + strut, it was possible to observe the streamline behavior along the flow around the entire geometry and understand where adjustments or additions were needed.

For these simulations, the turbulence effects were modeled using the robust k-ω SST closure, which is particularly suited for predicting flow separation and accurately calculating hydrodynamic performance via the kinetic energy (k) and specific dissipation rate (ω) fields. A high-resolution computational mesh was generated, incorporating a local refinement near the hydrofoil. This refinement was essential to accurately capture the flow gradients such as separation and re-attachment, along the foil surface. Finally, boundary conditions were applied to simulate realistic flow behavior. A range of angles of attack (from 0° to 12°) was submitted along with a range of target flow speeds (from 0 to 12m/s).

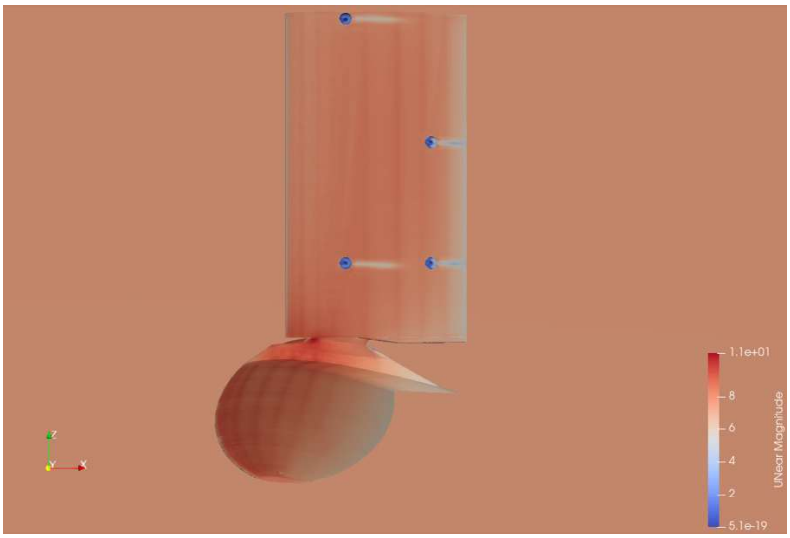


Figure 2.38: OpenFOAM simulation on the hydrofoil wing + strut assembly (for the definition of the critical areas [71]

The results were clear and the primary design optimization targeted the geometric transition (fillet) between the vertical strut and the foil. This involved smoothing transitions and aligning local flow, which successfully yielded a significant reduction in drag and a corresponding decrease in turbulence intensity within the junction area. Further enhancement was achieved by incorporating an hydrofoil tail, strategically implemented to improve the hydrofoil's stability and the uniformity of the lift. The addition of this extension resulted in a more even pressure distribution and notably achieved a reduction of the mean lift forces along the total chord length of the hydrofoil [71].

ATLANTICO's Type-B hydrofoil wing is therefore a symmetric varying incidence control elliptical wing that is centrally actuated with an added trailing edge tail as shown in 2.39.



Figure 2.39: Final hydrofoil wing configuration

In order to guarantee the structural integrity of the wing, the wingtip was slightly trimmed to a minimum tip profile chord of 20mm. This geometric detail is not expected to have a significant hydrodynamic effect on the wing behavior. However, given the limited resources of the team both in experience when dealing with composites and tight time constraints, this strongly accelerated the mold design, manufacturing and preparation.

The final hydrofoil wing geometrical configuration can then be found in Table 2.5:

Table 2.5: Wing geometric features

Variable	**Description**	**Value**	**Units**
b	Wingspan	810	mm
$\bar{c}$	MAC (Mean Aerodynamic Chord)	113	mm
$c_{\text{root (w/o tail)}}$	Root-chord (without tail)	125	mm
$c_{\text{root (w/ tail)}}$	Root-chord (with tail)	185	mm
c_{tip}	Tip-chord	20	mm
λ	Taper Ratio ($c_{\text{tip}}/c_{\text{root (w/o tail)}}$)	0.16	-
S	Planform Area	0.085	m^2
AR	Aspect Ratio	7.72	-
Λ	Root tip sweep	0.291	$\circ$
-	Airfoil	NACA 63_1412	-

Chapter 3

Experimental testing

In this chapter, relevant aspects concerning the experimental testing on forged carbon material are exposed and discussed. The entire process from the standard selections and respective modifications to the mold design, development and laboratory work is covered in this section.

3.1 Specimen preparation

All the specimens were manufactured performing the impregnation manually and respecting the respective gelation time for the temperature of the laboratory at the time of each process.

After de-molding it is then necessary to perform the complete specimen preparation given the desired experimental tests. For this case, the procedures and methodology were taken from the ASTM D3039 [55] since these are suitable for all the experimental testing intended for this work.

The first phase of the preparation included the correct labeling of each specimen. For this work, the scale chosen was based on the timeline relative to the time when the specimen was manufactured. The extensions for the labeling process were mostly based on the mold optimization process (detailed in the next section), where when the second D3039 specimen mold was used, the extensions “xx_1” and “xx_2” were used in order to distinguish between the two sides of the mold.

Given the recommendations on [55], several rectangular tabs were manufactured using 2024 Aluminum and glued using the *3M DP490 Scotch-Weld* epoxy adhesive in order to ensure the correct introduction of loads into the specimens as well as to prevent premature failure as a result of an eventual discontinuity. Each tab had exactly 56 mm x 25 mm x 2 mm - dimensions obtained by taking into consideration a conservative approach of the equation regarding bonded tab length in [55]

$$L_{\text{min}} = \frac{F^{\text{tu}} h}{2F^{\text{su}}} \tag{3.1}$$

where

$L_{\mathbf{min}}$ minimum required bonded tab length, mm

$F^{\mathbf{tu}}$ ultimate tensile strength of coupon material, MPa

h coupon thickness, mm

$F^{\mathbf{su}}$ ultimate shear strength of adhesive, coupon material, or tab material (whichever is lowest), MPa

This way, the procedure for specimen preparation was performed with the following structure:

- Grinding of the excess material (the majority is removed during de-mold)

- Polishing with sequences of 80, 180 and 320 SiC Microcut discs using the *RotoPol-21* rotative disc grinder machine
- Surface cleaning using pure isopropyl alcohol (99,9%)
- Manually grinding the bonding areas for the tabs at $+45/-45°$
- Cleaning the bonding areas using pure isopropyl alcohol (99,9%)
- Apply any release agent on the surface intended to use for bonding the tabs
- Apply constant pressure on the tabs for 4 hours to guarantee correct bonding and respective alignment in order to avoid bending during the tests
- De-mold and clean excess glue

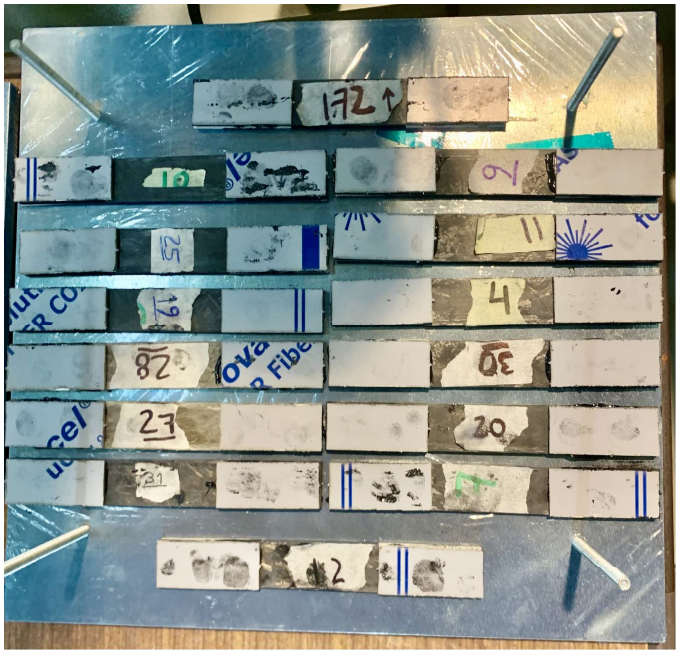


Figure 3.1: Specimen preparation - labeled specimens after compression for bonding of the tabs

Finally, after all these procedures, the specimens must go through the dimensional control regarding their geometry (recommended not to exceed ±1% in width and ±4% in thickness, as well as ±1% in tab thickness variation) and regarding the quality control of the manufacturing process in order to detect any possible dents or even cracks from the manufacturing process - after passing this inspection phase, the specimens are fully prepared for further testing.

For the case of the specimens that were analyzed via DIC technique, there is yet another part of the preparation process encompassing the painting of the front surface. Since in this case the number of specimens for each testing session was reduced, it was enough to align them manually on a protected surface and spread the white matte acrylic spray paint followed by the black burst in a random speckle pattern.



Figure 3.2: Optimal DIC painting speckle.

Specimen no	Type	Curing	Mold used	Suitable for testing	Failure Code
N/A	Regular	AT30 Slow	1		Not tested
N/A	Regular	AT30 Slow	1		Not tested
1	Regular	AT30 Slow	2		Not tested
2	Regular	AT30 Fast	2		Not tested
3	Regular	AT30 Fast	2		Not tested
4	Regular	AT30 Fast - Cured at 60ºC	2		LAB
5	Regular	AT30 Fast	2		Not tested
6	Regular	AT30 Fast - Cured at 60ºC	2		Not tested
7	Regular	AT30 Fast	2		LGB
8	Regular	AT30 Fast	2		Not tested
9	Regular	AT30 Fast - Cured at 60ºC	2		AGT
10	Type 2	AT30 Fast - Cured at 60ºC	2		AGM
11	Type 2	AT30 Fast - Cured at 60ºC	2		LGM
12	Regular	AT30 Slow - Cured at 60ºC	2		LGM
13	Resin	AT30 Fast	2		Not tested
14	Resin	AT30 Slow	2		Not tested
15	Resin	AT30 Slow	2		Not tested
16	Resin	AT30 Slow	2		Not tested
171	Longitudinal	AT30 Fast	3		Not tested
172	Regular	AT30 Fast	3		LGM
18	Hybrid	AT30 Fast	2		XGM
19	Regular	AT30 Fast - Cured at 60ºC	2		LGM
20	Regular	AT30 Fast - Cured at 60ºC	2		LGM
21	Regular	AT30 Fast	2		Not tested
22	Full resin	AT30 Fast	2		Not tested
23	Regular	AT30 Fast	2		LGM
24	Regular	AT30 Fast	2		LAT
25	full longitudial	AT30 Fast	2		XGM
26	Regular	AT30 Fast	2		Not tested
27	Flax (longitudinal)	AT30 Slow - Cured at 60ºC	2		AGM
28	Flax chopped fibres	AT30 Slow - Cured at 60ºC	2		LGM
29	Type 2	AT30 Fast	2		Not tested
30	Regular	AT30 Fast - Cured at 60ºC	2		AGM
31	Regular	AT30 Fast	2		LGM
32	Type 2	AT30 Fast	2		Not tested
331	Regular	AT30 Fast	3		LGM
332	Regular	AT30 Fast	3		Not tested
341	Regular	AT30 Fast	3		Micro-CT
342	Regular	AT30 Fast	3		Not tested

Description	
	Suitable
	Dry fibers
	Unusable after demold
	Dimensional tolerance bellow limit
Type 2	Lamination outside the mold

Figure 3.3: Specimen preparation - Excel table regarding the complete process

3.2 Standards

3.2.1 Laboratory methodology

In this section, a preliminary approach to the experimental testing methodology followed is described for each of the tests performed given their specific standard. The standards were selected based on the methodology described for experimental testing in composites on the bibliographic review.

ASTM D792-00

For the measurement of the density and specific gravity obtained for the specimens, the Standard Test Method ASTM D792-00, Method-A (test in water) was followed [54].

Regarding the description of the method made in the previous section, the procedure followed the requested test conditions, taking into consideration a few modifications.

- The test temperature was bellow the recommended limits - $T_{real} = 18°C$ and therefore the water density was modified to $\rho_{\text{water}} = 0.998\,\text{g/cm}^3$
- During the laboratory session it was impossible to measure relative humidity - estimated $50 \pm 5\%$ relative humidity
- In some of the specimens, there was clear evidence of porosity of the material

To compensate for these modifications and limitations, the volume of the specimens was measured using a Mitutoyo outside micrometer from 102 series with a graduation of 0.01 mm - allowing to get a confirmation of the values obtained from the standard.

The weight of the specimens was measured using an A&D HR-250AZ balance that guaranteed 0.1 mg precision. The void percentage (estimated to be around 4.5% via Micro-CT) was considered and compensated in the final values in order to get the real density of the forged carbon material.

After cleaning the specimens using pure isopropyl alcohol (99,9%), the required measurements were performed and are presented in Table 3.1.

Specimen 32 section characteristics					
Cross section no	**Lenght [mm]**	**width [mm]**	**thickness [mm]**	**Volume [mm^3]**	**Weight [g]**
1	17,76	11,86	1,39	292,780	0,3866
2	35,55	15,69	2,49	1388,870	1,8501
3	85,02	16,64	1,75	2475,782	3,3546

Table 3.1: Specimen 32 volumetric measurements

Density values for specimen 32				
Cross section no	**Volumetric [g/mm^3]**	**792-00 [g/mm^3]**	**Average [g/mm^3]**	**Final [kg/m^3]**
1	1,3204	1,2763	1,2983	–
2	1,3320	1,4426	1,3873	–
3	1,3549	1,4040	1,3794	–
Forged Carbon	1,39877	1,37431	1,38654	1386

Table 3.2: Density for specimen 32

This way, it was then possible to achieve a final density value of 1386 kg/m^3 (from this point on, rounded to 1390 kg/m^3) based on the average between the two tests method results and by taking into consideration the void percentage compensation by considering the values obtained from the Micro-CT. The maximum relative error reported was no larger then 4.73%.

ASTM D3039

For the first tensile tests, the standard ASTM D3039 was followed [55] - Tensile Properties of Polymer Matrix Composite Materials - which is design to produce tensile property data for material specifications such as ultimate tensile strength, ultimate tensile strain, tensile chord modulus of elasticity, poisson ratio and transition strain.

The several interferences described on the standard were taken into consideration and measures were implemented to avoid them:

- Material and specimen preparation - poor material fabrication and preparation are one of the main causes of high material data scatter in composites and therefore, proper parameters had to be defined in order to select the specimens suitable for testing. As it will be seen in the specimen preparation phase, from a grand total of more then 40 specimens, only 16 specimens were considered suitable for testing for parameters such as dimensional toleranc-ing, condition after de-molding and finishing (dry spots, surface voids, resin pockets and any other form of manufacturing defects).

- Gripping - each head of the testing machine took a mechanical wedge-action tensile grip so that the direction of load applied to the specimen is coincident with the longitudinal axis of the specimen. Given that the documented ultimate tensile strengths for materials with the same morphology of forged carbon are not expected to exceed 250 MPa, in order to avoid grip induced failures, a minimum grip pressure was applied - around 2 Nm per screw. This was expected to apply sufficient lateral force to avoid slippage, however the first specimen of the set was tested in order make sure of this by analyzing the force X displacement graph from the machine, since significant slippage would be identifiable on this curve.

- System alignment - excessive bending will cause premature failure as well as an inaccurate modulus of elasticity determination. The system alignment for this case encompassed the alignment of the specimen on the grip via bench vise with predefined marks and further alignment with the DIC during the pre-load (or zero strain point) by checking the four installation permutations.

- Edge effect in angle ply laminates - not applicable.

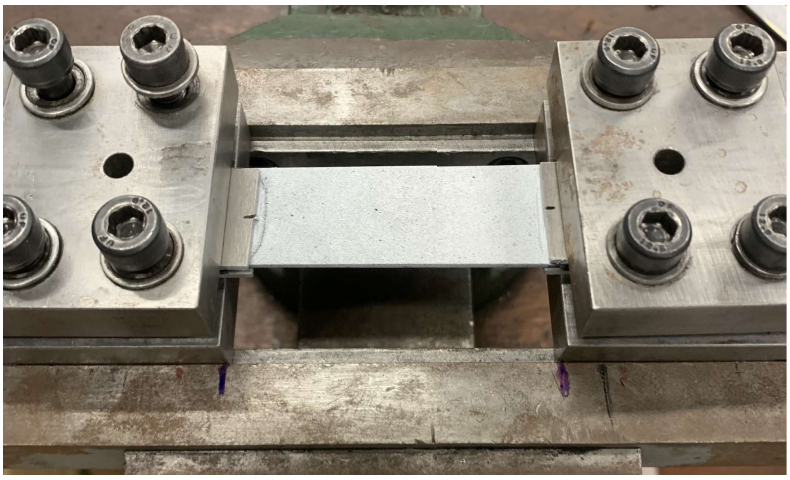


Figure 3.4: System alignment - Specimen alignment on the grip using a bench vise and a clipper.

The standard also states that all the modifications during the experimental testing must be discretized prior to the results presentation. The modifications, mostly due to equipment and material limitations are described bellow:

- Strain measuring - The standard suggests measuring the longitudinal strain on opposite faces of the specimen to allow for the correction of any bending of the specimen. This was not performed since the DIC equipment was limited to a 2D analysis. It was assumed that the bending effect is negligible.

- Temperature compensation - The temperature effect was not considered or compensated.
- Geometry - The following specific geometry requirements for the specimens were changed: Specimen dimensions (to 25 mm x 175 mm x 2 mm), since that if the mold design followed the recommended dimensions, it would not fit in the printer (Bambu Lab P1S); Specimen width tolerance (to ±3% of width); Specimen thickness tolerance (to ±15% of thickness).
- Usage of tabs - Matched thickness aluminum tabs were used, defined according to Equation 3.1 for bonded tab length. It was impossible to guarantee a perfectly uniform adhesive thickness, however, not a single specimen failed near the tabs.
- Speed of testing - The recommended speed for constant head-speed testing was decreased so that the DIC software could capture more detailed information considering the 0.5 frames per second limitation of the system.

Stress concentration around a circular hole

For the second testing phase regarding the determination of the stress (or strain) concentration around a circular hole, the procedure followed in every aspect the methodology described in the previous section for the D3039 standard since the specimens used were from the same batch. However, given the further operations performed in order to achieve the final geometry, it is still important to consider the following topics:

- Hole machining - The hole was machined using a drill press with a composite drill bit with 5 mm. The dimensional tolerancing was evaluated afterwards using as references the real diameter of the hole, the transversal distance of the hole to the specimen edges.
- Geometry - The specific geometry requirements for the specimens width tolerance were relaxed in order to capture the behavior considering different specimen width and strain field redistribution.

3.3 Mold design

The first mold used in this project was a 3D printed mold (using PETG filament for optimized strength) containing the cross section of the real hydrofoil model used as reference for this project. The mold was designed following the most common practice in forged carbon parts for three part molds where there is no draft angle on the piston walls. However, a piston over-travel length must be added in order to achieve a proper resin flow out of the mold cavity. The recommended values for this length tend to vary slightly and for this case, it was decided to follow the solution proposed by the manufacturer (Easy Composites Ltd [19]) of around 30% piston over-travel - in this case, 15mm nominal depth + 4mm effective compression zone and therefore the final piston length on this mold was around 19mm.

Table 3.3: Ideal material proportions for a 3D printed forged carbon mold

Component	**Volume (mm^3)**	**Carbon (g / %)**	**Resin (g / %)**
Hydrofoil cross section	23 040	22.35 / 29.8%	52.65 / 70.2%
ASTM D3039 specimen	8 750	8.5 / 30%	20 / 70%

This mold allowed to characterize the ideal quantities of resin/fiber to achieve the best finish on the carbon fiber parts as well as their proportions. These proportions were kept along all other specimen manufacturing processes.



Figure 3.5: 2D Hydrofoil section mold after de-molding

Subsequently, another mold was printed using ASA filament containing a single rectangular cavity with the dimensions of an ASTM D3039 [55] rectangular specimen (175 mm x 25 mm x 2 mm). No draft angle was included for this case, however a 0.5 mm gap was kept to ensure proper excess resin flow.

Finally, a third mold had to be printed. Being a 3D printed mold, the previous prototype was already showing clear signs of exhaustive usage, and it became difficult to guarantee an acceptable finish after de-molding, and so a new mold was required. Despite this, the main reason for printing this mold was to be able to use the experience from the 15+ specimens manufactured using the single mold and build a more robust and optimized version that could double the cadence of manufacturing. The third (and last) mold was then manufactured using black PETG.

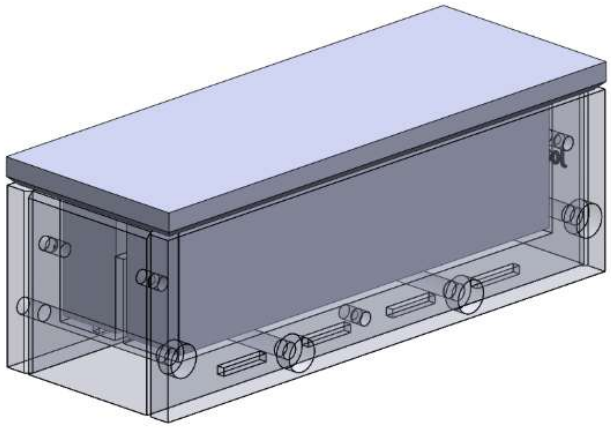


Figure 3.6: Final PETG mold assembly model

This final mold consists of a four part assembly with two side covers fixed using four M5 x 80 - ISO 1580 screws. This design ensures the complete independence between the two specimens manufactured on each side of the mold. Resin overflow cavities were also added, having a total volume equivalent to the one that was noticed to overflow on the second mold, this way ensuring a cleaner impregnation process, despite having the inconvenience of requiring cleaning after de-molding. Finally, alignment pins were added on the side covers (using a conical feature to ensure 3D fitting) and 30° chamfers were added on edges highly solicited during de-mold to ensure their structural integrity and achieve minimum infill - therefore reducing significantly the filament waste.

3.4 Microstructure analysis

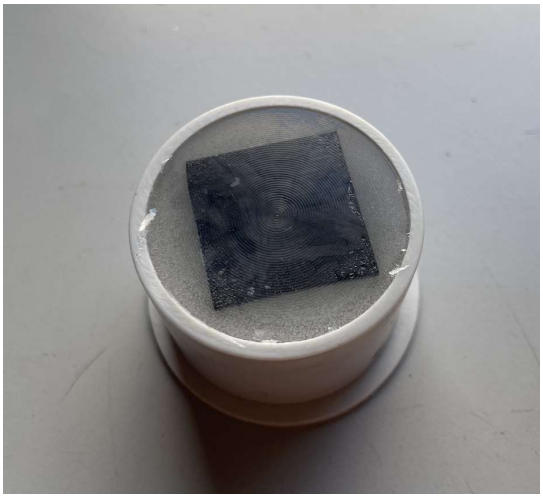
Two main methods were used in order to depict the microstructure of the forged carbon material: The Optical Micrography and the Micro-CT. The results from both methods are described and discussed in this section.

3.4.1 Optical Micrography

For the micro-structural analysis several additional steps were required for the specimen preparation.

- Grinding of the excess material
- Sample mounting - Mounting the samples in an acrylic resin using a circular mold
- Polishing - Sequences of sanding with 320, 800, 1200 and 4000 SiC Microcut discs
- Finishing - Synthetic cloth with a 3 μm and 1 μm diamond suspension

At the end of this procedure, it was possible to analyze the microstructure of each specimen in all directions, allowing for a better understanding of the mold performance and the identification of flaws arising from the manufacturing process.



(a) Specimen 9 embedded in resin before de-mold

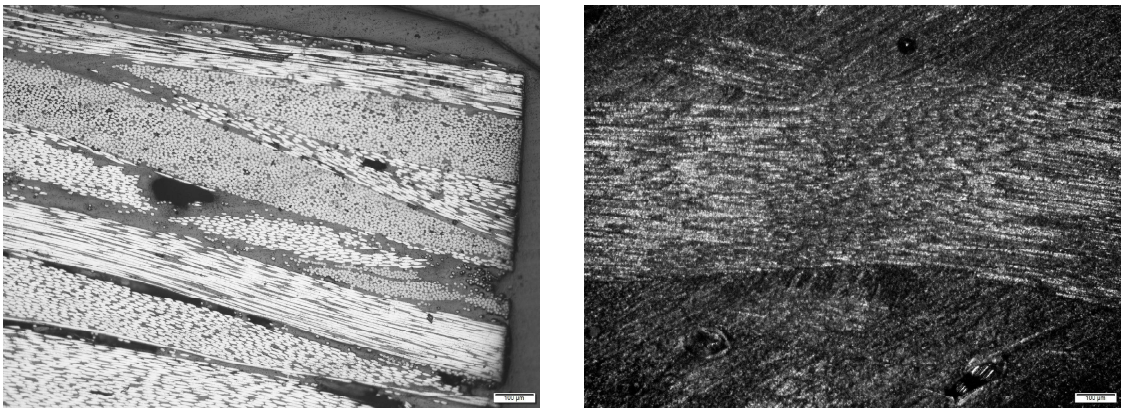


(b) Specimen 9 ready for analysis after polishing

Figure 3.7: Specimen preparation - Optical microscopy

The optical microscope ZEISS Axiophot with an integrated digital camera from Olympus model DP-22 was used in order to record the several microstructures. Two specimens were submitted for analysis one being cut in the transversal and longitudinal directions and the other being placed horizontally on the mold with the complete in-plane section visible.

The first objective was to clearly visualize the difference between the in-plane and the out-of-plane microstructures since that given the morphology of the process, it was expected that the specimens would show a significant difference. As it is possible to see in Figure 3.8, this difference in the microstructure is clear and is mostly due to a layup like structure visible along the transversal direction that is completely different from what is seen any other directions. On the other hand, a more uniform distribution of the fibers can be seen in the planar directions where, given the randomness of the process, there is an aleatory fiber orientation and therefore an isotropic behavior.



(a) Fiber orientation - transversal direction

(b) Fiber orientation - in-plane direction

Figure 3.8: Specimen preparation - Optical microscopy

Also, the layer stacking seen on the transversal direction helps to justify the common assumption in this kind of composites that the mechanical properties along the thickness directions will be matrix dominated such as in the works of Wisnom and Camanho [73] [74]. This is mostly due to the resin rich regions between the different fiber layers where the tendency for matrix cracking and debonding is much higher.

Finally, it is also visible that there are many regions with preferred local fiber alignment due to the resin overflow along the mold and the compression applied during the manufacturing. This overflow tends to reorientate the chopped fibers leading to the creation of orthotropic regions on the component that are will locally alter the mechanical behavior of the material.

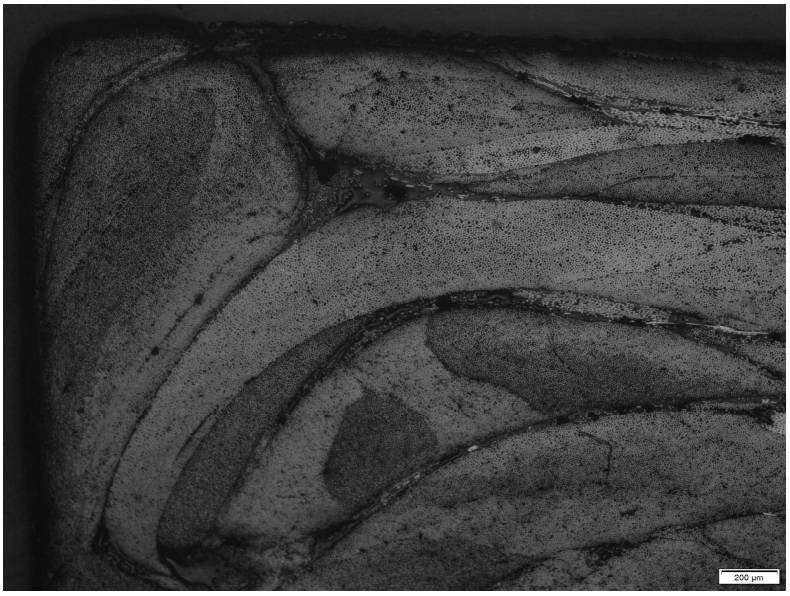
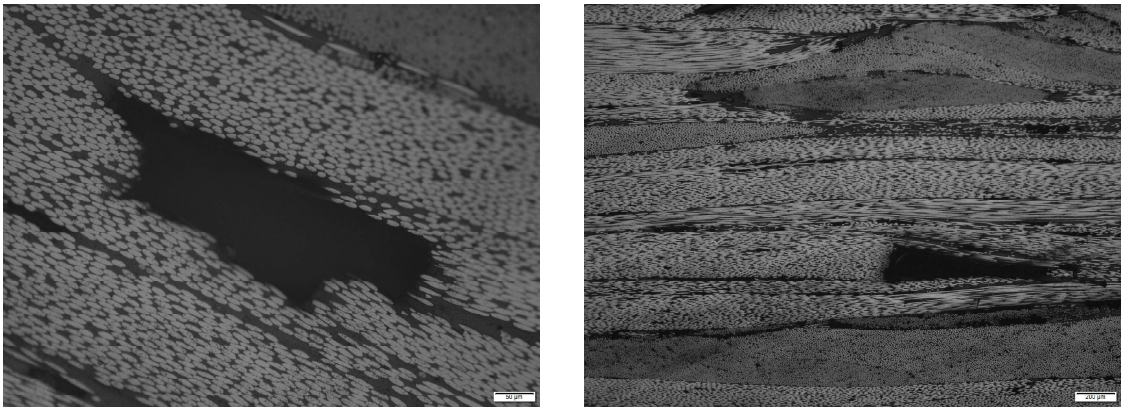


Figure 3.9: Distortion on the fiber alignment

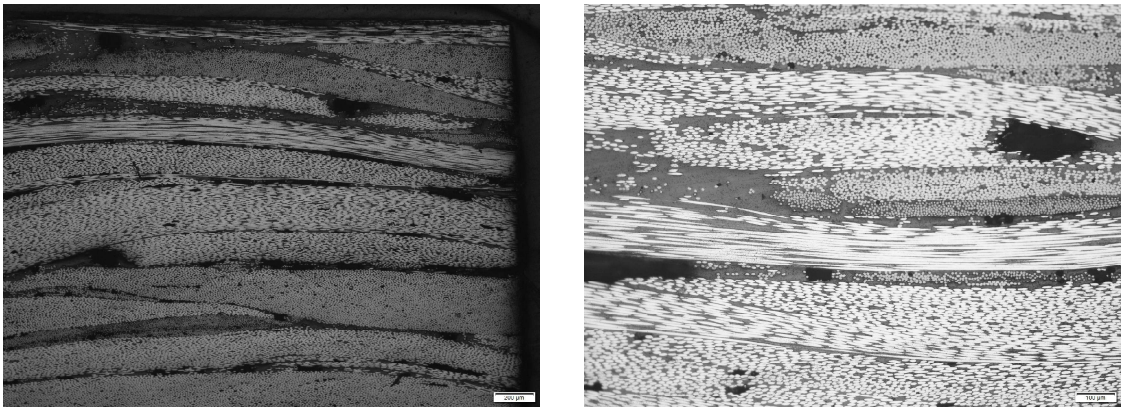
Regarding the void size and distribution, a significant amount of voids was detected from various different types. This is mainly due to the simplistic approach on the manufacturing that by avoiding the usage of temperature or pressure (pulling vacuum on the resin mixture or directly on the layup), leads to the introduction of air directly from the resin itself as well as from the air bubbles that are trapped during the excessive resin flow, leading to the presence of various kinds of

voids. Both intra and inter-tow voids were detected, being expected to decrease both tensile and shear strength locally. Additionally, several voids were detected in areas where resin accumulates between clusters of fibers, as it can be seen in Figure 3.12.



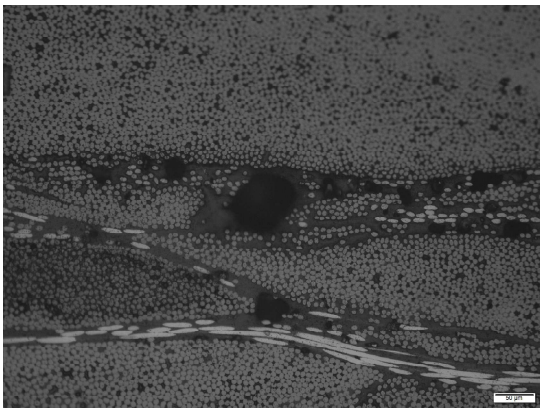
(a) Section 1 - 20x amplification (b) Section 2 - 5x amplification

Figure 3.10: Examples of intra-tow voids

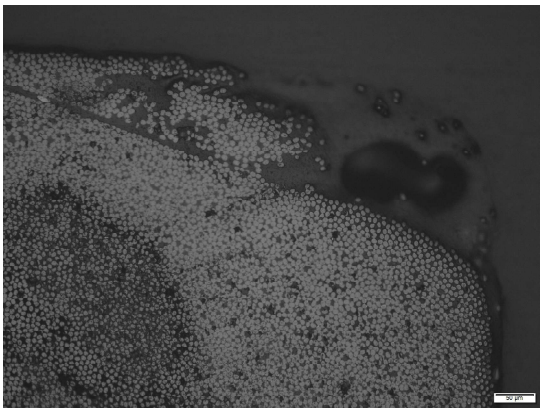


(a) Section 1 - 5x amplification (b) Section 2 - 10x amplification

Figure 3.11: Examples of inter-tow void



(a) Section 1 - 20x amplification



(b) Section 2 - 20x amplification

Figure 3.12: Examples of resin-pocket void

Given that the failure types for the tensile tested specimens were only classified visually according with the standard, a more detailed analysis was performed for the case of the specimen number 9 after ultimate failure on the tensile tests described in section 4. Since the specimen did not fail completely, the procedure for preparation encompassed cutting the specimen to a length bellow 25 mm in order to place it on a suitable mold and afterwards, follow the procedures described for the other cases for the optical microscopy preparation. Once the preparation was completed, the specimen was placed on the microscope in order to identify further details on the typical tensile failure on forged carbon. Some of the failure modes described in the first section were identified such as fiber breakage 3.13 and matrix cracks 3.14, confirming the hypothesis based on the bibliography review for this of materials.



Figure 3.13: Fiber breakage example

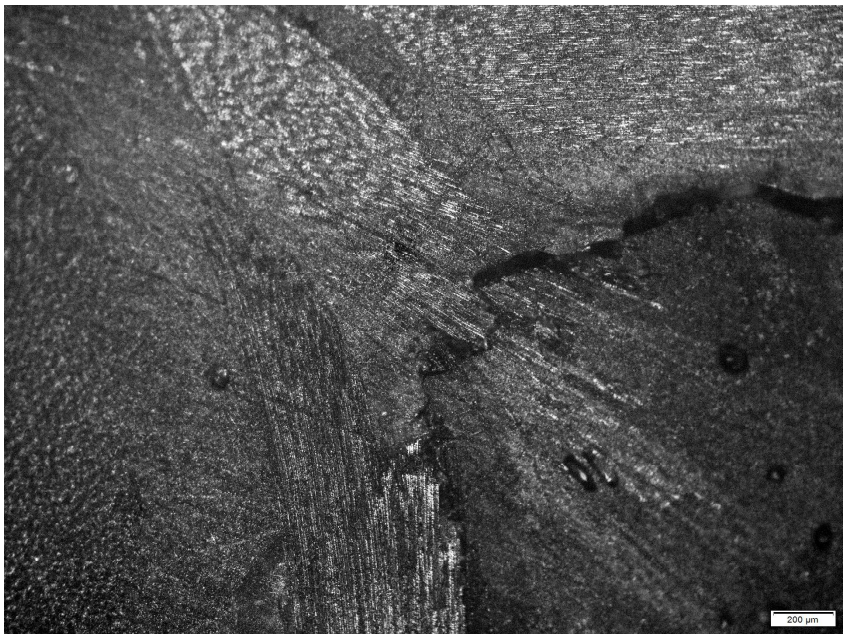


Figure 3.14: Matrix crack example

The visualization on these last examples was slightly compromised due to the acrylic resin infiltration on the crack, that leads to a much harder focusing, specially for higher magnifications, limiting the analysis to very small regions. Despite this fact, the failure modes were still at a certain extent, possible to be identified.

3.4.2 Micro-CT

The specimens were analyzed via X-ray microtomography (Micro-CT, ZEISS VersaXRM 615) at INEGI (*Instituto de Ciência e Inovação em Engenharia Mecânica e Engenharia Industrial*) in order to get a more detailed perspective of the material composition both in terms of void size, concentration and distribution but also to try to obtain an idea of the FVF and fiber orientation taken in two different areas of the specimen.

As the specimen is expected to present an aleatory composition, the preparation of the specimen consisted in supporting the specimen vertically and pointing the beam at the most central area possible in both tests, in an attempt to ensure that the region analyzed is representative of the main characteristics of this material. A safety distance was also defined in the beginning of the analysis.

The Figure 3.15 shows the disposition of the main hardware components inside the machine right before introducing the specimen for analysis: On the left hand side it is possible to see the X-ray source, the central sample rotation stage with the viewer's camera and the detector turret with its multiple objectives on the right hand side.



Figure 3.15: Interior view of the ZEISS VersaXRM 615

This configuration stands out due to its dual-stage magnification process. Unlike conventional systems that rely solely on geometric magnification, the VersaXRM 615 maximizes both absorption and phase contrast by incorporating a secondary optical magnification stage.

The main technical configurations for the system are presented in Table 3.4 (data from [75]).

Table 3.4: Main technical specifications of the ZEISS VersaXRM 615.

Parameter	**Specification**
Imaging Performance	
Spatial resolution	500 nm
Resolution at a Distance (RaaD)	1.0 μm (@ 50 mm working distance)
Minimum achievable voxel size	40 nm
X-ray Source	
Architecture	Sealed transmission tube, fast activation
Voltage range	30–160 kV
Maximum power output	25 W
Detector System	
Standard objectives	0.4×, 4×, 20×
Optional objectives	40×
Flat panel extension (FPX)	Available
Sample stage load capacity	25 kg

Scan parameters and procedure

Given the limited time for performing the Micro-CT tests, only two scans were performed. Both scans were performed with BIN1 in order to achieve the highest resolution (at the cost of higher recording times). The slight variation in some parameters, such as voxel size and exposure time, reflects minor adjustments made to optimize the scan for each specific specimen. The resulting scan time for each sample was approximately nine hours, each produced a dataset of approximately 22 GB.

The first one, performed using 50 kV of X-ray voltage was a less detailed scan, covering a total specimen length of around 15 mm, in order to be able to provide a proper characterization of the voids. A total of 2048 projections were taken at a rate of approximately 6.5 s per projection. The second one, performed using 60 kV of X-ray voltage, was a more refined scan, covering a small cylindrical region of the specimen with 3 mm diameter and 5 mm length, in order to provide a good characterization of the fibers. A total of 2030 projections were taken at a rate of approximately 6.5 s per projection.

Data visualization and analysis

The reconstructed 3D volumes were processed and visualized using the Dragonfly software (Version 2024.1, build 1627, ZEISS edition). The preliminary analysis was performed by Dr. Nathan in INEGI and the 2 scans were then exported and analyzed individually. The less detailed scan allowed to get the most clear approximation to the voids size/volume.

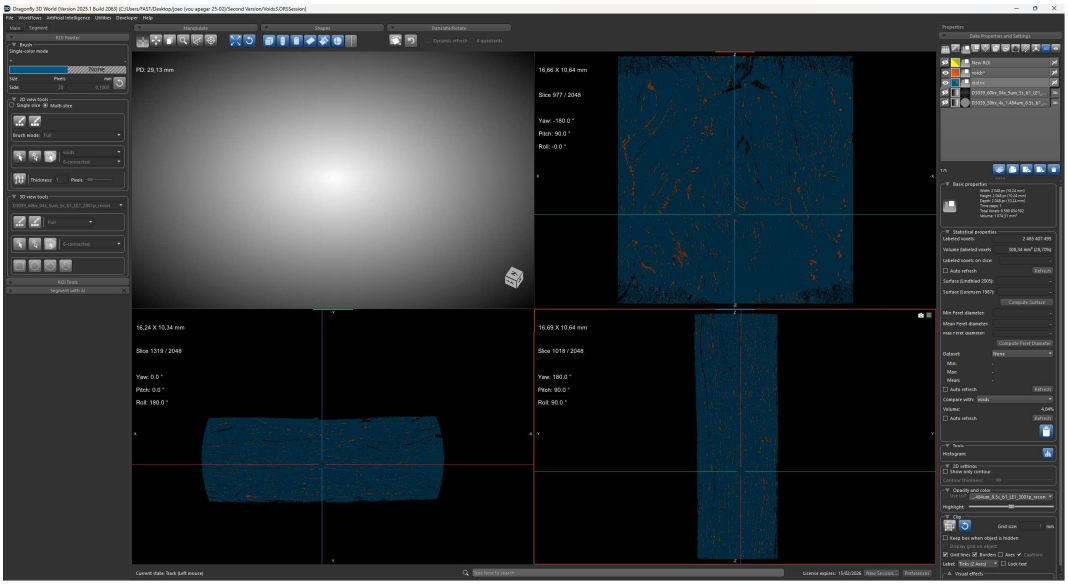


Figure 3.16: Dragonfly interface during void segmentation.

The first challenge on the visualization workflow was adjusting the parameters to distinguish the solid material from lower-density features such as voids or cracks using the *lower otsu* and adjusting the values on the segmentation histogram in order to create a region of interest (ROI) containing all the voxels that correspond to these defects. In order to estimate their percentage, another region of interest was defined representing the reference volume, which in this case contains both the chopped fibers and matrix.

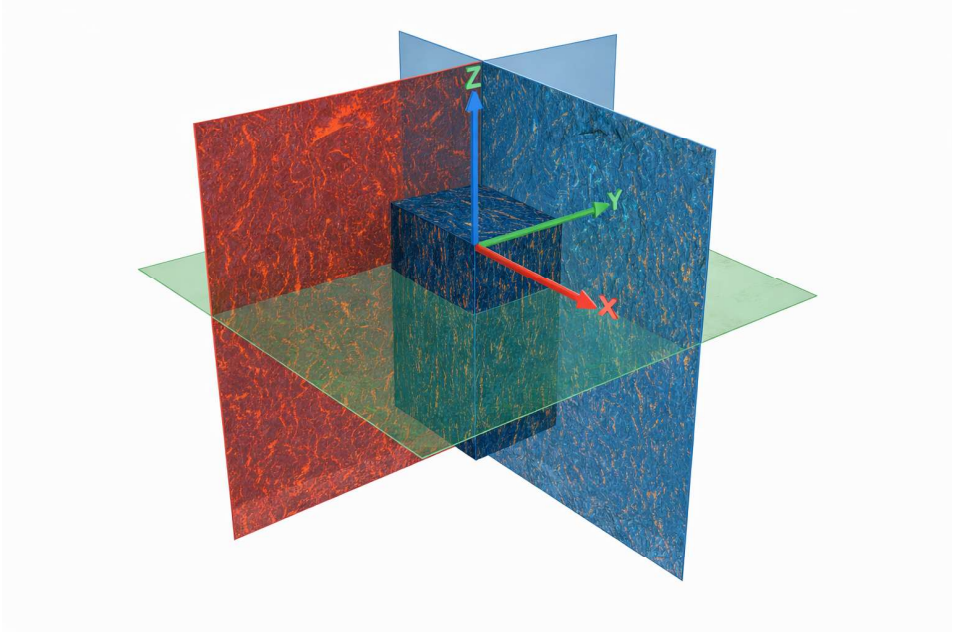


Figure 3.17: Definition of the orthogonal viewing planes used for volumetric analysis.

It is important to notice that even tough the upper and lower otsu range features provide a very decent segmentation between these two phases, it is likely that neither of the ROI's will get fully segmented just after this method. In order to get a more exact estimation of the void percentage it was required to first refine the ROI by removing all islands bellow 27 voxels (3x3x3 pores) that are likely to be segmentation errors rather than real pores (since they would be equivalent to a $8.5 \times 10^{-8}\,mm^3$ pore). Additionally, extensive manual segmenting process was required in order to capture other pores or even clusters of pores that were not identified by using the ROI painter tool, this way incorporating it into the ROI.

After segmentation the final value for void percentage was 4,84% - a much more significant value then the 3,90% obtained just by the lower otsu thresholding method.



Figure 3.19: 3D discretization - color code for void volume - during segmentation (using only lower ostu).

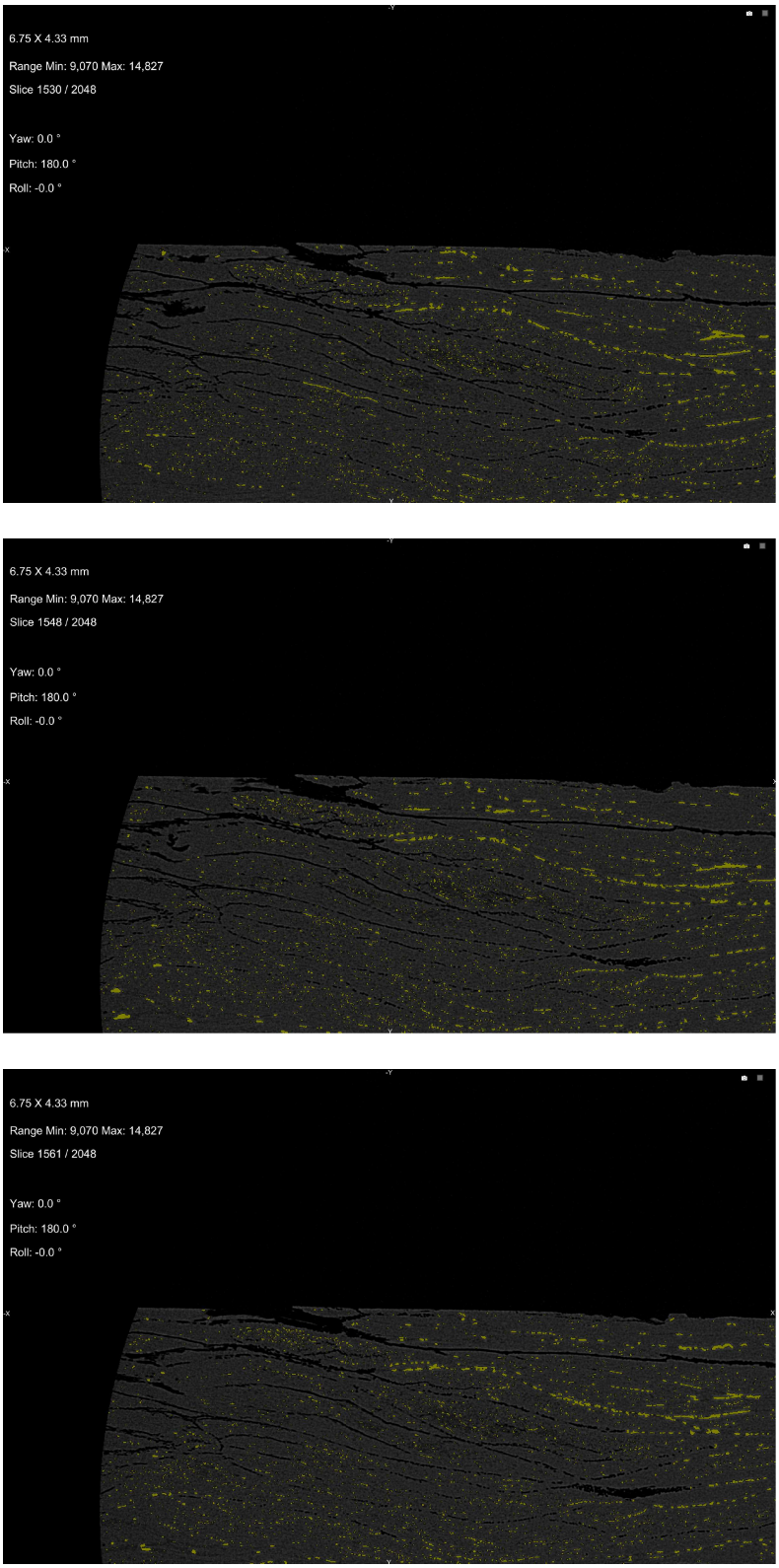


Figure 3.18: Stacked orthogonal views of the reconstructed volume during ROI segmentation.

The complete void volumetric histogram is presented in Figure 3.20. The distribution exhibits a high concentration of small void volumes and a rapidly decreasing frequency as the void size increases. The majority of detected voids are concentrated in the lower volumetric range, while only a limited number of larger defects appear as isolated events in the tail of the distribution. This long tail of larger void volumes suggests the presence of localized damage mechanisms such as cracks or delamination regions that were then identified during the segmentation process, which generate volumetrically significant defects compared to the background porosity. However, it is also important to notice that the predominance of the smaller voids may also be due to noise on the several image artifacts described in the previous section, that will fragment each void in smaller separated islands, therefore leading to this phenomena.

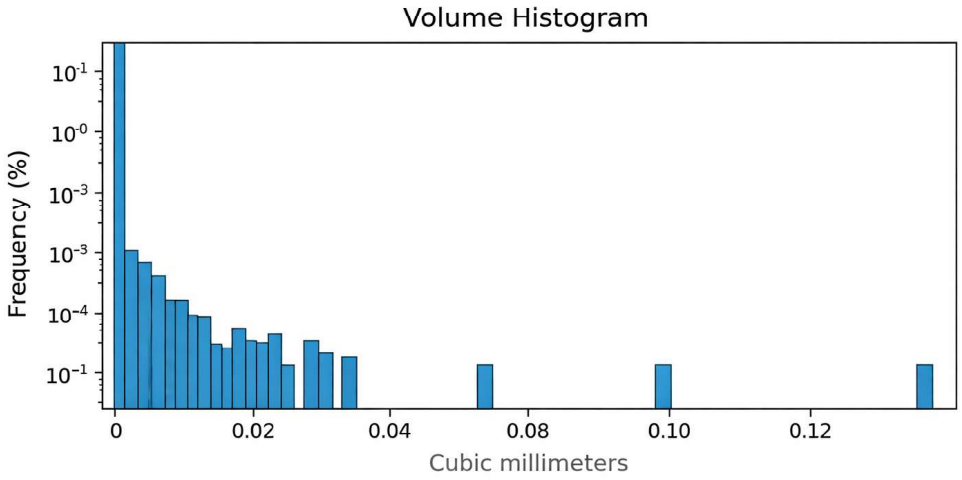


Figure 3.20: Void volume histogram.

Despite all the possible artifacts affecting these results, a similar distribution has been obtained when compared with the study performed at *Cinfu - Vocational Training Center for the Foundry Industry* presented in [76] where three hydrofoil Type-B wings have been analyzed via micro-CT and the three histograms this clear right-skew tendency. The clusters of voids that have been identified on this study (encopassing only a few milimeters) have also been detected for the real hydrofoil models, sometimes reaching diameters higher then 3 cm.

3.5 Experimental Results

3.5.1 Tensile Test - ASTM D3039

The preliminary tensile tests were performed according to the standard ASTM D3039 and included 10 different specimens manufactured according to the same standard, even tough only 7 were suitable for being taken into consideration for getting the final values due to the standards impositions.

The tests were performed using an MTS 810 Material Test System that kept track of time, force applied and displacement. On the other hand, the strain was obtained by means of the DIC tech-

nique, enabling accurate and non-contact evaluation of the overall behavior during these tests. A 2D-DIC was performed using a Canon EOS Camara, a LED light panel and three-axis adjustable camera support tripod. The capture was performed using the digiCamControl software and the post processing was done in GOM correlate.

Part	**Testing parameters**
Camera body	Canon EOS 80D
Lens	Canon EF 100 f/2.8 Macro IS
Extender	Canon Ext 2x V3
Light	GSVITEC Multiled LT-V9-15
Accessory	2 tripods
Shutter speed	1/80 s
Aperture	f/8
ISO	100
Acquisition rate	0.5 Hz
Dimensions	3904 × 6960 pixel
Resolution	240 dpi

Table 3.5: DIC setup and acquisition parameters

In GOM, the several images from the tensile tests (taken at a rate of one frame for every 2 seconds) were imported as a sequence given their reference name recorded directly from digiCamControl. Once in GOM, a scale was defined in the first frame given the dimensional control presented on Table 3.6 and several surface components were created. For each of these, given that for the previously described tensile test the ideal strain field should be uniform on the central region, the average strain along the longitudinal and transversal directions were exported. A facet size of 60 pixels with a 20 pixel point distance were used.

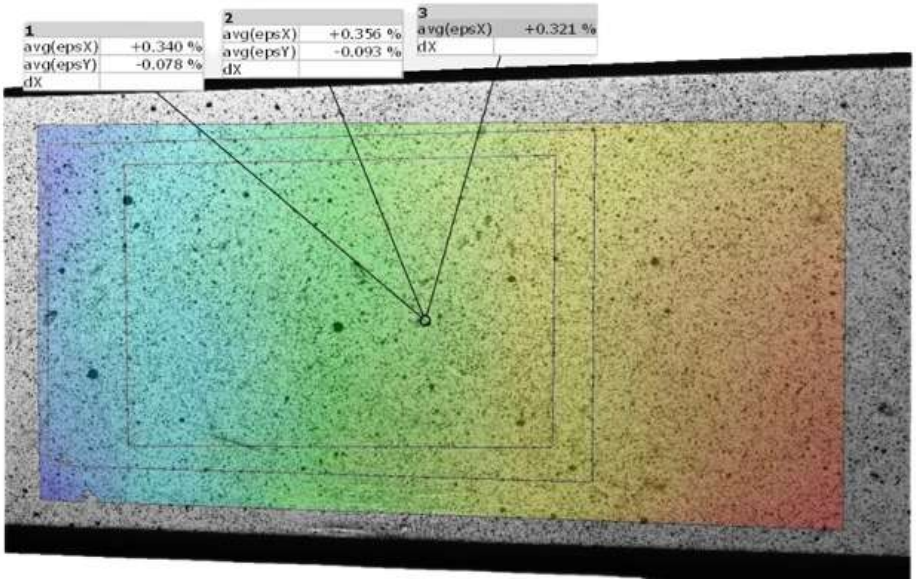


Figure 3.21: GOM Correlate output - Displacement field for specimen 7.

Given that during the laboratory work both the testing machine and the DIC capture were set virtually at the same time, it was then possible to associate each value of the strain measured using the DIC to the correspondent value of stress from the testing machine in order to be able to draw the typical Stress-Strain curve (Figure 4.6) and determine the required parameters.

Despite the application of a nominal pre-load intended to fully seat and stabilize the specimen prior to each test, during the post-processing of the DIC recordings revealed that, in some cases, the specimen still underwent a small initial rotational adjustment during the first acquisition frames before the onset of effective tensile loading. For these cases, the results from the DIC were exported as measured and the compensation was applied in *Excel*. The compensated tests were considered as valid.

The complete description of the modifications, labeling scheme and methodology for the testing preparation is presented in the beginning of this chapter. The geometric tolerancing defining the eligibility of each specimen for testing is presented in Table 3.6.

Specimen no	Rel. error (width) [%]	Rel. error (thickness) [%]	Suitable for testing
10	1.93	9.35	Yes
9	1.85	15.00	Yes
19	1.70	10.65	Yes
20	4.05	18.15	No
4	2.78	3.65	Yes
25	1.85	44.35	No
11	5.84	1.50	No
7	0.96	13.35	Yes
172	2.20	13.15	Yes
331	0.08	7.00	Yes

Table 3.6: Relative dimensional errors and suitability of specimens for testing

The results of each test with the respective precision statistics are also presented in Table 3.7.

Table 3.7: Mechanical properties of suitable specimens (Regular FC)

Specimen No	E [GPa]	ν_{12}	Ult. tensile stress [MPa]	Ult. tensile strain [%]
9	29.5286	0.4056	89.4872	0.2779
19	10.7728	0.3339	69.3498	0.5813
4	25.2827	0.3713	120.0475	0.4542
7	22.5182	0.2053	107.9657	0.4945
331	24.6362	0.0609	147.4482	0.8168
10	40.0379	0.3680	124.5306	0.3267
172	31.7251	0.3265	117.5543	0.3431
Sample Mean	26.35	0.3243	110.91	0.4707
Standard Deviation	9.01	0.06	25.30	0.18
CV [%]	34.21	20.58	22.81	39.46

The typical stress-strain curve for this material presents an approximately linear behavior in the entire strain range, except right before failure where a brief stagnation of the stress levels is observed over a strain interval of approximately $\Delta\varepsilon \approx 2 \times 10^{-4}$ (which can be attributed to rapid damage propagation). This is a very narrow transition region which makes the determination of a transition strain not applicable for this material.



Figure 3.22: Experimental setup.

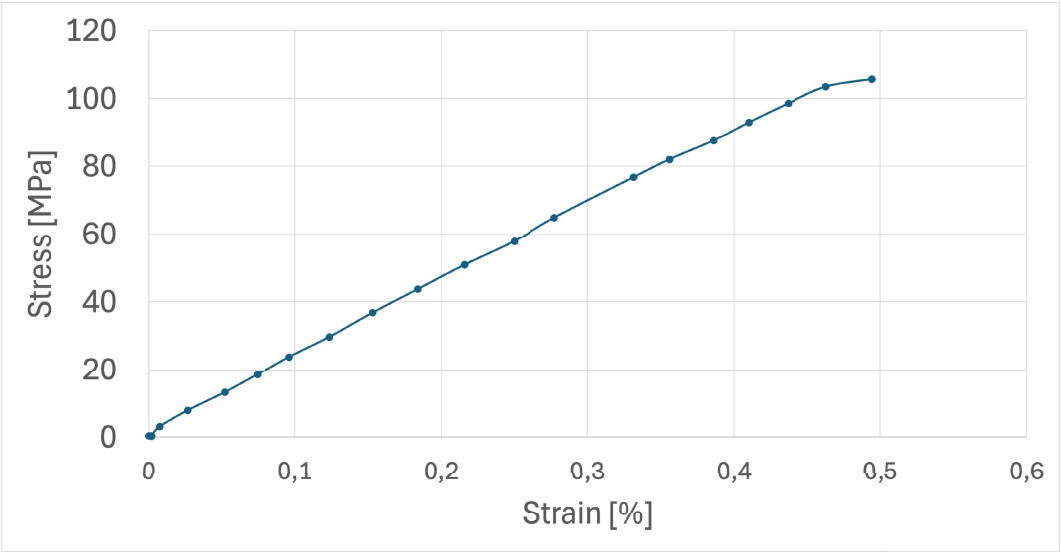


Figure 3.23: Stress–strain curve obtained from DIC for Specimen 7.

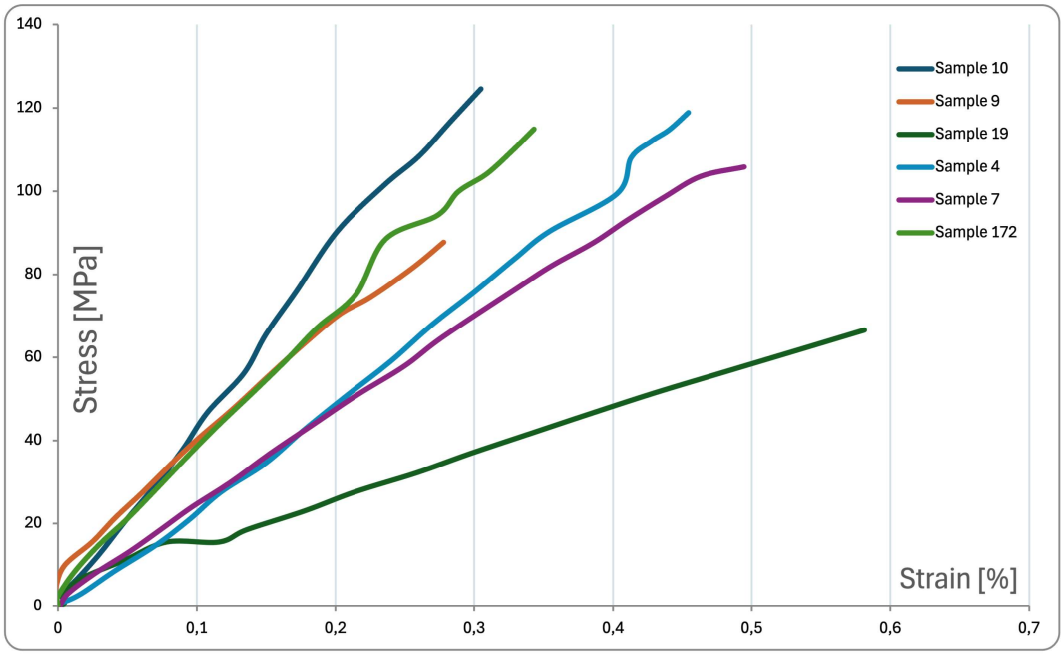
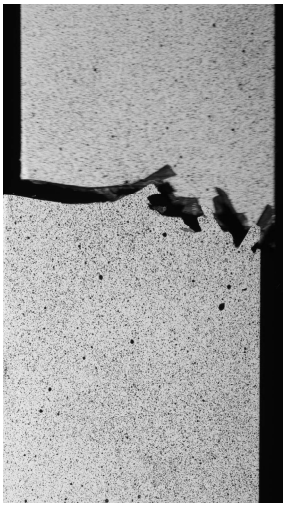
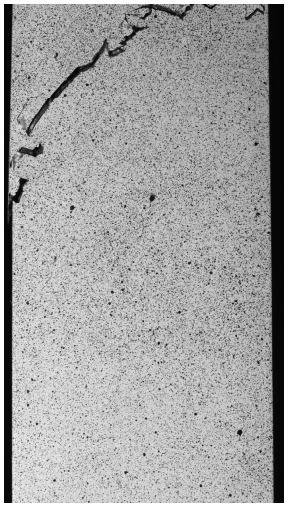


Figure 3.24: Stress–strain curves for the specimen batch.

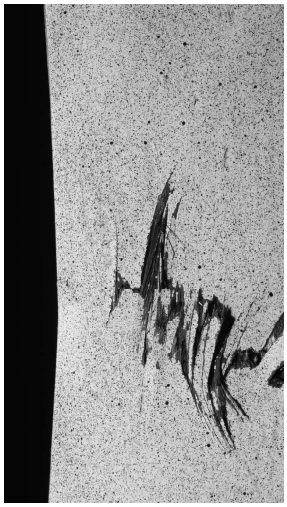
Regarding the failure types, their definition was performed according to the failure code types from the D3039 standards presented in Figure 3.26. For the tensile tests, the most common failure code was LGM (Lateral Gage Middle failure) which was ideal for DIC correlation and getting the strain concentration leading to ultimate failure. Some variation on the failure region was noticed



(a) Specimen 19 LGM failure

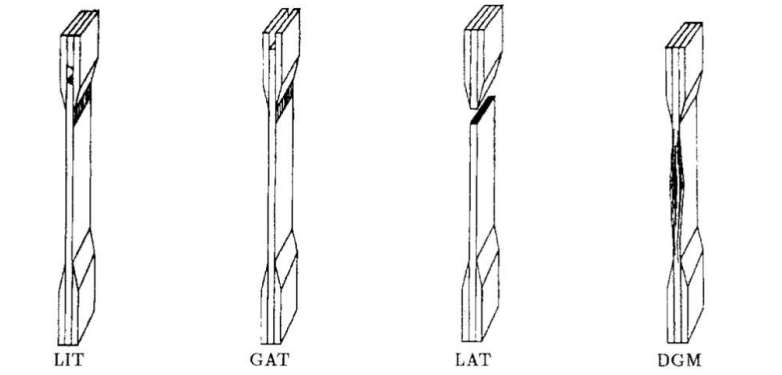


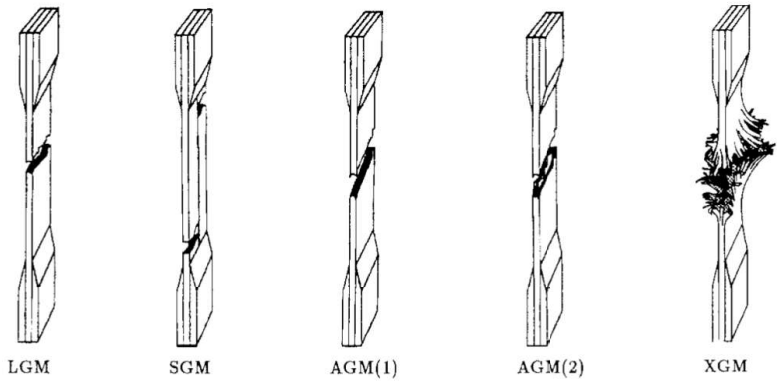
(b) Specimen 10 AGM failure



(c) Specimen 25 XGM failure

Figure 3.25: Examples of failure types





First Character

Failure Type	Code
Angled	A
edge Delamination	D
Grip/tab	G
Lateral	L
Multi-mode	M(xyz)
long. Splitting	S
eXplosive	X
Other	O

Second Character

Failure Area	Code
Inside grip/tab	I
At grip/tab	A
<1W from grip/tab	W
Gage	G
Multiple areas	M
Various	V
Unknown	U

Third Character

Failure Location	Code
Bottom	B
Top	T
Left	L
Right	R
Middle	M
Various	V
Unknown	U

Figure 3.26: Failure codes according to D3039 standard [55].

The final properties were then obtained given the data obtained from this preliminary test session. As it is possible to see from Figure 3.3, the failure codes were mostly LGM's and in some cases AGM (probably due to bending). One exception was noticed in the longitudinal specimens presenting *explosive* XGM modes, however, that was not the case for the specimens analyzed in this section. These results were then used as the foundational reference for all subsequent experimental procedures as well as for the numerical simulations carried out (described in the next chapter).

Table 3.8: Mechanical properties of the forged carbon material

Mechanical Properties	**Mean (standard deviation)**
Density [kg/m^3]	1386 ± 17
Young Modulus [GPa]	26.36 ± 9.01
Poisson Coefficient	0.3322 ± 0.068
Ult. Tensile Strength [MPa]	110.91 ± 25.31
Ult. Tensile Strain	0.47 ± 0.18

3.5.2 Tensile Test for strain concentration at an open circular hole

The specimens used on this test were prepared in a similar way to the one described for the ASTM D3039 tests. Before cleaning and adding tabs, 5 mm circular holes were machined at *Oficinas DEMec* using a vertical drill that centered its position in both longitudinal and transversal axis. Additionally to the regular type specimen composition (using aleatory chopped fibers) a batch of specimens manufactured using 10% (in mass) longitudinal fibers was also used on these tests in an attempt to test the orthotropy detection capabilities of the method. The longitudinal fibers used are also from *Easy Composites* [19] and come in long strands of medium weight 6 k carbon fiber tow, manually cut to a length around 170 mm (mold length). The ordered list containing the specimen characterization is presented on Table 3.9.

Specimen no	Type	Rel. error (width) [%]	Rel. error (thickness) [%]	Rel. error (hole alignment) [%]
12	Regular	1.25	7.65	5.69
18	Ortho (10%)	8.45	21.65	0.45
23	Regular	2.92	14.85	1.88
24	Regular	4.96	11.00	2.08
30	Regular	2.38	11.00	6.79
31	Regular	2.52	15.85	5.82

Table 3.9: Geometric tolerancing of specimens used for strain concentration at an open circular hole

The main reason for performing this alternative type of tests was related with the fact that a high in-mold resin flow was noticed during manufacturing, being expected to alter the fiber orientation of the specimens. The resin flow has also proven to be highly dependent on the mold geometry, being intensified on thinner edges or convergent surfaces. This second test phase intended to identify eventual changes suffered during the resin overflow that result on an increasing orthotropy of this material [77].

For the case of a slender rectangular mold such as this one, it is expected that the fibers tend to align with the longitudinal direction due to this phenomenon, resulting in different values for the different mechanical properties of the material on the transversal direction when compared with the values obtained in the previous section, being valid exclusively for the longitudinal direction. The same behavior is expected for the hydrofoil wing given the mold design.

As it will be seen in the next sections, a slight tendency to orthotropic behavior would affect the stress distribution at the opened circular hole and therefore, the strain concentration would be affected as well. With the results of this test, it is intended to implement a reverse engineering approach to the problem and compare the experimental strain fields with the ones simulated on the finite element analysis software *Abaqus* in order to determine experimentally this level of orthotropy.

In order to achieve this, the strain field was obtained in the same way as the one described in the previous chapter for the D3039 case. Additionally, two sections were defined on GOM for each test: one along the traversal direction of the specimen, placed at the $\theta = 90°$ line of the circular hole edge, and the second being along the longitudinal direction of the specimen, placed at the $\theta = 0°$ line of the circular hole edge.

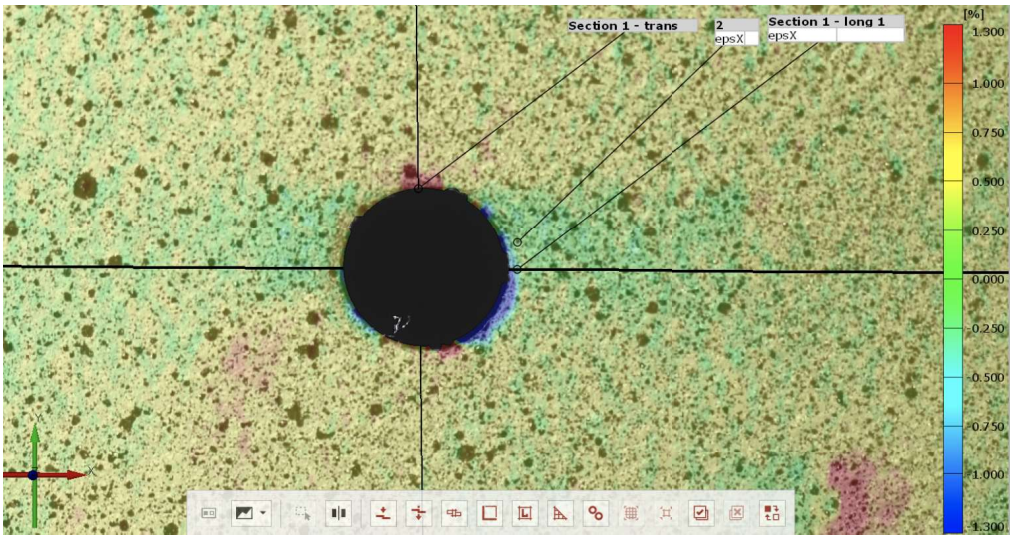


Figure 3.27: Strain field around the circular hole obtained using GOM interface - sections at $\theta = 90°$ and $\theta = 0°$.

Even tough the enforced facet size was kept as low as possible, the limit in order to achieve an acceptable pattern quality was to keep the 60 pixel with 25 pixel of point distance used in the preliminary correlations. This, allied with the fact that the DIC inherently adds significant noise due to slight vibrations from the camera and light fluctuations lead to a highly sensitive strain curve acquisition along these directions, making it very challenging to export a smooth curve that showed good correlation with the strain distribution as expected by taking into consideration the theoretical solid mechanics on this issue (and the numerical approach).



Figure 3.28: Location of the remote stress furface component on GOM.

In order to be able to compare these results with the theoretical and numerical simulations, all curves had to be smoothed and adimensionalized using a suitable parameter. The parameter chosen for this purpose was the remote strain, obtained by creating a new surface component close to the tabs and measuring the average value of strain on that region. Then, the three frames that presented a suitable distribution were selected for analysis and exported directly from GOM in *.csv* format. The average for those three values was taken for each test and the matrix containing these average strain values and their respective location relative to the hole position were introduced in a *Maltab* script specially developed in order to smooth and export a suitable curve fitting in order to compare it with the numerical results obtained for the same specimen modeled using *Abaqus*.

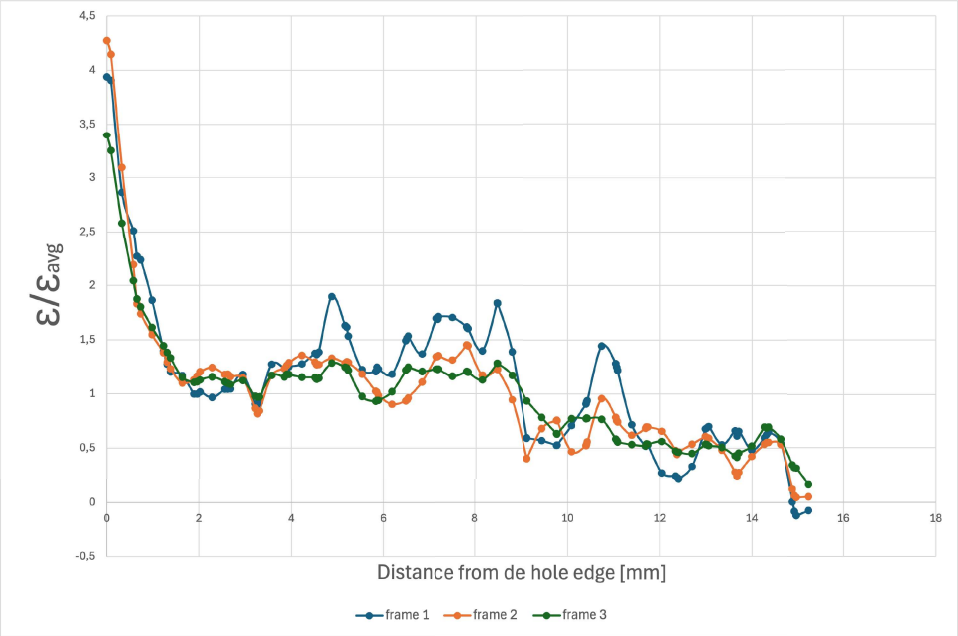


Figure 3.29: Adimensional strain for 3 different DIC frames (obtained using GOM Correlate).

In order to reduce the measurement noise of the extracted strain profiles while preserving the strain gradients near the hole edge, the raw data was smoothed using a *moving least squares* (MLS) procedure. In the implemented approach, a low-order polynomial is fitted locally around each query position s_0 by minimizing a weighted least-squares error, where points closer to s_0 are given higher weight. Compared with global polynomial fits, MLS is particularly appropriate for strain or stress distributions around stress raisers such as circular holes, because it provides a smooth curve while remaining local enough to follow the distribution variation close to the hole boundary.

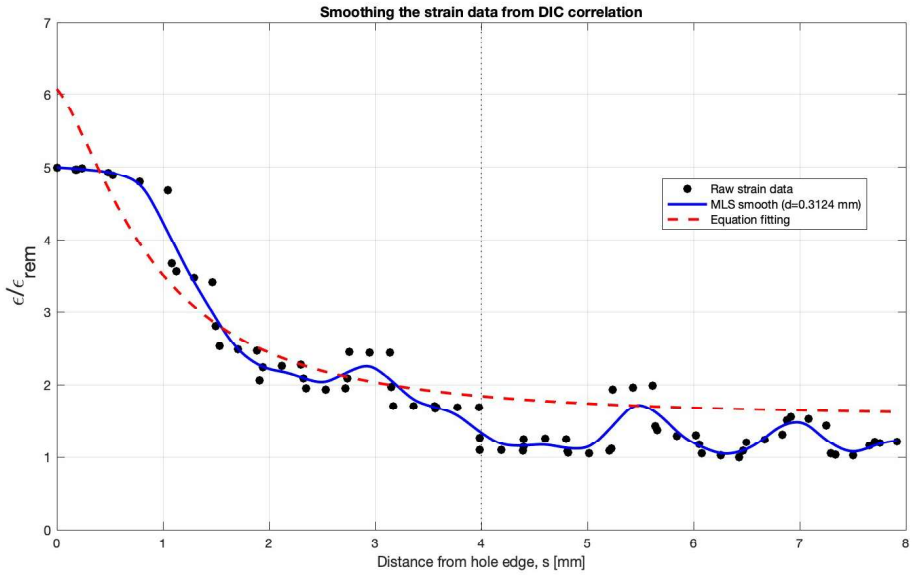


Figure 3.30: Strain field distribution curves - Raw data; MLS Smoothing and Curve fitting equation.

Once the smoothed curve equation was defined, the next step was to determine a fitting curve that represented the overall behavior of each specimen as captured from the DIC. In order to do that, the Matlab script approximates the smoothed curve to an 8^{th} polynomial equation, adapted from the stress distribution equation defined in [78]:

$$\sigma_{xx}(0,y) = \frac{K_T}{K_T^\infty}\frac{\bar{\sigma}^\infty}{2}\left[2+\left(\frac{R}{y}\right)^2+3\left(\frac{R}{y}\right)^4-(K_T^\infty-3)\left(5\left(\frac{R}{y}\right)^6-7\left(\frac{R}{y}\right)^8\right)\right] \tag{3.2}$$

Where K_T^∞ denotes the stress concentration factor at the edge of the hole for an infinite plate:

$$K_T^\infty = 1+\sqrt{2\left(\sqrt{\frac{E_x}{E_y}}-\nu_{xy}\right)+\frac{E_x}{G_{xy}}} \tag{3.3}$$

and $\frac{K_T}{K_T^\infty}$ is the Finite-Width Correction (FWC) factor:

$$\frac{K_T}{K_T^\infty} = \left\{\frac{3(1-2R/W)}{2+(1-2R/W)^3}+\frac{1}{2}\left(\frac{2R}{W}M\right)^6(K_T^\infty-3)\left[1-\left(\frac{2R}{W}M\right)^2\right]\right\}^{-1} \tag{3.4}$$

In Equation for K_T^∞, E_x, E_y, G_{xy} and ν_{xy} are the laminate elastic constants; the parameter M can also be calculated as:

$$M^2 = \frac{\sqrt{1-8\left[\frac{3(1-2R/W)}{2+(1-2R/W)^3}-1\right]}-1}{2(2R/W)^2} \tag{4.25}$$

Since these equations have proven to be valid for hole diameter-to-width ratios $2R/W < 0.6$ (for these specimens $2R/W = 0.2$), and by assuming that this type of distribution can be extrapolated for the strain distribution at the same region around the hole (given their elastic relationship described in the first chapter), it is then possible to use this equation format to find a suitable fitting curve for each of the tensile test results using a compensation factors take take into account the transition to adimensionalized strain ($\epsilon/\epsilon_{\text{rem}}$).

These parameters were identified by minimizing the sum of squared residuals between the smoothed experimental data and the analytical prediction within a region close to the hole edge. The optimization problem was solved using the Nelder-Mead simplex algorithm implemented in MATLAB through the `fminsearch` function. This derivative-free method iteratively adjusts the unknown parameters until the difference between the model prediction and the experimental data is minimized.

The results from this approximation allowed for the determination of the E_y experimental values, that should be enough for providing an approximation of the different orthotropy levels between the specimens. The results are presented in Table 3.10.

Specimen no	E_y **[GPa]**	K_t	S **[MPa^{-1}]**	C
23	8.414	3.611	0.0242	-0.588
30	72.235	1.800	0.0581	-2.0581
24	16.0350	3.393	0.135	-2.0645
18	0.0595	8.031	0.00518	-0.0313
31	10.309	3.537	0.0105	1.335
12	16.9876	3.116	0.0106	-0.368
Average	**20.673**	**3.915**	**0.0406**	**-0.629**
Std. dev.	**26.239**	**2.084**	**0.0494**	**1.319**

Table 3.10: Interpolation results exported by the script for the experimental tests. Being S and C the fitting parameters for the equation $\frac{\epsilon}{\epsilon_{rem}}(y) = S\sigma_{xx}(0,y)+C$.

As it is possible to see, despite that the average results are between the expected range of values for a quasi-isotropic material it is important to notice that the standard deviation values are in many cases higher then the actual average values. This indicates a high level of dispersion in the measured parameters, suggesting that for similar the tests, either the identified properties vary significantly between specimens or the script is not being able to identify them with enough precision.

In the next chapter, several numerical simulations will be performed and analyzed in order to verify the validity of the script interpolation as well as the expected behavior for each of these specimens and in this way be able to establish the most accurate mechanical characterization possible for the forged carbon material.

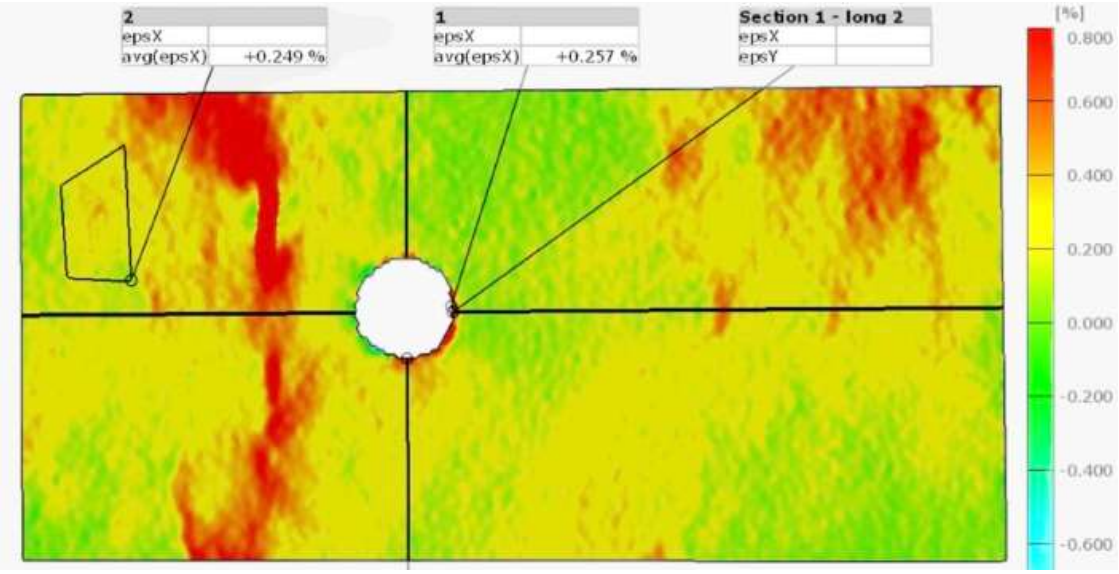


Figure 3.31: Strain field longitudinal distribution in GOM - Sections + Surface component for remote strain determination.

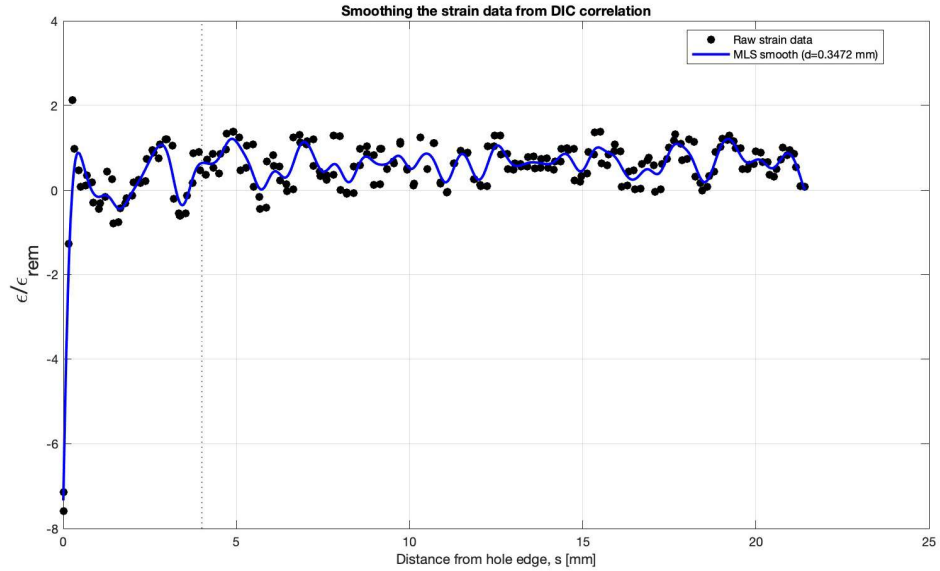


Figure 3.32: Strain field longitudinal distribution.

Finally, it is worth considering that for the case of exporting the strain field along the longitudinal direction, it proved to be a less reliable alternative due to the typical overall strain distribution of these specimens. As it is possible to see in Figure 3.31, the forged carbon material is prone to forming large concentrations of high stress zones - probably due to extreme void size and cluster (as seen in the last section) - that makes it very challenging to get any information along this direction, with the exception that almost all of the tests presented a clear convergence to the remote strain value. Additionally, as it will be seen in the next section, the strain re-distribution for the most orthotropic cases, is in many times off the limit length of the specimens, making the longitudinal strain a even more unreliable parameter.

Chapter 4

Numerical Simulations

In this chapter, the physical reasoning behind several numerical simulations is described aiming the ultimate validation of the hydrofoil model. In order to achieve this goal, preliminary numerical models were defined aiming to represent the stress concentration around a circular hole in order to provide a suitable reference for comparison with the experimentally obtained results. This comparison can then be used to determine the degree of orthotropy of the material considering the current mold design.

Regarding the real hydrofoil wing model, the loads for the were estimated using the classical theory for the case of an elliptical wing on the software XFLR5 and the boundary conditions that better represent the real model are defined regarding a model that considered only half of the wing, achieving a significant decrease of the computational cost due to symmetry of the model.

Finally, the load cases established in the beginning of this report will be simulated taking into consideration the mechanical properties obtained via experimental testing in order to achieve the most accurate representation possible and validate this material given the high performance application.

4.1 Stress concentration around a circular hole - ASTM D3039 Specimen

As it was seen in the second chapter, the theory on the stress and strain concentration around a circular hole is already well studied, specially for the infinite, isotropic and incompressible plate. In order to validate the comparison established between the DIC results and the numerical model developed along this section, it was first necessary to confirm that the results obtained for this simpler case were correct. In order to achieve this, the optimal ratio between the hole diameter D and the plate width W was determined in order to obtain the theoretical stress concentration factor, $K_0 = 3$ at the minimum ratio value according to [79].

The methodology for all models was first to run an unitary force model. Then, a more realistic approach was tested taking displacement as the external solicitation. If these results were coherent, the model was suitable for analysis. All models were made using shell elements.

4.1.1 The infinite plate load case verification

For the case of the infinite plate, the ratio chosen was $W/D = 12.5$ since according to the literature, any ratio above 10 will converge to the infinite plate solution. The plate was created using a shell extrusion and performing the cut extrude feature at the center of the geometry. Additionally, several partitions were created in order to simulate the tab placement on the real specimen and at the same time, guarantee a structured mesh generation.

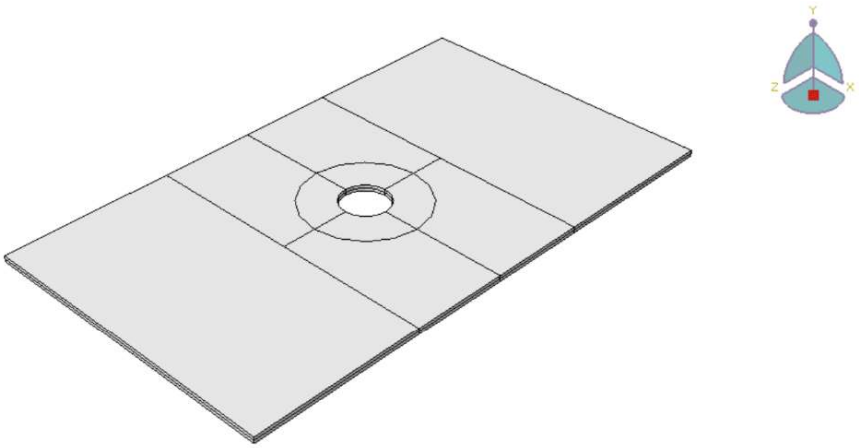


Figure 4.1: Infinite plate simulation part module and partitions

On the property module three different representations of the forged carbon material were created:

- Isotropic Material - fully isotropic material with Density, Young Modulus and Poisson Coefficient values obtained from the experimental testing.

- Quasi-Isotropic Material - on this case, all the values were kept the same from the isotropic model, however, the Young Modulus in the transversal direction - not measured experimentally - was reduced to 85% of the value on the longitudinal direction.

- Orthotropic Material - for the orthotropic case, the value of the Young Modulus in the transversal direction was lowered to 5% of the initial value in an attempt to represent a fully orthotropic (expected to add enough resolution in order to detect the difference regarding the fully orthotropic).

It is important to notice that on these preliminary models, the values of the different material properties may not actually coincide with the final values obtained from the experimental testing part since many of the experimental results were only obtained much later then the time that these simulations were performed. They were kept since that the ratios are the same and therefore, the small discrepancy of these values is not expected to change the intended outcome for this cases. For now, the Shear Modulus values were kept the same as is the isotropic model, however, a further analysis on this parameter will be performed in the next sections.

The BC's for this first model were as simple as possible in order to avoid artificial stress concentrations or numerical artifacts that can happen for overly restricted models. For this case, the bottom edge was simply supported along its entire length and one of the points was limited in all directions. Additionally, for the force model, a shell load was applied on the top edge and for the displacement model, a unitary displacement was imposed on the top load.

The mesh generation was also quite straight forward since the partitions allowed for a single bias seeding on the edges around the hole and by using S4R (quadrilateral reduced-integration shell element) it was possible to efficiently capture in-plane stresses around stress concentrators while reducing the risk of shear locking [80]. Its reduced integration also improves computational efficiency without significantly compromising accuracy in regions of high stress gradient, being excellent for the application.

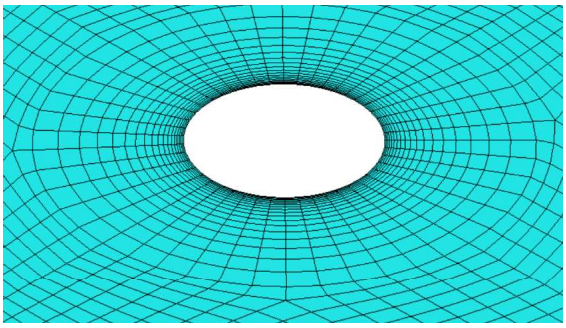


Figure 4.2: Meshing around the circular hole

Finally, the analysis was run for a total of 6 different scenarios (three for the force model and three for the displacement model) and two paths were created in the results module: a transversal path (along the width direction) and a longitudinal path (going from the periphery of the hole to the end of the tab partition). For both of these paths, the K_t values were computed (using the values of stress along the longitudinal direction), therefore verifying this model.

Table 4.1: Stress concentration factors K_t for circular hole transverse path tests - relative error between the force/displacement models.

Test	K_t	**Relative error [%]**
Isotropic plate	3.02324	-
Quasi-isotropic plate	3.05993	-
Orthotropic plate	4.42731	-
Isotropic plate (displ.)	3.10931	0.0285
Quasi-isotropic plate (displ.)	3.14142	0.0265
Orthotropic plate (displ.)	4.25844	0.0381

4.1.2 Simulation of the D3039 specimen

Once the infinite plate model was validated, the next step was to model the D3039 specimen geometry - the geometry of the specimens for which the molds were designed - and add a centered circular hole. The procedure for the optimum W/D ratio determination was similar to the one described above: on this case, it was intended to achieve the highest hole diameter possible, while still maintaining a predictable outcome for the K_t factors. The importance of achieving such high diameters for the hole is based on the results obtained on the first experimental tests (the ASTM D3039 tensile tests): the low tensile strength values obtained for the first forged carbon specimens are mostly justified due to the extremely high void size and percentage detected on the Micro-CT performed on specimen 341 (see the section relative to the X-ray micro tomography in the previous chapter). To mitigate this effect and avoid fracture outside of the hole area, it is critical that the size of the hole exceeds the maximum void size detected so far.

By taking all these factors into consideration, the hole diameter of 5 mm was selected, obtaining a final ratio $W/D = 3.125$ - that considering the experimental work documented on the literature, and for the isotropic case, is expected to have a K_t of around 3.3, as it is possible to see in Figure 4.5:

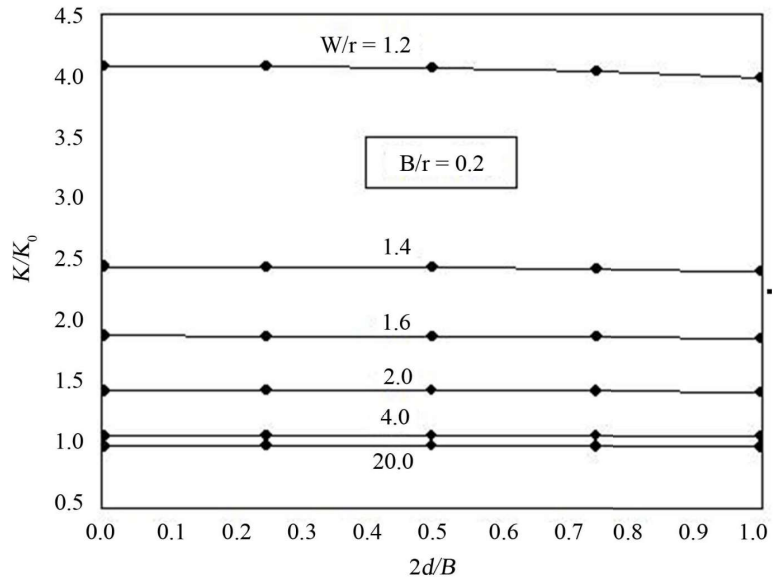


Figure 4.3: Distributions of stress concentrations for different relations of half-width to hole radius W/r along the distance to the mid-plane through half-thickness $2d/B$. Adapted from [79].

Once the geometry was fully established, the next step was to model the part geometry. This was also done in the same way as the infinite plate model by using shell extrusion feature and the same partitions were drawn, considering the 56 mm long tab selected in the specimen preparation phase.

In order to achieve the maximum sensitivity when comparing the DIC data with the numerical models, two more intermediate materials were added on this analysis between the isotropic and orthotropic cases where the Young Modulus in the transversal direction decreased, respectively, to 10 GPa (*mid* model) and 4 GPa (*quasi-othotropic* model).

Regarding the mechanical properties, the values obtained in the first experimental testing were used as a reference for these simulations as it is possible to see in 4.4. The Young Modulus in the longitudinal direction was kept for all cases since it was the one measured experimentally. Regarding the Young Modulus in the transversal direction, an incremental sequence from 1 GPa (for the fully orthotropic case) to 23 GPa (for the isotropic case) were used. For multiple ply carbon fiber reinforced polymers, for the wide majority of the cases, it has been documented that the behavior in the thickness direction is matrix and fiber-matrix dominated [74] [73], being a common approach to approximate the properties in this direction to the values of the mechanical properties documented for the resin datasheet (Appendix B). For this case, an Young Modulus of 3 GPa was kept for the thickness direction, despite its influence in this case being negligible (shell elements being loaded on the longitudinal direction). Regarding the Poisson Coefficient, the values from the experimental testing were used for all directions rather than for the in-plane properties, since their variation and influence on the results have proven to be negligible

Finally, in order to define a material using the engineering constants, in addition to the Young Modulus and Poisson Coefficient values in all three directions, it is also needed to define the Shear Modulus in these directions (G_{12}, G_{23}, G_{31}). However, for the case of significantly orthotropic materials such as the ones intended to analyze, the known relation between G with E and ν is no longer valid [81]. The approach on this case was to keep the isotropic shear modulus by computing it using the given relation for orthotropic materials:

$$G = \frac{E}{2(1+\nu)} \tag{4.1}$$

The value of 8500 MPa was then used for the preliminary analysis. It is important to notice that according to the literature, the typical values for a carbon fiber reinforced polymers show variations around 10 to 20 per cent [82] (depending on the considered direction). Since this results will be used as a reference for comparison, in order to validate them, two more models were tested for a high shear modulus case of $G_{12} = 10000MPa$ and a low shear modulus case $G_{12} = 7000MPa$ in order to depict the two extremes. The results are shown in Tables 4.2 and 4.3, and despite the clear decrease in the disparity (relative error when compared with the constant shear modulus models) of these values for increasing orthotropy, it is safe to conclude that a realistic shear modulus variation would not bring significant discrepancies to the K_t values or stress distribution, therefore validating the single model with constant shear modulus that will be used for comparison.

Table 4.2: Reference values for G_{12} = 10000 MPa

Model	E_2 **[GPa]**	K_t	**Relative Error [%]**
ISO	23	3.182278	0
Quasi-iso	20	3.121058	-2.90
Mid	10	3.328981	-2.28
Quasi-ortho	4	3.711578	-1.52
Ortho	1	4.465258	-0.74

Table 4.3: Reference values for G_{12} = 7000 MPa

Model	E_2 **[GPa]**	K_t	**Relative error [%]**
ISO	23	3.182278	0
Quasi-iso	20	3.337033	3.81
Mid	10	3.510861	3.05
Quasi-ortho	4	3.828129	1.57
Ortho	1	4.545191	1.03

The complete list with the referenced mechanical properties is presented bellow.

Table 4.4: Representative orthotropic material properties for different layups

	E1 [MPa]	**E2 [MPa]**	**E3 [MPa]**	ν	**G12 [MPa]**	**G13 [MPa]**	**G23 [MPa]**
ISO	23	23	23	0.35	8500	8500	8500
Quasi-iso	23	20	3	0.35	8500	8500	8500
Mid	23	10	3	0.35	8500	8500	8500
Quasi-ortho	23	4	3	0.35	8500	8500	8500
Ortho	23	1	3	0.35	8500	8500	8500
High shear	–	–	–	–	10000	8500	8500
Low shear	–	–	–	–	7000	8500	8500

Once the properties were defined, the next step was to modify the BC's given that the fixation method of the specimens by their tabs on the testing machine would represent a restriction of moment not only on the bottom edge of the specimen but also on the lateral motion of the lateral edge. These modification were performed and the uniform imposed displacement condition was applied on the top edge, representing the recorded effect of the testing machine for each specimen.

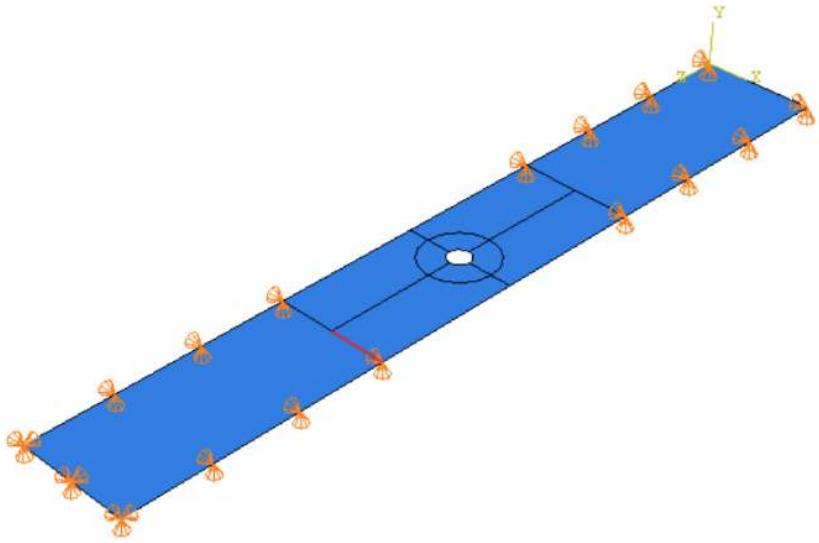


Figure 4.4: Final model with the modified BC's.

As it was possible to see, the K_t values obtained in the simulations verify the theoretical predictions, showing a clear convergence to $K_t = 3.15$ value due to final ratio $W/D = 3.125$. the small discrepancy with the $K_t = 3.3$ value predicted based on the 4.5 can be justified by the introduction of the modified BC's that are only representative of the tensile test condition and not of an ideal infinite plate like behavior.

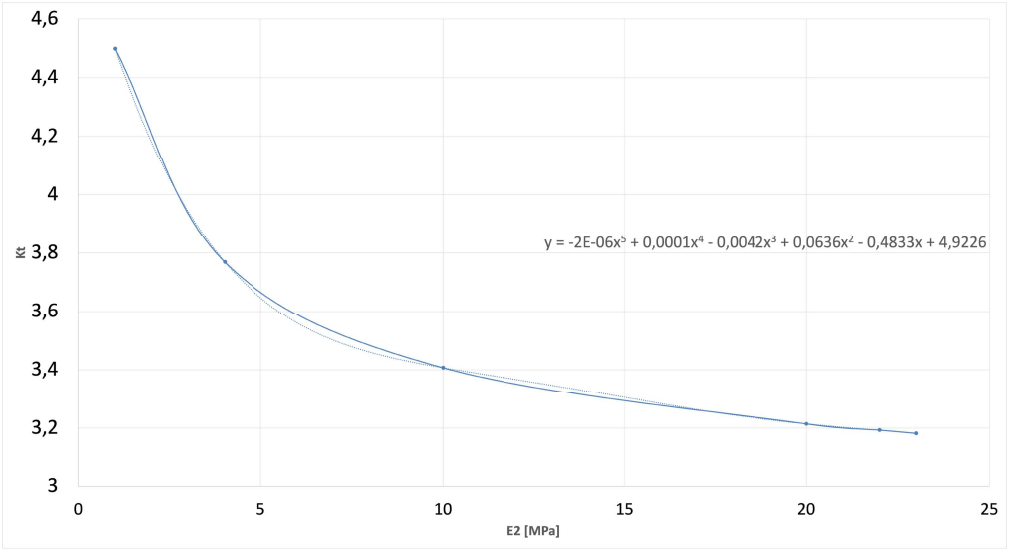


Figure 4.5: Obtained values for K_t for the different values of E_2 with polynomial regression curve equation for the ASTM D3039 specimen.

4.1.3 Strain concentration around on the D3039 specimen circular hole

In order to take a proper conclusion regarding the orthotropy of a material like forged carbon, we must be able to compare the results obtained experimentally via laboratory (DIC) testing with the numerical approach described in this chapter. For this, the field variables used in this analysis must be of the same type.

Since that it is not possible to measure stress directly, another parameter - ideally, one such that presents a similar behavior as the one studied previously - must be chosen for this comparison. Strain is a suitable candidate, as DIC provides full-field displacement measurements from which strain fields can be derived (having direct relation with stress). Moreover, strain is directly related to displacement through the kinematics of deformation, displacement being the primary variable of the numerical model.

Furthermore, the strain and stress values are linked through the constitutive behavior of the material (Hooke's law), meaning that, as it will be described in this section, the variations in stress induced by anisotropy are inherently reflected in the strain field. Therefore, by analyzing the spatial distribution and directional dependence of strain, it is possible to infer the underlying anisotropic characteristics of the material.

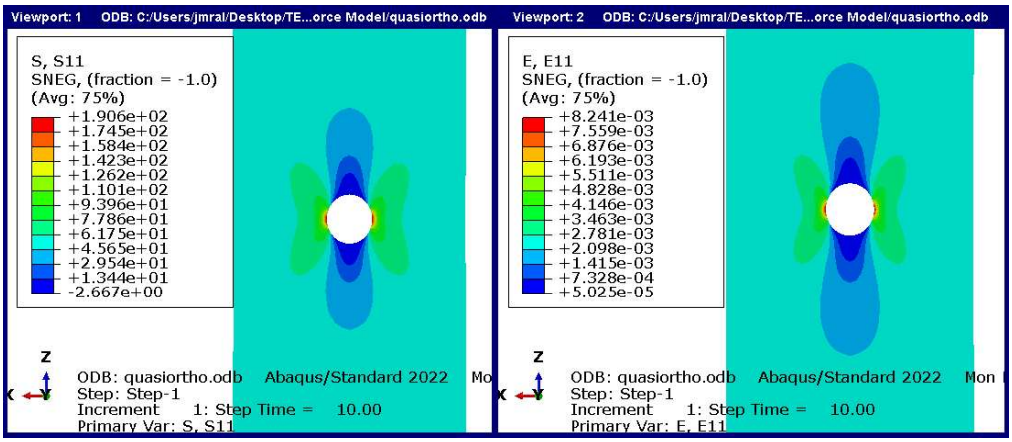


Figure 4.6: Stress and strain distributions similarity for the quasi-orthotropic model.

After plotting the different strain curves along the transversal and longitudinal directions for all the analysis performed, it was clear that the behavior of the strain field tended to specific identifiable shapes.

Analysis on the transversal direction

A transversal path was created in Abaqus given the direction at $\theta = 90°$ as represented in Figure 4.7.

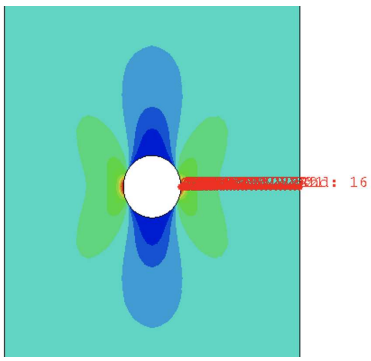


Figure 4.7: Set of nodes from the transversal path created on Abaqus

The numerical results obtained for the given stress field show that the specimen is expected to present the typical curve determined experimentally for the stress concentration around a circular

hole: Increase in the values of K_t with the material's increasing orthotropy and a clear convergence of the stresses closer to the specimen edge tending to the remote stress.

Table 4.5: Ke and Kt values for the different material models

Model	Ke	Kt
ISO	3.165238077	3.182278082
Quasi-iso	3.197025429	3.214295087
Mid	3.388400507	3.406877495
Quasi-ortho	3.748450129	3.768877411
Ortho	4.47520739	4.498817079

Analysis on the longitudinal direction

A longitudinal path was created in Abaqus, from the circular hole edge at $\theta = 0°$ to the node before the section where the tabs are glued, as represented in Figure 4.8.

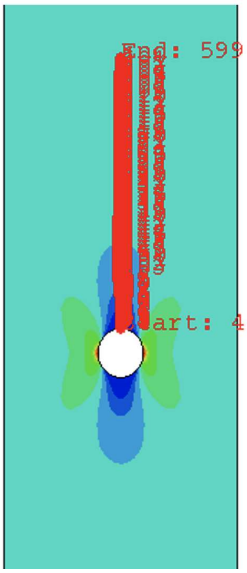


Figure 4.8: Set of nodes from the longitudinal path created on Abaqus

It is important to notice that for the longitudinal case, there is no stress concentration around the hole but rather a stress redistribution at $\theta = 0°$ since it is usual to have very small (sometimes even compressive stresses) values around this area. Additionally, this stress redistribution is much less pronounced then the transversal case and the ratio between either the stresses or strains along this path would not be very informative. It is a usual practice to normalize the stress field via any suitable adimensional parameter or to use a *characteristic length* - L_r - the length along that path required to achieve the remote stress.

In order to compute the remote stress, the reaction forces were plotted for the bottom edge of the specimen using the *sum* function in order to get the total resultant force being imposed on the specimen section. Then the value relative to the last frame (in *Newtons*) was divided by the cross section area (50 mm^3) in order to achieve the remote stress value (in MPa). Finally, using Hooke's law it was possible to compute the respective strain value for the given remote stress. The results are presented in Table 4.6.

Table 4.6: Remote stress and characteristic length for an imposed displacement of 4 mm.

Model	L_r **[mm]**	$\sigma_{\textbf{remote}}$ **[MPa]**
ISO	18.1245	56.3678
Quasi-iso	18.5445	55.7293
Mid	18.9628	53.6702
Quasi-ortho	–	52.4312
Ortho	–	51.6768

The reaction force distribution along to time (from zero to 4 mm imposed displacement) is also represented bellow, where it is possible to see the decrease of remote stress with increasing orthotropy.

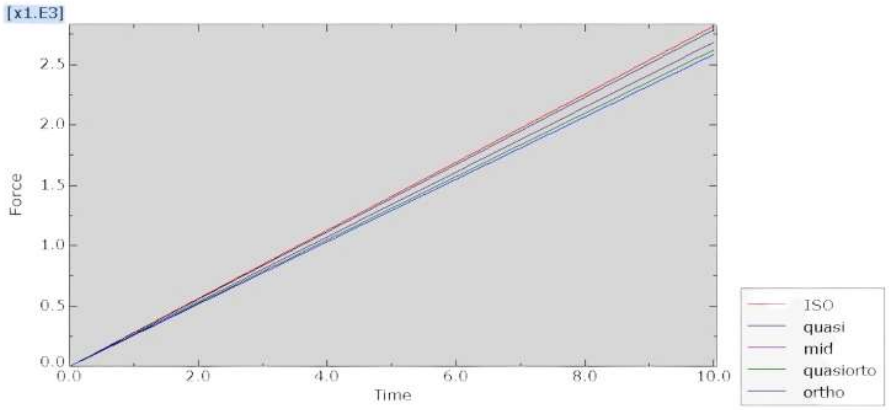


Figure 4.9: Reaction forces [N] for the different material models plot from *Abaqus*

Finally, the two strain distributions are represented bellow for both the transversal and longitudinal models.

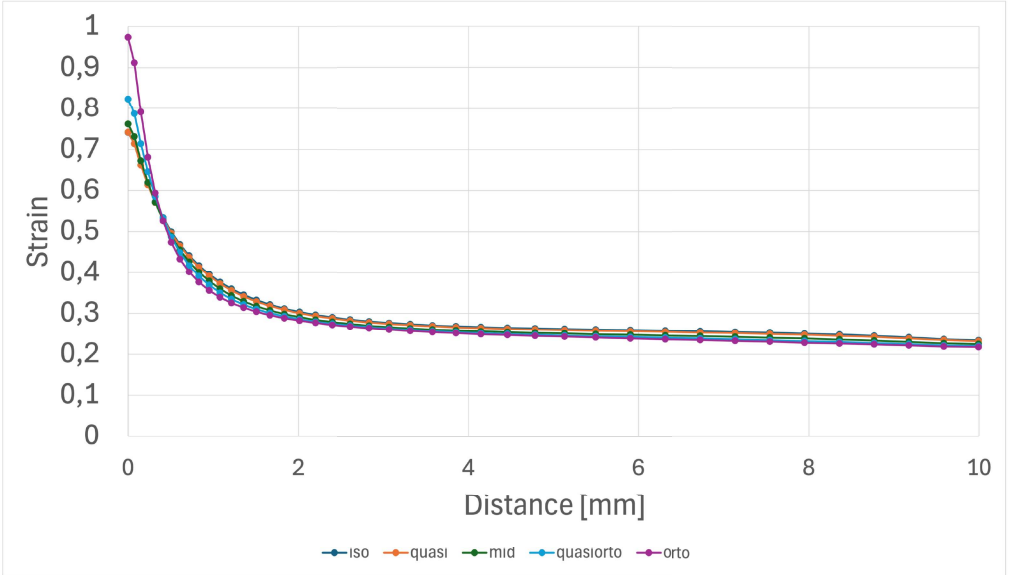


Figure 4.10: Transversal strain distribution.

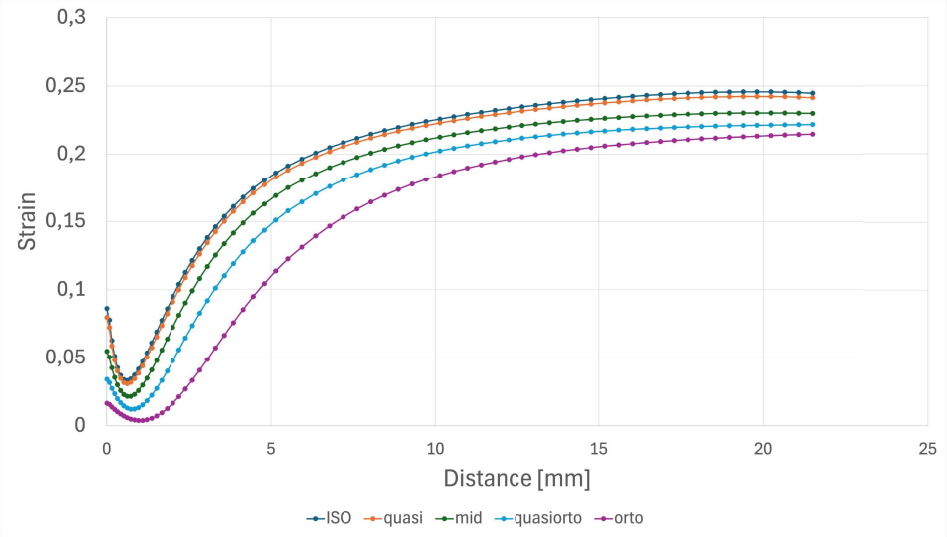


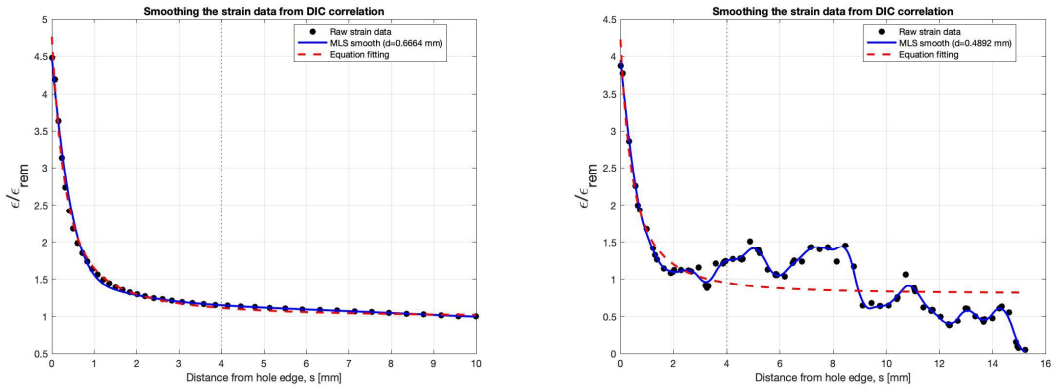
Figure 4.11: Longitudinal strain distribution.

Both the stress and adimensionalized strain results (obtained numerically) were then introduced on the script described in the last chapter regarding the determination of E_y in order to validate de results and serve as reference for the experimental tests. The results are presented on Table 4.7.

Model (reference value)	E_y **[MPa] (displacement)**	E_y **[MPa] (stresses)**	K_t **(from script)**
ISO (23 GPa)	20,12	23,91	3,269
QUASI (20 GPa)	18.48	20,18	3,293
MID (10 GPa)	11.73	9,08	3,433
QUASI-ORTHO (4 GPa)	5.72	3,37	3,706
ORTHO (1 GPa)	1.76	0,95	4,322

Table 4.7: Interpolation results exported by the script for Abaqus simulations.

As it is possible to see, the values estimated by the script provide a reasonably good approximation, specially for the stress data (given that there is almost no influence of the fitting parameter and no influence of the offset parameter). Given the numerical results the script proved to have a strong correlation with the variation of the mechanical properties and, on the other hand, the experimental results simply do not show any correlation to any of the possible ranges of orthotropy predicted using the solid mechanics theory. This difference between the numerical models testing in *Abaqus* and the experimental models tested on the laboratory via DIC, can be justified due to a combination of different factors that, for this specific case, brought significant limitations on the determination of the orthotropy level of the specimens. A critical reason was the noise typical from the DIC that, when allied with eventual bending loads added unintentionally during the tests, translated the strain values to locally obtained discrepant values that change the overall strain distribution along these paths. Additionally, the weight of E_y in the iterative process to find the fitting curve for the experimental data is not as considerable as some of the other parameters. Let us remind the equation for K_T^{∞} where it is possible to see that parameters such as the shear modulus or the Poisson coefficient have much more higher contribution than the E_y and despite these values have been estimated trough extensive experimental testing, given the morphology described for forged carbon, there is always the possibility that they present local variations and that the values introduced on the script do not correspond to the reality measured by DIC.



(a) Numerical Model obtained in *Abaqus*.

(b) Experimental model obtained using DIC

Figure 4.12: Comparison between the script results on models obtained numerically and experimentally

4.2 Hydrodynamic model

For the two load cases discussed in the first chapter - the take-off and cruise conditions - the hydrofoil wing will experience two different kinds of distributions according to several factors such as the AoA, the Reynolds number along the wing, the C_l and the C_d distributions among others. In order to achieve the best approximation for the real loads, the total $C_l(y)$, $C_d(y)$ and $C_m(y)$ coefficients along the wing span were directly imported from *XFLR5* into a *Matlab* script that based on those values and given the wing geometry, integrates these values along a strip of the wing defined by the user, this way obtaining the total Lift, Drag and Pitching Moment for the specified strip.

4.2.1 XFLR5

XFLR5 is an open source software that despite being designed for wing aerodynamics, can be also used for the design and analysis of low Reynolds number hydrofoils or even complete wings. The software is based on methods originally developed for *XFOIL* and extends them to three-dimensional lifting surfaces. For foil analysis, XFLR5 uses a viscous panel method coupled with a boundary layer solver to compute aerodynamic coefficients, and extends them for three-dimensional wing analysis. The software applies potential flow methods such as the Lifting Line Theory (LLT), the Vortex Lattice Method (VLM), and a 3D panel method [83].

By using this software, it is expected to be able depict the load distribution around an elliptical wing in a more accurate way since many important effects would not be captured by using only the idealized analytical elliptical lift distribution. While the analytical methods usually assume a perfectly elliptical circulation and can not easily provide an accurate representation of the local variations caused by the finite wing geometry, the numerical methods implemented in XFLR5 allow to compute all these phenomena in a both simpler and faster way: The induced drag can be estimated more accurately, since the software directly evaluates the downwash generated by the trailing vortex system. It is then also possible to capture the interaction between different spanwise sections of the wing and the resulting redistribution of aerodynamic loads. Finally, by incorporating foil aerodynamic data obtained from XFOIL, the software also evaluates the viscous effects and boundary layer behavior at each spanwise station.

Model definition

The XRF5 interface is mostly subdivided into two main types of modules. The first being the direct 2D foil design, and the second, the 3D wing design. The hydrofoil model definitions for analysis started by introducing the NACA profile parameters on the XFoil direct foil design module by importing the geometry from the Airfoil Tools website [84].

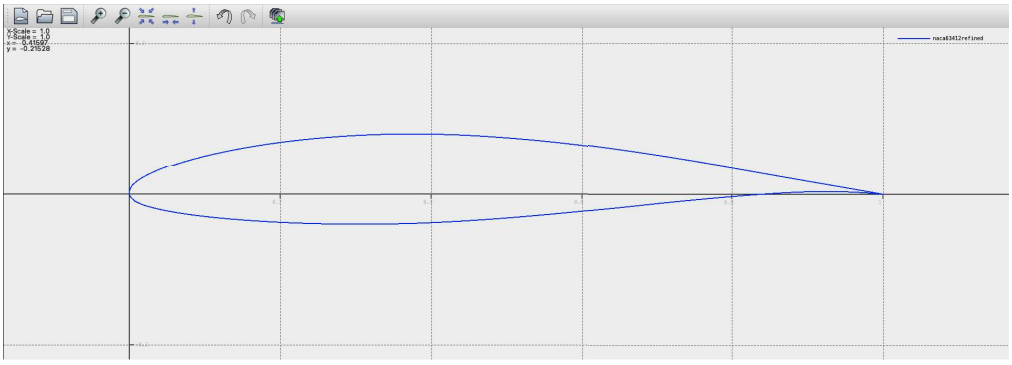


Figure 4.13: XFLR5 interface for direct foil design - NACA63-412.

All the characteristic parameters regarding the foil section can be computed by performing a batch analysis on the XFoil Direct Analysis module, by considering the respective ranges of the Reynold number and AoA.

Having defined the 2D geometry, the next step is to introduce the 3 dimensional parameters using the plane editor feature. As it is possible to see in Figure 4.14 the parameters y (location along the span), chord (chord length), offset (the offset along the horizontal direction of the airfoil section relative to the root section) and foil profile will have to be introduced according with the geometry defined for the wing. Other parameters such as the number of panels or panel distribution were not modified since the standard values are usually suitable for a general wing analysis.

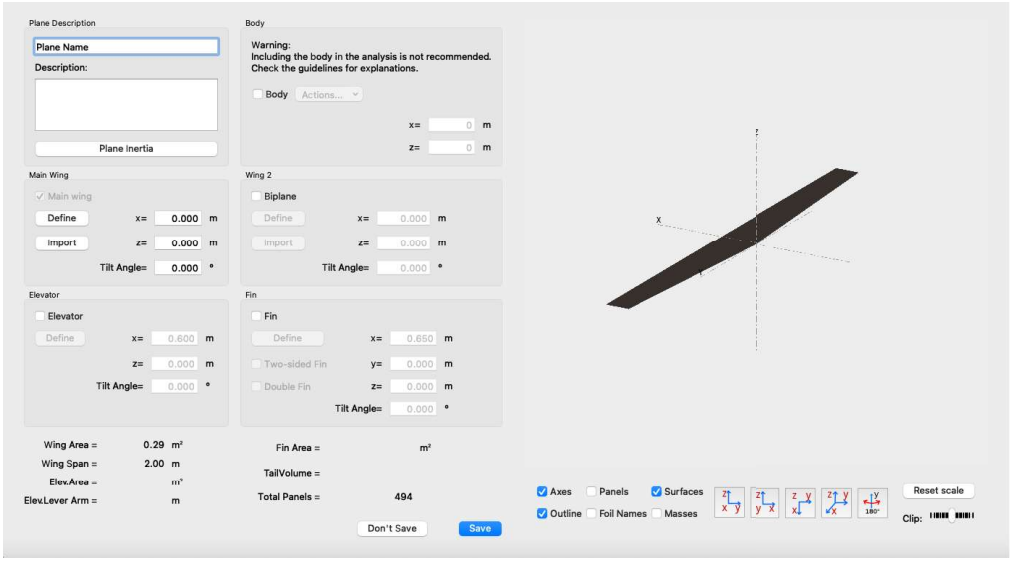


Figure 4.14: XFLR5 interface for direct foil design - NACA63-412.

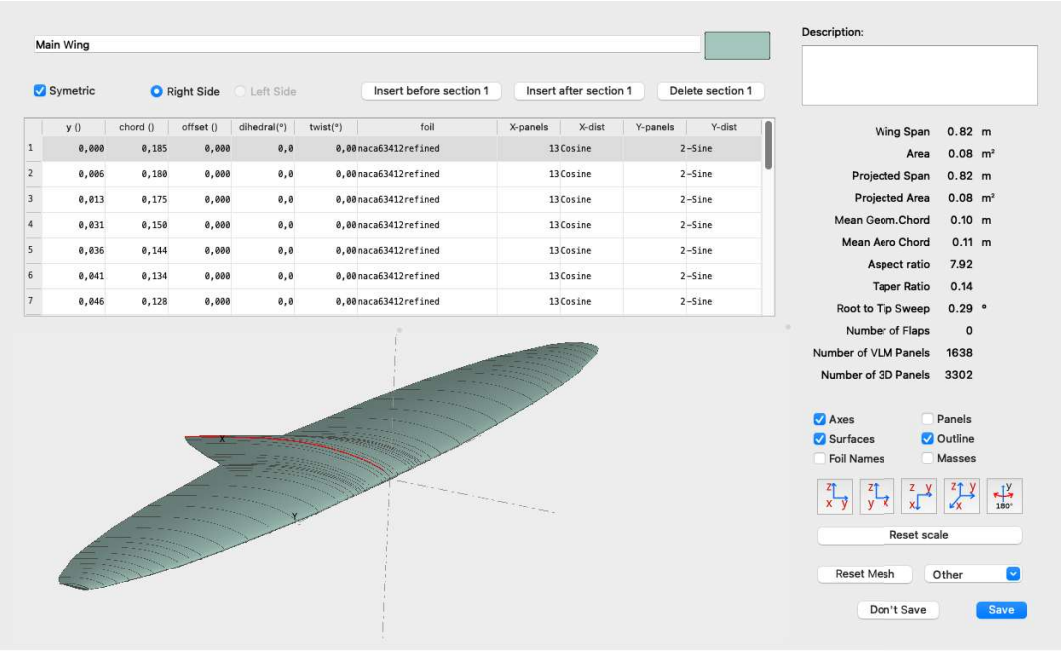


Figure 4.15: XFLR5 interface for direct foil design - Wing geometry edition.

Once the geometry was fully defined, the next step was to define an analysis for the wing by considering a fixed lift given a total mass of 140 Kg - a value that is expected to guarantee a stable flight even given any eventual added resistance due to wind, waves, inertial loads or even turbulence - generating for a total range of AoA from $-2°$ to $12.5°$ (achieved by varying flow speed). At the end of this procedure, the model definition was complete and all the parameters, such as the C_l, C_D and C_m coefficients can be computed efficiently using the 3D panel method.

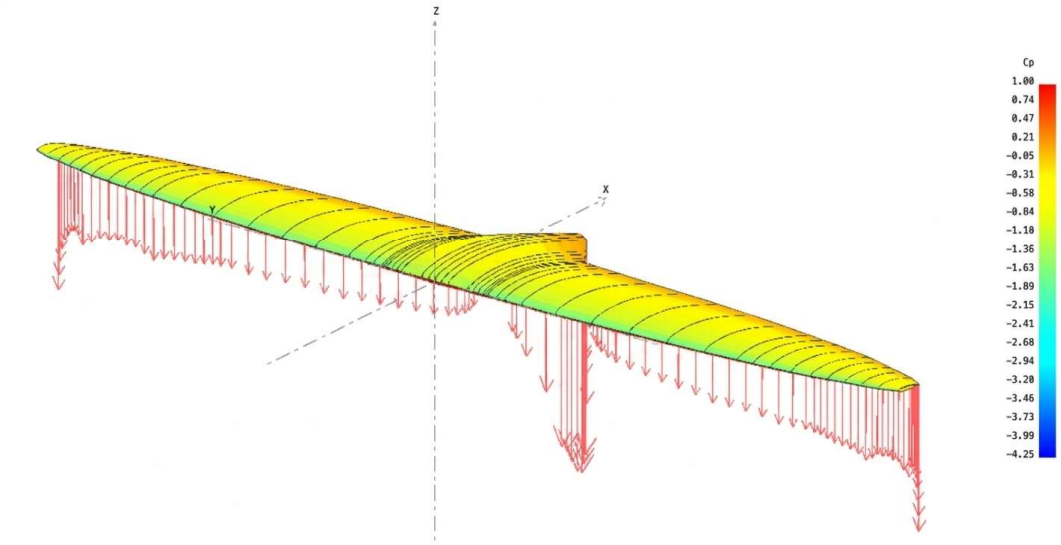


Figure 4.16: Example of C_p and downwash visualization using XFLR5 - defined for 6° AoA.

Load Cases

After having defined the model for analysis, it was then possible to establish the conditions for the two load cases that will be considered for the scope of this work - the take-off and cruise conditions. Given the analysis made by the team that considered the full boat, it was possible estimate an ideal take-off velocity of around 12.6 knt (or 6.5 m/s). By analyzing the range of results obtained in XFLR5, for the given velocity the total lift required is achieved at an AoA of 6°. Regarding the cruise conditions, an optimal point was found for the region with maximum C_l/C_D ratio and that at the same time would not require an excessively high thrust. This procedure was implemented via polar plots computed for the wing, obtaining a point at around 1° AoA and a velocity of 9.802 m/s.

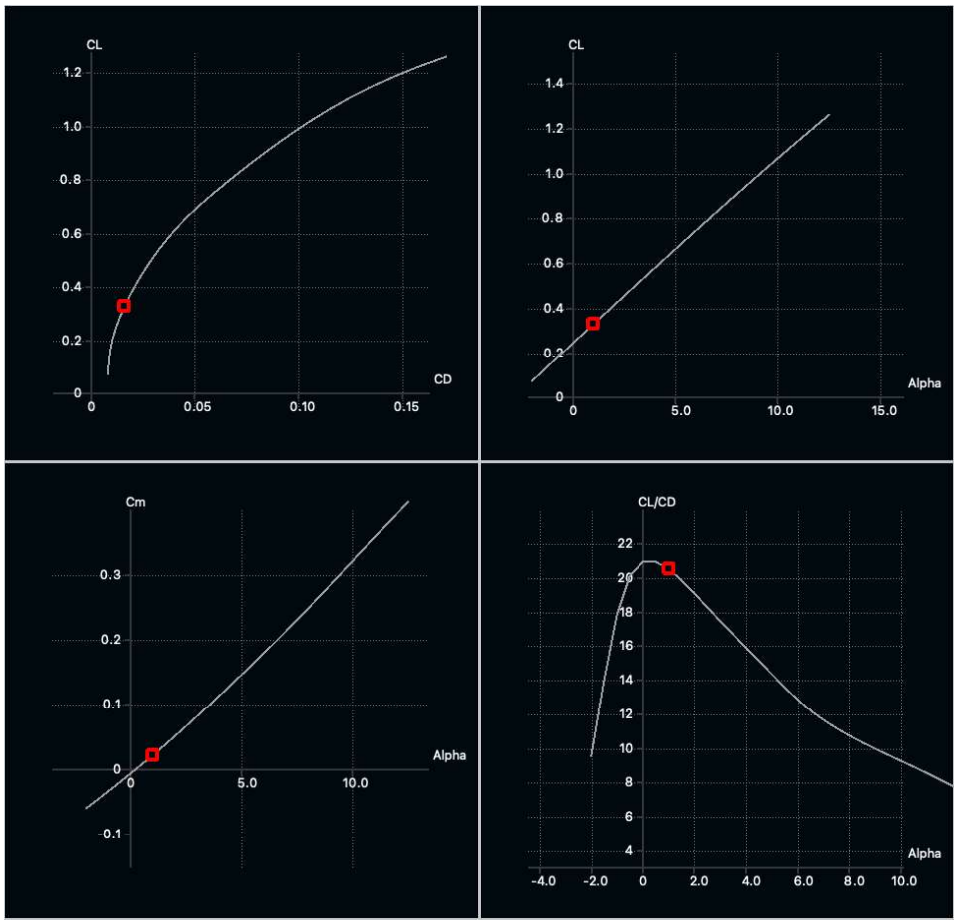
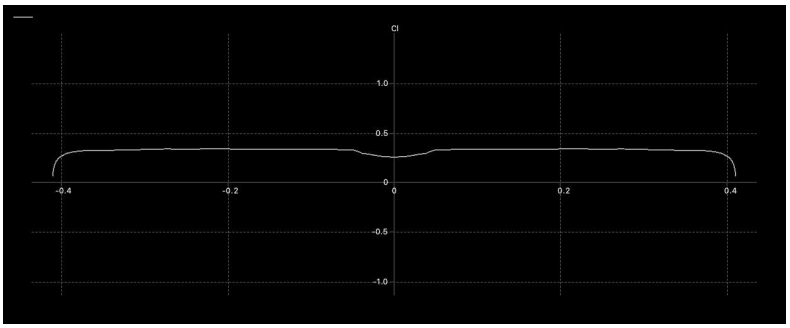
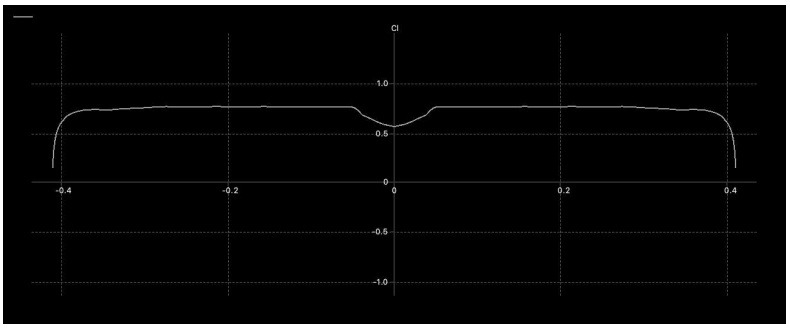


Figure 4.17: Polar plots obtained in XFLR5 for the cruise speed AoA 1°.

The approach as to subdivide the wing span in several strips and to determine the loads for each strip that were applied on the aerodynamic center for the middle chord section along that strip. For this, the distributions along the wingspan were computed for these two conditions. Given that the scope of this thesis does not include the optimization of the geometry, the only variables taken into consideration were the $C_l(y)$, $C_d(y)$ and $C_m(y)$ coefficients, presented bellow.

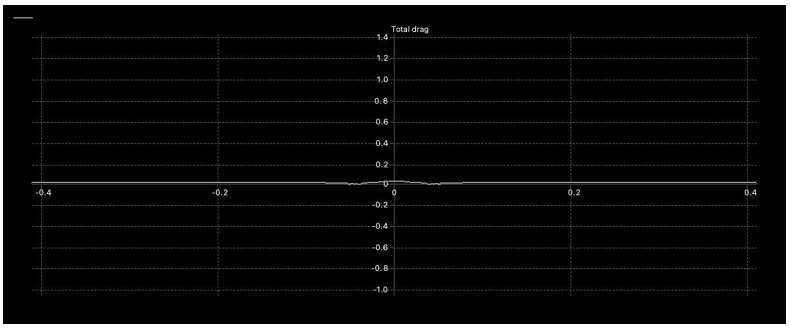


(a) Total lift Coefficient at 1°.

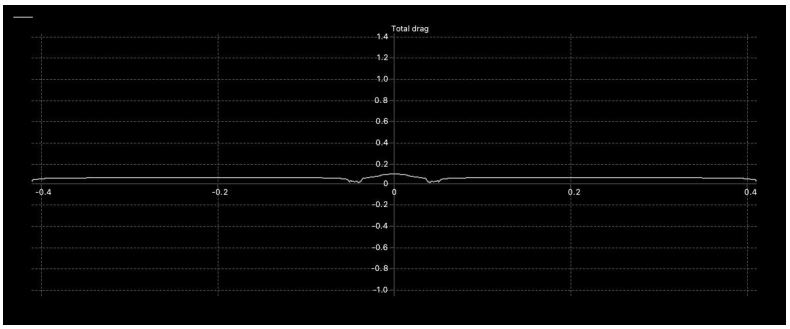


(b) Total lift Coefficient at 6°.

Figure 4.18: Lift Coefficient distributions

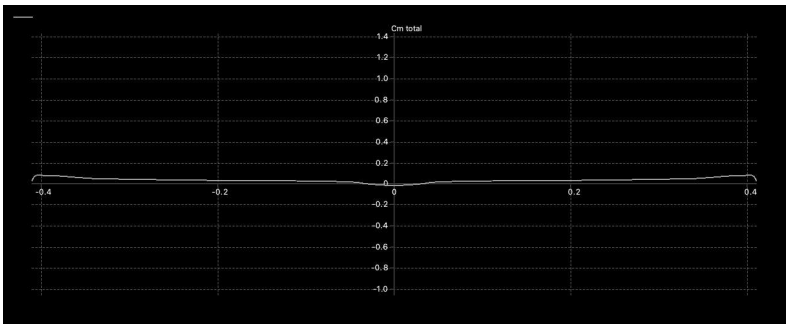


(a) Total Drag Coefficient at 1°.

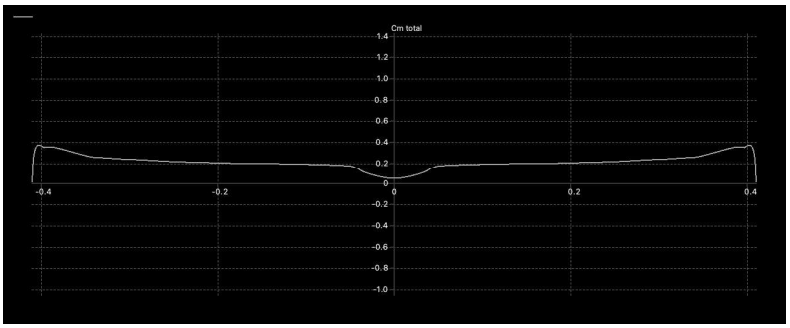


(b) Total Drag Coefficient at 6°.

Figure 4.19: Drag Coefficient distributions



(a) Total Pitching Moment Coefficient at 1°.



(b) Total Pitching Moment Coefficient at 6°.

Figure 4.20: Pitching Moment Coefficient distributions

4.2.2 Load distribution

Given that the numerically obtained coefficients already capture the influence of the most relevant hydrodynamic effects, a *Matlab* script was developed in order to integrate these distributions along the wing span and determine the loads given a user defined strip of the wing (using two inputs y1 and y2).

Given the elliptical planform, the parameter c (local chord distribution) is defined for the span values b

$$c(y) = c_{\text{root}}\sqrt{1-\left(\frac{y}{b/2}\right)^2}, \qquad -\frac{b}{2} \le y \le \frac{b}{2}. \tag{4.2}$$

To quantify the loads over a specific spanwise interval $[y_1, y_2]$ on the positive semi-span, the script interpolates the distributions to a uniform grid $y \in [y_1, y_2]$ and integrates the corresponding loads using the trapezoidal rule. Assuming symmetry, the strip contribution is doubled to account for both sides of the wing:

$$L_{[y_1,y_2]} = \int_{y_1}^{y_2} q\, c(y)\, c_l(y)\, dy, \tag{4.3}$$

$$D_{[y_1,y_2]} = \int_{y_1}^{y_2} q\, c(y)\, c_d(y)\, dy, \tag{4.4}$$

$$M_{[y_1,y_2]} = \int_{y_1}^{y_2} q\, c(y)^2\, c_m(y)\, dy. \tag{4.5}$$

It is important to notice that these loads are computed for the aerodynamic center position along the chord and, therefore, in order to be able to introduce them in Abaqus, additional couplings will have to be enforced.

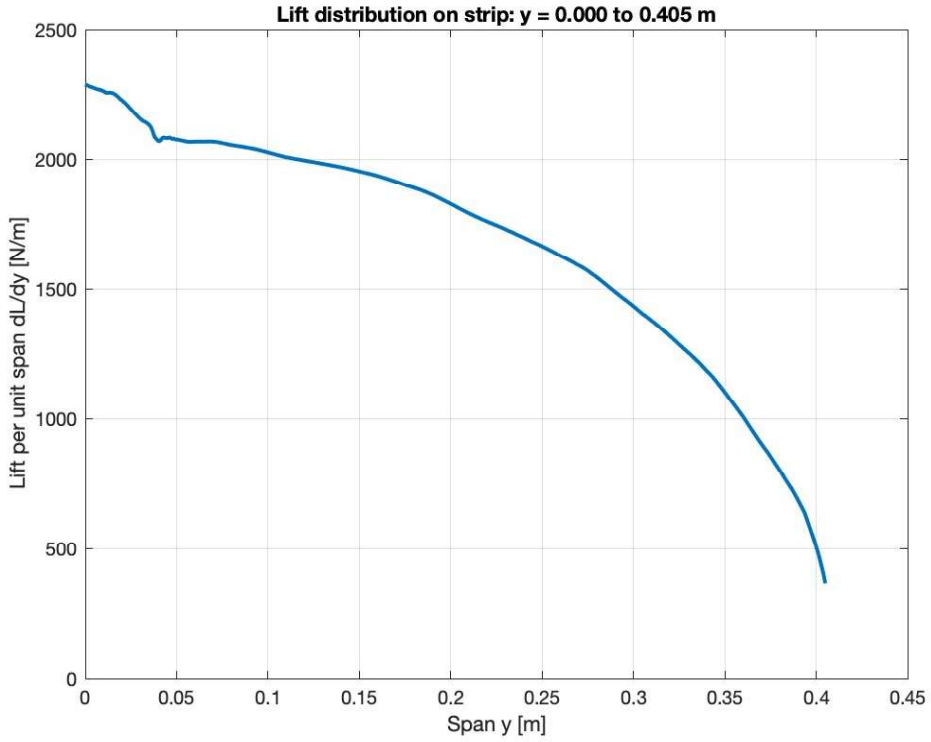


Figure 4.21: Lift per unit span during Take-off conditions.

4.3 Hydrofoil load cases

Once the load cases were fully defined, a numerical CAE model was created in order to be able to perform a structural analysis for these two conditions. Considering the symmetry of the component, a simplified model consisting on an half section of the hydrofoil wing was evaluated using *Abaqus* software.

4.3.1 Numerical model

The hydrofoil geometry used in this project maintains the original design made by the Team, modeled using *Solidworks*. As this is a relatively complex geometry, requiring advanced features in order to achieve an accurate model, it was too complex to perform the modeling of the part geometry using only the *Abaqus* interface. Also, it was not suitable to be simply imported into *Abaqus* as a complete part since it contained undefined geometry and this would result in mesh related problems. Alternatively, the solution found was to use the *split* function in *Solidworks* in order to subdivide the hydrofoil wing in several spanwise sections. Additionally, some details on the geometry such as fillets, holes and the top part of the support were removed from the global geometry since in order to improve the meshing procedure as it is expected that their contribution to the final result is negligible.

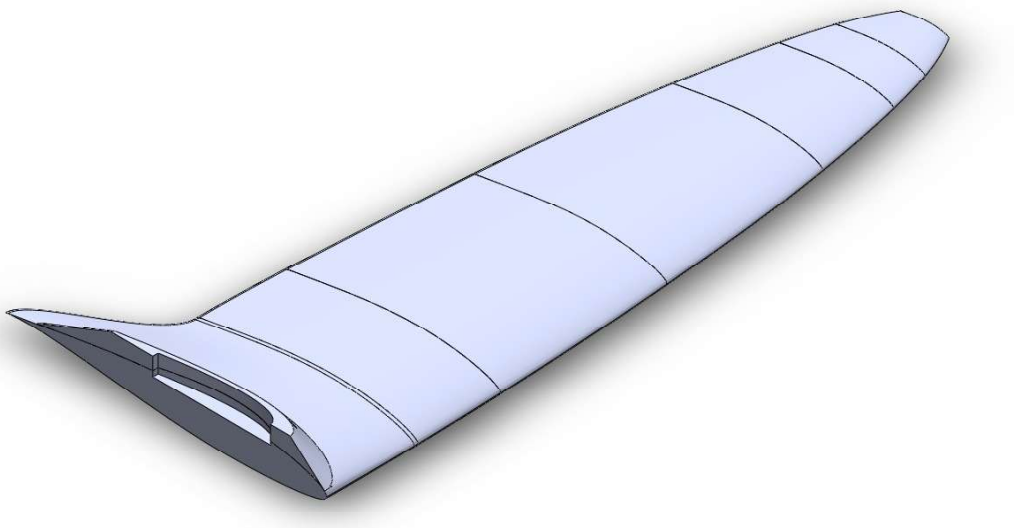


Figure 4.22: Hydrofoil model - Split Solidworks feature.

Regarding the property definition, two different approaches were implemented: the first admitting the hypothesis of a fully isotropic material (given that for the case of a thick laminate the staking is not expected to be as organized as for a thin rectangular specimen) and the second being defined by the material properties considered as the best approximation given the experimental testing (i.e. an orthotropic material presenting the same in-plane properties and the resin properties along the thickness direction).

The solid section was created for each of the materials and these sections were then respectively assigned to the entire model after merging the instances.

Property	**Isotropic**	**Orthotropic**
E_1 [GPa]	26.36	26.36
E_2 [GPa]	26.36	26.36
E_3 [GPa]	26.36	3.00
ν_{12}	0.33	0.33
ν_{13}	0.33	0.33
ν_{23}	0.33	0.33
G [GPa]	8.50	8.50

Table 4.8: Material properties used for isotropic and orthotropic models

This approach allowed to create a set of simpler, well defined and easier to seed/mesh sections that could then be imported into *Abaqus* and by using the *merge* feature in the assembly model it was possible to connect the full hydrofoil assembly. Even tough this approach guaranteed a structured mesh along the wing span, some regions (specially along the trailing edge and on the central area close to the support) were still presenting poor geometry, which still made it challenging to have good quality mesh along the complete component.

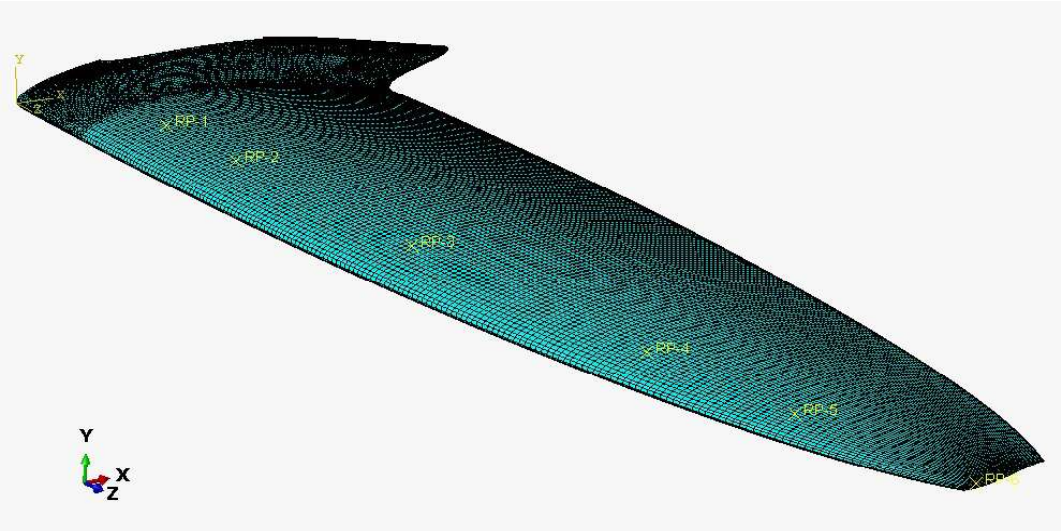


Figure 4.23: Hydrofoil model mesh.

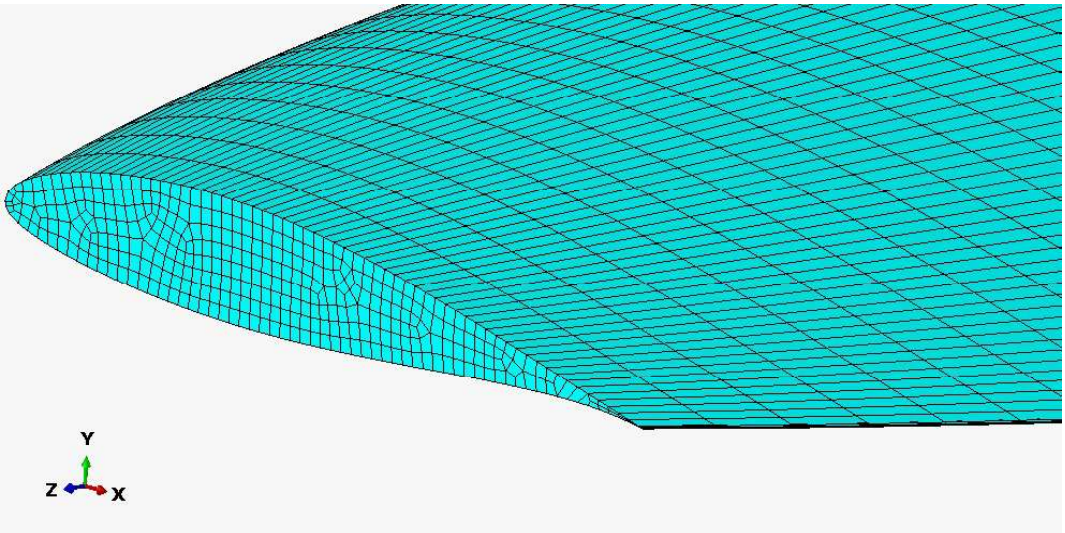


Figure 4.24: Hydrofoil model trailing edge mesh detail - poor geometry.

The meshing process was done by using total of 180974 elements, having to limit their geometric order to linear instead of quadratic in order to avoid excessive geometric liberty of each element that initially led to the failure of several programs due to RAM limitation of the computer in use. This limitation led to the creation of two different types of elements, the first being a total of 63189 C3D8R elements created along the spanwise sections and 117785 C3D4 elements generated around the central area.

Since the loads have already been computed for the aerodynamic center (estimated to be around 25% of the chord length), several reference points were created at those locations for every partition made in *Solidworks* and a *coupling* constraint was imposed regarding each reference point and the corresponding 2D foil edges.

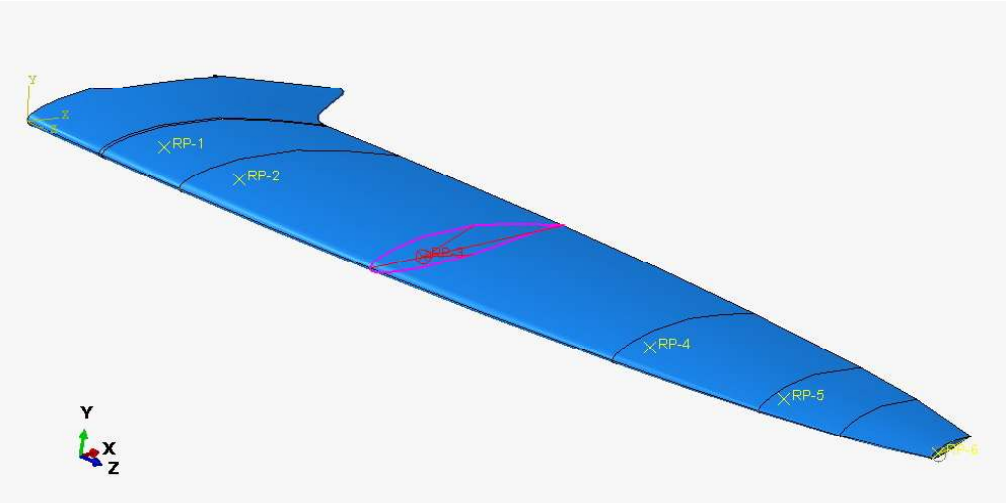


Figure 4.25: Hydrofoil model RF kinematic couplings.

As it was seen in the beginning of this chapter, it is possible to assume that the forged carbon material is approximately isotropic and therefore, the mechanical properties were defined by taking into consideration the average values obtained on the tensile tests (presented in Table 3.7).

As referred before, the symmetry of the model allowed for the reduction of the computational cost of the analysis and therefore the motion of the symmetry plane face was fixed and the support region was encastered on the bottom and pinned on the lateral faces (in order to avoid stress concentration on these areas, since goal was to analyze the complete stress distribution along the wing).

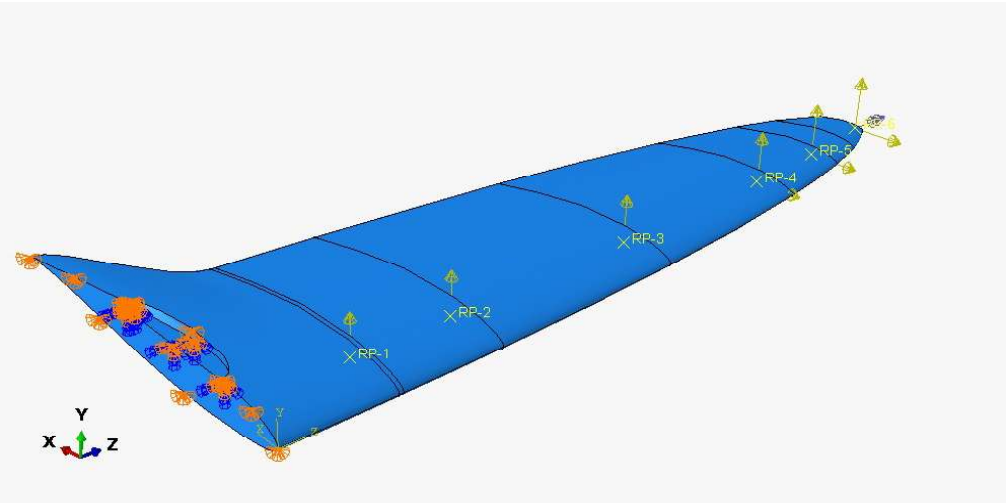


Figure 4.26: Hydrofoil model Loads and BC's.

The loads were applied at the aerodynamic center for both scenarios and despite it is expected that these vectors coincide with the lift and drag direction, on this case, after the 6° compensation, the lift component along the x exceeded the drag component along that direction. This led to the unintuitive negative x force component represented in Figure 4.26. The compensated load distribution is also presented in Tables 4.10 and 4.12 for each of the considered load cases.

6AoA					
Section number	**Span min**	**Span max**	**Lift [N]**	**Drag [N]**	**Pitching Moment [Nm]**
1	0	0.076	162.83	14.02	3.91
2	0.076	0.15	148.43	10.96	4.42
3	0.15	0.25	182.06	13.99	5.25
4	0.25	0.325	112.00	8.43	3.064
5	0.325	0.375	54.46	4.06	1.38
6	0.375	0.405	19.84	1.48	0.469

Table 4.9: Sectional hydrodynamic load distribution for take-off conditions - taken from XFLR5.

Section number	**Span position**	**Vertical comp. [N]**	**Horizontal comp. [N]**
1	0.052	163.403	-3.077
2	0.1	148.762	-4.615
3	0.2	182.525	-5.117
4	0.3	112.267	-3.323
5	0.35	54.586	-1.654
6	0.4	19.886	-0.601

Table 4.10: Vertical and horizontal force components along the span - compensation for 6°.

1AoA					
Section number	**Span min**	**Span max**	**Lift [N]**	**Drag [N]**	**Pitching Moment [Nm]**
1	0	0.076	162.47	12.10	0.009
2	0.076	0.150	148.32	8.55	2.414
3	0.150	0.250	181.97	11.48	2.716
4	0.250	0.325	111.85	6.56	1.413
5	0.325	0.375	54.15	2.93	0.582
6	0.375	0.405	19.70	1.04	0.21

Table 4.11: Sectional hydrodynamic load distribution for cruise conditions - taken from XFLR5.

Section number	**Span position**	**Vertical comp. [N]**	**Horizontal comp. [N]**
1	0.052	162.656	-11.472
2	0.1	148.447	-7.196
3	0.2	182.143	-11.478
4	0.3	111.947	-2.334
5	0.35	54.193	1.757
6	0.4	19.715	0.985

Table 4.12: Vertical and horizontal force components along the span - compensation for 1°.

4.3.2 Stress analysis

After the estimation of the loads, the two models were run considering a safety coefficient of 1.5, taking a total time of around 70 seconds, as expected for such refined model. The von Mises stress distribution indicates that the highest stresses are concentrated near the root region of the wing (where bending moments are higher), having a local maximum around the joint region from the

wing training edge tail. The displacement field is characteristic of a cantilever-like structure subjected to hydrodynamic lift forces, where the root remains relatively constrained while the free end experiences the largest deflection (with the maximum displacement occurring at the wing tip).

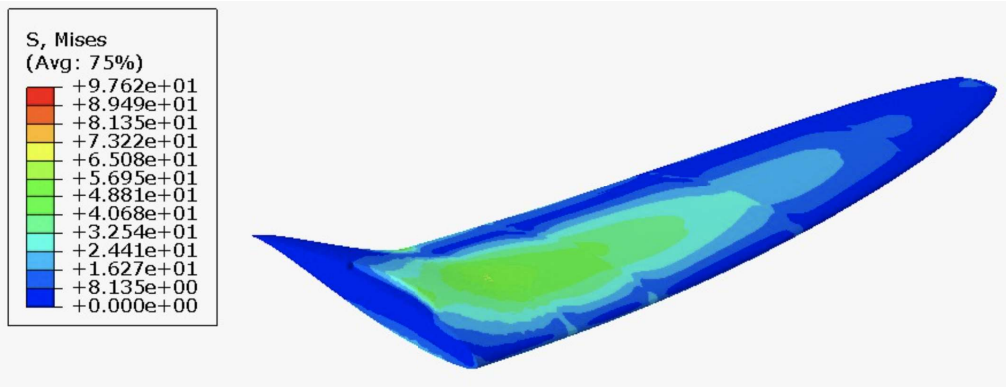


Figure 4.27: Von Mises stress distribution - Take-off conditions (isotropic model).

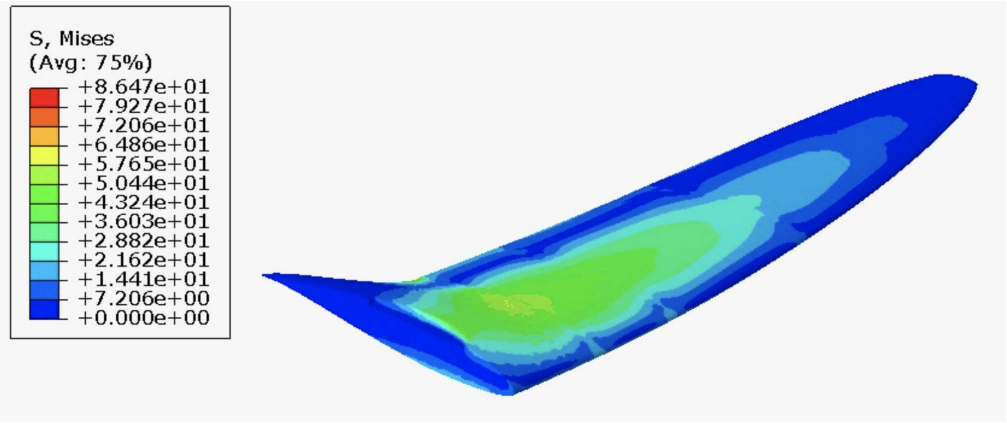


Figure 4.28: Von Mises stress distribution - Cruise conditions (isotropic model).

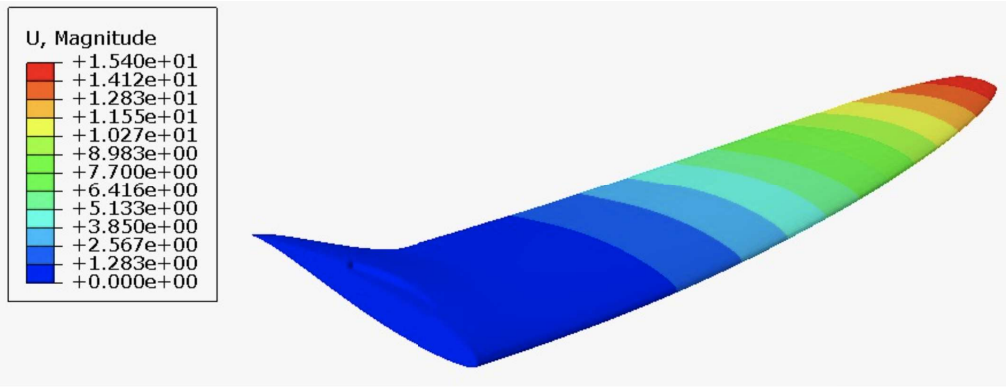


Figure 4.29: Displacement distribution - take-off conditions (isotropic model).

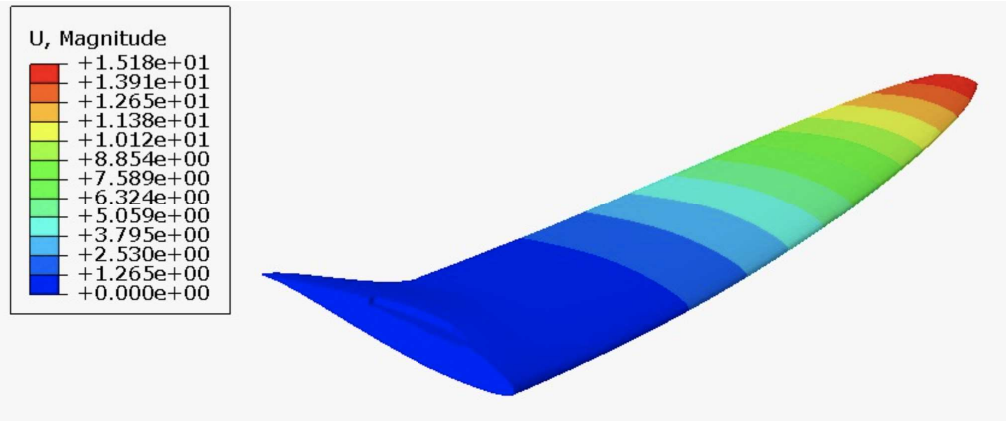


Figure 4.30: Displacement distribution - cruise conditions (isotropic model).

It was noticed that the region around the trailing edge tail transition contained a localized group of elements that were not consistent with the rest of the model, in many cases containing both the maximum and minimum stress values. Despite the fact that this zone is in fact prone to stress concentrations due to its reduced thickness and abrupt chord change, such small discrepancies in the stress values in less then 5 mm region are likely to happen due to artifacts related with mesh generation operations. Despite the local mesh refinement and nodal averaging, this discrepancy kept practically the same and therefore, the results for stress analysis will disregard the values obtained for this region.

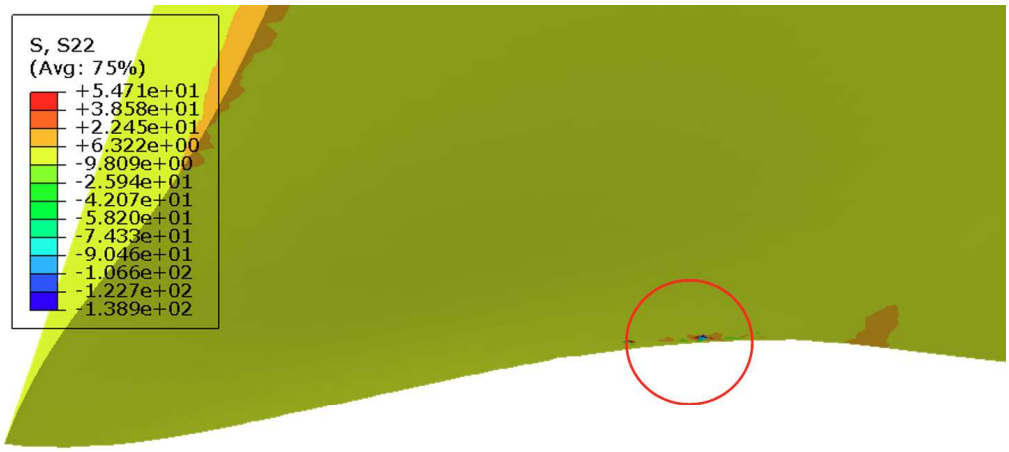


Figure 4.31: Nodal discrepancies on the trailing edge elements.

As it is possible to see in Tables 4.13 and 4.14 the dominant stress component is clearly S_{33}, indicating that, as expected, the hydrofoil structure is mostly bending dominated. Another important note on these results is that the S_{22}, as expected, were relatively close to zero at all regions, except for a couple exceptions around the edges where the coupling interaction was applied. It wa decided to keep the values from those regions on the result table. Finally, it is also possible to see that the maximum displacement of all load cases occurs for the take-off conditions. This slight difference can be justified with the increasing AoA leading to a higher pitching moment applied on the successive sections and therefore, a more pronounced bend-twist coupling, increasing the displacement at the trailing edge of the wingtip point - where the displacement was maximum.

Model	**Von Mises [MPa]**	S_{11} **[MPa]**	S_{22} **[MPa]**	S_{33} **[MPa]**	U_{max} **[mm]**
Isotropic	55.09	26.37	13.09	63.77	15.40
Orthotropic	55.01	25.25	19.91	63.18	15.34

Table 4.13: Stress and strain values for the take-off conditions (neglecting the stress field discrepancies around the trailing edge).

Model	**Von Mises [MPa]**	S_{11} **[MPa]**	S_{22} **[MPa]**	S_{33} **[MPa]**	U_{max} **[mm]**
Isotropic	64.77	33.45	12.06	65.32	15.12
Orthotropic	64.77	26.11	12.02	65.05	15.12

Table 4.14: Stress and strain values for the cruise conditions (neglecting the stress field discrepancies around the trailing edge).

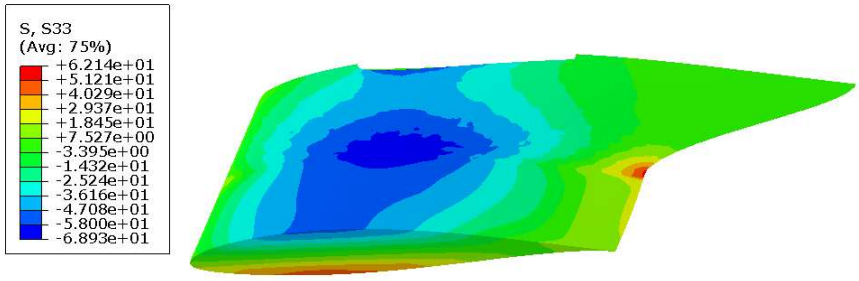


Figure 4.32: S_33 distribution along a spanwise section.

Mesh convergence study

A mesh refinement study was conducted to verify the convergence of the finite element results while maintaining a balance between accuracy and computational cost. The mesh convergence was evaluated by varying the number of seeds assigned to each component of the model rather than prescribing a single characteristic element size, which resulted in different node and element counts for each refinement level. The parameter used for the convergence analysis was maximum displacement since that most of the stress component values were affected by the local trailing edge artifact described in the last section. The results are presented in Table 4.15.

No of Nodes	**No of Elements**	**Computational Time [s]**	**Maximum Displacement [mm]**
5023	7193	22	17.44
8800	13939	26	16.39
41914	65957	40	15.02
54803	87488	44	15.06
98931	180974	70	15.12

Table 4.15: Mesh refinement study showing the influence of mesh density on computational cost and maximum displacement.

In any model tested for a number of nodes higher then 40 000, the maximum displacement value showed very limited sensitivity to refinement, with a variation in between the two finest meshes was below 0.5%, indicating that the solution had effectively converged. Based on this analysis, the mesh containing the smallest seed size was selected since the solution proved to be accurate and any discrepancies - specially common in stress distribution - would be easily detected.

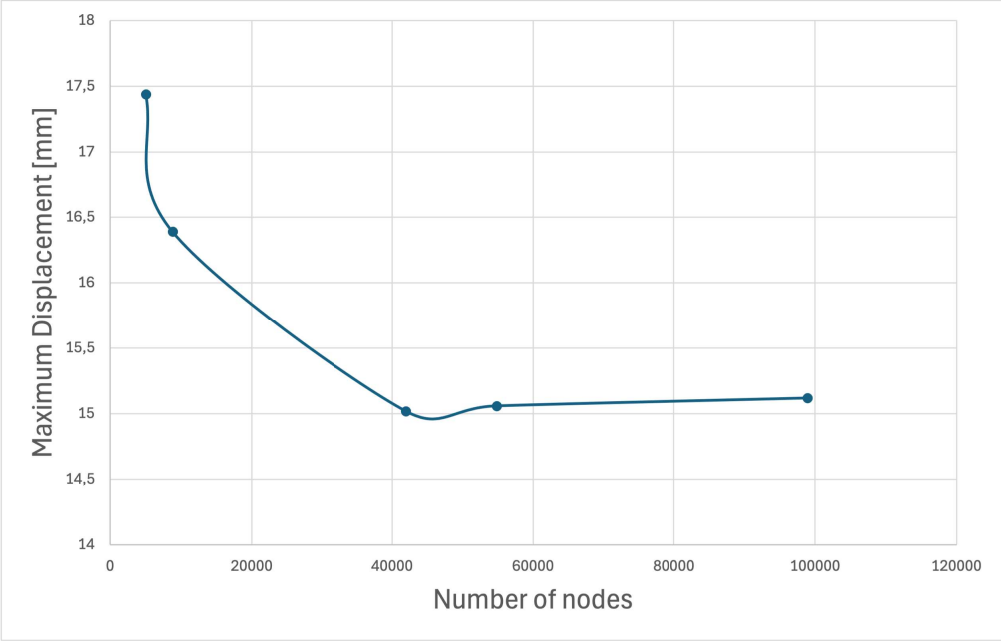


Figure 4.33: Mesh convergence study.

4.3.3 Margin of safety

Considering the previously described typical failure modes for forged carbon composites, it is possible to identify the indicators of which of them would be predominant. For the case of matrix cracking, it will be driven by tensile stress concentrations along the matrix specially around void cluster areas or even surface defects. On the other hand, for the fiber breakage the most critical aspect to detect would be high tensile stress aligned with the predominant fiber directions. Finally, for the debonding case, it would be most related with a mixed-mode failure, localized in regions where there was the presence of both shear and peel stresses.

The margins of safety were computed for tensile stress, given the properties obtained from experimental testing by considering the two approaches: the first admitting the hypothesis of a fully isotropic material (given that for the case of a thick laminate the staking is not expected to be as organized as for a thin rectangular specimen) and the second being defined by the material properties considered as the best approximation given the experimental testing (i.e. an orthotropic material presenting the same in-plane properties and the resin properties along the thickness direction).

For the first, being fully isotropic, the safety margin for tensile stress is evaluated using the Von Mises stress criterion, as defined in Equation 4.6.

$$SM = \frac{F_{tu}}{f_{vm}} - 1 \tag{4.6}$$

In this equation, F_{tu} stands for the ultimate tensile strength of the material, f_{vm} is the highest Von Mises stress derived from the Abaqus simulations, and SM is the calculated safety margin.

The SM values were obtained for the most critical element on the model. For certification purposes, a positive safety margin is required. With this criterion, the results can be presented ensuring that the safety margin is calculated for each model component.

Table 4.16: Tensile safety margin evaluation for the hydrofoil under cruise and take-off conditions - Isotropic approach.

Component	Take-off conditions	Cruise conditions
F_{tu} (MPa)	110.91	110.91
f_{vm} (MPa)	63.63	64.77
SM	0.74	0.71

As it is possible to see, all components exhibit positive safety margins, indicating that the design satisfies the tensile stress certification requirements.

For the orthotropic approach, since the von Mises failure criterion would not be suitable for this analysis (because it assumes isotropic material behavior and identical strength in all directions) and the hydrofoil wing will now exhibit direction dependent properties and failure mechanisms dominated by stresses along specific material directions, a different stress component parameter was selected in order to achieve a more physically coherent assessment: since the hydrofoil primarily experiences bending loads during operation, the stress state in the structure can be approximated by the normal (longitudinal) stresses generated by bending loads. In this context, the stress component S_{33} (along the spanwise direction) obtained in *Abaqus* was selected for evaluation because it corresponds to the same in-plane material direction as the loading direction used in the tensile tests performed according to ASTM D3039. Therefore, the ultimate tensile strength obtained experimentally can be used as a reference value for assessing the stress levels predicted by the numerical model for this longitudinal direction stress, a methodology that can be seen as an adaptation of the Rankine theory for brittle materials - a theory based on the maximum principal stress limit, being a suitable approach given the observed typical forged carbon failure type.

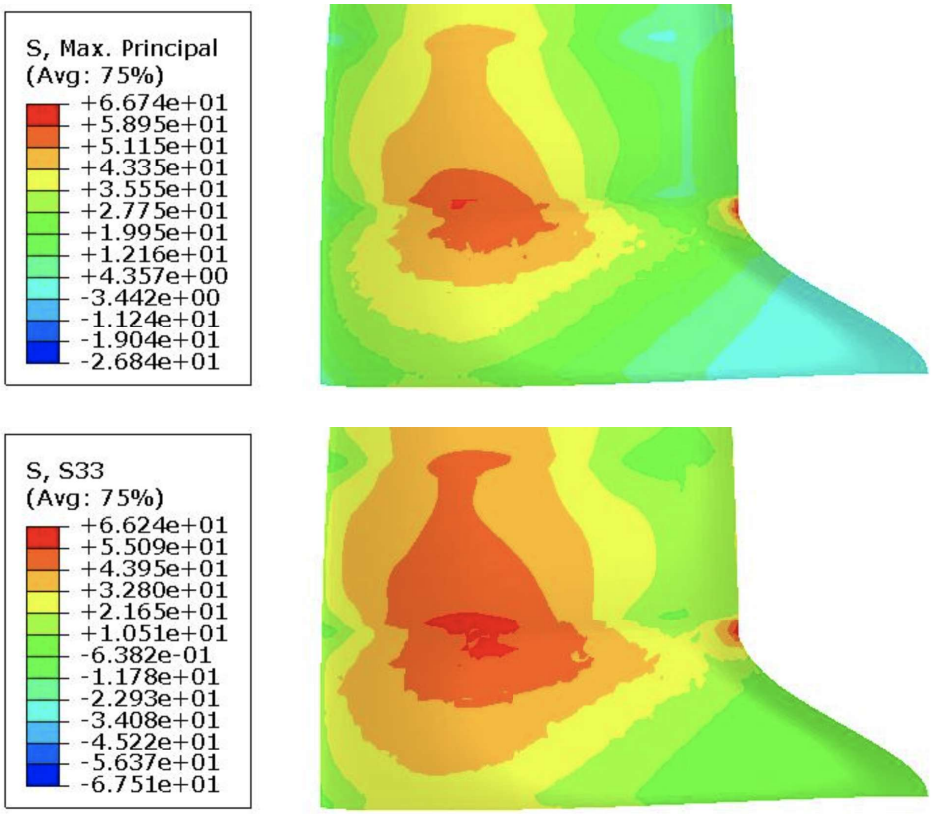


Figure 4.34: Similarity between the Principal and Longitudinal Stresses.

Although the hydrofoil behaves structurally as a bending element, the use of the ultimate tensile strength rather than a bending strength value is justified because bending in slender structures primarily produces normal tensile and compressive stresses in the longitudinal material direction and therefore, for example on the intrados of the wing, it is expected that the maximum principal stress value would be practically the same as the longitudinal stress component. Consequently, the comparison between the numerical S_{33} stress component and the experimentally measured tensile strength provides a reasonable first-order estimate of the structural safety of the hydrofoil.

This way, it was also possible to establish the margin of safety for the orthotropic approach, having used the same experimentally obtained allowables, having reached very similar results. It is still important to notice that this approach will represent a slight simplification of the analysis since the compressive phenomena will not be captured and this way, some of the previously considered failure modes may be neglected.

Table 4.17: Tensile safety margin evaluation for the hydrofoil under cruise and take-off conditions - Orthotropic approach.

Parameter	**Take-off conditions**	**Cruise conditions**
F_{tu} (MPa)	110.91	110.91
f_{vm} (MPa)	63.18	65.05
SM	0.75	0.70

Chapter 5

Life Cycle Analysis

In this chapter, the results from experimental testing are analyzed and the impacts from the different aspects related with the manufacturing of these components are quantified and compared with the most common alternatives and manufacturing solutions.

Heading toward a more sustainable maritime industry future, many efforts have focused on the determination of the most suitable parameters that quantify the impact and challenges in using high performance materials. Several studies in the literature such as the example of [85] or [86] have investigated these effects and the tendency is clear: when analyzed and compared with other materials regarding diverse parameters, composites are found to be preferable both in terms of global efficiency and environmental impact. However it is important to account for variations in these environmental impacts resulting from strategic choices in constituent types, manufacturing processes and disposal scenarios - specially for the case of of CFRP composites. This is a topic where the innovative manufacturing process described in this project is expected to bring significant advantages when compared with the classic technologies used for hydrofoil wing manufacturing.

The primary objective in this chapter is to address the environmental impacts of the hydrofoil wing manufacturing, quantify them and perform a comparative study using similar manufacturing process alternatives and variations.

A consistent and reliable balance between the level of environmental impacts and the most important variables given the application of the component was also performed in this chapter.

5.1 Methodology

5.1.1 Goal and scope definition

The objective of this LCA - Life Cycle Assessment (or Life Cycle Analysis for broader business or engineering contexts) is to evaluate and compare the environmental impacts associated with the forged carbon technology, performing a comparison with different manufacturing approaches for hydrofoil wings such as the construction using marine grade aluminum and the conventional carbon fiber reinforced polymer (CFRP) laminates - the cradle-to-gate analysis [87].

This analysis proved to be critical in these kinds of industry segments, not only given the framework of the Paris Agreements [88], where it is stated that industrial fields such as transport have to reduce their greenhouse emissions, but specially given the component's application in competitive prototypes where the sustainability of each component is precisely measured, evaluated and scrutinized [69], representing the ability to bring a clear prescriptive on the strengths and flaws of each component as well as highlighting the opportunities for improvement in high-performance applications. One of the most relevant advantages of the proposed method, is the possibility to easily modify the type of both matrix and reinforcements used, allowing for local optimizations or even the usage of recycled chopped carbon fibers or bioresins. This is possible while still achieving robust specific mechanical properties, and therefore allowing for a significant increase in the overall

efficiency of the vessel (by reducing the total required energy for each mission), at the same time reducing the environmental impacts that are associated with the typical CFRP materials - energy intensive thermal treatments (specially stabilization, carbonization and graphitization), storage (specially prepeg refrigeration), autoclave curing cycles, consumables (specially vacuum bagging), and material scrap generated during laminate cutting operations.

The standard ISO 14044 [89] will be followed during this analysis by using two types of data typologies: primary and secondary data. Primary data is experimental data and secondary data is evaluated via calculations, expert estimations and documentation on the literature.

Having performed such comparisons, the *use* phase of the hydrofoil is considered functionally equivalent for the three alternatives, since the geometry and hydrodynamic performance of the component remain unchanged regardless of the manufacturing material. Consequently, the operational stage is assumed to contribute equally to the environmental performance of each scenario and is therefore not considered as a differentiating factor in the comparison: Neither the end-of-life or the usage were considered on this LCA.

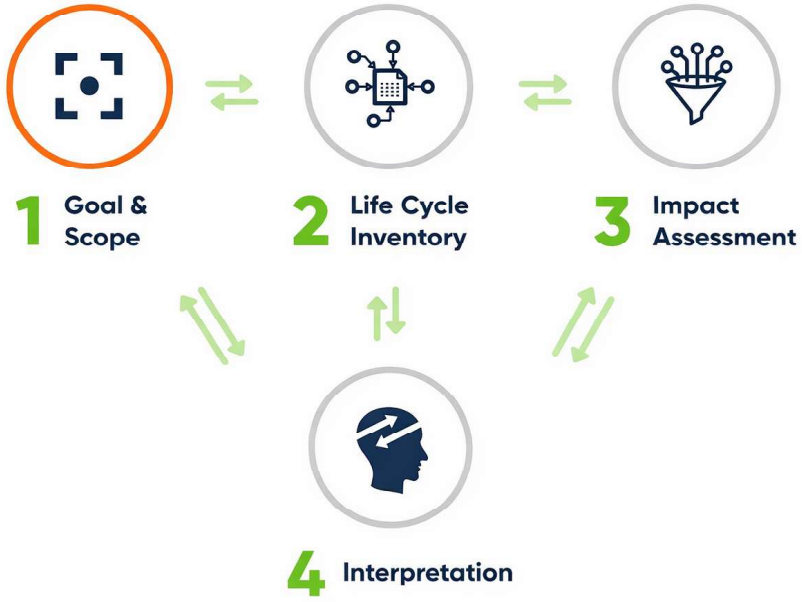


Figure 5.1: LCA structure and main phases.

5.1.2 Functional unit - Materials and methods

In order to ensure a meaningful comparison between the different manufacturing approaches considered in this study, a functional unit must be defined, representing the reference against which all environmental impacts are quantified and compared. For the purposes of this analysis, the functional unit is defined as the manufacturing of a a full set of Type-B hydrofoil wings (a total of three wings) using the forged carbon material, allowing for the estimation of the decrease on the mold when compared with producing only one wing. Four different manufacturing scenarios are considered for comparison:

- Forged carbon composite manufactured using chopped carbon fiber and epoxy resin through a compression molding process.

- Forged carbon composite manufactured using recycled chopped carbon fiber and epoxy resin through a compression molding process.
- Conventional hand lay-up CFRP laminate manufacturing using carbon fiber epoxy prepreg plies manually placed according to a stacking schedule. Assuming storage of the fiber rolls in sub-zero temperatures prior to lamination, where the resin remains in a partially cured state. In this process, plies are cut and placed by hand with the use of polypropylene film manufacturing templates on two single sided molds containing the top and bottom cavities of the hydrofoil geometry (machined in MDF). Epoxy resin is applied to tooled surfaces to seal the surface and remove small imperfections. During lamination, vacuum is applied with a 10 minutes period to ensure adequate packing of the plies and decrease void content. The low-temperature cure epoxy prepreg has a curing cycle of 12 hours at $80°C$ in an oven.
- Machined hydrofoil wing manufactured from marine grade aluminum alloy using subtractive machining processes and anodization of the final part.

For each scenario, the quantities of raw materials, manufacturing operations, and auxiliary consumables required to produce the final hydrofoil are estimated. For the scenario considering forged carbon, the values were mostly obtained from manufacturing records and data directly from FAST. For the other scenarios, these values are obtained using a combination of experimental measurements, technical specifications of the materials and mostly data available in the literature.

Although the structural performance of the component is governed by parameters such as stiffness, strength, and overall weight, these characteristics are treated as design constraints rather than impact indicators. The environmental assessment therefore focuses on quantifying the impacts associated with material production and manufacturing processes required to obtain a component capable of satisfying the design requirements identified in the previous chapters.

	Weight percentage		**Density**	**Young Modulus**	**Reference**
Material	**Fibers**	**Matrix**	$[kg/m^3]$	[GPa]	
Forged Carbon	29%	67%	1386	26.32	–
Aluminum	0%	100%	2700	69.00	[85]
Woven CF prepreg	54%	42%	1482	64.43	[90]

Table 5.1: Material properties and constituent weight percentages used for the hydrofoil manufacturing scenarios.

Property	**RC200T-SE84LV (HEC)**	**Units**
E_1	64.43	*GPa*
E_2	64.43	*GPa*
E_3	3.90	*GPa*
ν_{12}	0.0302	–
ν_{13}	0.301	–
ν_{23}	0.301	–
G_{12}	3.224	*GPa*
G_{13}	1.478	*GPa*
G_{23}	1.747	*GPa*

Table 5.2: Orthotropic woven ply equivalent mechanical properties adapted from [90].

5.1.3 System boundaries

For the three manufacturing scenarios considered in this study, the system boundaries include the extraction and processing of raw materials, the production of constituent materials, and the specific manufacturing operations required to produce each hydrofoil wing. For composite solutions, this includes the production of carbon fibers, the production of epoxy resin matrices, the preparation of reinforcement materials, and the respective molding or curing processes required to obtain the final laminate structure.

For the aluminum alternative, the analysis includes the production of marine grade aluminum alloy, the subtractive machining operations required to obtain the final hydrofoil geometry and finishing.

Assumptions and data quality

Several assumptions are introduced in order to simplify the analysis while maintaining a consistent comparison between the evaluated alternatives. The electricity consumption associated with manufacturing processes is assumed to follow the average European electricity mix. Material waste generated during manufacturing is estimated based on typical scrap rates reported in the literature for both composite lay-up and machining operations ([85] and [91]).

Based on the hypothesis and references where the inventory is based on, specific additional assumptions had been made:

- Some minor consumables and tooling manufacturing are excluded from the analysis due to their relatively small contribution when compared with the impacts associated with raw material production and primary manufacturing processes.
- Fiber/resin ratios on the Woven CF prepeg solution were manually estimated according to the references as well as some of the mechanical properties (using *ROM*).
- The molds used in composite material processes are assumed to be represented by the same quantities and effects (both in terms of materials and manufacturing statistics).
- For the mold sealing product (Mickon398), a generic petrochemical epoxy resin available in the MarineShift360 database was used for the estimate. This approximation was considered adequate for estimating the global warming potential, since the material is applied in a very thin layer and the difference in its contribution to the total impact is expected to be negligible.
- The aluminum anodizing treatment process stages were estimated according to similar processes presented on the bibliographic references [92].
- In the case of aluminum machining, the removed material is considered as recyclable aluminum scrap.

Although these simplifications introduce a degree of uncertainty in the results, they allow the analysis to focus on the dominant contributors to the environmental footprint of the hydrofoil wing manufacturing process.

5.1.4 Impact assessment and indicators

Global warming potential fossil (GWP) is expressed in kilograms of carbon dioxide equivalents ($kg\,CO_2$-eq) per functional unit. It represents the effect of the gradual increase in the overall temperature of the Earth's lower atmosphere, which is generally attributed to the greenhouse effect caused by increased levels of carbon dioxide (CO_2) and other contributing gases such as methane (CH_4), nitrogen dioxide (NO_2), and chlorofluorocarbons. This impact is measured in kilograms

of carbon dioxide equivalent, meaning that any gas emitted represents a different amount of CO_2 equivalent ($kg\,CO_2$-eq) depending on its impact, atmospheric effects, and duration [93].

Cumulative Energy Demand (CED) represents the total amount of primary energy required throughout the life cycle of a material or process. This indicator accounts for the energy consumed during raw material extraction, material processing, manufacturing operations, and associated auxiliary processes.The energy demand is typically expressed in megajoules (MJ) per functional unit. It includes contributions from both renewable and non-renewable energy sources, providing an estimate of the total energy intensity associated with the production of a material or component.

In order to determine these indicators in the most precise way possible, the MarineShift360 software (Explorer version) was be used. MarineShift360 is a LCA platform specifically developed for the maritime sector, providing integrated environmental modeling tools for vessels, materials, and maritime technologies. As stated before, this software incorporates established life cycle inventory databases and predefined maritime process models, allowing for an easy and direct estimate of the environmental impacts associated with materials, manufacturing processes, energy consumption, and operational scenarios.

By combining background environmental datasets with simplified modeling interfaces, MarineShift360 enables a rapid yet reliable estimation of key environmental indicators such as global warming potential and cumulative energy demand. Despite the need to get part of the inventory from the literature, this approach significantly reduces the complexity typically associated with building the complete LCA inventory from scratch while maintaining consistency with internationally recognized LCA methodologies.

5.2 Life Cycle Inventory (LCI)

5.2.1 Bill of materials and process

Table 5.3: Bill of materials for the hydrofoil alternatives.

Item	FC (kg)	CFRP prepreg (kg)	Aluminum (kg)
Chopped CF tow	0.58	–	–
RC200T Woven Twill (CF prepeg)	–	1.25	–
IN2 Epoxy resin	1.06	–	–
Hardner (AT30 Slow)	0.32	–	–
Release wax	0.01	0.01	–
MDF (mold)	33.00	33.00	–
Sealant Mickon398	0.90	0.90	–
Laser cut PMMA	–	1.00	–
Aluminum alloy (block)	–	–	15.00
Total mass (component)	0.985	1.059	1.925

Considering the effect of the complete bill of materials in each of the aforementioned methods, the system boundary workflow during manufacturing can now be established for each of the processes.

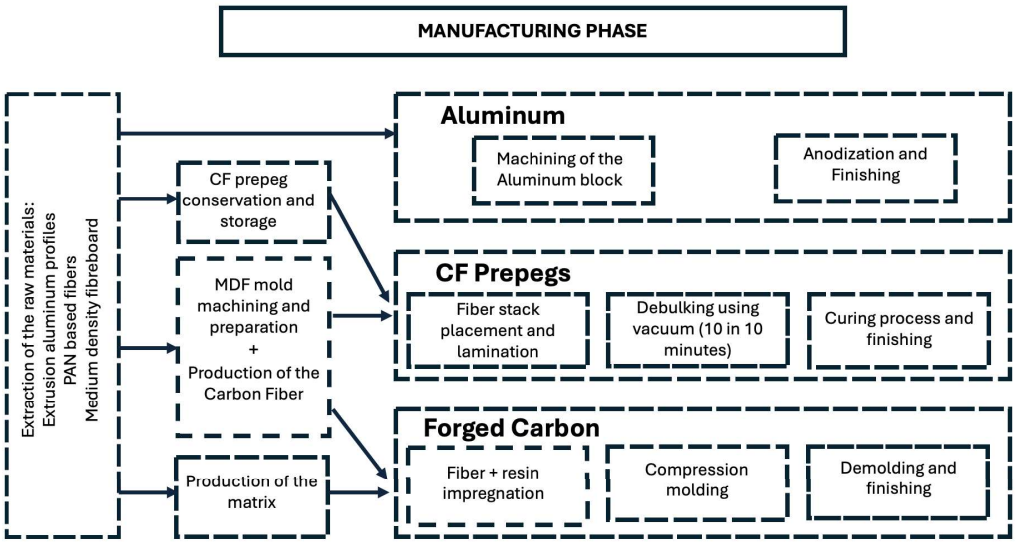


Figure 5.2: System boundaries considered for this study (manufacturing phase only).

Raw material production

Regarding the raw material production, Marineshift360 database is able to quantify the its effect for all cases just by imputing basic information, amounts, type of processes and waste estimates. The main segments of this phase are presented bellow for each of the models:

- For the case of aluminum machining, it was assumed that the block would be obtained by extrusion. Standard MarineShift360 downstream transportation was used.

- On the CF prepeg case, the standard modulus CF was considered to be the most suitable and a regular epoxy resin information was used.

- For the forged carbon process, two models were created for the fiber inventory, one being unspecified modulus and the other a fully recycled carbon fiber, expected to have around 2.0 MJ/kg process energy consumption (based on [85]). A regular epoxy resin database was also used.

These last two processes using composite materials also include the MDF wood resource production as well as an epoxy petrol-based resin, introduced as an approximation to the GWP of the sealant. For most of these parameters, the total contribution was compared with specific references, case studies or other inventories in order to guarantee their compliance. This was achieved by searching and comparison with inventory as the example of Figure 5.3.

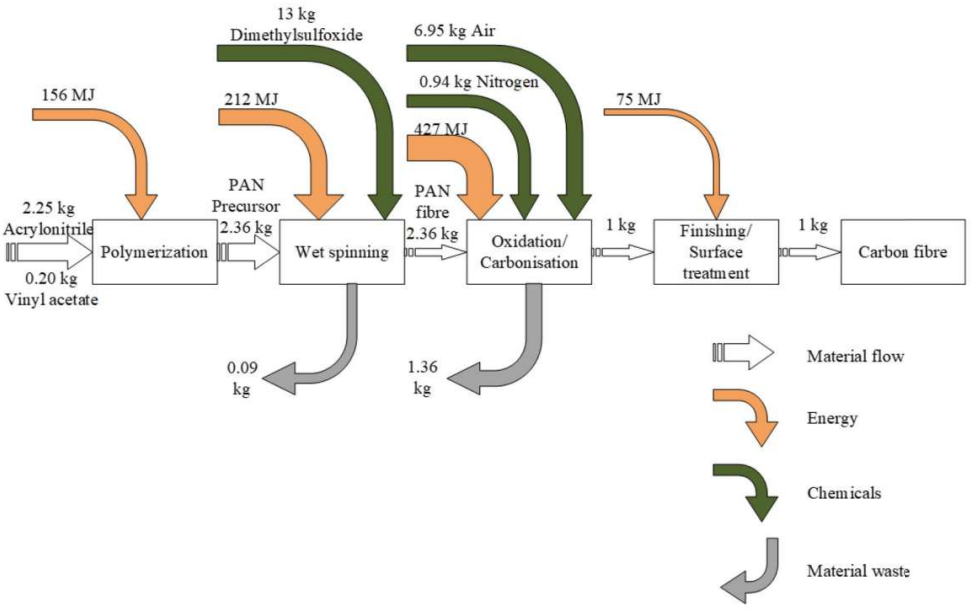


Figure 5.3: Production process of 1kg carbon fiber from PAN fibers (adapted from [85]).

Specific details on the inventory (references, databases and data accuracy) can be found on the Appendix D with the *Inventory Explanation Report*.

Manufacturing phase inventory

The manufacturing phase inventory includes all processes required for the production of the foil components using both composite and metallic manufacturing routes. The energy consumption and environmental impacts associated with the different processes were also estimated using data from the MarineShift360 LCA databases, considering typical industrial operations and confirming the main values with relevant information from the literature.

For the both composite material components, the manufacturing process begins with the machining of a mold made from medium-density fiberboard (MDF). After machining, the mold undergoes preparation which includes surface sealing and the application of release agents to prevent adhesion of the composite material during curing.

Additionally, the forged carbon process involves the placement of carbon fiber and resin mixture on the mold and even tough the compression of the mold does not require energy, the finishing operations after demold were considered to have a energy consumption proportional to the average number of workers and man hours needed to perform the process. On the other hand, the CF prepreg process involves the storage of prepegs at sub-zero temperatures and performing the lamination with successive debulking (to ensure proper compaction during curing). The curing stage is performed under controlled temperature conditions for a total of 12 hours, allowing the epoxy matrix to polymerize and achieve the final mechanical properties of the composite part. After curing, several finishing operations are required, for which the total consumable weight and the total energy were also estimated based on the total man hours time.

The aluminum alternative was slightly different, where the manufacturing process primarily consisted of subtractive machining operations starting from a raw aluminum billet. CNC machining is used to obtain the final geometry of the wing. After machining, the aluminum component undergoes an anodization treatment, which improves corrosion resistance and enhances surface durability.

5.3 Life Cycle Impact Assessment

5.3.1 Results

In Figures 5.4 and 5.5 it is possible to find the relative contributions of the different methods considering the predefined parameters of Global warming potential fossil (GWP) and Cumulative Energy Demand (CED).

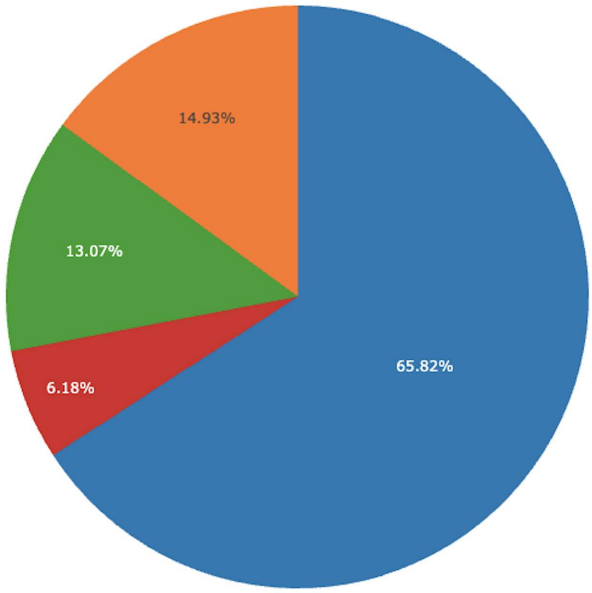


Figure 5.4: Relative Global warming potential fossil (GWP). Three aluminum wings (in blue); Three CF Prepeg wings (in orange); Three FC wings (in green); Three FC re-use wings (in red).

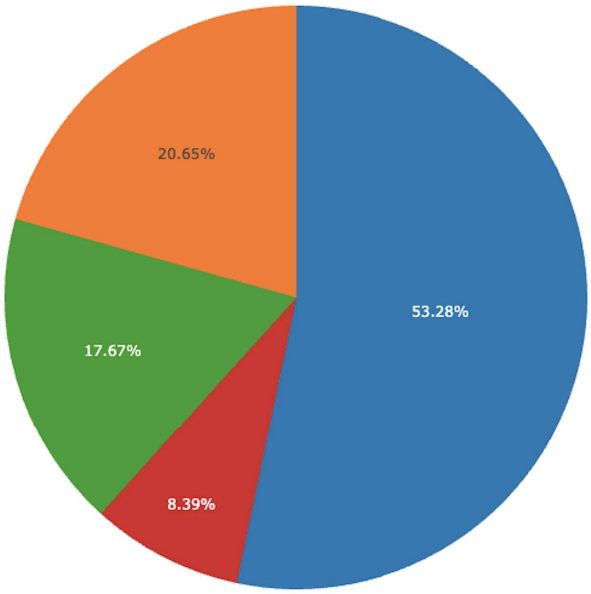


Figure 5.5: Relative Cumulative Energy Demand (CED). Three aluminum wings (in blue); Three CF Prepeg wings (in orange); Three FC wings (in green); Three FC re-use wings (in red).

As it is possible to see, the machining of the three hydrofoil wings in aluminum leads to the higher GWP and CED values followed by the CF Prepeg method, that presents practically the same impact as the Forged Carbon Composite. As referred in the begging of this project, one of the main advantages of the Forged Carbon method is the possibility to integrate different kinds of matrices and reinforcements, therefore, as it is possible to see, the hypothetical situation where using 100% recycled reinforcement fibers appears as a significantly less harmful alternative.

The main reasons for the discrepancy of results of the aluminum alternative (even considering 30% recycled aluminum) are related with the exhaustive machining process that is required for each of the three components. As the number of manufactured components increases, the impact of the MDF mold production is attenuated to the point that machining in aluminum can have a 10 times higher GWP (or even more, depending on the MDF mold production and treatment quality).

For this reason, allied to the fact that an aluminum would also require an anodization process, for whom the downstream transportation has not been accounted for, the aluminum alternative is at a much lower level in comparison with these composite alternatives both in terms of environmental impact but also man power - also revealing to be one of the most expensive alternatives.

Focusing on the two alternatives for CFRP manufacturing, the forged carbon method is in any case the solution that brings the least environmental impact even after considering the usage of non-recycled CF reinforcements. After an analysis on the MarineShift360 results, it was concluded that despite the material amounts being relatively similar, this phenomenon happens mostly due to two reasons: The first and most significant, is the *part prepeg cure* high electricity demand (more then 85 KWh) due to the extensive 12 hour autoclave curing process. The second, being the successive vacuum pulling process (debulking), having a much less pronounced energy requirement, however is responsible for a significant increase in the auxiliary (and wasted) material weight, inevitability leading to the increase in the GWP.

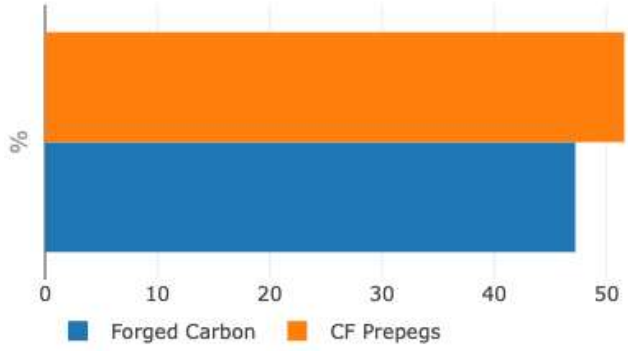


Figure 5.6: Waste factor discrepancy for FC (in blue) and CF Prepeg (in orange).

Finally, it is known that there are many important parameters to consider alongside the environmental impact when analyzing high-performance components such as this hydrofoil wing. Given that this project focused on the mechanical behavior of this component when manufactured using forged carbon composite material, a basic comparison considering the main aspects that characterize this response can be revealing when comparing the alternatives. For this reason, stiffness, strength and cost are characterized for each of the alternative manufacturing processes submitted for comparison in this LCA. For this analysis (numerical models), the properties detailed in Tables 5.1 and 5.2 will be used.

Strength

Strength is mostly governed by the intrinsic mechanical limits of each material, are therefore, the margin of safety given the maximum stresses along the spanwise direction obtained along with the respective allowables found on the literature will be used as an indicator.

Table 5.4: Margin of Safety for the different materials.

Material	$\mathbf{F_{tu}}$ [MPa]	$\mathbf{f_{vm}}$ [MPa]	**SM**
Forged Carbon	110.91	65.05	0.70
Aluminum	221.05 [94]	65.05	2.39
Woven CFRP Prepreg	550.00 [95]	65.05	7.45

The results show the expected hierarchy of the SM, with forged carbon being on the bottom for having the lowest Margin of Safety of all the different approaches, showing its vulnerability to unexpected tides, waves or any load case that largely exceeds the regular load distribution along the wing. Since the SM values are computed by taking a safety coefficient in order to compensate for these factors, it is possible to say that despite the aluminum and CF prepeg materials being a safe and robust choice to guarantee structural integrity, for the case of forged carbon, since this work is considering exclusively the experimentally obtained data, this can not yet be totally ensured.

Stiffness

Regarding stiffness, the one of the possible quantification parameters is the maximum displacement (measured at the wingtip). This parameter allows for the quantification of the ability of the wing to resist deformation. Studies such as [76] or [90] have already addressed the negative influence geometry deformation in hydrofoil wings and their negative effects on the pressure distribution around the wing and therefore in its overall performance as well as load distribution.

Table 5.5: Maximum displacement and relative difference for each model.

Material	$\mathbf{U_{max}}$ [mm]	**Relative error [%]**
Forged Carbon	15.12	–
Aluminum	5.78	61.78
Woven CFRP Prepreg	7.11	52.98

As it is possible to see, for this model, forged carbon has more then double the displacement value at the wing tip when compared with aluminum for example. To be able to take any concrete conclusions regarding the hydrodynamic validity of the deformed wing, further studies regarding the load redistribution would have to be performed. However, it is possible to see that similarly to the strength behavior, both aluminum and CF prepeg solution show a much more reliable response to the considered loading scenarios.

Cost

Regarding cost, it is possible to perform an estimate based on two main factors: material and production price. The material price can be estimated using the total components mass and dimensions in order to allocate for each case a budget that is consistent with the average commercially available solutions. For the case of aluminum, in order to achieve the final part in solid marine grade aluminum weighting a total of 1.92 kg (for one hydrofoil wing), an initial rectangular block of around 15 kg is estimated to be the ideal size regarding the machining operations (values taken

from [96] where price per block with transportation costs included is around 460 €). The CF prepeg solution encompasses a more extensive bill of materials: The RC200T woven twill prepeg can be found in [97] at around 60 €per m^2 (estimated total of 532.5 €), the MDF wood required for the mold (around 100 €), the 0.9 kg of sealant around 96.5 €and assuming that the release wax and acrylic price is negligible for this case, the total material price is around 728.5 €. For the Forged Carbon approach, the costs regarding the mold are assumed to be the same, and the assumptions regarding consumables were also kept. The chopped carbon fiber is available at [19] being labeled at 40 €per kg and the IN2 epoxy resin + harder is at 25 €per kg. The total material price for this case is around 375 €.

The production costs (neglecting man hours) will be mostly dependent on the total energy and type of processes involved. For the aluminum the machining and anodization, energy costs gather a total of 60 KWh (around 10 €in local low voltage energy market) and regarding consumables a total of 40 kg of waste material was estimated at MarineShift360 with a total cost of 240 €. The Woven CF prepeg material showed a similar behavior with a total energy cost of due to machining processes and vacuum + curing prepeg of around 14 €and a smaller waste estimated to be around 25 kg reflected on a 170 €total cost. Finally, the forged carbon method presented much lower values for production costs given that it does not require energy during curing (either from heat or vacuum) having a total energy demand of 20 KWh (less then 3 €) and a total waste of 22 kg during production, that reflected on 125 €.

	Material Costs [€]	**Production costs [€]**	**Total cost per part [€]**
Forged Carbon	375.00	125.00	166.67
Aluminum	1380.00	240.00	540.00
Woven CR Prepreg	728.50	170.00	299.50

Table 5.6: Cost comparison between different manufacturing materials.

The cost issue for the composite materials has a similar dynamic to the one described for the GWM or CED - as the number of produced components increases for the same mold, the initial cost is returned in comparison with the constant cost per part of the machined aluminum solution.

5.3.2 Discussion and limitations

The results of the present cradle-to-gate assessment indicate that the forged carbon approach is a competitive solution for hydrofoil wing manufacturing when compared with conventional CF prepreg processing and especially with the more basic machined aluminum alternative. In terms of environmental performance, the aluminum scenario showed the highest values of both global warming potential and cumulative energy demand, whereas the forged carbon solution presented the lowest impact among the non-recycled composite cases and an even more favorable profile when recycled carbon fiber is considered. This behavior is consistent with the inventory defined in this chapter, since the aluminum route is strongly penalized by the large amount of removed material, the required energy during machining operations, and the additional anodization treatment. In contrast, the forged carbon process benefits from a reduced number of manufacturing stages, the absence of refrigerated storage, and the elimination of long thermal curing cycles and repeated vacuum debulking operations that characterize the prepreg route. These tendencies are directly supported by the LCA inventory, the impact comparison, and the waste-factor discrepancy presented in the chapter.

From a manufacturing perspective, the comparison between forged carbon and CF prepreg is particularly relevant, since both routes aim to produce lightweight composite hydrofoils - around 70% lighter then the solution in solid aluminum. Although the total mass of the final components are relatively close, the prepreg alternative requires additional energy and auxiliary consumables

associated with ply cutting, refrigerated storage, repeated debulking, and the 12-hour oven curing cycle. These process requirements explain why the prepreg solution exhibits higher environmental burdens than forged carbon, despite its superior structural performance. The results therefore suggest that, for applications where manufacturing simplicity, reduced waste generation, and lower environmental impact are prioritized, forged carbon may constitute a promising alternative to conventional laminate-based CFRP technologies.

The comparison of margin of safety and maximum displacement showed that forged carbon remains the least favorable solution from a structural standpoint among the three materials considered. In the present study, it exhibited the lowest margin of safety and the highest wingtip displacement, indicating reduced stiffness and strength when compared with aluminum and woven CFRP prepreg. Consequently, the selection of the most adequate material cannot be based exclusively on LCA indicators, but rather on a compromise between environmental performance, manufacturing feasibility, structural response, among other factors.

Cost analysis actually reinforced this trade-off. Forged carbon was estimated to have the lowest cost per part, followed by prepreg CFRP, while the aluminum solution was clearly the most expensive. This difference is largely explained by the high raw material requirement and machining waste of the aluminum solution, as well as by the additional surface treatment. For composite solutions, the reuse of the same mold across several parts tends to dilute tooling related impacts and considering a regular MDF mold, it has already been proved to be possible to at least double the three hydrofoil wing set manufacturing. All these characteristics make forged carbon an increasingly attractive material for small to medium scale production of high-performance components.

Limitations

Despite these relevant findings, the present analysis is subject to important limitations that should be acknowledged. First, the study is restricted to a cradle-to-gate perspective, therefore, the use phase and end-of-life stages were excluded from the comparison - where the mechanical properties of the component are expected to have a significant impact on the results. This is mostly because although the use phase was assumed to be functionally equivalent for the three alternatives, this assumption may not be fully valid if the different stiffness and strength levels lead to distinct hydrodynamic efficiencies, deformation patterns, maintenance requirements, or service lives.

Likewise, excluding end-of-life prevents the assessment of possible benefits associated with recyclability, reuse, or disposal burdens, which are particularly relevant when comparing aluminum and composite materials. As referred by several studies [98–100], end-of-life management plays an important role in the environmental performance. In particular, aluminum benefits from well-established recycling systems with high recovery rates and significantly lower energy requirements compared to primary production, while carbon fiber composites still face important technological and economic challenges related to fiber recovery and reuse in order to compensate for the energy intensity of carbon fiber production. Consequently, the exclusion of the end-of-life phase in the present cradle-to-gate assessment may influence the relative environmental performance of the analyzed alternatives.

Table IV. Environmental impacts of different types of composites under different end-of-life scenarios.

	Landfill		Recycling		Incineration with energy recovery	
	CED (MJ/kg)	GHG (kg of CO_2e/kg)	CED (MJ/kg)	GHG (kg of CO_2e/kg)	CED (MJ/kg)	GHG (kg of CO_2e/kg)
SMC	NA	NA	7[86]	0.4[86]	–7.5[87]	0.9[87]
GMT	0.09[34,55]	0–0.02[34,55]	11[86]	0.9[86]	–25.2[87]	1.9[87]
CFRP	0.11[55]	0.02[55]	10–15[34,41]	NA	–31.7 to –34[87,88]	3.2–3.4[87,88]
NFRP	NA	NA	NA	NA	–12 to –34[32,37,39,87]	2.3–2.9[37,87]
Steel	NA	NA	11.7–19.2[89]	0.5–1.2[89]	NA	NA
Aluminum	NA	NA	2.4–5.0[90]	0.3–0.6[90]	NA	NA

Figure 5.7: Envionmental impact of composites under end-of-life scenarios (adapted from [98]). GMT, (Glass-Mat-Reinforced Thermoplastics); NFRP (Natural Fiber Reinforced Plastics).

Second, part of the life cycle inventory was based on secondary data, literature values, engineering estimates, and adapted datasets from MarineShift360 platform, which combines internally developed datasets with background data from databases such as *EcoInvent* 3.11. Several composite manufacturing processes, including hand laminating and prepreg autoclave curing, are represented in MarineShift360 using algorithm-based inventories derived from marine composite industry best practices rather than real specific measurements. These algorithms estimate consumables usage, transport distances for upstream materials, and electricity consumption associated with manufacturing operations. In addition, some energy-intensive process steps, such as laminate post-curing or autoclave curing electricity consumption, are not explicitly included in the datasets used for the modeling. Consequently, the environmental impacts associated with these stages may be underestimated. Despite this, the same databases, modeling assumptions, and system boundaries were applied consistently across all material scenarios analyzed in this study. Therefore, while the absolute environmental impact values have relative accuracy, the comparative results between the aluminum, prepreg CFRP, and forged carbon alternatives remain meaningful for identifying relative trends in environmental performance and for supporting early-stage design decisions.

Third, the mechanical comparison is very simplified. Although these indicators are useful for an initial comparison, they do not fully capture other relevant aspects such as fatigue resistance, damage tolerance, manufacturing defects, among others. This would be especially important for forged carbon, whose structural behavior is strongly influenced by fiber orientation, void content, local resin-rich zones, and manufacturing variability as seen throughout this work. Therefore, the lower safety margin observed for forged carbon should not be interpreted as a definitive limitation of the material itself, but rather as an indication that further characterization is still necessary.

Finally, the hypothetical scenario with recycled carbon fiber demonstrates the significant environmental potential of the forged carbon concept, but its results should be interpreted considering several nuances. The actual performance of recycled reinforcements depends on fiber quality, length distribution, contamination, interfacial adhesion, and process induced damage, all of which may influence both the structural response and the true environmental balance [100]. A sensitivity analysis should be included, considering the most influential inventory parameters, experimental validation of the recycled fiber route, and an expansion of the system boundaries to a full life cycle perspective, since that despite being unlikely, it is possible these modifications in the mechanical properties could jeopardize the viability of the process. Only through this combined environmental and mechanical assessment will it be possible to determine the definite applicability of recycled forged carbon as a sustainable alternative for high-performance hydrofoil structures.

Chapter 6

Conclusions

The viability of an innovative manufacturing process based on forged carbon for the production of a high-performance hydrofoil wing was investigated throughout this work. Following an introduction to the topic, a review of the most common manufacturing methods, relevant standards, and microstructural analysis and measurement techniques was conducted. In addition, the fundamental hydrodynamic theory relevant to hydrofoil operative conditions was presented. The complete laboratory methodology and the iterative mold design process were described in detail in order to contextualize the experimental results obtained from both the microstructural analysis and the mechanical testing. The standards ASTM D792-00 and ASTM D3039, together with several adaptations required for the specific characteristics of the material, were successfully implemented. In the numerical simulation phase, both configurations of the tensile tests were modeled in order to perform a comparative analysis and estimate the degree of orthotropy of the forged carbon material. Hydrodynamic loads were also determined numerically using the *XFLR5* software, complemented by a *Matlab* script used to compute the corresponding load components for specific regions along the wingspan. Finally, several load cases were simulated using a dedicated half-wing numerical model, adopted to reduce computational cost, and a complete stress analysis of the structure was performed. A Life Cycle Assessment (LCA) was also conducted to evaluate and compare the environmental impacts associated with this manufacturing technology relative to other approaches commonly used for hydrofoil wings, focusing specifically on a cradle-to-gate analysis.

6.1 Achievements

A dedicated manufacturing methodology was developed in order to produce forged carbon specimens and structural components representative of the intended hydrofoil geometry. The manufacturing process was progressively refined through several iterations of mold design and fiber impregnation strategies, enabling improved control over fiber distribution and material consolidation. These developments were essential to ensure that the experimental specimens were representative of the final structural component.

The mechanical behavior of the forged carbon composite was experimentally characterized through tensile testing following ASTM standards, complemented by Digital Image Correlation (DIC) measurements. In addition, microstructural analysis using optical microscopy and X-ray micro-computed tomography provided valuable insight into the internal morphology of the material, allowing the identification and classification of voids, fiber misalignment, and other microstructural features that influence mechanical performance. It is important to notice that the segmentation was mostly performed using automated methods on both scans, having a limited manual segmentation work. Therefore, in order to achieve more refined results for the VVF values, a more detailed segmentation and possibly new scans would have to be performed given the high variability of voids sizes, locations, shapes and intensity.

The experimental results enabled the estimation of representative mechanical properties for the forged carbon material, which were subsequently implemented in numerical simulations. For the simulations, the 2D in-plane orthotropy was neglected given the relatively high standard deviation of the obtained results and since that, despite its high sensitivity, the value predicted by the *Matlab* script approximations was very close to total isotropic behavior. For this reason, the results presented on this thesis consider only two material approaches: a fully isotropic and 2D orthotropic material (having the matrix mechanical properties along the thickness direction). This isotropic approach was kept since the behavior of forged carbon in thick laminates is expected to present a less pronounced effect of this orthotropy.

Finite Element Method models were developed to validate the mechanical behavior observed during experimental testing and to evaluate the structural response of the hydrofoil wing under representative hydrodynamic loading conditions. These loads were estimated using aerodynamic panel methods implemented in XFLR5. The numerical analysis showed that the proposed forged carbon structure is capable of withstanding the expected loading conditions for both cruise and take-off scenarios with acceptable safety margins. However, it is important to notice that these simulations account for distributed loads along the wingspan that on the real model may not be so well distributed if unsteady flow (waves, maneuvering, rapid pitch changes) occur. Their effect is expected to significant lower the SM values specially on the critical areas if structural discontinuities are present. For this work, the contribution of the safety coefficient of 1.5 was considered to be sufficient for accounting these situations.

As stated before, the experimental testing proved to be much more complex then expected: Both the manufacturing process and the test procedures were incredibly difficult to perform according to the standards recommendations given the low geometric tolerancing ensured by the 3D printed mold technology and surface finishing. Additionally, as it was seen on the Micro-CT scan, the extremely high void percentage caused all the specimens with a 5 mm circular hole to fail outside of the hole meaning that, for a 50 mm^3 cross section, the void clusters "compete" with the 5 mm hole. This allied with the non-uniform strain fields obtained on the DIC (mostly due to the random fiber orientation) and the difficulty of the mold design given the standards, led to the decision of restricting the experimental testing to tensile tests (neglecting higher complexity tests such as for determining compression or shear).

During the stress analysis, despite the fact that many of the failure modes (specially fiber breakage) are mostly caused by tensile stress concentrations, a the study of both compression and shear for the several load cases would be relevant, however this study focused only on the tensile stresses. This was mostly due to the fact that no experimental data on compressive and shear properties was measured and in order to keep a consistent framework during the project, this was not taken into consideration for stress analysis. Regarding the tensile stresses, given that the wing is subjected to a bending dominated loading, the Von Mises stress was the parameter used for SM calculation on the isotropic models the S_{33} (stress along the spanwise direction) was assumed to be the best indicator of the orthotropic models (given that neither the Von Mises or the principal stresses would be a suitable option).

In parallel, a Life Cycle Assessment (LCA) was conducted in order to evaluate the environmental implications of the proposed manufacturing process and to compare it with alternative materials and manufacturing approaches. The results suggest that forged carbon composites may offer advantages in terms of manufacturing efficiency and material utilization, although the environmental impact remains influenced by the production of carbon fibers and resin systems.

Overall, the results obtained in this work indicate that forged carbon composites constitute a promising alternative for the manufacturing of hydrofoil wings, particularly in applications where complex geometries, reduced manufacturing time, and low production costs are required. Nevertheless, several limitations remain, particularly regarding the variability of the mechanical properties inherent to discontinuous fiber composites and the need for more extensive experimental characterization.

Despite these limitations, the proposed methodology demonstrates that forged carbon manufacturing techniques can be successfully adapted for maritime design and may represent a viable solution for the production of lightweight structural components in zero-emission vessels. Further developments in process control, material characterization, and structural validation are expected to improve the reliability and performance of this technology in future applications.

6.2 Future Work

As this project encompasses multiple aspects of forged carbon composite production, the findings of the present study open several avenues for future work and further investigation. These may be broadly divided into four main categories:

- **Mechanical characterization** - Despite the increased complexity, significant benefits could be obtained by manufacturing specimens that can be tested along the mold compression direction. In addition, performing micro-computed tomography on the complete hydrofoil wing structure would provide a clearer understanding of the void distribution and characteristics. This analysis could also help determine whether, rather than being strictly orthogonally orthotropic, the material tends to align its mechanical properties along the direction normal to the wing surface.

- **Manufacturing and design -** Iterative geometry modifications should be performed to mitigate the low safety factor (SF) concentrations observed near the trailing edge, as well as to compensate for stiffness limitations that may influence hydrodynamic performance.

- **Experimental testing** - Testing the hydrofoil wing in a real operating environment would allow a more accurate assessment of its structural and hydrodynamic behavior. To support this, additional compression and shear tests should be performed. Furthermore, improvements to the experimental procedures used for stress concentration testing around circular holes could be implemented.

- **Life Cycle Assessment (LCA) -** LCA studies can always be refined and expanded. As stated at the beginning of the previous chapter, the analysis presented in this work considers a limited number of parameters, and several inventory values were estimated based on similar case studies and literature references. Real field measurements and the evaluation of additional databases would improve the accuracy of the results. In particular, it would be important to quantify the effect of increasing the total number of parts manufactured per mold and to compare the results with alternative manufacturing processes.

Due to time constraints, the load distribution was estimated using simple open source tools, which may present limited accuracy in certain cases. More complex phenomena, such as ventilation, unsteady hydrodynamics, and foil-strut interaction, also influence the load distribution and should be investigated using more refined CFD simulations.

Finally, given the limited material availability and resources during this project, it was only possible to test materials obtained from a single supplier. A broader study could therefore be conducted, taking advantage of the versatility of the forged composite manufacturing method to evaluate alternative material solutions. Different types of reinforcements (such as natural fibers), more sustainable matrices (such as bio-resins), or lower-cost resin systems (such as polyester) could be explored.

Bibliography

[1] Gibbs and Cox, Inc. and Bath Iron Works Corp. *Hydrofoil Handbook: Volume 1, Design of Hydrofoil Craft*. Tech. rep. Hydrofoil Research Project; Contract No. NONR-507(00). New York, NY: Office of Naval Research, Navy Department, 1954.

[2] John W. Muir. *Ships That Fly...: A Story of the Modern Hydrofoil*. Hydrofoil Technology, Inc., 1998. URL: http://foils.org/wp-content/uploads/2018/07/ShipsThatFly.PDF.

[3] Kevin John et al. "New composite structural member for high dynamic machinery applications using cold forging-based manufacturing method". In: *Mechanics Based Design of Structures and Machines* (2025). DOI: 10.1080/15376494.2025.2491137.

[4] Steven Wusterbarth and Koichi Akiyama. *Forged Molding Compound: High Performance Chopped Carbon Fiber Composites*. Mitsubishi Chemical America and Gemini Composites LLC. Mitsubishi Chemical. 2021.

[5] Paolo Feraboli et al. "Lamborghini "Forged Composite" Technology". In: *Proceedings of the 27th International Congress of the Aeronautical Sciences (ICAS)*. Nice, France: ICAS, 2010.

[6] James C. Jr. Haller, Jacob C. Clark, and James T. Gayton. "Mechanical Performance of Pultruded and Compression-Molded CFRTP Laminates: A Comparative Study". In: *Journal of Composites Science* (2025). DOI: 10.3390/jcs9010001.

[7] Zeyu Sun et al. "Preparation of High-Performance Carbon Fiber-Reinforced Epoxy Composites by Compression Resin Transfer Molding". In: *Materials* 11.12 (2018), p. 2570. DOI: 10.3390/ma11122570.

[8] J. L. Thomason. "The influence of fibre length and concentration on the properties of glass fibre reinforced polypropylene. 6. The properties of injection moulded long fibre PP at high fibre content". In: *Composites Part A: Applied Science and Manufacturing* 36.8 (2005), pp. 995–1003. DOI: 10.1016/j.compositesa.2004.11.002.

[9] Lucas F. M. Silva, F. J. L. Alves, and A. T. Marques. *Materiais de Construção*. Porto: Publindústria, 2013.

[10] Alexios Argyropoulos. "Process development of pre-impregnated hybrid thin-ply composites". PhD thesis. Lausanne, Switzerland: École Polytechnique Fédérale de Lausanne (EPFL), Dec. 2023.

[11] Christophe Baley et al. "Sustainable polymer composite marine structures: Developments and challenges". In: *Progress in Materials Science* 145 (2024), p. 101307. DOI: 10.1016/j.pmatsci.2024.101307.

[12] Leigh Stuart Sutherland. "A review of impact testing on marine composite materials: Part 1 Marine impacts on marine composites". In: *Composite Structures* 118 (Mar. 2018). Article in Composite Structures, pp. 197–208. DOI: 10.1016/j.compstruct.2017.12.073.

[13] Nils Lundqvist and Elias L. Farum. "Hydro-dynamic design, system design and control system for a model-scale foiling boat". Joint project with SSRS and SSPA. MA thesis. Gothenburg, Sweden: Chalmers University of Technology, Department of Mechanics and Maritime Sciences, 2022.

[14] Hugh R. Dougherty. “The Design, Verification, and Validation of a Personal Hydrofoil Craft”. Submitted to the Faculty of the Virginia Polytechnic Institute and State University. MA thesis. Blacksburg, Virginia: Virginia Polytechnic Institute and State University, Dec. 2021.

[15] Gurit. *Guide to Composites*. GTC-6-0417. Technical guide. Available at: https://www.gurit.com/wp-content/uploads/2022/12/guide-to-composites-1.pdf. Gurit. 2017.

[16] Andrzej Kubit et al. “Analysis of the Influence of Manufacturing Technology on Selected Static, Fatigue and Morphological Properties of CFRP Composites”. In: *Materials* 17.23 (2024), p. 7502. DOI: 10.3390/ma17237502.

[17] O. A. Ekuase et al. “A review on the out-of-autoclave process for composite manufacturing”. In: *Journal of Composites Science* 6.6 (2022). Available at: https://www.mdpi.com/2504-477X/6/6/172, p. 172. DOI: 10.3390/jcs6060172.

[18] Serpil Edebali. “Biopolymers”. In: *Methods of Engineering for Biopolymers and Biocomposites* 15 (2025). Chemical Engineering Department, Konya Technical University, Konya, Turkey.

[19] Easy Composites Ltd. *Make Forged Carbon Fibre Parts Using Compression Moulding*. YouTube video. Published Dec. 9, 2021. Accessed: June 2025. Available at: https://www.youtube.com/watch?v=25PmqM24HEk. 2021.

[20] B. van Voorn et al. “Natural fibre reinforced sheet moulding compound”. In: *Composites Part A: Applied Science and Manufacturing* 32.9 (2001), pp. 1271–1279. DOI: 10.1016/S1359-835X(01)00004-4.

[21] Christopher Oberste. *Investigating the Relationship between Fiber Length, Volume Fraction, and Mechanical Properties of Fiber-Reinforced Plastics*. Tech. rep. Technical White Paper. WEAV3D Inc., 2019.

[22] J. L. Thomason. “The influence of fibre length and concentration on the properties of glass fibre reinforced polypropylene: 5. Injection moulded long and short fibre PP”. In: *Composites Part A: Applied Science and Manufacturing* 33 (2002), pp. 1641–1652.

[23] *A Practical Guide to Composites*. 1st. UK: Multi-Sport Composites Ltd, 1995. ISBN: 1900213001.

[24] Isaac M. Daniel and Ori Ishai. *Engineering Mechanics of Composite Materials*. 2nd. New York and Oxford: Oxford University Press, 2006.

[25] Zhangxing Chen et al. “Failure of chopped carbon fiber Sheet Molding Compound (SMC) composites under uniaxial tensile loading: Computational prediction and experimental analysis”. In: *Composites Part A: Applied Science and Manufacturing* 118 (2019), pp. 117–130. DOI: 10.1016/j.compositesa.2018.12.021.

[26] Mingmeng Wang et al. “Micro-Computed Tomography Non-Destructive Testing and Defect Quantitative Analysis of Carbon Fiber-Reinforced Polymer, Glass Fiber-Reinforced Polymer and Carbon/Glass Hybrid Laminates Using Deep Learning Recognition”. In: *Applied Sciences* 13.23 (2023), p. 12192. DOI: 10.3390/app132312192.

[27] M. P. Alves, C. A. Cimini Junior, and S. K. Ha. “Fiber waviness and its effect on the mechanical performance of fiber reinforced polymer composites: An enhanced review”. In: *Composites Part A: Applied Science and Manufacturing* 149 (2021), p. 106526. DOI: 10.1016/j.compositesa.2021.106526.

[28] Hongfeng Li, Feng Li, and Lingxue Zhu. “Effect of Resin-Missing Defects on Tensile Behavior of Carbon Fiber/Epoxy Composites”. In: *Polymers* 16.3 (2024), p. 348. DOI: 10.3390/polym16030348.

[29] Sandeep Chava and Sirish Namilae. “Evolution of Composite Defects during Manufacturing: Wrinkles and Delamination”. In: *SAMPE Virtual Conference Proceedings*. Society for the Advancement of Material and Process Engineering. Daytona Beach, Florida, USA: SAMPE North America, 2020.

[30] Zhu Liu et al. “Effect Mechanism and Simulation of Voids on Hygrothermal Performances of Composites”. In: *Polymers* 14.5 (2022), p. 901. DOI: 10.3390/polym14050901.

[31] Robert Livingston and Behrad Koohbor. “Characterizing fiber-matrix debond and fiber interaction mechanisms by full-field measurements”. In: *Composites Part C: Open Access* (2025). DOI: 10.1016/j.jcomc.2025.100123.

[32] C. V. Opelt, G. M. Cândido, and M. C. Rezende. “Compressive failure of fiber reinforced polymer composites – A fractographic study of the compression failure modes”. In: *Materials Today Communications* 15 (2018), pp. 218–227. DOI: 10.1016/j.mtcomm.2018.02.020.

[33] Michael W. Davidson and Mortimer Abramowitz. “Optical Microscopy”. In: *Encyclopedia of Imaging Science and Technology* (2002). New York.

[34] Luis Villegas. “Optical nanoscopy of tissue sections”. MA thesis. Norway: UiT The Arctic University of Norway, 2018.

[35] Ijjas Fahi A et al. “A review on stereomicroscope”. In: *International Dental Journal of Student’s Research* 12.1 (2024), pp. 13–17. DOI: 10.18231/j.idjsr.2024.003.

[36] Peter Michael Wright. “Investigation of Damage in Laminated Carbon Fibre Composites Using High Resolution Computed Tomography”. PhD thesis. University of Southampton, 2011.

[37] Ralf Ditscherlein and Urs A. Peuker. “Three-Dimensional Particle-Discrete Datasets: Enabling Multidimensional Particle System Characterization Using X-Ray Tomography”. In: *Powders* 4.2 (2025), p. 12. DOI: 10.3390/powders4020012.

[38] Rigaku Corporation. *What is Micro-CT?* Rigaku website. Available at: https://rigaku.com/products/imaging-ndt/x-ray-ct/learning/micro-ct#micro-ct-what-is-it. Accessed: 2025-10-02. 2025.

[39] L. A. Feldkamp, L. C. Davis, and J. W. Kress. “Practical cone-beam algorithm”. In: *Journal of the Optical Society of America A* 1.6 (June 1984), pp. 612–619.

[40] Peng-fei He et al. “A procedure to detect, construct, quantify, numerically simulate and validate fracture networks in coal blocks”. In: *Geomechanics and Geophysics for Geo-Energy and Geo-Resources* 2 (2016). Published online: 25 July 2016, pp. 257–274. DOI: 10.1007/s40948-016-0035-1.

[41] F. Reyes et al. “Calibrated X-ray micro-tomography for mineral ore quantification”. In: *Minerals Engineering* 110 (2017), pp. 122–130. ISSN: 0892-6875. DOI: 10.1016/j.mineng.2017.05.010.

[42] F. Edward Boas and Dominik Fleischmann. “CT artifacts: Causes and reduction techniques”. In: *Imaging in Medicine* 4.2 (2012), pp. 229–240. DOI: 10.2217/IIM.12.13.

[43] J. Martínez-Martínez, D. Benavente, and M. A. García del Cura. “Petrographic quantification of brecciated rocks by image analysis. Application to the interpretation of elastic wave velocities”. In: *Engineering Geology* 90 (2007), pp. 41–54. ISSN: 0013-7952. DOI: 10.1016/j.enggeo.2006.12.003.

[44] Pratama Istiadi Guntoro et al. “X-ray Microcomputed Tomography (μCT) for Mineral Characterization: A Review of Data Analysis Methods”. In: *Minerals* 9.3 (2019), p. 167. DOI: 10.3390/min9030167.

[45] Aly Badran et al. “Validation of Deep Learning Segmentation of CT Images of Fiber-Reinforced Composites”. In: *Journal of Composites Science* 6.2 (2022), p. 60. DOI: 10.3390/jcs6020060.

[46] Aly Badran et al. “Automated Segmentation of Computed Tomography Images of Fiber-Reinforced Composites by Deep Learning”. In: *Journal of Materials Science* 55 (2020), pp. 16273–16289. DOI: 10.1007/s10853-020-04981-4.

[47] Marco Palanca, Gianluca Tozzi, and Luca Cristofolini. “The use of digital image correlation in the biomechanical area: a review”. In: *International Biomechanics* 3.1 (2016), pp. 1–21. DOI: 10.1080/23335432.2015.1117395.

[48] Digital Image Correlation Community. *Digital Image Correlation*. Online resource. Available at: https://digitalimagecorrelation.org/. Accessed: 2026-01-09. 2026.

[49] Chhoung Lim et al. “Strain Measuring of Composite Grid Using Digital Image Correlation”. In: *Journal of Sensors* 2022 (2022), pp. 1–12.

[50] International Digital Image Correlation Society. *A Good Practices Guide for Digital Image Correlation*. Standardization, Good Practices, and Uncertainty Quantification Committee. Oct. 2018.

[51] Michael A. Sutton, Jean-José Orteu, and Hubert W. Schreier. *Image Correlation for Shape, Motion and Deformation Measurements: Basic Concepts, Theory and Applications*. New York, NY: Springer Science & Business Media, 2009. ISBN: 978-0-387-78746-6. DOI: 10.1007/978-0-387-78747-3.

[52] B. Pan. “Recent Progress in Digital Image Correlation”. In: *Experimental Mechanics* 51.8 (2011), pp. 1223–1235. DOI: 10.1007/s11340-010-9418-3.

[53] C.-L. Tsai and I. M. Daniel. “Determination of Shear Modulus of Single Fibers”. In: *Experimental Mechanics* 39.4 (Dec. 1999), pp. 284–290.

[54] ASTM International. *Standard Test Methods for Density and Specific Gravity (Relative Density) of Plastics by Displacement*. ASTM Standard D792-08. West Conshohocken, PA. 2008.

[55] ASTM International. *Standard Test Method for Tensile Properties of Polymer Matrix Composite Materials*. ASTM Standard D3039/D3039M-20. West Conshohocken, PA. Available at: https://www.astm.org/DATABASE.CART/HISTORICAL/D3039-20.htm. 2020.

[56] Elbridge Z. Stowell. *Stress and Strain Concentration at a Circular Hole in an Infinite Plate*. Tech. rep. TN 2073. Washington: National Advisory Committee for Aeronautics, Apr. 1950.

[57] Sighard F. Hoerner and Henry V. Borst. *Fluid-Dynamic Lift: Practical Information on Aerodynamic and Hydrodynamic Lift*. 2nd. Mrs. Liselotte A. Hoerner, 1985.

[58] Jan R. Wright and Jonathan E. Cooper. *Introduction to Aircraft Aeroelasticity and Loads*. 2nd. Wiley, 2008.

[59] Aqua Flight. *The Best Efoils Have the Most Reliable Technology*. Aqua Flight website. Available at: https://aqua-flight.com/the-best-efoils-have-the-most-reliable-technology-aqua-flight/. Accessed: 2025-06-01. 2021.

[60] Luna Rossa Challenge. *The AC75 Wings*. Luna Rossa Challenge website. Available at: https://www.lunarossachallenge.com/en/news/761/_THE-AC75-WINGS-. Accessed: 2025-06-01. May 2021.

[61] Frank M. White. *Mecanica dos Fluidos*. 8th ed. Tradução da 8ª edição norte-americana. Porto Alegre, Brasil: AMGH Editora, 2016. ISBN: 978-85-8055-143-0.

[62] Patrick Ploé. “Surrogate-based optimization of hydrofoil shapes using RANS simulations”. Available at: https://theses.hal.science/tel-02050026v1. PhD thesis. École Centrale de Nantes, 2018.

[63] Vasco Brederode. *Aerodinâmica Incompressível: Fundamentos*. Lisboa, Portugal: Calouste Gulbenkian, 2014.

[64] Edward L. Houghton and Alan E. Brock. *Aerodynamics for Engineering Students*. London: Edward Arnold (Publishers) Ltd., 1960.

[65] John D. Anderson. *Fundamentals of Aerodynamics*. 6th. New York: McGraw-Hill Education, 2017.

[66] E. C. Yates. “Modified strip analysis method for predicting wing flutter at subsonic to hypersonic speeds”. In: *Journal of Aircraft* 3.1 (1966), pp. 25–29.

[67] Y. L. Young et al. “Load-dependent bend-twist coupling effects on the steady-state hydroelastic response of composite hydrofoils”. In: *Composite Structures* 189 (Apr. 2018), pp. 398–418. ISSN: 0263-8223. DOI: 10.1016/j.compstruct.2017.09.112.

[68] Gustavo A. Zarruk et al. *Experimental study of the steady fluid-structure interaction of flexible hydrofoils*. Unpublished or undated technical report. Australian Maritime College; Defence Science and Technology Organisation.

[69] F. Allavena. *History - MEBC*. Monaco Energy Boat Challenge website. Available at: https://energyboatchallenge.com/challenge/history/. Accessed: 2025-05-10. May 2021.

[70] Sighard F. Hoerner. *Fluid-Dynamic Drag: Practical Information on Aerodynamic Drag and Hydrodynamic Resistance*. Bakersfield, CA, USA: Liselotte A. Hoerner, Hoerner Fluid Dynamics, 1965.

[71] FEUP Academic Solar Team. “Atlântico - Desenvolvimento de uma Embarcação Elétrica com Hydrofoils e Casco de Fibras Naturais”. In: *Jornadas do Mar* (Oct. 2025).

[72] Dauntless Aviation. *Wing Planform*. Online resource. Available at: https://www.dauntless-soft.com/PRODUCTS/Freebies/Library/books/FLT/Chapter17/WingPlanform.htm. Accessed: 2025-06-01. 2025.

[73] P. P. Camanho et al. “Comparison of Specimen Geometries for Measuring Through-Thickness Tensile Mechanical Properties of Fibre-Reinforced Polymer Composites”. In: *Composites Part A: Applied Science and Manufacturing* 37.10 (2006), pp. 1654–1663. DOI: 10.1016/j.compositesa.2005.09.017.

[74] M. R. Wisnom. “Determination of Through-Thickness Tensile Strength of Carbon Epoxy Laminated Composites”. In: *Composites Science and Technology* 55.1 (1995), pp. 79–88. DOI: 10.1016/0266-3538(95)00041-0.

[75] Carl Zeiss Microscopy GmbH. *Extend the Limits of Your Exploration with Advanced 3D X-ray Microscopy: ZEISS VersaXRM 615*. Product brochure. Document ID: EN_44_012_115, Rel. 1.0, CZ 08/2024. Available at: https://www.zeiss.com/VersaXRM615. Accessed: 2026-01. 2024.

[76] Diogo de Azeredo Leitao et al. “FAST Hydrofoil in CMCF: experimental tests to detect any non-conformities or defects”. Master in Mechanical Engineering (M.Mec), Specialization in Aeronautical Structures and Vehicles. MA thesis. Porto, Portugal: Faculty of Engineering, University of Porto, 2025.

[77] Luca M. Martulli et al. “Carbon fibre sheet moulding compounds with high in-mould flow: linking morphology to tensile and compressive properties”. In: *Composites Part A: Applied Science and Manufacturing* 126 (2019), p. 105600. DOI: 10.1016/j.compositesa.2019.105600.

[78] Carolina Furtado Pereira da Silva. “Damage and Fracture in Advanced Composite Laminates: Thin-ply and Nanoengineered Composites”. PhD thesis. Porto, Portugal: Faculty of Engineering, University of Porto, 2020.

[79] Murilo Augusto Vaz, Julio Cesar Ramalho Cyrino, and Gilson Gomes da Silva. “Three-Dimensional Stress Concentration Factor in Finite Width Plates with a Circular Hole”. In: *World Journal of Mechanics* 3.3 (2013), pp. 153–159. DOI: 10.4236/wjm.2013.33013.

[80] M. Smith. *Abaqus Analysis User's Manual*. Version 6.9. Dassault Systèmes Simulia Corp. Providence, RI, USA, 2009.

[81] Andrew N. Norris. "Extreme Values of Poisson's Ratio and Other Engineering Moduli in Anisotropic Materials". In: *Journal of Mechanics of Materials and Structures* 1.4 (2006), pp. 793–812.

[82] Tiantong Lv et al. "Parametric Design and Modeling Method of Carbon Fiber Reinforcement Plastic-Laminated Components Applicable for Multi-Material Vehicle Body Development". In: *Journal of Computational Design and Engineering* (2023).

[83] Chaitanyaa K. K. et al. "Aerodynamic Analysis and Optimization of Airfoils Using Vortex Lattice Method". In: *IOP Conference Series: Materials Science and Engineering* 1013 (2021), p. 012023. DOI: 10.1088/1757-899X/1013/1/012023.

[84] AirfoilTools. *NACA 63-412 Airfoil (n63412-il)*. Online airfoil database. Available at: http://airfoiltools.com/airfoil/details?airfoil=n63412-il. Accessed: 2026-01-11. 2026.

[85] Yagmur Atescan-Yuksek et al. "Comparative life cycle assessment of aluminium and CFRP composites: the case of aerospace manufacturing". In: *The International Journal of Advanced Manufacturing Technology* 131 (2024), pp. 4345–4357. DOI: 10.1007/s00170-024-13241-3.

[86] Andrew J. Timmis et al. "Environmental impact assessment of aviation emission reduction through the implementation of composite materials". In: *The International Journal of Life Cycle Assessment* 20.2 (2015), pp. 233–243. DOI: 10.1007/s11367-014-0824-0.

[87] Michael Z. Hauschild, Ralph K. Rosenbaum, and Stig Irving Olsen, eds. *Life Cycle Assessment: Theory and Practice*. Springer, 2018. ISBN: 978-3-319-56474-6. DOI: 10.1007/978-3-319-56475-3.

[88] United Nations. *Transforming our world: the 2030 Agenda for Sustainable Development*. United Nations Sustainable Development Goals website. Available at: https://sdgs.un.org/goals. 2015.

[89] International Organization for Standardization. *Environmental Management — Life Cycle Assessment — Requirements and Guidelines*. ISO 14044:2006. Geneva, Switzerland. 2006.

[90] Tomas La Teixeira Matias Carreira. "FSI Analyses of a High-Performance Zero-Emission Small Craft Composite Hydrofoil". MA thesis. Lisbon, Portugal: IST, Universidade de Lisboa, Dec. 2024.

[91] Dennis Olsson and Felix Glaunsinger. *Comparative Life Cycle Assessment of Electric Hydrofoil Boats and Fossil Driven Alternatives*. Tech. rep. TRITA-ABE-MBT 22472. Degree Project in Industrial Ecology. Stockholm, Sweden: KTH Royal Institute of Technology, 2022.

[92] European Aluminium. *Environmental Profile Report for the European Aluminium Industry*. Tech. rep. Available at: https://european-aluminium.eu/wp-content/uploads/2023/01/European-Aluminium_Environmental-Profile-Report-2018_full-version.pdf. Brussels, Belgium: European Aluminium Association, 2018.

[93] MarineShift360 Consortium. *MarineShift360 Life Cycle Assessment Tool*. Online software platform. Available at: https://marineshift360.org. Accessed via MarineShift360 online interface for maritime life cycle assessment modelling. 2023.

[94] Muneer Baig et al. "Effect of Microstructure and Mechanical Properties of Al5083 Alloy Processed by ECAP at Room Temperature and High Temperature". In: *Crystals* 11.6 (2021), p. 683. DOI: 10.3390/cryst11060683.

[95] Jaehyun Kim et al. "Mechanical properties of woven laminates and felt composites using carbon fibers. Part 1: In-plane properties". In: *Composites Science and Technology* 64.13 (2004), pp. 2221–2229. DOI: 10.1016/j.compscitech.2004.03.012.

[96] Aluminium Warehouse. *50 mm - 5083 Aluminium Plate Cut to Size*. Online product page. Available at: https://www.aluminiumwarehouse.co.uk/products/50-mm-5083-aluminium-plate-1. Accessed: 2026-03-01. 2024.

[97] Haufler Composites. *Woven carbon fibers 200 g per m2 Epoxy Prepreg*. Online product page. Available at: https://www.compositeshop.de/xoshop/lng/en/fibers/carbon-fiber/woven-carbon-fibers-200gm-epoxy-prepreg.html. Accessed: 2026-03-01. 2026.

[98] Joost R. Duflou et al. "Do fiber-reinforced polymer composites provide environmentally benign alternatives? A life-cycle-assessment-based study". In: *MRS Bulletin* 37.4 (2012), pp. 374–382. DOI: 10.1557/mrs.2012.33.

[99] Jin Zhang et al. "Current status of carbon fibre and carbon fibre composites recycling". In: *Composites Part B: Engineering* 193 (2020), p. 108053. DOI: 10.1016/j.compositesb.2020.108053.

[100] Géraldine Oliveux, Luke O. Dandy, and Gary A. Leeke. "Current status of recycling of fibre reinforced polymers: Review of technologies, reuse and resulting properties". In: *Progress in Materials Science* 72 (2015), pp. 61–99. DOI: 10.1016/j.pmatsci.2015.01.004.

Appendix A

Carbon fiber datasheet

SAFETY DATA SHEET

in accordance with regulation (EC) N°1907/2006 – REACH

1 - PRODUCT AND COMPANY IDENTIFICATION

Product name	**Carbon Fibre Chopped Tow**
Relevant uses	rubber belts, thermosetting composites, textile yarns, paints, non-wovens, ablatives and friction materials
Uses advised against	None
Company name	Easy Composites Ltd
Address	Unit 39, Park Hall Business Village Longton, Stoke on Trent ST3 5XA, United Kingdom
Telephone number	+44 (0) 1782 454499
Email	sales@easycomposites.com

2 - HAZARDS IDENTIFICATION

Main product risks	**Electricity conducting material**. Airborne fibers can short circuit electrical equipment. **Our carbon fibers are NOT ATEX nor hazardous.**
Human health risks	Fine dust may irritate skin, eyes and mucous membranes. No case of disease reported.
Environmental risks	Known as a non-polluting product, but which **may cause electrical short circuits** when dispersed.
Specific risks	None
Supplemental hazard risks	Could contain traces of epoxy resin that may produce an allergic reaction: EUH 208.

*This product is an **ARTICLE** that is **NOT classified as hazardous** according to the decree of 07/12/2009, or regulations (EC) n°1272/2008 (CLP), 67/548/EEC and 1999/45/EC.*

3 - COMPOSITION / COMPONENT INFORMATION

Substance/mixture/Article	≥ 94% of carbon fiber (in graphite form)
Standard or chemical name	Carbon fiber on basis polyacrylonitrile
CAS number	7440-44-0
EINECS/ELINCS number	Polymer (231-153-3)
GHS/CLP or hazard symbols	**Not classified**
R-phrase	Not applicable
Substances of Very High Concern (SVHC)	None or below 0.1%
CMR	None or below 0.1%
Other components	original sizing (epoxy or polyether resins traces) ≤ 1.8 %

SAFETY DATA SHEET

in accordance with regulation (EC) N°1907/2006 – REACH

4 - FIRST AID MEASURES

General advice	Dust may be irritating. Change clothing.
Eye contact	Rinse thoroughly with plenty of water for at least 15 min and seek medical advice.
Skin contact	Wash thoroughly with water and soap.
Inhalation	Remove subject to fresh air. Seek medical attention if symptoms persist.
Ingestion	Rinse mouth and drink water. No medical treatment required.

5 - FIRE-FIGHTING MEASURES

Suitable extinguishing media	All usual extinguishing products appropriate for the surrounding fire are allowed. Avoid full water jet.
Specific hazards	Not flammable or combustible under normal uses. Risk of formation of toxic pyrolysis products (CO).
Special protective equipment for firefighters	Wear full-face, self-contained breathing apparatus to avoid inhalation of fumes or decomposition products.
Specific methods	None

6 - ACCIDENTAL RELEASE MEASURES

Individual precautions	Use an individual protection equipment.
Environmental precautions	Avoid worsening the dispersion. Prevent entry into waterways, sewers, basements or confined areas.
Cleaning methods	Avoid dust formation. Clean up with sweep or vacuum.

7 - HANDLING AND STORAGE

Handling precautions	Keep away from sources of ignition - **no smoking**. Avoid the dispersion of discharging loose fibres into open air. Wash thoroughly after handling. **No electrical appliances** or protect them in sealed or pressurised cases. Insulating varnish may be applied to electronic boards and electrical terminals.
Technical measures	**Electrical conducting material** - do not cut the carbon fibre unnecessarily. **DO NOT ALLOW CONTACT WITH ELECTRIC CURRENT SOURCES.**
Storage	Store in a cool (<50°C), dry and well-ventilated area.

SAFETY DATA SHEET

in accordance with regulation (EC) N°1907/2006 – REACH

8 - EXPOSURE CONTROLS / INDIVIDUAL PROTECTION

Engineering measures	Ensure adequate ventilation on workstation to avoid dust accumulation.
Control parameters	See local regulations. VME for total dust: 10 mg/m³. Long-term exposure for carbon fibers: 0.5 mg/m³ or 0.5 RFP/ml (respirable fiber-shaped particles).
Personal protective equipment:	
Respiratory protection	Use appropriate certified breathing apparatus in the event of high concentrations (poor ventilation, fine dust production). Filter apparatus FFP2 or FFP3.
Skin/hand protection	Gloves and protective clothing. Avoid skin contact.
Eye protection	Safety glasses with side shields or face protection.
Hygiene measures	Wash face and hands before eating, drinking or smoking and do it in separate areas. Use barrier skin cream or baby cleaning milk to wash hands and face.

9 - PHYSICAL AND CHEMICAL PROPERTIES

Physical state	solid
Form	**short fiber (filament)**
Colour	black or charcoal grey
Odour	none
pH	not applicable
Boiling point	not applicable
Melting point	> 2760 °C or 5000 °F
Vapour pressure/ Vapour density	not applicable
Specific gravity (filament)	1.6 to 2.0 g/cm³
Bulk density (short fibers)	0.1 to 0.5 kg/dm³ depending on whether the fiber is cut, chopped or milled ; depending on its length and the sizing type.
Flash point	no information available
Viscosity	no information available
Flammability	not applicable
Autoignition temperature	not applicable
Oxidizing properties	none
Decomposition temperature	> 650°C in air, > 290°C in preparation
Solubility in water and solvents used	insoluble fibre - sizing agent soluble in chlorinated solvents, acetone, DMF
Partition coefficient (n-octanol/water)	no information available

SAFETY DATA SHEET

in accordance with regulation (EC) N°1907/2006 – REACH

10 - STABILITY AND REACTIVITY

Stability	Stable.
Conditions to avoid	See section 7. **Avoid contact with heat, flame, spark**.
Hazardous reactions	Reactions with strong oxidizing agents. In the supplied form our product is not explosive however the processing and buildup of fine dust can lead to a risk of dust explosion (accumulation of fine dust in a closed area).
Hazardous decomposition products	Oxides of carbon (CO, COx).

11 - TOXICOLOGICAL INFORMATION

Acute toxicity	Product presumed **non toxic**.
Local effects	Carbon fibers and dust may cause mechanical irritation of the eyes, skin, nose and throat. The filament is not breathable (IARC). None carbon fibers with diameter below 3.5 µm (≥ 7 µm) and length below 80 µm, therefore they are not considered as "respirable fiber-shaped particles" (RFP ≤ 3.5 µm diameter).

12 - ECOLOGICAL INFORMATION

Ecotoxicity	This material is **not classified as dangerous** for the environment. Ecological data are not available.
Persistence and degradability	Non-polluting, stable product.
Mobility in soil	No information available.
Bioaccumulation	No information available.
PBT/vPvB	These products are not classified as PBT or vPvB.

13 - DISPOSAL CONSIDERATIONS

Waste disposal	Dispose of wastes in a suitable place according to local regulations - do not incinerate. Incineration may cause carbon fibre particles to be dispersed into the air which may damage electrical equipment.
Treatment of contaminated packaging	Packaging that cannot be cleaned should be disposed of as for product.

SAFETY DATA SHEET

in accordance with regulation (EC) N°1907/2006 – REACH

14 – TRANSPORT INFORMATION

Carbon products are **not classified as hazardous** in terms of national and international transport regulations – **no specific transport label** required (not ADR). **Not CLP-classified nor GHS classified.**

15 – REGULATORY INFORMATION

These products **are not** submitted to regulations (EC) n°1272/2008 (CLP), 67/548/EEC, nor n°1999/45/EC. This SDS has been established in accordance with REACH regulations (EC) N°1907/2006 and N°453/2010. All our products don't contain substances of very high concern (SVHC, REACH: EC 1907/2006 & 453/2010) or substances submitted to authorization (ANNEX XIV, REACH) or substances in current GADSL.

These products comply with **TSCA** (USA), **DSL/NDSL** (Canada), **EINECS/ELINCS** (Europe), **REACH UK** (UK), **CH INV** (Switzerland), **IECSC** (China), **ENCS** (Japan), **KECL** (Korea) and **AICS** (Australia) regulations.

16 – OTHER INFORMATION

We believe that the information contained in this safety data sheet is correct to the best to our knowledge. However, the information contained in this sheet is not exhaustive. This safety data sheet does not anticipate all the circumstances in which the product may be used, nor all the physical and mental characteristics of each individual responsible for its transport or transformation. It is the duty of the user to test and use this product safely, in accordance with the laws and regulations in force. Unless otherwise stated in writing, we accept no responsibility for complaints or damage caused related to the use of this product. For all additional information, please contact Easy Composites.

Appendix B

IN2 Epoxy Infusion Resin datasheet

TECHNICAL DATA SHEET

PRODUCT: IN-2 EPOXY INFUSION RESIN

DESCRIPTION

High performance low viscosity epoxy resin formulated specifically for use in resin infusion composites production.

USES

As an infusion resin it is ultra-low viscosity ensuring that it is able to quickly infuse through a range of reinforcements. Its excellent mechanical strength makes it ideally suited for use with high performance reinforcements such as carbon fibre and aramids like Kevlar.
Our IN-2 Epoxy Infusion Resin cures at room temperature with full mechanical properties achieved after only a moderate temperature post cure (50-60°C).

IN-2 Epoxy Infusion Resin is available with a choice of hardeners to achieve different pot-life and demould times. Available hardeners can themselves be blended to achieve even more precise reactivity control.

PROPERTIES

Property	Units	Resin	Hardener	Combined
Material	-	Epoxy Resin	Formulated Amine	Epoxy
Appearance	-	Straw	Straw	Clear
Viscosity @25 °C	mPa.s.	500 - 600	25 - 50	225
Density	g/cm^3	1.14 – 1.16	0.94 – 0.97	1.105

POT LIFE & CURE

Hardener	Pot-Life @ 25°C	Gelation Time @ 25°C	Demould Time @ 25°C
AT30 SLOW*	80-100mins	8-11hrs	18-24hrs
AT30 FAST*	9-14mins	2-4hrs	6-8hrs

*Fast and slow hardeners can be blended to achieve pot-life and demould times anywhere between those stated above.

CURED PROPERTIES

Property	Method	Units	AT30 SLOW	AT30 FAST
Colour			Pale yellow	Pale yellow
Machinability			Excellent	Excellent
Density 25°C	ASTM D 792	g/ml	1.08 – 1.12	1.08 – 1.12
Hardness 25°C	ASTM D 2240	Shore D/15	84.5 – 88.5	86 – 90
Maximum Tg	ASTM D 3418	°C	92 – 98	75 – 81
Water absorption (24h RT)	ASTM D 570	%	0.12 – 0.20	0.22 – 0.27
Water absorption (2hr 100°C)	ASTM D 570	%	0.58 – 0.70	0.95 – 1.00
Flexural strength	ASTM D 790)	MN/m²	112 – 124	95 – 109
Maximum strain	ASTM D 790)	%	5 – 7	4 – 6
Strain at break	ASTM D 790)	%	6 – 8	7 – 9
Flexural modulus	ASTM D 790)	MN/m²	3.15 – 3.55	2.5 – 3.1
Tensile strength	ASTM D 638	MN/m²	65.5 – 73.5	67.0 – 75.0
Elongation at break	ASTM D 638	%	6 – 8	5 – 7

MIXING RATIO

100 p.b.w. Epoxy Infusion Resin

	30 p.b.w. Epoxy Infusion Resin Hardener
MIXING INSTRUCTIONS	Mix Resin and hardener thoroughly, according to the indicated mixing ratio, avoiding air entrapment and make certain that material at the bottom and sides of the container is well stirred into the centre.
PROCESSING	For large infusion projects, always choose a hardener speed that will allow sufficient time for the part to infuse without any gelling occurring. To avoid premature gelling caused by exotherm in the resin feed pot, mix the resin in smaller batches and transfer into the resin feed pot as the part infuses. When doing this, take great care to ensure that the resin feed pot never runs out of resin. If in danger of going so before a new batch of resin can be added, clamp off the resin feed line to prevent air from being drawn into the infusion.
POST CURING	Post curing at elevated temperature is always advisable for room temperature curing resins in order to stabilize the component and to achieve the best possible mechanical properties from the resin. An elevated temperature post-cure is *required* for parts that will be subjected to higher temperatures during operation. The rate of heating and the indicated post-curing time are for typical sized components. Users should evaluate the best conditions of curing or post-curing depending on the component size and shape. For larger parts decrease the thermal gradient and increase the post-curing time. For best results, conduct the post cure in the mould without prior release (first ensure that the mould and release agent are compatible with the post cure temperature). Guideline post cure: 24h at room temperature 6 h @ 40°C 6 h @ 50°C 12 h @ 60°C
STORAGE	The resin and hardener should be stored in original, unopened containers between 15 and 25°C. KEEP THE PACKING TIGHTLY SEALED WHEN NOT IN USE.
SHELF LIFE	If stored under the above conditions the resin and hardener will have a shelf life of 12 months, from the date of production.

Our technical advice, whether verbal, or in writing is given in good faith, but without warranty - this also applies where proprietary rights of third parties are involved. It does not release you from the obligation to test the products supplied by Easy Composites as to their suitability for the intended processes and uses.
Easy Composites, Unit 39 Park Hall Business Village, Longton, Stoke on Trent. ST3 5XA
Tel. 01782 454499 Web. www.easycomposites.co.uk Email. sales@easycomposites.co.uk

Appendix C

Effect of Laminate Layup and Stacking Sequence on Stress Concentration

The ultimate strength is a function of both stress concentration and percentage of 0° plies. Laminates with a high percentage of 0° plies, but with a sufficient number of 45° plies to mollify the stress concentration factor, are the strongest. The $[0/90]_{2s}$ layup with a high percentage (50%) of 0° plies is not strong because of the high stress concentration factor. The $[\pm 45]_{2s}$ lay-up is the weakest because of the absence of 0° plies, although the stress concentration factor is the lowest. Stacking sequence was also found to have a noticeable influence on strength and failure patterns.

Table C.1: Comparison of Measured and Predicted Stress Concentration Factors and Strengths for Various Layups

Layup	**Axial Modulus $\bar{E}_x$, GPa (Msi)**	**Measured Stress Conc. Factor k_σ**	**Predicted Stress Conc. Factor k_σ**	**Notched Strength $\bar{F}_N$, MPa (ksi)**	**Unnotched Strength $\bar{F}_0$, MPa (ksi)**	**Strength Ratio $k_F = \bar{F}_N / \bar{F}_0$**
$[0/90/0/90]_s$	115.2 (16.70)	4.82	5.80	194 (28.1)	617 (89.5)	0.314
$[0_2/\pm 45/\bar{0}]_s$	133.9 (19.40)	3.58	3.68	498 (72.2)	807 (117.0)	0.617
$[\pm 45/0_2/0]_s$	127.3 (18.45)	4.02	3.68	426 (61.7)	807 (117.0)	0.529
$[0/\pm 45/0/\overline{90}]_s$	115.2 (16.70)	3.34	3.45	291 (42.2)	669 (97.0)	0.435
$[0_2/\pm 45/90]_s$	116.3 (16.85)	3.15	3.45	291 (42.2)	669 (97.0)	0.435
$[0/\pm 45/90]_s$	79.5 (11.52)	3.08	3.00	180 (26.1)	457 (66.2)	0.394
$[45/90/0/-45]_s$	81.4 (11.80)	3.10	3.00	213 (30.9)	459 (66.5)	0.465
$[\pm 45/0/\pm 45]_s$	59.3 (8.59)	2.46	2.45	206 (29.9)	378 (54.8)	0.546
$[\pm 45/\pm 45]_s$	19.9 (2.88)	2.06	1.84	125 (18.1)	137 (19.9)	0.909
$[45_2/-45_2]_s$	20.2 (2.93)	2.55	1.84	115 (16.6)	137 (19.9)	0.833

Appendix D

Inventory Explanation Report

Inventory Explanation

Data quality scoring methodology

A QA (Quality Assurance) rating of data is crucial for Marineshift360 to ensure the accuracy, reliability, and validity of the data it provides. Given the sensitivity of maritime operations to precise and high-quality data, a QA rating system helps maintain the integrity and trustworthiness of the platform's outputs. Therefore, we aimed to achieve and investigate the following features through the QA rating:

1. **Data Accuracy:** The data collected often come from diverse sources. Inaccurate or erroneous data can lead to faulty conclusions, inefficient operations, or environmental mishaps. A QA rating helps ensure that only accurate, verified data points are used in models or decision-making tools.
2. **Reliability and Consistency:** Consistent data quality is essential for ongoing monitoring and trend analysis. A QA system filters out unreliable or corrupted data, ensuring that long-term studies or operational decisions are based on consistent and dependable data sets.
3. **Stakeholder Confidence:** Users need to trust the data for their respective applications. A robust QA process fosters confidence in the platform, encouraging more users to rely on it for critical operations and decision-making.

MarineShift360 use a data quality assessment framework to ensure the data used within an LCA assessment is suitable for decision making and offers an acceptable level of confidence to stakeholders regarding the environmental assessments performed using LCI methodologies.

Each inventory datapoint used within your MarineShift360 project has been scored using the below data quality table. The averaged score for each datapoint is shown within the inventory data export within this report, this provides an aggregated score for the 5 categories (Precision, Inventory data time representativeness, Database time representativeness, technical representativeness and Geographical representativeness)

Please note – you should conduct your on data quality assessment on all the primary data inputs you have entered into the tool (material mass, energy consumption, transport distances etc) and declare your findings clearly within this section.

Table 1: QA rating dimension and scores definition.

Score	Precision	Inventory Data - Time representativeness	Database - Time representativeness	Technical representativeness	Geographical representativeness
1	Measured/ calculated and verified	The data (collection date) can be maximum 2 years old with respect to the “reference year” of the dataset	The “reference year” of the tendered dataset falls within the time validity of the secondary dataset	Technology aspects have been modelled exactly as described in the title and metadata, without any significant need for improvement	The processes included in the dataset are fully representative for the geography stated in the “location” indicated in the metadata
2	Measured/ calculated/ literature and plausibility checked by a reviewer	The data (collection date) can be maximum 4 years old with respect to the “reference year” of the dataset	The “reference year” of the tendered dataset is maximum 2 years beyond the time validity of the secondary dataset	Technology aspects are very similar to what described in the title and metadata with need for limited improvements. For example, use of generic technologies’ data instead of modelling all the single plants.	The processes included in the dataset are well representative for the geography stated in the “location” indicated in the metadata

3	Measured/ calculated/ literature and plausibility not checked by a reviewer OR qualified estimate based on calculations plausibility checked by a reviewer	The data (collection date) can be maximum 6 years old with respect to the “reference year” of the dataset	The “reference year” of the tendered dataset is maximum 3 years beyond the time validity of the secondary dataset	Technology aspects are similar to what is described in the title and metadata but merits improvements. Some of the relevant processes are not modelled with specific data but using proxies	The processes included in the dataset are sufficiently representative for the geography stated in the “location” indicated in the metadata. E.g., the represented country differs but has a very similar electricity grid mix profile
4	Qualified estimate based on calculations; plausibility not checked by reviewer	The data (collection date) can be maximum 8 years old with respect to the “reference year” of the dataset	The “reference year” of the tendered dataset is maximum 4 years beyond the time validity of the secondary dataset	Technology aspects are different from what described in the title and metadata. Requires major improvements	The processes included in the dataset are only partly representative for the geography stated in the “location” indicated in the metadata. E.g., the represented country differs and has a substantially different electricity grid mix profile The processes included in the dataset are not representative for the geography stated in the “location” indicated in the metadata
5	Rough estimate with known deficits	The data (collection date) is older than 8 years with respect to the “reference year” of the dataset	The “reference year” of the tendered dataset is more than 4 years beyond the time validity of the secondary dataset	Technology aspects are completely different from what described in the title and metadata. Substantial improvement is necessary	The processes included in the dataset are not representative for the geography stated in the “location” indicated in the metadata

Inventory explanation

[This section will be automatically populated with details of all the factors used in your project.]

All templates - Utility

- Description of product system: Electricity - Renewable - EU-27 low voltage - 40% Renewable - 60% EU Average
- Used in the following assessment(s): Three aluminum foils (30% re-use) (copy), Three CF Prepeg hydrofoils (copy), Three CF Prepeg hydrofoils (copy), Three FC Hydrofoil (normal), Three FC Hydrofoil (re-use)
- Functional unit: kWh

- System boundaries: Cradle to consumer
- Data geographical coverage: RER-Europe
- LCIA methodology: % of Electricity - per region - Europe (electricity mix low voltage) & % of Electricity - Renewable (average)
- Database used for calculation: MS360
- Assumptions: N/A

Metals - Material

- Description of product system: Metal - Aluminium sheet (30% recycled)
- Used in the following assessment(s): Three aluminum foils (30% re-use) (copy)
- Functional unit: kg
- System boundaries: Cradle to gate
- Data geographical coverage: Global
- LCIA methodology: Aluminium, wrought alloy {GLO}| market for + Sheet rolling, aluminium {GLO}| market for. Aluminiun primary ingot assumptions: 9% Europe, 5% North America, 86% ROW (source: Gemini query - backed up by assumptions in Ecoinvent markets).
- Database used for calculation: ecoinvent 3.11
- Assumptions: Please visit [https://ecoquery.ecoinvent.org/3.11/cutoff] for more details

Composites - Laminating Process

- Description of product system: Laminating - Hand Laminated
- Used in the following assessment(s): Three CF Prepeg hydrofoils (copy), Three CF Prepeg hydrofoils (copy), Three FC Hydrofoil (normal), Three FC Hydrofoil (normal), Three FC Hydrofoil (re-use), Three FC Hydrofoil (re-use)
- Functional unit: kg
- System boundaries: Cradle to distributor
- Data geographical coverage: EU
- LCIA methodology: MS360 vacuum consumable inventory estimate based on an algorithm developed using the Marine Composite industry best practice, taking into account an estimate for materials upstream transport to the site of distribution. Upstream transport impact based on 1500km Transport - Road - Freight, lorry >32t and 9500km Transport - Water - Freight, sea container ship. Wastage factor as per the detailed material inventory. Laminate post-cure electricity consumption not included. Functional unit is the process of 1sqm of finished part.
- Database used for calculation: MS360
- Assumptions: BOM consumable inventory detail modelled for 5sqm of Hand Laminated Process: Consumable - Peelply - qty ordered = Area x 1.0

Composites - Release Prep

- Description of product system: Releasing agent - Wax
- Used in the following assessment(s): Three CF Prepeg hydrofoils (copy), Three FC Hydrofoil (normal), Three FC Hydrofoil (re-use)
- Functional unit: kg
- System boundaries: Cradle to distributor
- Data geographical coverage: Global
- LCIA methodology: market for Wax, lost-wax casting / GLO / 3.11 cut off
- Database used for calculation: ecoinvent 3.11
- Assumptions: Please visit [https://ecoquery.ecoinvent.org/3.11/cutoff] for more details

Wood - Timber

- Description of product system: Timber - MDF
- Used in the following assessment(s): Three CF Prepeg hydrofoils (copy), Three FC Hydrofoil (normal), Three FC Hydrofoil (re-use)
- Functional unit: kg
- System boundaries: Cradle to distributor
- Data geographical coverage: RoW-Rest of the World
- LCIA methodology: market for medium density fibreboard, RoW, 3.11 cut-off. The original inventory has as reference unit m3, but here it is divided by 750 to adapt the inventory to kg
- Database used for calculation: ecoinvent 3.11
- Assumptions: Please visit [https://ecoquery.ecoinvent.org/3.11/cutoff] for more details

Composites - Resin

- Description of product system: Resin - Epoxy / Petrolbased
- Used in the following assessment(s): Three CF Prepeg hydrofoils (copy), Three FC Hydrofoil (normal), Three FC Hydrofoil (re-use)
- Functional unit: kg
- System boundaries: Cradle to gate
- Data geographical coverage: RER-Europe
- LCIA methodology: market for epoxy resin, liquid / RER / 3.11 cut off
- Database used for calculation: ecoinvent 3.11
- Assumptions: Please visit [https://ecoquery.ecoinvent.org/3.11/cutoff] for more details

Composites - Laminating Process

- Description of product system: Laminating - Prepreg Autoclave Cured
- Used in the following assessment(s): Three CF Prepeg hydrofoils (copy)
- Functional unit: kg
- System boundaries: Cradle to distributor
- Data geographical coverage: EU
- LCIA methodology: MS360 vacuum consumable inventory estimate based on an algorithm developed using the Marine Composite industry best practice, taking into account an estimate for materials upstream transport to the site of distribution. Upstream transport impact based on 1500km Transport - Road - Freight, lorry >32t and 9500km Transport - Water - Freight, sea container ship. Wastage factor as per the detaied material inventory. Prepreg Autoclave Cured Laminating power consumption estimate based on on 1x 1.5 kW motor running 24hrs and 1x 7.5 kW motor running 6hrs and 1x 16.5 kW compressor running 2hrs for 5sqm / Electricity - EU-27 <1kV (Europe mix low voltage). Autoclave cure electricity consumption not included. Functional unit is the process of 1sqm of finished part.
- Database used for calculation: MS360
- Assumptions: BOM vacuum consumables inventory detail modelled for 5sqm of Prepreg Autoclave Cured Process: Consumable - Peelply - qty ordered = Area x 1.25 / Vacuum consumable - P3 plastic - qty ordered = Area x 1.25 / Vacuum consumable - 175gsm e-glass - qty ordered = Area x 1.25 / Vacuum consumable - P6 plastic - qty ordered = Area x 1.25 / Vacuum consumable - Plastic mesh - qty ordered = Area x 1.25 / Vacuum consumable - High temp vac bag - qty ordered = Area x 2 / Vacuum consumable - Vac sealant tape - qty ordered = (Length x 2 + Width x 2) x 1.5 / Vacuum consumable - Plastic mesh - qty ordered = Area x 1.25 x 2 / Vacuum consumable - Low temp vac bag - qty ordered = Area x 2 x 2 / Vacuum consumable - Vac sealant tape - qty ordered = (Length x 2 + Width x 2) x 1.5 x 2 / Vacuum intensifier - Rubber sheet - qty ordered = Area x 0.1

Composites - Dry Fibre

- Description of product system: Dry fibers - Carbon Standard Modulus
- Used in the following assessment(s): Three CF Prepeg hydrofoils (copy)
- Functional unit: kg
- System boundaries: Cradle to distributor
- Data geographical coverage: Global
- LCIA methodology: This process is an approximation to the production of carbon fiber, based on the information available in: Environmental impact analysis of composite use in car manufacturing; J.R. Duflou (2)a,*, J. De Moor a, I. Verpoest b, W. Dewulf. Assumption of carbonization between 1000˚C and 1700˚C for Standard Modulus Carbon (up to 250GPa). Primary data-points sourced via "Ecoinvent 3.11 cut off" and computed by MS360, taking into account an estimate for raw materials upstream transport to the site of carbon fibre production. Transport impact based on 1500km Transport - Road - Freight, lorry >32t and 9500km Transport - Water - Freight, sea container ship. Functional unit is 1kg of dry fibre tow.
- Database used for calculation: MS360
- Assumptions: PAN average of "market for Acrylonitrile / GLO / 3.11 cut off / market for weaving, synthetic fibre / GLO / 3.11 cut off / market group for Electricity, low voltage / GLO / 3.11 cut off" & "acrylonitrile production, Sohio process / RoW / 3.11 cut off / market group for Electricity, low voltage / RER / 3.11 cut off / market group for heat, district or industrial, other than natural gas / RER / 3.11 cut off / heat production, heavy fuel oil, at industrial furnace 1MW / RoW / 3.11 cut off". PAN environmental impact alinged with the 2023 study "Bringing Light into the Dark—Overview of Environmental Impacts of Carbon Fiber Production and Potential Levers for Reduction"

Composites - Resin

- Description of product system: Resin - Epoxy / Bioresin

- Used in the following assessment(s): Three CF Prepeg hydrofoils (copy), Three FC Hydrofoil (normal), Three FC Hydrofoil (re-use)
- Functional unit: kg
- System boundaries: Cradle to gate
- Data geographical coverage: RER-Europe
- LCIA methodology: market for epoxy resin, liquid / RER / 3.11 cut off. Bioresin impacts reduced by 17,5% based on Information based on: https://entropyresins.com/blog/2021/01/19/understanding-our-life-cycle-assessment
- Database used for calculation: ecoinvent 3.11
- Assumptions: Please visit [https://ecoquery.ecoinvent.org/3.11/cutoff] for more details

Composites - Dry Fibre

- Description of product system: Dry fibers - Carbon Unspecified Modulus
- Used in the following assessment(s): Three FC Hydrofoil (normal)
- Functional unit: kg
- System boundaries: Cradle to gate
- Data geographical coverage: RER-Europe
- LCIA methodology: Weighted average using the environmental value of MS360 datapoints: Dry fibers - Carbon Standard Modulus, Dry fibers - Carbon Intermediate Modulus, and Dry fibers - Carbon High Modulus.
- Database used for calculation: MS360
- Assumptions: The global market breakdown by modulus type for carbon fiber manufacturing: • Standard Modulus (SM): Represents around 70% of the global market share. • Intermediate Modulus (IM): Commands approximately 20% of the market. • High Modulus (HM): Takes up roughly 10% of the total.

Composites - Resin

- Description of product system: Resin - Epoxy resin hardener
- Used in the following assessment(s): Three FC Hydrofoil (normal), Three FC Hydrofoil (re-use)
- Functional unit: kg
- System boundaries: Cradle to distributor
- Data geographical coverage: Global
- LCIA methodology: market for phthalic anhydride / RoW / 3.11 cut off
- Database used for calculation: ecoinvent 3.11
- Assumptions: Please visit [https://ecoquery.ecoinvent.org/3.11/cutoff] for more details

All templates - Material

- Description of product system: Material - Reused
- Used in the following assessment(s): Three FC Hydrofoil (re-use)
- Functional unit: kg
- System boundaries: Waste treatment
- Data geographical coverage: Global
- LCIA methodology: As per the 100:0 allocation procedure
- Database used for calculation: MS360
- Assumptions: For entry related to material that is reused (not recycled) onsite, at the same boat yard. The second use of the material is essentially “free” of burden with all emissions at zero value.